



TECHNISCHE  
UNIVERSITÄT  
WIEN

Vienna University of Technology

## DISSERTATION

# Superconductivity and Magnetism in Rare-Earth Nickel Boronitrides

ausgeführt zum Zwecke der Erlangung des akademischen Grades eines  
Doktors der technischen Wissenschaften unter der Leitung von

a.o. Univ. Prof. Dr.techn. Herwig Michor

E138

Institut für Festkörperphysik

eingereicht an der Technischen Universität Wien

Fakultät für Physik

von

Tahir Ali

Matr.-Nr. 0627700

Weyringergasse 39/3/33

1040 Wien

February 4, 2011

*To*  
the memory of my *mother*

# Kurzfassung

Quaternäre Selten-Erd Nickel Boronitride  $R_3\text{Ni}_2\text{B}_2\text{N}_{3-\delta}$  sind intermetallische Verbindungen mit einer einzigartigen, geschichteten Kristallstruktur, die sich aus alternierenden NiB Lagen (Anordnung im PbO-Typ) und LaN dreifach Lagen (Schicht im NaCl-Typ) zusammensetzt. Ihre besonderen physikalischen Eigenschaften wie Supraleitung und Selten-Erd Magnetismus qualifizieren diese Verbindungen für Untersuchungen der Wechselwirkung von Supraleitung und Magnetismus.

Im Rahmen dieser Dissertation werden kristallchemische und elektronische Grundzustandseigenschaften von  $R_3\text{Ni}_2\text{B}_2\text{N}_{3-\delta}$  mit  $R = \text{La, Ce, Pr}$  und  $\text{Nd}$  untersucht. Wie mit Pulver-Röntgendiffraktion gezeigt wird, kristallisieren alle diese Verbindungen und deren Mischkristallreihen in der raumzentriert tetragonalen  $\text{La}_3\text{Ni}_2\text{B}_2\text{N}_3$  Struktur. Das Substituieren von La durch Ce, Pr oder Nd in  $(\text{La,R})_3\text{Ni}_2\text{B}_2\text{N}_{3-\delta}$  führt zu einer sukzessiven Unterdrückung der Supraleitung, die im Rahmen der Abrikosov-Gorkov Paarbrechungstheorie analysiert wird. Während die erstmalig hergestellte Verbindung  $\text{Nd}_3\text{Ni}_2\text{B}_2\text{N}_{3-\delta}$  zwei magnetische Phasenübergänge, einen ferrimagnetischen und eine Spin-Reorientierung zu einem nahezu antiferromagnetischen Zustand, zeigt, wurde für  $\text{Pr}_3\text{Ni}_2\text{B}_2\text{N}_{3-\delta}$  keine langreichweitige magnetische Ordnung festgestellt. Die Temperaturabhängigkeiten der physikalischen Eigenschaften von  $\text{Ce}_3\text{Ni}_2\text{B}_2\text{N}_{3-\delta}$  charakterisieren diese Verbindung als zwischenvalentes System mit einer Cer Valenz nahe 3.2. Das Verhalten des elektrischen Widerstandes und der Thermokraft werden im Rahmen eines Anderson Gittermodells diskutiert.

Untersuchungen mittels Röntgen- und Neutronendiffraktion an  $\text{La}_3\text{Ni}_2\text{B}_2\text{N}_{3-\delta}$  offenbaren eine endliche Ausdehnung der Phasenbildung bezüglich der N-Stöchiometrie. Eigenschaften im normalleitenden und supraleitenden Zustand wurden durch Messungen von Transporteigenschaften, der Magnetisierung und der spezifischer Wärme untersucht. Eine systematische Abnahme der supraleitenden Sprungtemperatur  $T_c$  von 14 K auf 12 K und bemerkenswerte Zusammenhänge mit Änderungen normalleitender Eigenschaften wie dem Restwiderstand mit zunehmender Häufigkeit von N-Fehlstellen wurden festgestellt. Starke paarbrechende Effekte durch Fehlstellen oder andere nichtmagnetische Gitterstörungen weisen im Allgemeinen auf einen unkonventionellen supraleitenden Ordnungsparameter hin. Die Auswertung thermodynamischer Eigenschaften des supraleitenden Zustandes von  $\text{La}_3\text{Ni}_2\text{B}_2\text{N}_{3-\delta}$  sowie Vergleiche mit theoretischen Modellen bezeugen aber einen  $s$ -Wellen Ordnungsparameter mit einer vollständig ausgebildeten Energielücke.

# Abstract

Quaternary rare-earth nickel boronitrides  $R_3\text{Ni}_2\text{B}_2\text{N}_{3-\delta}$  are intermetallic compounds with a unique layered crystal structure where NiB layers (PbO-type sheets) alternate with LaN triple-layers (rock salt type sheets) and they exhibit interesting physical properties such as superconductivity and rare earth magnetism and are, thus, candidates for studying the interplay of superconductivity and magnetism.

In the scope of this thesis crystal-chemistry and electronic ground state properties of  $R_3\text{Ni}_2\text{B}_2\text{N}_{3-\delta}$  ( $R=\text{La, Ce, Pr, Nd}$ ) were investigated. Powder X-ray diffraction studies confirmed all these compounds and their solid solutions to crystallize in the body centered tetragonal  $\text{La}_3\text{Ni}_2\text{B}_2\text{N}_3$  structure type. The substitution of La by Ce, Pr or Nd in  $(\text{La},R)_3\text{Ni}_2\text{B}_2\text{N}_{3-\delta}$  leads to a gradual suppression of superconductivity which is analyzed in terms of Abrikosov-Gorkov pair breaking effects. The novel compound  $\text{Pr}_3\text{Ni}_2\text{B}_2\text{N}_{3-\delta}$  is found to exhibit no long range magnetic order while  $\text{Nd}_3\text{Ni}_2\text{B}_2\text{N}_{3-\delta}$  shows ferrimagnetic ordering and a spin re-orientation transition to a nearly anti-ferromagnetic state. Temperature dependent physical properties characterize  $\text{Ce}_3\text{Ni}_2\text{B}_2\text{N}_{3-\delta}$  as an intermediate valence system with a cerium valence near 3.2. The electrical resistivity and thermoelectric power of  $\text{Ce}_3\text{Ni}_2\text{B}_2\text{N}_{3-\delta}$  are analyzed in terms of the degenerate Anderson lattice model.

From X-ray and neutron powder diffraction studies on  $\text{La}_3\text{Ni}_2\text{B}_2\text{N}_{3-\delta}$  a finite width of formation with respect to the N-stoichiometry is observed. The normal and superconducting state properties of  $\text{La}_3\text{Ni}_2\text{B}_2\text{N}_{3-\delta}$  were investigated by means of transport, magnetic and calorimetric measurements. A remarkable correlation and systematic reduction of the superconducting transition temperature  $T_c$  from about 14 K to 12 K as well as changes of normal state characteristics like the residual resistivity with an increasing density of N-vacancies are established. A strong pair-breaking effect caused by vacancies or other non-magnetic impurities usually points towards an unconventional superconducting order parameter. The analysis of thermodynamic features of the superconducting state of  $\text{La}_3\text{Ni}_2\text{B}_2\text{N}_{3-\delta}$  as well as a theoretical modeling, however, indicate a fully-gapped  $s$ -wave order parameter.

# Acknowledgement

Foremost, I would like to express my sincere gratitude and appreciations to my supervisor Prof. Herwig Michor for the continuous support of my Ph.D study and research, for his patience, motivation, enthusiasm, and immense knowledge. His guidance and personal interest helped me in all the time of research and writing of this thesis. His never-ending encouragement and valuable supervision have been essential for this work.

My deepest gratitude to Prof. Gerfried Hilscher for his help and support. His expertise and invaluable discussions helped greatly during experimental work as well as in completion of this dissertation. Many thanks to Prof. Ernst Bauer also for his kind assistance and cooperation throughout this work and to Prof. Peter Rogl for evaluating this thesis.

I am thankful to Christian Rupprecht, Rao Tahir Khan and Kamran Ali for their help in performing many measurements and to Sherryl Manalo for doing some important calculations. I am grateful to Clemens Simson and Saleh Muhammad for their sincere help on many occasions and to Muhammad Atif and Nasir Mehboob for their nice company.

Many thanks to Prof. Herbert Sassik, Doz. Dr. Martin Pieper and Ing. Peter Hundegger for their cooperation at various phases of the experimental work.

I am obliged to Higher Education Commission, Government of Pakistan for giving me the opportunity with financial support to pursue my Ph.D research and to Austrian Science Foundation for their support under project number P-16250 . I am grateful to Austrian Exchange Services (ÖAD) for their sincere help throughout my stay in Vienna.

Last but not the least, I would like to thank my family and especially my wife Sumbal. I would like to extend my heartily appreciations to my wife for her patience and kind enough support in taking very good care of our kids Uzair and Aayan.

# Contents

<b>Introduction</b>	<b>4</b>
<b>1 Experimental</b>	<b>6</b>
1.0.1 Electrical resistivity measurements . . . . .	6
1.0.2 Specific heat measurements . . . . .	7
1.0.3 Thermopower measurements . . . . .	7
1.0.4 Thermal conductivity measurements . . . . .	7
<b>2 Some theoretical Concepts of superconductivity</b>	<b>9</b>
2.1 The critical magnetic fields . . . . .	9
2.2 Concepts of GLAG theory . . . . .	10
2.3 BCS theory . . . . .	11
2.4 Eliashberg theory and impurity scattering . . . . .	13
<b>3 Preparation, structure and width of formation of <math>\text{La}_3\text{Ni}_2\text{B}_2\text{N}_{3-\delta}</math></b>	<b>19</b>
3.1 Introduction . . . . .	19
3.2 Sample preparation . . . . .	21
3.3 Thermal treatment and phase purity . . . . .	22
3.4 Powder X-ray diffractometry . . . . .	22
3.4.1 Phase analysis and nominal width of formation . . . . .	23
3.5 Nuclear magnetic resonance spectroscopy . . . . .	26
3.6 Neutron powder diffractometry . . . . .	28
3.6.1 Phase analysis . . . . .	31
3.6.2 Structure analysis and real width of formation . . . . .	31
3.6.3 Thermal expansion . . . . .	34
3.6.4 Atomic displacement parameters . . . . .	38
<b>4 Normal state properties of <math>\text{La}_3\text{Ni}_2\text{B}_2\text{N}_{3-\delta}</math></b>	<b>42</b>
4.1 Introduction . . . . .	42
4.2 Transport properties . . . . .	43
4.2.1 Electrical resistivity . . . . .	43
4.2.2 Thermopower . . . . .	48

4.2.3	Thermal Conductivity . . . . .	49
4.3	Magnetic Properties . . . . .	52
4.4	Specific Heat . . . . .	54
<b>5</b>	<b>Superconducting properties of <math>\text{La}_3\text{Ni}_2\text{B}_2\text{N}_{3-\delta}</math></b>	<b>59</b>
5.1	Introduction . . . . .	59
5.2	Results of resistivity measurements . . . . .	59
5.2.1	Resistivity in zero field . . . . .	59
5.2.2	Magnetoresistance measurement . . . . .	61
5.2.3	Resistivity under hydrostatic pressure . . . . .	64
5.3	Magnetic measurements . . . . .	67
5.4	Specific heat measurements . . . . .	69
5.4.1	Electronic specific heat and superconducting gap . . . . .	73
5.4.2	Thermodynamic critical field . . . . .	76
5.4.3	Electron phonon mass enhancement $\lambda_{ep}$ . . . . .	77
5.4.4	Ginzburg-Landau parameter $\kappa$ and characteristic lengths $\xi$ and $\lambda_{GL}$ . . . . .	79
5.4.5	Field dependent Sommerfeld coefficient $\gamma(H)$ . . . . .	79
5.4.6	Discussion and analysis in terms of Eliashberg model calculations . . . . .	81
<b>6</b>	<b>Ground state properties of <math>\text{Ce}_3\text{Ni}_2\text{B}_2\text{N}_{3-\delta}</math></b>	<b>84</b>
6.1	Introduction . . . . .	84
6.2	Sample preparation . . . . .	85
6.3	Structural Characterization . . . . .	85
6.4	Superconductivity in $\text{La}_{3-x}\text{Ce}_x\text{Ni}_2\text{B}_2\text{N}_{3-\delta}$ . . . . .	89
6.5	Ground state properties of $\text{Ce}_3\text{Ni}_2\text{B}_2\text{N}_{3-\delta}$ . . . . .	90
6.5.1	Results of thermodynamic and transport studies . . . . .	90
<b>7</b>	<b>Formation and ground state properties of <math>\text{La}_{3-x}\text{R}_x\text{Ni}_2\text{B}_2\text{N}_{3-\delta}</math> with <math>\text{R}=\text{Pr}, \text{Nd}</math></b>	<b>98</b>
7.1	Sample preparation . . . . .	98
7.2	Structural characterization . . . . .	99
7.2.1	Phase analysis of $\text{La}_{3-x}\text{Pr}_x\text{Ni}_2\text{B}_2\text{N}_{3-\delta}$ . . . . .	99
7.2.2	Phase analysis of $\text{La}_{3-x}\text{Nd}_x\text{Ni}_2\text{B}_2\text{N}_{3-\delta}$ . . . . .	101
7.3	Magnetic and resistivity measurements . . . . .	101
7.3.1	Magnetic measurements . . . . .	101
7.4	Discussion of Abrikosov Gor'kov type pair breaking . . . . .	106
7.5	Ground state properties of $\text{Pr}_3\text{Ni}_2\text{B}_2\text{N}_{3-\delta}$ . . . . .	108
7.6	Ground state properties of $\text{Nd}_3\text{Ni}_2\text{B}_2\text{N}_{3-\delta}$ . . . . .	110
	<b>Summary</b>	<b>116</b>

<b>A Additional X-ray diffraction data</b>	<b>118</b>
<b>Bibliography</b>	<b>118</b>
<b>List of publications</b>	<b>129</b>
<b>List of conference contributions</b>	<b>130</b>



# Introduction

In search for superconductors with higher superconducting (SC) transition temperatures  $T_c$ , various more complex multinary SC compounds have been discovered. The most exciting systems among them are the high- $T_c$  cuprates, iron-pnictides and among others, quaternary borocarbides and boronitrides. The SC compound  $\text{La}_3\text{Ni}_2\text{B}_2\text{N}_{3-\delta}$  was reported around the same time when superconductivity in the closely related borocarbide superconductors  $R\text{Ni}_2\text{B}_2\text{C}$  ( $R$ ...rare earths and Y) was discovered. Many compounds  $RT_2\text{B}_2\text{C}$  ( $T$ ...transition metals, e.g. Ni, Pd, Pt) have been explored revealing a large variety of low-temperature ground states ranging from superconductivity (for e.g. Y- and  $\text{LuNi}_2\text{B}_2\text{C}$ ) with possibly an unconventional order parameter, superconductivity coexisting with magnetic order (for  $R\text{Ni}_2\text{B}_2\text{C}$  with  $R = \text{Dy, Ho, Er, Tm}$ ) to magnetic order without superconductivity (with  $R = \text{Pr, Sm, Nd, Gd, Tb}$ ). On the other hand, in the case of the related triple layer boronitrides, no compounds other than the SC  $\text{La}_3\text{Ni}_2\text{B}_2\text{N}_{3-\delta}$  and non-SC  $\text{Ce}_3\text{Ni}_2\text{B}_2\text{N}_{3-\delta}$  have been reported yet.

$\text{La}_3\text{Ni}_2\text{B}_2\text{N}_{3-\delta}$  was reported to be a moderate to strong coupling superconductor with a  $T_c$  of about 12 K which exhibits various interesting features of the SC state, some of them very similar to those of the related borocarbide superconductors, some of them clearly different. An important aspect of the boronitride superconductors yet to be explored is the specific role of nitrogen vacancies with respect to the significant (up to 20%) spread of  $T_c$  values observed in earlier studies. If caused by impurity scattering, the latter may refer to an unconventional (other than s-wave) SC order parameter. One aim of this work is, thus, to explore the interrelationship between nitrogen vacancies,  $T_c$ , and SC state properties and to test models that have been developed e.g. for anisotropic electron-phonon mediated s-wave superconductors with paramagnetic impurities.  $\text{La}_3\text{Ni}_2\text{B}_2\text{N}_{3-\delta}$  could prove to be a model system if it can be shown that nitrogen vacancies act as potential scattering centers without changing the electronic structure.

An equally important aim of the present work is to explore novel boronitride intermetallics  $R_3\text{Ni}_2\text{B}_2\text{N}_{3-\delta}$  with magnetic rare earth ions  $R = \text{Ce, Pr, Nd}$  with respect to structural, superconducting and magnetic properties. Ce based intermetallic compounds are known to exhibit a rich variety of ground

states namely, Kondo lattice, intermediate valence, Kondo insulator, and in some cases unconventional superconductivity. Also, many cases are known where Ce causes a strong pair breaking effect if added as an impurity in a superconducting matrix. The structural, superconducting, and Ce ground state properties of  $(\text{La,Ce})_3\text{Ni}_2\text{B}_2\text{N}_{3-\delta}$  are, thus, studied here in detail by means of x-ray diffraction, susceptibility, specific heat, and transport measurements.

In this work, the compounds  $\text{Pr}_3\text{Ni}_2\text{B}_2\text{N}_{3-\delta}$  and  $\text{Nd}_3\text{Ni}_2\text{B}_2\text{N}_{3-\delta}$  are characterized for the first time. They are studied with respect to magnetic pair-breaking in their solid solutions with  $\text{La}_3\text{Ni}_2\text{B}_2\text{N}_{3-\delta}$  and with respect to the magnetic ground state properties of the pure compounds.

# Chapter 1

## Experimental

Most measurements were carried out on home made setups while some selected measurements were performed on commercially available systems like the vibrating sample magnetometer (VSM) of the *Quantum Design PPMS* and the *Cryogenic SQUID* magnetometer. Powder x-ray diffraction studies were performed on a *Siemens D5000* equipped with a graphite monochromator. A brief summary of the home made systems is given below.

### 1.0.1 Electrical resistivity measurements

Electrical resistivity measurements were performed by standard 4 probe a.c. and d.c. techniques. Measurements were carried out from 4.2 K to room temperature in a conventional  $^4\text{He}$  cryostat with sample dimension of approximately  $1 \times 1.5 \times 5 \text{ mm}^3$ . The specimen are mounted on an electrically isolated brass plate and contacted by four gold needles, serving as electrical contacts. For temperature measurements, calibrated resistive Ge sensors for  $T < 30 \text{ K}$  and Pt PT100 for  $T > 30 \text{ K}$ , respectively, were used. A *Lakeshore* a.c. resistance bridge 370 with low resistance scanner acquired the experimental data.

Electrical resistivity down to 400 mK in external magnetic fields up to 12 T was measured in a *Cryogenics*  $^3\text{He}$  cryostat. Sample geometry and contacting resemble those of the  $^4\text{He}$  cryostat setup. Temperature was determined using calibrated *Cernox* temperature sensors by *Lakeshore Cryogenics*. A description of the cryostat, the operation principles, the sample holder as well as measurement setup and equipment are given in Ref. [1].

Electrical resistivity under pressure up to 19 kbar was measured in the temperature range 1.45-300 K by means of a standard four-probe electrical resistivity measurement technique. The current was supplied by a Knick J152 DC-Calibrator and a Keithley K-181 Nanovoltmeter was used to measure the voltage. A current reversal method was employed to avoid any influence from thermoelectric voltage. Hydrostatic pressures were generated in a double wall

piston-cylinder cell made from non-magnetic MP3-N alloy. Daphne oil was used as the pressure-transmitting medium while the pressure was measured by the shift of the first order magnetic phase transition in  $\text{HoCo}_2$ .

### 1.0.2 Specific heat measurements

Specific heat measurements were carried out on samples of about 2 – 3 g in the temperature range 1.8 K to 180 K employing a quasi adiabatic step heating technique in external magnetic fields up to 9 T. Temperature was obtained from a field calibrated *Cernox* resistor; heat capacity data were calibrated against NBS Cu. By means of a design originating from a quasi-adiabatic Nernst setup [2], a temperature sensor (*Cernox*) is placed in the bore of a sapphire plate sample holder fixed by nylon wires and surrounded by a radiation shield. Details concerning implemented algorithms as well as calibration are found in [3, 4].

### 1.0.3 Thermopower measurements

Thermopower measurements were carried out from 4 K to 300 K with a so-called a differential seesaw-heating method [5]. The absolute thermopower  $S_x(T)$  was calculated using the following equation:

$$S_x = S_A - \frac{V_A}{V_A - V_B}(S_A - S_B). \quad (1.1)$$

where  $S_A$  and  $S_B$  represent the absolute thermopower of Chromel and Constantan and  $V_A$  and  $V_B$  are the voltages along Chromel and Constantan circuits depending on the temperature difference  $\Delta T$ , respectively. The spot welded junctions of thermocouple pairs Chromel-Constantan were connected to the surface of the sample by soldering or by a two component silver conductive Epoxy. During the measurement a temperature gradient  $0.2 < T < 2$  K is applied to the specimen, in both directions (seesaw heating). The heaters provides the essential temperature gradient. The voltages between the thermocouple wires were measured in both directions by a *Keithley 192* nanovoltmeter. The sample temperature and the absolute temperature were measured with a Pt sensor in the range from 40 to 300 K and a Ge sensor below 40 K [1].

### 1.0.4 Thermal conductivity measurements

Thermal conductivity measurements from 4 to 300 K were carried out by a steady state heat flow method in a  $^4\text{He}$  Cryostat. The sample was surrounded by three radiation shields; the inner is held on the same temperature as the heat sink. Generally the rectangular shaped samples with a typical cross section  $A$  of 1-2 mm<sup>2</sup> and a length of about 10 mm were studied. One end of

the sample was placed to a copper stage at a reference temperature  $T_0$ . At the other end of the sample, a strain gauge was attached as heater establishing the temperature gradient  $\Delta T_S$ .  $\Delta T_S$  was determined by a differential thermocouple, which had its reference temperature from Pt and Ge sensors at the heat sink. The temperature gradient between the heat sink and the lower sample end is  $\Delta T_B$ . The voltage drop at the strain gauge was measured, allowing to deduce the thermal flux  $Q$ . Using these temperatures the average sample temperature  $T_S$  is given as:

$$T_S = T_0 + \frac{\Delta T_S}{2} + \Delta T_B \quad (1.2)$$

and the thermal conductivity  $\lambda$  is calculated

$$\lambda = \frac{l}{A} \frac{Q}{\Delta T_S}. \quad (1.3)$$

$A$  is the sample cross-section and  $l$  the effective length. This configuration has been used for high accuracy measurements by including a radiation shield and establishing about the same temperature profile along the shield as exists along the sample. This helps to minimize the radiative losses making  $T_0 \approx T_S$ .

# Chapter 2

## Some theoretical Concepts of superconductivity

### 2.1 The critical magnetic fields

The investigation of magnetic properties of elementary superconductors by Meissner and Ochsenfeld [6] revealed that when a superconductor is cooled below its transition temperature in a magnetic field, it expels the magnetic flux (perfect diamagnetism). The existence of the Meissner effect implies the existence of a critical magnetic field above which the superconducting (SC) state will be destroyed. This critical field is related thermodynamically to the free energy difference between the SC and normal state in the zero field,  $\Delta F = F_s - F_n$ , the so called thermodynamic condensation energy of the SC state. The thermodynamic critical field  $H_c$  is defined by equating the difference in free energy  $\Delta F$  to the magnetic energy  $\mu_o H_c^2/2$

$$\frac{\mu_o H_c^2(T)}{2} = \int_{T_c}^T \int_{T_c}^{T'} \frac{(C_s - C_n)}{T''} dT'' dT'. \quad (2.1)$$

Up to the critical field  $H_c$  a type I superconductor is always in the Meissner state (except for some special geometries) where  $M = -H$ , while flux penetration occurs in a type II superconductor already at a lower critical field  $H_{c1}$  which is smaller than the thermodynamic critical field  $H_c$ . Almost all elementary superconductors belong to this group, but the much larger group of SC alloys and compounds show a more complex magnetic behaviour. In 1957 Abrikosov [7] explained that a continuous increase in the flux penetration starting at a lower critical field  $H_{c1}$  and reaching full penetration at an upper critical field  $H_{c2}$  which is higher than the thermodynamic critical field. Between  $H_{c1}$  and  $H_{c2}$  is the so called mixed state, where magnetic field penetrates the superconductor by forming vortices, which have a constant value of magnetic flux, i.e. a flux quantum  $\phi_o = h/2e = 2.07 \times 10^{-15}$  Wb.

## 2.2 Concepts of GLAG theory

The fundamental ideas for a basic understanding of the magnetic properties of type II superconductors have been worked out by Ginzburg, Landau [8], Abrikosov [7] and Gor'kov [9], referred to as GLAG theory.

The theoretical advance came in 1950 with the theory of Ginzburg and Landau (GL) [8]. They presented a phenomenological theory of SC which is related to Landau's theory of second order phase transition. Ginzburg and Landau formulated a complex pseudo wave function  $\psi$  as an order parameter for the SC state which is related to the local density of the SC charge carriers as  $n_s = |\psi(r)|^2$ . The *GL* formalism describes situations where  $n_s$  varies in space and also the nonlinear response to fields that are strong enough to change  $n_s$ . Ginzburg and Landau argued that the free energy  $F$  of a superconductor near the SC transition can be expressed in  $\psi$ . The free energy  $F$  can be expanded in a Landau series of the form

$$F_s - F_n = \alpha |\psi|^2 + \frac{\beta}{2} |\psi|^4 + \frac{1}{2m^*} \left| \left( -i\hbar\vec{\nabla} - \mu_0 e^* \vec{\mathbf{A}} \right) \psi \right|^2 + \frac{\mu_0 \mathbf{H}^2}{2} \quad (2.2)$$

where  $F_n$  is the free energy in the normal phase, the  $e$  and  $m$  refers to the SC charge carriers and  $\alpha$  and  $\beta$  are phenomenological parameters.  $\mathbf{A}$  is the electromagnetic vector potential, and  $\mathbf{H}$  is the magnetic field. Introducing boundary conditions and applying variational principles to minimize the overall free energy, Ginzburg and Landau derived the so called GL equations [10]. From these equations they obtained qualitatively the temperature dependencies of the spatial variation length of the order parameter (Cooper-pair density),  $\xi_{GL}$  and the penetration depth of the local magnetic field,  $\lambda_{GL}$ . Since within the GL theory these two parameters are related to each other via the thermodynamic critical field  $H_c$ , they introduced the dimensionless Ginzburg-Landau parameter  $\kappa$ , which is defined as the ratio of the two characteristic lengths, penetration depth  $\lambda$  and coherence length  $\xi$ ,

$$\kappa_{GL} \equiv \frac{\lambda}{\xi} = \frac{2\pi\sqrt{2}\mu_0 H_c(T)\lambda_{GL}^2(T)}{\Phi_0} \quad (2.3)$$

where  $\Phi_0 = h/2e = 2.07 \times 10^{-15}$  Wb. The question of flux penetration depends on the energy balance between flux expulsion and the condensation energy on the two length scales  $\lambda$  and  $\xi$ . This yields for  $\kappa < 1/\sqrt{2}$  a positive surface energy and  $\kappa > 1/\sqrt{2}$  a negative surface energy between a normal and SC domain (i.e. mixed state).

The analysis of the consequence of negative surface energy was analyzed by Abrikosov [7]. He argued that in case of negative surface energy ( $\kappa > 1/\sqrt{2}$ ), the magnetic flux penetrating into a so-called type II superconductor will be subdivided into distinct flux lines (vortices) each carrying a quantum of flux

$\Phi_0 = h/2e$ . This vortex state reduces the diamagnetic energy and therefore SC can persist up to the so-called upper critical field  $H_{c2}$  gives by

$$H_{c2}(T) = \frac{\Phi_0}{2\pi\mu_0\xi^2(T)} = \frac{4\pi\lambda^2(T)H_c^2(T)}{\Phi_0} = \sqrt{2}\kappa(T)H_c(T). \quad (2.4)$$

This implies that materials with a high value of  $\kappa$  remain in the mixed state until external magnetic field exceeds  $H_{c2}$ . According to an approximation for  $\kappa \gg 1$ , Abrikosov related the lower critical field  $H_{c1}$  to the penetration depth  $\lambda$  as follows

$$H_{c1}(T) = \frac{\Phi_0}{4\pi\mu_0\lambda^2(T)} \ln \kappa(T). \quad (2.5)$$

Equations 2.4 and 2.5 can be used to estimate the coherence length from specific heat measurements. Gor'kov [9] showed that the phenomenological Ginzburg-Landau equations follow from the microscopic BCS theory in the temperature region close to  $T_c$ . He proposed that  $\psi$  is proportional to the gap parameter  $\Delta(r)$ , which for a homogeneous medium reduces to the BCS gap  $\Delta$ , and that  $\psi$  can be thought of as the wave function of Cooper pairs.

## 2.3 BCS theory

Despite the fact that the Ginzburg-Landau theory is phenomenological, it had surprising success in explaining many of the principal properties of superconductor. Nevertheless, it has limitations since it does not explain the microscopic origins of superconductivity. The biggest complication in the development of the microscopic theory of superconductivity was to discover the nature of the interaction responsible for the appearance of superconductivity. Fröhlich [11] and Bardeen [12] suggested that the superconductivity is based on an electron-phonon mechanism and that the interaction between electrons and phonons may lead to an effective interaction between electrons themselves. The possibility of electron-phonon mediated SC was reinforced by the experimental discovery of the isotope effect [13]. The theories by Fröhlich and Bardeen are based primarily on the effect of electron-phonon interaction energy upon the self energy of electrons and do not present a suitable model for the phonon mediated electron-electron interaction. The problem was later solved by Cooper who formulated a wave function for a single pair of electrons excited above the Fermi surface [14]. He found that for a negative interaction a bound state is formed no matter how weak the interaction may be.

In 1957 Bardeen, Cooper, and Schrieffer [15] proposed a general microscopic theory (BCS theory) of superconductivity that quantitatively predicts many properties of superconductors and is now widely accepted as providing a satisfactory explanation of the phenomenon. The basic assumptions of the BCS theory are as follows:



- The normal state is characterized by the Bloch individual-particle model.
- The ground state wave function of a superconductor is formed by taking a linear combination of many normal-state configurations in which the Bloch states are occupied by pairs of opposite momenta and spin known as Cooper pairs. If the state  $k_{\uparrow}$  is occupied in any configuration,  $-k_{\downarrow}$  is also occupied. The average excitation energy of the Cooper pairs above the Fermi sea is of the order of transition temperature  $T_c$ .
- The interaction between electrons resulting from the virtual exchange of phonons is attractive. Once this attractive interaction dominates over the repulsive Coulomb interaction, the system would produce as many Cooper pairs as possible to lower its energy. The energy difference between the electronic states involved is lower in energy than the phonon energy  $\hbar\omega_D$  characterized by the characteristic phonon Debye frequency  $\omega_D$ .
- Excited states of the superconductors are formed by a specific occupation of certain Bloch states and by using all of the rest to form a linear combination of virtual pair configuration.
- The electron phonon coupling strength,  $N(E_f)V$ , is much smaller than one (weak coupling limit) where  $N(E_f)$  represents density of states of the normal state electrons at the Fermi energy and  $V$  is the net coupling between electrons at Fermi surface as a consequence of phonon mediated attraction and Coulomb repulsion.

An attractive interaction between electrons mediated by phonons can lead to a ground state separated from excited states by an energy gap. The critical field, the thermal properties, and most of the electromagnetic properties are consequences of the energy gap. The essential (and universal) thermodynamic properties of the SC state in terms of BCS theory (see Ref. [10] for review) are the BCS relation for the critical temperature and the expression for the free-energy. The SC transition temperature in framework of the BCS theory is given as

$$T_c = 1.14\Theta_D \exp\left(-\frac{1}{N(0)V}\right) \quad (2.6)$$

where  $\Theta_D$  is Debye temperature. Near the transition temperature  $T_c$ , the temperature dependent gap width can be approximated by the following relation:

$$\Delta(T) \approx 3.2k_B T_c \sqrt{1 - \frac{T}{T_c}}. \quad (2.7)$$

Another important BCS result is the ratio of the critical temperature  $T_c$  and the energy gap  $\Delta(0)$  at  $T = 0$ , given by

$$\Delta(0)/k_B T_c = 1.76. \quad (2.8)$$

The expression for the free-energy of the SC state yields an exponential temperature dependence of the electronic specific heat in the SC state ( $2.5 < T_c/T < 6$ )

$$C_{eS} \cong 8.5\gamma T_c \exp \left[ -1.44 \left( \frac{T_c}{T} \right) \right]. \quad (2.9)$$

The BCS theory predicts a sharp jump in the electronic specific heat at  $T_c$  from the normal state value  $\gamma T_c$  to the SC state value  $C_{eS}(T_c)$  [15]. The height of the specific heat jump is given by

$$\frac{\Delta C}{\gamma T_c} = 1.43. \quad (2.10)$$

## 2.4 Eliashberg theory and impurity scattering

Many formulas of the BCS theory are of an universal character, for example gap to critical temperature ratio (equation 2.8) and the normalized specific heat jump (equation 2.10). The universal nature of the BCS theory is due to the fact that it was developed in the weak coupling approximation and on the basis of a single spherical Fermi surface. In other words, the electron-phonon interaction is assumed to be weak ( $\lambda \ll 1$ ) and the entire model is determined by two parameters: The Sommerfeld coefficient  $\gamma$  [i.e. the electronic density of states  $N(E_f)$ ] and the transition temperature  $T_c$ . Superconductors with significant electron mass enhancement  $\lambda$ , due to electron-phonon many body interactions are called strong coupling superconductors and have to be treated by a theory going beyond the BCS approximations. Eliashberg derived a pair of coupled integral equations which relate a complex energy gap function  $\Delta(\omega)$  and a complex renormalization parameter  $Z_s(\omega)$  for the SC state to the electron-phonon and electron-electron interaction in the normal state. Details about the Eliashberg equations and further references are e.g. given in the books by Grimvall [16] and Vonsovsky *et al.* [17]. The important parameter of the Eliashberg equations [18] is the electron-phonon spectral function,  $\alpha^2(\omega)F(\omega)$ , where  $F(\omega)$  is the spectral function of the phonon density of states and  $\alpha^2$  is the effective square of the electron-phonon matrix element. The spectral function has to be determined experimentally from tunneling spectroscopy, specific heat measurements or from *ab initio* calculations of the phonon density of states. It has to be noted that the theoretical definition of the electron-phonon spectral function does not refer to the SC

state, thus the electron-phonon spectral function is the same as in the normal state. The details of the spectral function can be found in Ref. [19]. Within the Eliashberg formalism, the electron-phonon coupling strength  $\lambda$  is defined as

$$\lambda \equiv 2 \int \frac{\alpha^2 F(\omega)}{\omega} d\omega. \quad (2.11)$$

The Eliashberg theory has been successfully adopted to apply strong coupling corrections to the BCS theory as reviewed by Carbotte [20].

Starting from BCS theory, the effect of non-magnetic impurities on an anisotropic superconductor was investigated by Markowitz and Kanadoff [21]. They introduced a separable pairing potential given as

$$V(\mathbf{k}, \mathbf{k}') = (1 + \alpha_{\mathbf{k}}) V_{\text{BCS}} (1 + \alpha_{\mathbf{k}'}) \quad (2.12)$$

where  $a_{\mathbf{k}}$  is the temperature independent anisotropy matrix and  $V_{\text{BCS}}$  is the electron-phonon coupling potential of the BCS theory. The parameter  $a_{\mathbf{k}}$  determines the effect of anisotropic Fermi surface on the isotropic BCS coupling potential  $V_{\text{BCS}}$ . The mean square anisotropy parameter  $\langle a^2 \rangle$ , which denotes average of  $a^2$  over the Fermi surface, expresses the average deviation of the coupling from the isotropic case. Therefore  $\langle a^2 \rangle$  comprises in a rather simple way anisotropies of the electron phonon interaction. Markowitz and Kanadoff [21] argued that the electron-phonon interaction must depend on the direction of the electronic momenta relative to the crystal axes, and in pure material the electrons take maximum advantage of this anisotropy in forming pairs. However, in the impure material, scattering will act to smear the electronic states over Fermi surface resulting in a reduction of  $T_c$ . This separable model for the Eliashberg theory was later adopted to describe an anisotropic electron-phonon interaction spectral function [22]

$$[\alpha^2 F(\omega)]_{\mathbf{k}, \mathbf{k}'} = (1 + a_{\mathbf{k}}) \alpha^2 F(\omega) (1 + a_{\mathbf{k}'}) \quad (2.13)$$

where  $\mathbf{k}$  and  $\mathbf{k}'$  are the incoming and outgoing quasiparticle momentum vectors in the electron-phonon scattering process and  $a_{\mathbf{k}}$  is an anisotropy function describing the deviation of the anisotropic spectral function,  $[\alpha^2 F(\omega)]_{\mathbf{k}, \mathbf{k}'}$ , from the isotropic one,  $\alpha^2 F(\omega)$ , in the direction of  $\mathbf{k}$ . In the framework of the Eliashberg theory, non-magnetic impurities are treated in Born's limit [23] which assumes that the impurities are randomly distributed and are of dilute concentration. In such a limit, impurities are characterized by a scattering rate  $t_+$  which is proportional to impurity concentration and is given as

$$t_+ = \frac{1}{2\pi\tau_n} \quad (2.14)$$

where  $\tau_n$  in the normal state represents the mean scattering time, and in the superconducting state [24], the mean lifetime of the electronic excited states of the (anisotropic)  $s$ -wave order parameter.

The theory of the upper critical field  $H_{c2}$  for anisotropic polycrystalline superconductors including strong coupling effects, isotropic impurity scattering and mean-square anisotropies of the electron-phonon interaction and of the Fermi velocity, was developed by Prohammer and Schachinger [25]. The calculation of  $H_{c2}$  employs a separable ansatz to describe the anisotropy of the Fermi velocity  $v_{F,k}$  [25, 26]

$$v_{F,k} = (1 + b_k)\langle v_F \rangle \quad (2.15)$$

where  $\langle v_F \rangle$  is the isotropic Fermi velocity and  $b_k$  is the anisotropy matrix defined in the same way as  $a_k$ .

The effect of impurity scattering on  $T_c$ ,  $H_c$  and  $H_{c2}$  has been studied for elemental superconductors Indium (In) and Niobium (Nb) in terms of Eliashberg theory. In case of type-I In, Niel *et al.* [24] extended the work of Ref. [21] to strong-coupling Eliashberg theory and employed the separable model given in equation 2.13 which can be described in its simplest form by a Fermi surface split into two half spheres of equal weight

$$P(a) = \frac{1}{2}\delta(-a) + \frac{1}{2}\delta(a) \quad (2.16)$$

with radii  $r \pm a$ , if  $r$  is the radius of the equivalent isotropic Fermi sphere. Niel *et al.* [24] calculated  $T_c$  from linearized Eliashberg equations and found that the model gives an accurate interpretation of the experimental data in terms of mean square anisotropy of electron-phonon interaction not only for  $T_c$  but also for other bulk properties like  $H_c(T)$ . They analyzed the dependence of  $T_c$  on the impurity concentration in terms of scattering rate  $t_+$  and found a range  $0.035 \leq \langle a^2 \rangle \leq 0.04$  for the anisotropy parameter. The variation of  $H_c(0)$  with impurity concentration was also rather well described by the model for  $\langle a^2 \rangle = 0.035$ .

The elemental Nb is more relevant with respect to boronitrides because it is a type-II superconductor. The effect of impurities on the anisotropy in Nb were investigated by Weber *et al.* [27] within the Eliashberg theory. The impurity dependence of the normal state resistivity of Nb revealed an almost linear increase in the residual resistivity ( $\rho_o$ ) with increasing impurity concentration ( $c_i$ ). The residual resistivity is related to Ginzburg-Landau parameter  $\kappa$  in terms of Gor'kov-Goodman relation [28]

$$\kappa = \kappa_o + 0.0237\sqrt{\gamma}\rho_o \quad (2.17)$$

where  $\kappa_o$  is clean limit GL parameter,  $\gamma$  is Sommerfeld coefficient in units  $J/m^3K^2$  while  $\rho_o$  is given in  $\mu\Omega\text{cm}$ . A clear correlation between the experimentally determined  $\kappa$  and  $\rho_o$  was obtained which was rather well described by equation 2.17. The impurity dependence of the transition temperature was also described rather accurately with the anisotropy parameter

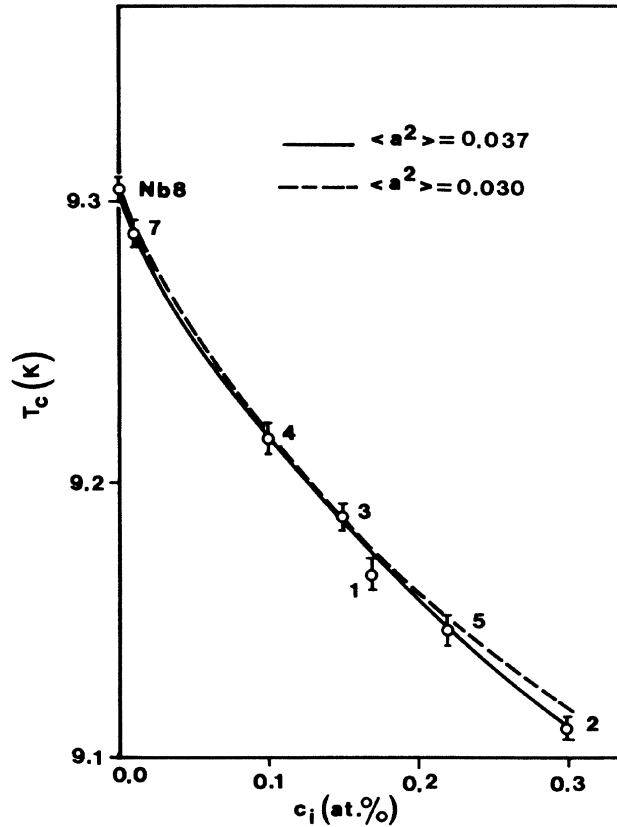


Figure 2.1:  $T_c$  depression of Nb as a function of the impurity concentration as adopted from Ref. [27]. The symbols with error bars represent experimental data while the two lines represent theoretical result for values of  $\langle a^2 \rangle$  as labeled.

$0.030 \leq \langle a^2 \rangle \leq 0.037$ . The  $T_c$  suppression as a function of the impurity (nitrogen) concentration in Nb is shown in figure 2.1 that fits equally well to the measured data for two values of  $\langle a^2 \rangle$ . Based on the anisotropic Eliashberg theory of  $H_{c2}$  [25] and using  $\langle a^2 \rangle$  as determined from  $T_c$  depression with impurity content, a mean square anisotropy of Fermi velocity,  $0.111 \leq \langle b^2 \rangle \leq 0.13$  was estimated. The upper critical field of Nb along with the theoretical curves of Ref. [27] are shown in figure 2.2 revealing good agreement between measured and calculated results. These results suggest that a certain set of anisotropy parameters can indeed explain the SC properties of pure and impure niobium with dilute impurity concentrations within the Eliashberg theory.

Besides elemental superconductors, the Eliashberg theory has also been applied to study the SC properties of borocarbides. A positive curvature of  $H_{c2}(T)$  near  $T_c$  has been reported for the single layer borocarbides  $\text{YNi}_2\text{B}_2\text{C}$  and  $\text{LuNi}_2\text{B}_2\text{C}$  [29, 30, 31]. The temperature dependence of  $H_{c2}$  of Y- and

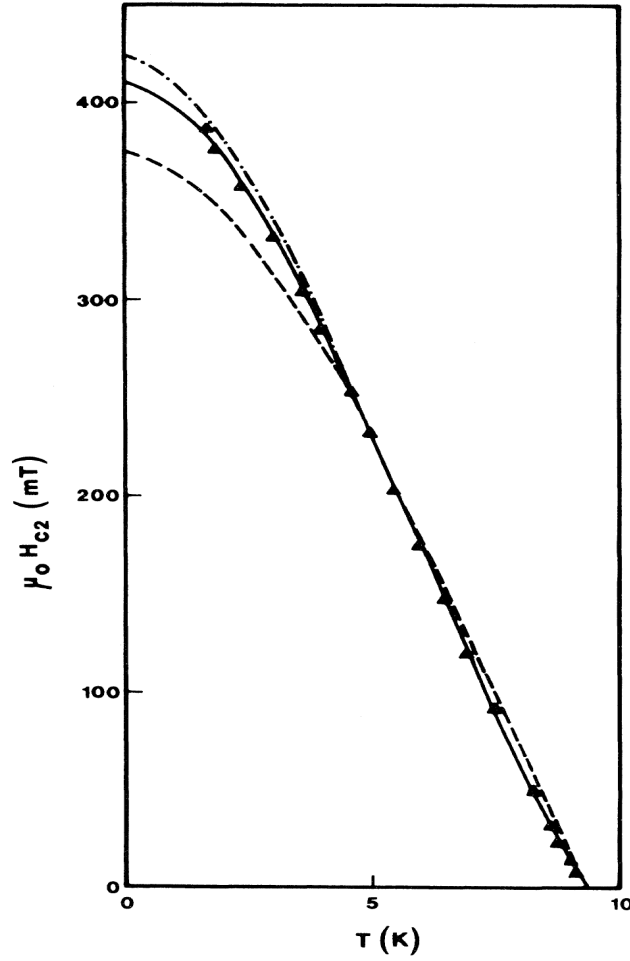


Figure 2.2:  $H_{c2}$  of Nb as adopted from Ref. [27]. Full line  $\langle a^2 \rangle = 0.037$ ,  $\langle b^2 \rangle = 0.111$ , dashed-dotted line  $\langle a^2 \rangle = 0.03$ ,  $\langle b^2 \rangle = 0.13$ .  $v_F$  in both cases is  $0.57 \times 10^6$  m/s. The dashed line represents the results for an isotropic system with  $0.42 \times 10^6$  m/s.

$\text{LuNi}_2\text{B}_2\text{C}$  has been analyzed by various authors within the isotropic single band model by Werthamer *et al.* [32] which fails to reproduce the experimental data [33, 34]. Shulga *et al.* [35] later extended the  $H_{c2}$  calculations to an isotropic two band model in terms of the Eliashberg theory and successfully modeled  $H_{c2}(T)$  of  $\text{YNi}_2\text{B}_2\text{C}$  and  $\text{LuNi}_2\text{B}_2\text{C}$  in the whole temperature range and associated the positive curvature of  $H_{c2}(T)$  near  $T_c$  to interband coupling of electrons.

The separable model was also adapted for  $\text{Y}_x\text{Lu}_{1-x}\text{Ni}_2\text{B}_2\text{C}$  by Manalo *et al.* [36] who obtained a set of anisotropy parameters to analyze the SC properties of the whole series. They also investigated the SC properties of

---

$\text{La}_3\text{Ni}_2\text{B}_2\text{N}_{3-\delta}$  assuming a clean limit case ( $t_+ = 0$ ) and reproduced the measured data rather well within the Eliashberg theory. However, the nitrogen vacancies in  $\text{La}_3\text{Ni}_2\text{B}_2\text{N}_{3-\delta}$  may act as scattering centers and reduce the electron-phonon coupling anisotropy resulting in depression in  $T_c$  and the clean limit assumption of Ref. [36] may not be valid. So it is important to investigate if  $\text{La}_3\text{Ni}_2\text{B}_2\text{N}_{3-\delta}$  could be a model system for vacancy induced changes in SC properties within the Eliashberg theory.

# Chapter 3

## Preparation, structure and width of formation of $\text{La}_3\text{Ni}_2\text{B}_2\text{N}_{3-\delta}$

### 3.1 Introduction

The borocarbides and boronitrides are complex quaternary compounds and a full knowledge of their quaternary phase diagrams is difficult to achieve. Many different phases of quaternary borocarbides R-T-B-C have been reported showing rich physics, including interplay of superconductivity and magnetism [34]. Techniques for producing high purity  $R\text{Ni}_2\text{B}_2\text{C}$  samples are well developed [37, 38, 39]. According to investigations on the formation of single crystals, the phase  $R\text{Ni}_2\text{B}_2\text{C}$  is formed by a peritectic reaction of the melt with the preperitectic phases  $RB_2C_2$  [37, 38]. The pseudobinary phase diagram of the Y based system obtained by differential thermal analysis (DTA) and is shown as an example in figure 3.1. Similar phase diagrams for Tb and Ho based  $R\text{Ni}_2\text{B}_2\text{C}$  borocarbides have been reported with slight variations of the peritectic temperature [39]. In the case of the boronitrides not even a rudimentary phase diagram has been reported yet. One has to expect a bigger complexity of the quaternary R-Ni-B-N phase diagram because of a gaseous component (nitrogen) involved.

The initially reported preparation technique [40] for  $\text{La}_3\text{Ni}_2\text{B}_2\text{N}_{3-\delta}$  is based on arc melting La-Ni-B under  $\text{N}_2$  atmosphere with subsequent annealing at 1050 °C. This technique may result in reasonably phase pure material but the amount of nitrogen absorbed by the matrix phase may not be optimal. An alternative method was employed for the preparation of bulk  $\text{La}_3\text{Ni}_2\text{B}_2\text{N}_{3-\delta}$  based on a two step process in which a LaNi alloy was reacted with a boron nitride pellet by dissolving it into the LaNi melt heated by the arc [41]. A technique based on a pyrolysis of La and Ni powder dispersed in



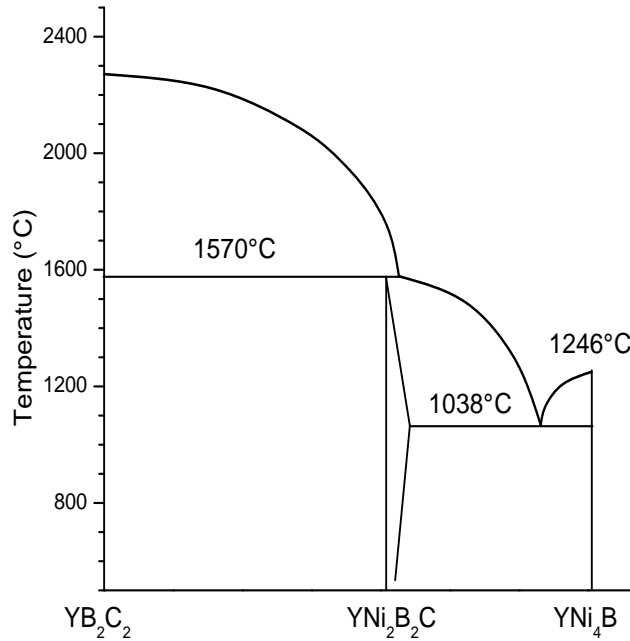


Figure 3.1: Phase diagram of the Y-Ni-B-C system [37].

polyborazylene was reported by Wideman *et al.* [42]. In all techniques mentioned above the nitrogen stoichiometry of  $La_3Ni_2B_2N_{3-\delta}$  was not in real control and may have effects on the phase purity and superconducting properties of the material. In two subsequent masters thesis works by Sieberer and Rupprecht [43, 44] the nitration and annealing of  $La_3Ni_2B_2N_{3-\delta}$  was investigated. Sieberer developed a process for the controlled nitration of  $La_3Ni_2B_2$  alloys and reported that the as-cast material shows very little or no  $La_3Ni_2B_2N_{3-\delta}$  phase suggesting that the phase formation occurs at annealing via a solid state reaction. The annealing process was later optimized by Rupprecht to produce bulk  $La_3Ni_2B_2N_{3-\delta}$  with reasonable phase purity.

The following chapter describes a process for preparing bulk  $La_3Ni_2B_2N_{3-\delta}$  with various nominal N-stoichiometries. The phase purity and crystal structure of the material is investigated by X-ray diffraction analysis and a width of formation of  $La_3Ni_2B_2N_{3-\delta}$  is established. To verify the width of formation, neutron powder diffraction studies on selected compositions were performed. Complementary local probe information obtained from nuclear magnetic resonance (NMR) spectroscopy of  $^{11}B$  and  $^{139}La$  isotopes is presented.

## 3.2 Sample preparation

For preparing bulk  $\text{La}_3\text{Ni}_2\text{B}_2\text{N}_{3-\delta}$  samples the following starting materials, La ingot (Metall Rare Earth, 99.9%) additionally purified by pre-melting in vacuum, Ni (Alpha Aesar, 99.99%), crystalline natural boron (HCTS, 99.5%) or for selected samples, highly isotope enriched  $^{11}\text{B}$  (Eagle Picher, chemical purity 99.9999% and  $^{11}\text{B}$  isotope purity 99.97%) and nitrogen gas (Linde, 99.999%) are used. Argon and nitrogen gases are additionally precleaned by OXISORB devices.

The samples are synthesized on a water cooled copper crucible by high frequency inductive levitation melting technique on a Hüttinger IG, 30/400, 220 kHz generator with a maximum primary power of 30 kW. To ensure a good homogeneity of the material, a three step melting procedure is applied. In the first step the NiB binary compound is prepared by taking stoichiometric amounts of Ni and B and alloying them in a protective Ar atmosphere in two to three melting cycles. The second step of the process is a melting of the NiB binary compound with La metal in several cycles till a homogeneous alloy  $\text{La}_3\text{Ni}_2\text{B}_2$  is obtained. The alloy is flipped between melting cycles to improve homogeneity.

The third step of the process is melting of the  $\text{La}_3\text{Ni}_2\text{B}_2$  precursor alloy in Ar/ $\text{N}_2$  atmosphere. Melting in pure  $\text{N}_2$  gas would result in a strong spitting of the melt due to the exothermic reaction. For preparing the atmosphere a mixture of Ar and  $\text{N}_2$  streams through the recipient for 1 to 1.5 hour with Ar flow always adjusted to 20  $\text{cm}^3/\text{min}$  while the  $\text{N}_2$  flow is adjusted according to envisaged atmosphere composition. The  $\text{La}_3\text{Ni}_2\text{B}_2$  alloy is then melted in a static reaction atmosphere in multiple melting cycles such that the N-stoichiometry is slowly increased to reach a composition close to the stoichiometric one. The latter is determined by measuring the mass gain after each melting cycle and by measuring the pressure drop within the recipient. Between successive melting cycles, the  $\text{N}_2$  in the atmosphere is readjusted by altering the Ar/ $\text{N}_2$  ratio (20:5 to 20:10) in the stream to get better control over the amount of nitrogen absorbed by the alloy button. The combination of measuring the mass gain and the pressure drop in the recipient allows to determine the nominal nitrogen stoichiometry of  $\text{La}_3\text{Ni}_2\text{B}_2\text{N}_x$  within  $\pm 0.05$  formula units when preparing bulk samples of about 10 g. In few cases the stoichiometry obtained by the mass gain differed from the stoichiometry obtained by pressure drop by about 2% at largest. The reason for this may be some material loss during the melting process. Throughout this thesis the samples are always referred to by their nominal compositions.

### 3.3 Thermal treatment and phase purity

The heat treatment of the material after the melting processes is an important factor which greatly affects the overall quality of the material. Annealing helps to improve the homogeneity and to establish the thermodynamic equilibrium between the phases present. In this work several nominal compositions of  $\text{La}_3\text{Ni}_2\text{B}_2\text{N}_{3-\delta}$  were annealed in two steps. In the first step the samples are wrapped in tantalum foil and annealed in a high temperature continuously pumped vacuum furnace at 1100 °C for one week. During the annealing most samples had minimal or no reaction with Ta foil and the weight loss is typically less than 1%. There is no indication that the compound would release nitrogen at 1100 °C. In the second step individual pieces of each sample are sealed in quartz ampoules under 200 mbar Ar atmosphere and annealed at 1130-1150 °C for 42 hours. After the annealing, samples are rapidly quenched in water at room temperature. Contrary to previous works, the material is sealed without any foil to achieve a maximal quenching speed. The samples obtained after this process have a bluish colour suggesting some oxidation on the surface which however, has little impact on overall quality of the material.

From heat treatment of  $\text{La}_3\text{Ni}_2\text{B}_2\text{N}_{3-\delta}$  with various N-stoichiometries it was observed that the second annealing with rapid quenching has a significant effect on phase purity of the material. The X-ray diffraction analysis of several nominal compositions revealed the main impurity phase in  $\text{La}_3\text{Ni}_2\text{B}_2\text{N}_{3-\delta}$  to be the two layer boronitride LaNiBN. The right annealing temperature for a particular stoichiometry also depends on its nitrogen composition. For  $\text{La}_3\text{Ni}_2\text{B}_2\text{N}_{3-\delta}$  with  $\delta$  ranging from 0.3 to 0.4 the optimum temperature before quenching is 1130 °C. For  $\text{La}_3\text{Ni}_2\text{B}_2\text{N}_{2.6\sim 2.7}$ , temperatures above or below 1130 °C tend to increase the impurity phases. With increasing nominal nitrogen composition of  $\text{La}_3\text{Ni}_2\text{B}_2\text{N}_{3-\delta}$  i.e. for  $\delta$  ranging from 0.1 to 0.3 the optimum annealing temperature was identified to be 1150 °C.

### 3.4 Powder X-ray diffractometry

Huang *et al.* [45] reported a detailed investigation of the structure by means of neutron powder diffraction showing  $\text{La}_3\text{Ni}_2\text{B}_2\text{N}_{3-\delta}$  to crystallize in a body centered tetragonal structure shown in figure 3.2 with space group  $I4/mmm$  and lattice parameters  $a$  and  $c$  of 0.3725 nm and 2.0517 nm respectively. The structure is layered having LaN triple layers with rock-salt type configuration separated by  $\text{Ni}_2\text{B}_2$  layers built from  $\text{NiB}_4$  tetrahedra.

The structure has two nitrogen and two lanthanum sites in the unit cell. The La(2) and N(2) sites are located in the central LaN layer while the La(1) and N(1) sites are adjacent to  $\text{Ni}_2\text{B}_2$  layer. The results of neutron diffraction in

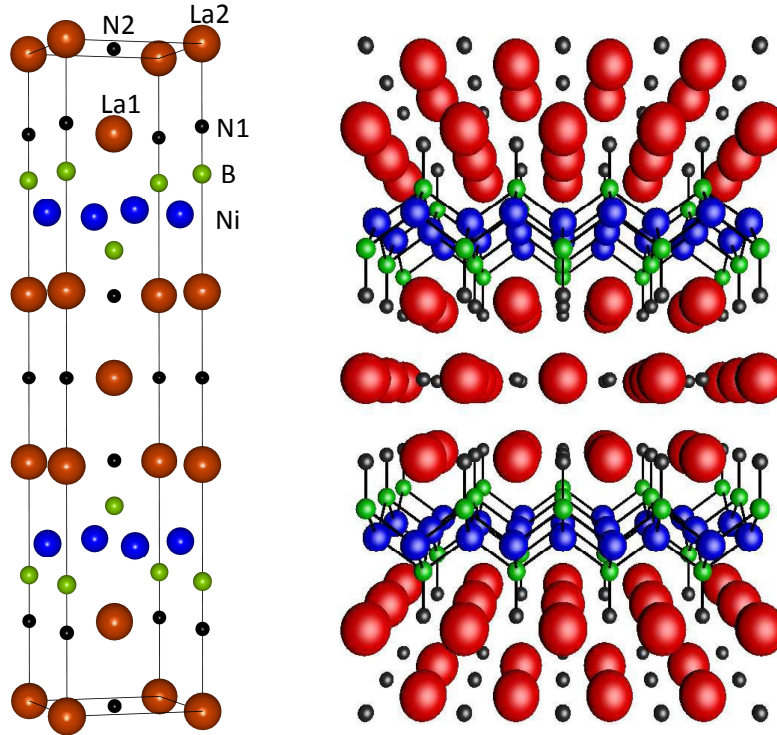


Figure 3.2: The crystal structure of  $\text{La}_3\text{Ni}_2\text{B}_2\text{N}_{3-\delta}$

Ref. [45] suggested that all crystallographic sites of  $\text{La}_3\text{Ni}_2\text{B}_2\text{N}_{3-\delta}$  have full occupancies except the N(2) which was reported to have about 10% vacancies. The related boronitride  $\text{LaNiBN}$  has two  $\text{LaN}$  layers stacked within  $\text{Ni}_2\text{B}_2$  layers with lattice parameters  $a$  and  $c$  of 0.372 nm and 0.759 nm respectively [46].

### 3.4.1 Phase analysis and nominal width of formation

In this work various compositions of  $\text{La}_3\text{Ni}_2\text{B}_2\text{N}_{3-\delta}$  are prepared with the aim to achieve a systematic variation of N(2) site occupancy. The effect of nitrogen off-stoichiometry on the crystal structure and phase purity of  $\text{La}_3\text{Ni}_2\text{B}_2\text{N}_{3-\delta}$  is initially analyzed by means of X-ray diffraction studies at room temperature with  $\text{Cu-K}\alpha$  radiation on a *Siemens D5000* equipped with a graphite monochromator. Data is collected at room temperature for a range  $20^\circ < 2\theta < 120^\circ$  with steps of  $0.02^\circ$  on powders which are ground and sieved to a particle size of less than  $32\mu\text{m}$ . The X-ray powder patterns for all the nominal compositions are indexed on the basis of the crystal structure of  $\text{La}_3\text{Ni}_2\text{B}_2\text{N}_3$  with space group  $I4/mmm$  and  $\text{LaNiBN}$  with space group  $P4/nmm$  using the Fullprof Rietveld refinement software [47]. The maximum number of refined parameters are 27 which reduces to 18 if the impurity

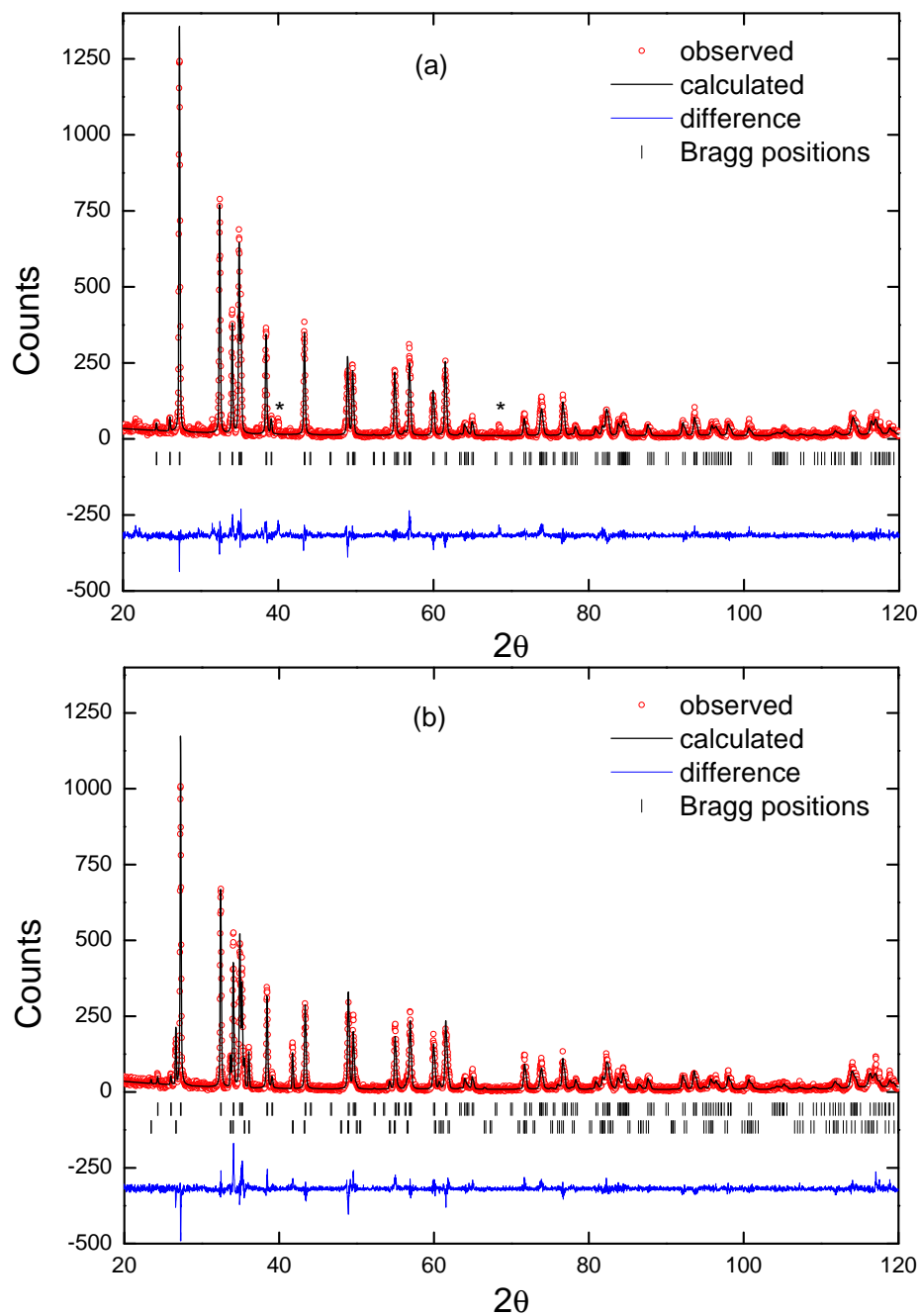


Figure 3.3: Measured, calculated and difference XRD pattern of  $\text{La}_3\text{Ni}_2\text{B}_2\text{N}_{2.7}$  (a) and  $\text{La}_3\text{Ni}_2\text{B}_2\text{N}_{2.6}$  (b). Vertical lines in (a) and (b), and lower vertical lines in (b) indicate Bragg positions of  $\text{La}_3\text{Ni}_2\text{B}_2\text{N}_3$  and  $\text{LaNi}_2\text{BN}$  respectively. Asterisks in (a) indicate an unidentified secondary phase.

phase LaNiBN is not included in the fit. The parameters refined are a scale factor, zero shift, shape profile, half width parameters, atomic parameters, thermal parameters and lattice constants. For profile refinement a flat plate like geometry with a preferential orientation [101] produced the best fit of measured patterns. This suggests that the powder grains tend to arrange plate like when being put on a flat glass sample holder. The total number of reflections of  $\text{La}_3\text{Ni}_2\text{B}_2\text{N}_3$  measured in the X-ray diffraction are 97 with about 30 having enough intensity to be relevant for the refinement.

The observed and calculated XRD pattern of an essentially pure sample  $\text{La}_3\text{Ni}_2\text{B}_2\text{N}_{2.7}$  are shown in figure 3.3(a). The pattern reveals an almost single phase material with  $< 2\%$  fraction of two layer LaNiBN. The asterisks in figure 3.3(a) mark reflections of an unidentified phase. The calculated intensity pattern represented by the solid line and the resulting difference pattern demonstrate the quality of the fit. For  $\text{La}_3\text{Ni}_2\text{B}_2\text{N}_{2.7}$  the refined  $a$  and  $c$  lattice parameters are 0.3720 nm and 2.054 nm respectively which are comparable to values reported earlier [41, 45]. The XRD pattern of  $\text{La}_3\text{Ni}_2\text{B}_2\text{N}_{2.6}$  shown in figure 3.3(b) is typical for a sample with a significant amount of LaNiBN impurity phase. Well defined peaks of LaNiBN are observed at  $2\theta = 26.7^\circ$ ,  $36.0^\circ$  and  $41.8^\circ$  with an overall phase fraction of  $\sim 10\%$ . X-ray powder diffraction analysis of various compositions of  $\text{La}_3\text{Ni}_2\text{B}_2\text{N}_{3-\delta}$  together with physical properties (see Chapter 5) suggest an approximate nominal width of formation with  $\delta \sim 0.1$  to 0.4. Nevertheless, the material always contains a small fraction of LaNiBN even in the approximate width of formation proposed here. The optimum composition for obtaining single phase samples is  $\text{La}_3\text{Ni}_2\text{B}_2\text{N}_{2.7}$  ( $\delta = 0.3$ ) while other compositions in the proposed width of formation contain LaNiBN phase fractions varying from 5% to 15%. Though having some fraction of impurity phases, all samples (with  $\delta$  varying from 0.1 to 0.4) have a clear composition dependence of the superconducting transition temperature and residual resistivity while showing reasonably sharp specific heat anomalies (see chapter 5).

The variation of lattice parameters  $a$  and  $c$  of  $\text{La}_3\text{Ni}_2\text{B}_2\text{N}_x$  as a function of the N-stoichiometry is shown in figure 3.4. The figure indicates an almost linear increase of the  $a$  lattice parameter with increasing nitrogen content while the  $c$  lattice parameter does not exhibit a clear trend. Rupperecht reported clearer trends for the variation of lattice parameters [44] which however, are an artifact of the LaNiBN phase which was not included in his profile refinements. Due to the very close values of  $a$  lattice parameters of both phases, fitting XRD data of  $\text{La}_3\text{Ni}_2\text{B}_2\text{N}_{3-\delta}$  without considering the LaNiBN impurity phase may cause a reduction of the  $a$  lattice parameter of  $\text{La}_3\text{Ni}_2\text{B}_2\text{N}_{3-\delta}$ . In the present work the XRD profiles of  $\text{La}_3\text{Ni}_2\text{B}_2\text{N}_{3-\delta}$  are refined including the LaNiBN phase. It has to be mentioned that the results of Ref [44] fit well to the present ones if both phases are refined simultaneously. Although the

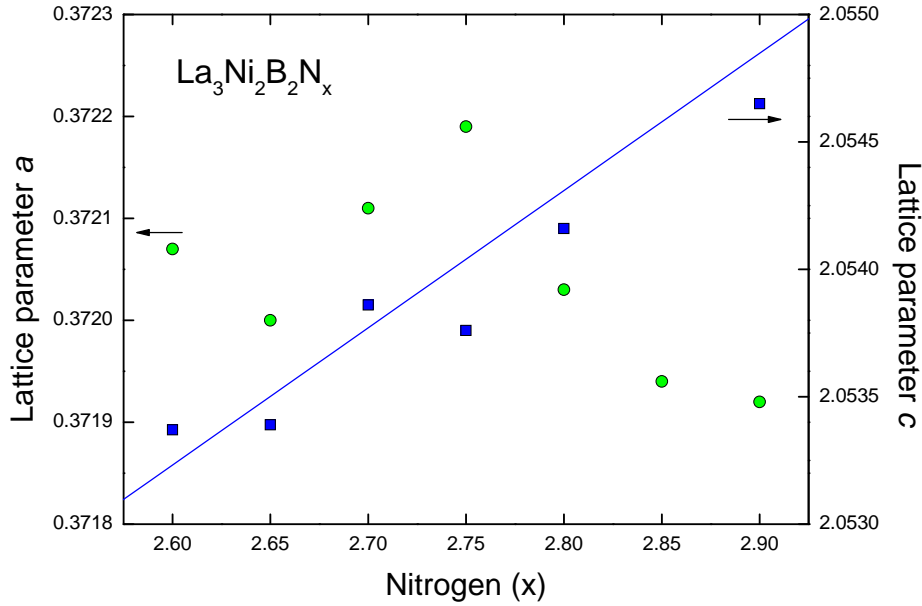


Figure 3.4: Variation of lattice parameters  $a$  and  $c$  for various nominal compositions of  $\text{La}_3\text{Ni}_2\text{B}_2\text{N}_{3-\delta}$

XRD analysis together with the observed systematic changes in the physical properties (see Chapter 5) indicates an approximate width of formation of  $\text{La}_3\text{Ni}_2\text{B}_2\text{N}_{3-\delta}$  with  $\delta$  varying from 0.1 to 0.4, a clear trend for the variation of lattice parameters with the nitrogen off-stoichiometry is not observed. It is a well known fact that the X-ray scattering cross-section varies smoothly as square of the atomic number and is very small for light elements. Accordingly N and B atoms in  $\text{La}_3\text{Ni}_2\text{B}_2\text{N}_{3-\delta}$  are hardly sensed by X-rays. On the other hand neutrons are scattered from atomic nuclei by neutron-nuclear force and their scattering cross-sections are usually high even for light elements. The neutron scattering lengths for La, Ni,  $^{11}\text{B}$ , and N are 8.24 fm, 10.3 fm, 6.65 fm, and 9.36 fm, respectively [48]. In order to get a deeper insight into the structural properties of  $\text{La}_3\text{Ni}_2\text{B}_2\text{N}_{3-\delta}$  and to verify the width of formation, neutron powder diffraction studies were carried out for selected nominal compositions (see section 3.6).

### 3.5 Nuclear magnetic resonance spectroscopy

In order to obtain microscopic local probe insight on the local structure at La and B sites, nuclear magnetic resonance (NMR) of selected compositions of  $\text{La}_3\text{Ni}_2\text{B}_2\text{N}_{3-\delta}$  were performed on a pulse spectrometer using Fourier-transformed spin echos technique [49] for  $^{11}\text{B}$  and  $^{139}\text{La}$  isotopes [50]. The

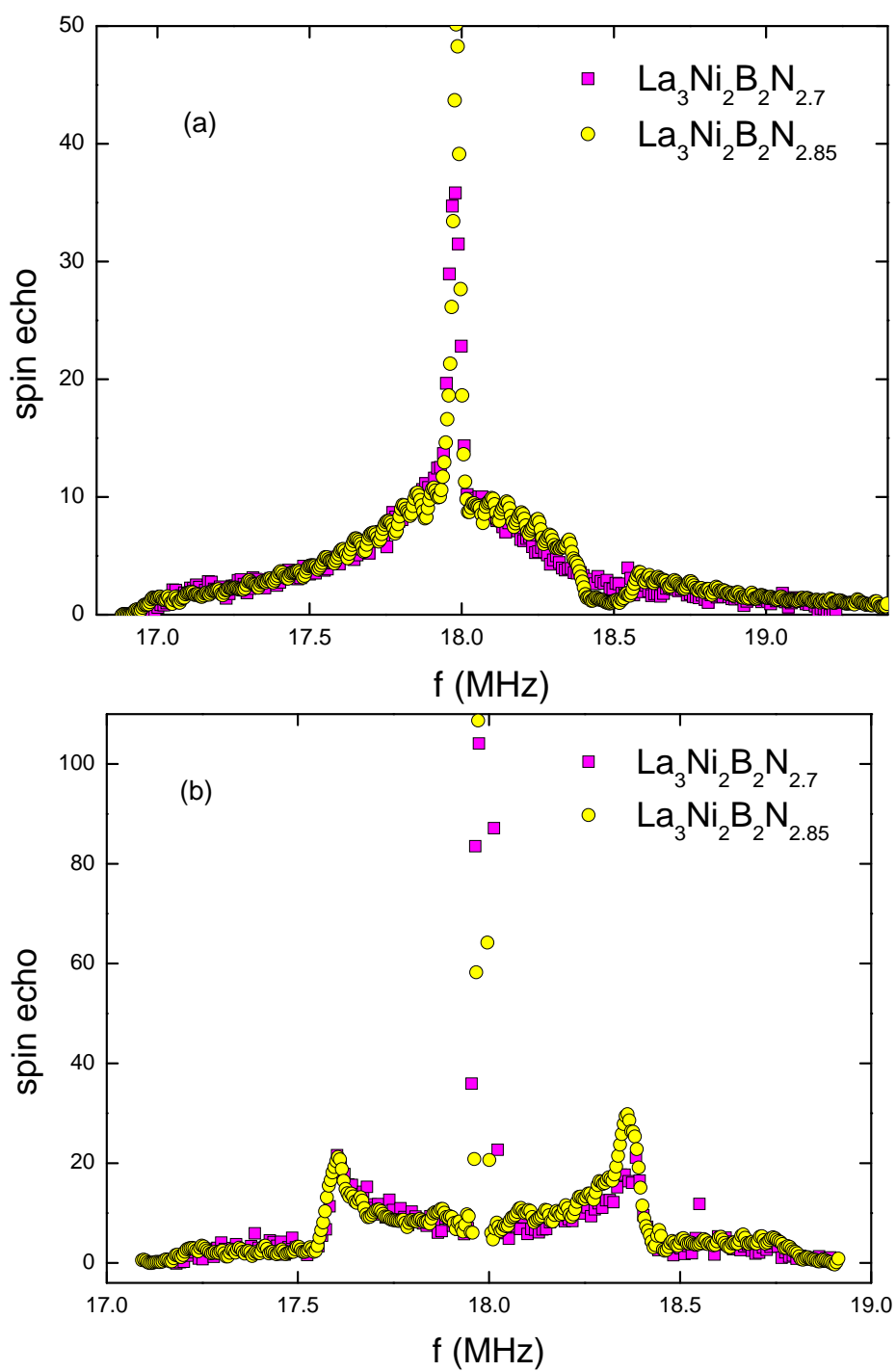


Figure 3.5:  $^{139}\text{La}$  (a) and  $^{11}\text{B}$  (b) NMR spectra of  $\text{La}_3\text{Ni}_2\text{B}_2\text{N}_{2.7}$  and  $\text{La}_3\text{Ni}_2\text{B}_2\text{N}_{2.9}$  at 17K and in an applied field of 1.316T. Spin echo intensities are given in arbitrary units.



$^{139}\text{La}$  NMR spectra of  $\text{La}_3\text{Ni}_2\text{B}_2\text{N}_{2.6}$  and  $\text{La}_3\text{Ni}_2\text{B}_2\text{N}_{2.9}$  obtained by sweeping the frequency at 17 K and in an applied field of 1.316 T is shown in figure 3.5 (a). The spectra of both samples are rather similar, except for a drop in the intensity for  $\text{La}_3\text{Ni}_2\text{B}_2\text{N}_{2.9}$  on the high frequency side which is an artifact of the measurement. The oscillatory behaviour is due to a resolution enhancement used to improve the representation of the central transition. The central transition is relatively narrow but sits on top of a broad spectrum which is clearly not the powder spectrum of a well defined electric field gradient at the La sites. No satellite transitions are observed indicating that the mean value of the electric field gradient distribution is small and the asymmetry parameter is quite large resulting in a collapse of the satellite lines in the central transition. This suggests that the 4-fold point symmetry is broken for all La sites which may be a consequence of N vacancies in the La-N triple layers.

The  $^{11}\text{B}$  NMR spectra of  $\text{La}_3\text{Ni}_2\text{B}_2\text{N}_{2.6}$  and  $\text{La}_3\text{Ni}_2\text{B}_2\text{N}_{2.9}$  are shown in figure 3.5 (b). The spin echo spectra of both compositions compare rather well except for two small bumps (marked by asterisks) symmetrically appearing at approximately 100 kHz left and right to the central transition. They could indicate a second B site either in the structure or in some secondary phase. Since the X-ray and neutron powder diffraction revealed that the composition  $\text{La}_3\text{Ni}_2\text{B}_2\text{N}_{2.9}$  contains large fraction of  $\text{LaNiBN}$  phase, the two bumps at may represent  $^{11}\text{B}$  located in the  $\text{LaNiBN}$  phase. No such bumps are seen in  $\text{La}_3\text{Ni}_2\text{B}_2\text{N}_{2.7}$  which is almost 100% phase pure. The central transition in figure 3.5(b) is well defined and the quadrupole splitting  $\nu_q$  obtained from the distance between the two satellite transitions is approximately 800 kHz. The steep drop of the intensity at the outer flanks of the satellite transitions reveals a well defined electric field gradient. The fact that the intensity drops to zero shows that the asymmetry parameter of the electric field gradient is zero as it should be due to the 4-fold point symmetry of the B site. Since B is in the vicinity of the nitrogen site N(1), the  $^{11}\text{B}$  spectra strongly advocate that there are no vacancies around the B site and that the nitrogen site N(1) is fully occupied. On the other hand the  $^{139}\text{La}$  spectra shows a broad distribution of field gradients which may be a consequence of vacancies at the nitrogen site N(2).

### 3.6 Neutron powder diffractometry

To directly measure the N-site occupancies in  $\text{La}_3\text{Ni}_2^{11}\text{B}_2\text{N}_{3-\delta}$ , neutron powder diffraction studies were performed for selected compositions using samples with highly isotope enriched (99.97%)  $^{11}\text{B}$ . The neutron powder diffraction data were acquired on the D1A diffractometer at the Institut Laue-Langevin (Grenoble, France). D1A is a high resolution powder diffractometer operating

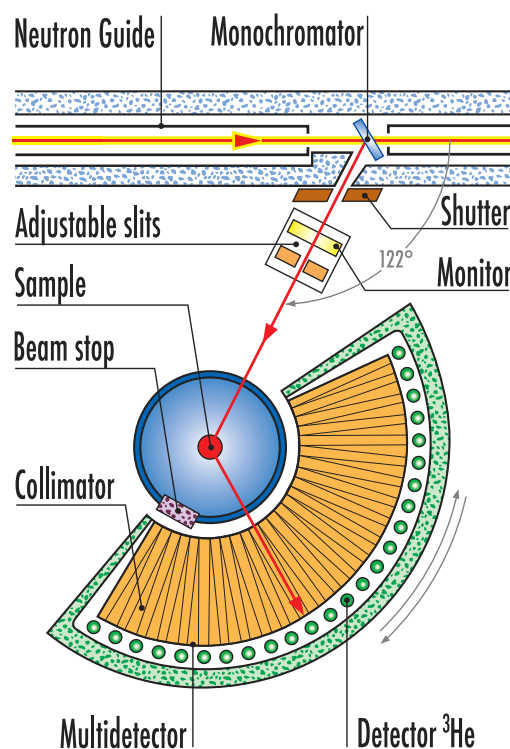


Figure 3.6: Schematic layout of the D1A diffractometer at ILL, Grenoble

at a take-off angle of the monochromator of  $122^\circ$ , giving high resolution at large scattering angles (up to  $160^\circ$ ). It has a bank of 25 high efficiency collimators and  $^3\text{He}$  counting tubes each spaced by  $6^\circ$ . A schematic representation of the instrument layout of D1A is shown in figure 3.6 while a more detailed description can be found elsewhere [51]. The neutron powder diffraction data were collected for three nominal compositions of  $\text{La}_3\text{Ni}_2^{11}\text{B}_2\text{N}_{3-\delta}$  with  $\delta \simeq 0.1, 0.15$  and  $0.35$ . A vanadium sample holder of diameter 1 cm and a length of 5 cm was used for samples of 6g mass. Neutron data was collected for a wavelength of  $1.3894 \text{ \AA}$  and a  $2\theta$  range  $8^\circ < 2\theta < 159.5^\circ$  with steps of  $0.05^\circ$  or  $0.1^\circ$ . The data were collected at five different temperatures ranging from 4 K to 300 K. The background was corrected by means of a linear interpolation between selected points taken from each profile. The program FULLPROF was used for the Rietveld refinement of the diffraction data. The parameters refined were zero shift, scale factor, shape profile, atomic parameters, thermal factors, half width parameters, lattice constants and fractional occupancies. The maximum number of refined parameters and the total number of reflections obtained for  $\text{La}_3\text{Ni}_2\text{B}_2\text{N}_x$  were 50 and 168 respectively. Accordingly, there is a better statistic in the neutron diffraction analysis as compared to XRD.

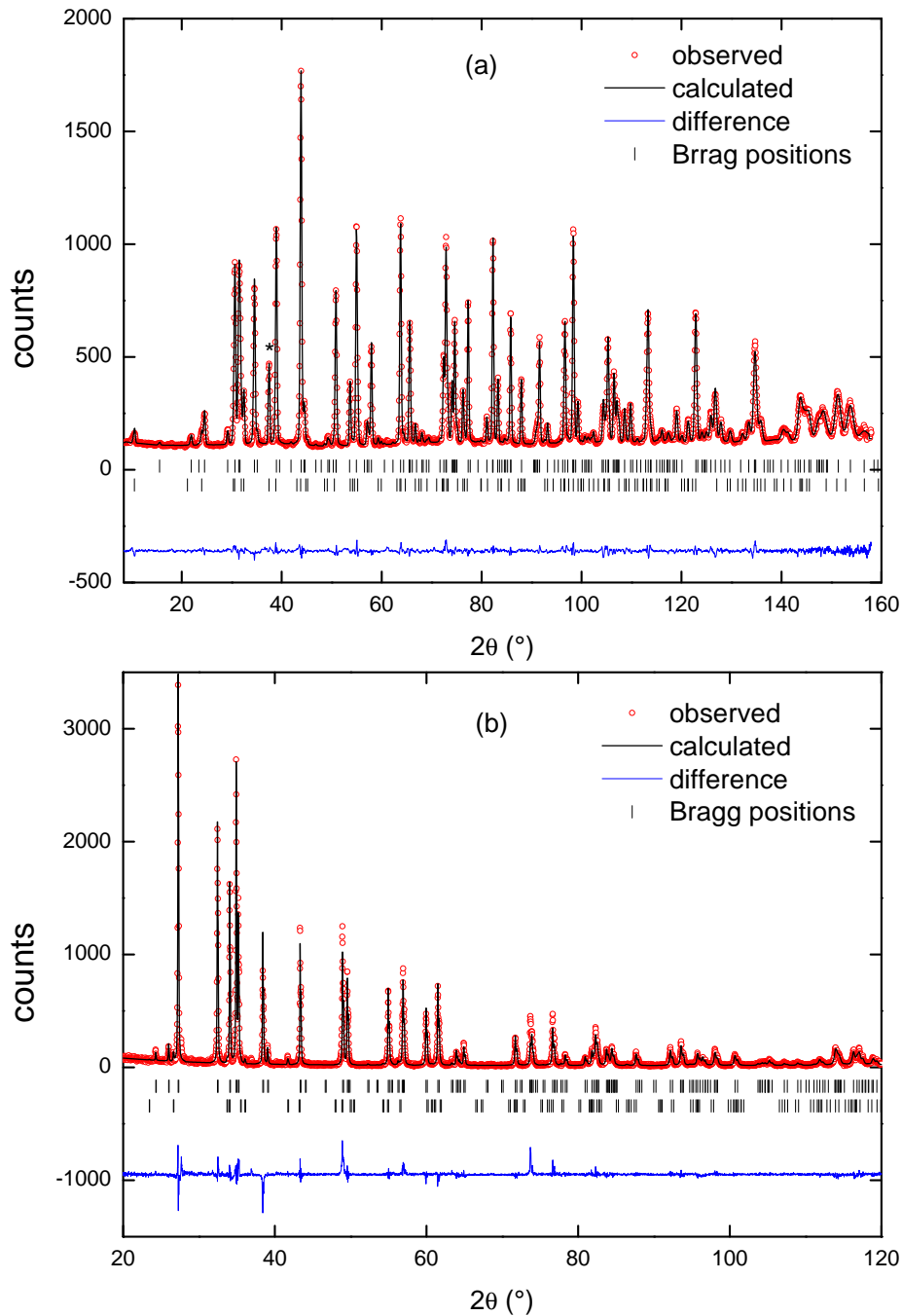


Figure 3.7: Measured, calculated and difference neutron (a) and X-ray (b) powder diffraction pattern of  $\text{La}_3\text{Ni}_2^{11}\text{B}_2\text{N}_{2.85}$  at room temperature. The upper and lower vertical bars indicate Bragg positions for  $\text{La}_3\text{Ni}_2\text{B}_2\text{N}_3$  and  $\text{LaNiBN}$ , respectively.

### 3.6.1 Phase analysis

The neutron powder diffraction pattern of  $\text{La}_3\text{Ni}_2^{11}\text{B}_2\text{N}_{2.85}$  measured at 300 K together with the calculated pattern is shown in figure 3.7(a). The LaNiBN impurity phase is included in the fit and the upper and lower vertical bars indicate the Bragg positions for  $\text{La}_3\text{Ni}_2\text{B}_2\text{N}_3$  and LaNiBN, respectively. The profile refinement of XRD data of the same sample is shown in figure 3.7(b) for a comparison of the amount of LaNiBN impurity phase. The XRD pattern indicates an almost phase pure sample with an amount of LaNiBN phase less than 2%. On the other hand the neutron powder diffraction pattern shows prominent peaks of LaNiBN phase, the strongest being marked by an asterisks in figure 3.7(a). The refinement of the neutron diffraction data reveals an amount of impurity phase near 19%. The neutron powder diffraction patterns for the compositions  $\text{La}_3\text{Ni}_2\text{B}_2\text{N}_{2.65}$  and  $\text{La}_3\text{Ni}_2\text{B}_2\text{N}_{2.90}$  are shown in figure 3.8(a) and 3.8(b) respectively. The results of the profile refinements indicate LaNiBN phase fractions of about 5% for  $\text{La}_3\text{Ni}_2^{11}\text{B}_2\text{N}_{2.65}$  and about 15% for  $\text{La}_3\text{Ni}_2^{11}\text{B}_2\text{N}_{2.9}$ . Interestingly, the X-ray diffraction analysis for both compositions indicated the LaNiBN phase to be less than 2%. It has to be noted that for X-ray diffraction measurements very small pieces of the sample with masses of 80-100 mg are used while the mass of the material used for neutron diffraction was  $\sim 6\text{g}$ . The discrepancy in the amount of impurity phase in X-ray and neutron diffraction results indicates that the impurity phase LaNiBN is not distributed homogeneously throughout the material. So a very small piece with mass  $\sim 100\text{mg}$  used for X-ray diffraction may not represent the bulk material. For this reason the phase analysis by X-ray diffraction can be ambiguous.

### 3.6.2 Structure analysis and real width of formation

The room temperature structural data for the three samples measured at D1A are summarized in table 3.1. Previous neutron powder diffraction studies of the material indicated a N(2) nitrogen site occupancy of 0.9 [45]. In the present work the  $\text{La}_3\text{Ni}_2\text{B}_2\text{N}_{3-\delta}$  samples were prepared with nominal composition  $\delta$  being varied in a systematic way from 0.0 to 0.5 and X-ray diffraction and physical properties propose a significant width of formation. The analysis of neutron powder diffraction data revealed that the refinement of occupancies of all crystallographic sites did not at all improve the fit indicating the positions to be fully occupied. In the final run the occupancies of other positions were kept fixed to fully occupied values except for nitrogen site N(2). Since the occupation of a certain crystallographic position is closely correlated to its related thermal parameter ( $B_{iso}$ ), the  $B_{iso}$  of nitrogen site N(2) is constrained with the  $B_{iso}$  of the fully occupied site N(1). The data in table 3.1 shows slight variation of crystallographic parameters but most interesting re-

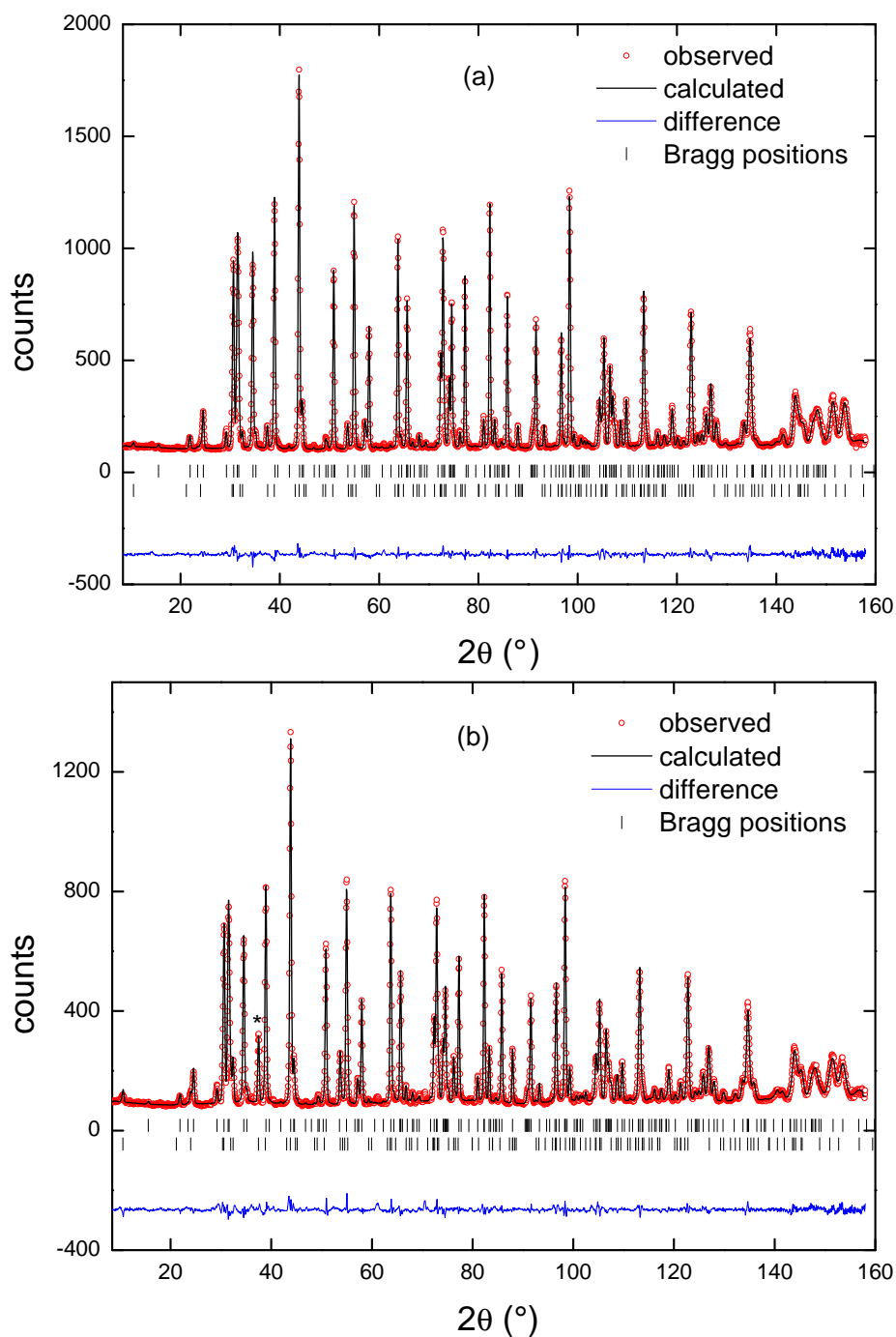


Figure 3.8: Measured, calculated and difference neutron powder diffraction pattern of  $\text{La}_3\text{Ni}_2^{11}\text{B}_2\text{N}_{2.65}$  (a)  $\text{La}_3\text{Ni}_2^{11}\text{B}_2\text{N}_{2.90}$  (b) at room temperature. The upper and lower vertical bars indicate Bragg positions for  $\text{La}_3\text{Ni}_2\text{B}_2\text{N}_3$  and  $\text{LaNiBN}$ , respectively.

sult is the occupation of the nitrogen site N(2). Interestingly, the structural refinement by neutron powder diffraction data resulted in fewer vacancies at the nitrogen site N(2) than expected from the nominal composition. The data in table 3.1 shows a N(2) site occupancy of 0.9 for the nominal composition  $\text{La}_3\text{Ni}_2\text{B}_2\text{N}_{2.65}$  which corresponds to the real composition of  $\text{La}_3\text{Ni}_2\text{B}_2\text{N}_{2.90}$ . The profile refinement results in relatively close values of  $B_{iso}$  of N(1) and N(2) indicating that the occupancy of 0.9 for the N(2) site is realistic. The thermal factors of N(1) and N(2) are in line with the mass relation to La, Ni and B. Similar neutron powder diffraction analysis of  $\text{La}_3\text{Ni}_2\text{B}_2\text{N}_{2.85}$  revealed a N(2) site occupancy of 0.93 corresponding to a real composition of  $\text{La}_3\text{Ni}_2\text{B}_2\text{N}_{2.93}$  while  $\text{La}_3\text{Ni}_2\text{B}_2\text{N}_{2.9}$  exhibits a N(2) occupancy of 0.92 and thus, a refined composition of  $\text{La}_3\text{Ni}_2\text{B}_2\text{N}_{2.92}$ . These results suggest that the matrix phase absorbs more nitrogen during the melting possibly indicating a systematic error in the nominal composition. The profile refinements of

$\text{La}_3\text{Ni}_2^{11}\text{B}_2\text{N}_{2.65}$						
$a = 0.37188(2) \text{ nm}, c = 2.05222(2) \text{ nm}, V = 0.2839(4) \text{ nm}^3, c/a = 5.5117$						
Atom	Site	x	y	z	$B_{iso}$	Occ.
La(2)	2a	0.0000	0.0000	0.00000	0.430(12)	1.00
La(1)	4e	0.0000	0.0000	0.37037(4)	0.413(12)	1.00
Ni	4d	0.0000	0.5000	0.25000	0.551(11)	1.00
B	4e	0.0000	0.0000	0.19433(6)	0.761(17)	1.00
N(1)	4e	0.0000	0.0000	0.12390(4)	0.611(13)	1.00
N(2)	2b	0.0000	0.0000	0.50000	0.656(13)	0.90
$\text{La}_3\text{Ni}_2^{11}\text{B}_2\text{N}_{2.85}$						
$a = 0.37187(2) \text{ nm}, c = 2.05285(2) \text{ nm}, V = 0.2838(4) \text{ nm}^3, c/a = 5.5203$						
Atom	Site	x	y	z	$B_{iso}$	Occ.
La(2)	2a	0.0000	0.0000	0.00000	0.419(15)	1.00
La(1)	4e	0.0000	0.0000	0.37074(5)	0.402(15)	1.00
Ni	4d	0.0000	0.5000	0.25000	0.578(13)	1.00
B	4e	0.0000	0.0000	0.19413(7)	0.791(21)	1.00
N(1)	4e	0.0000	0.0000	0.12395(5)	0.602(16)	1.00
N(2)	2b	0.0000	0.0000	0.50000	0.647(16)	0.93
$\text{La}_3\text{Ni}_2^{11}\text{B}_2\text{N}_{2.90}$						
$a = 0.37208(2) \text{ nm}, c = 2.05082(2) \text{ nm}, V = 0.2839(4) \text{ nm}^3, c/a = 5.5117$						
Atom	Site	x	y	z	$B_{iso}$	Occ.
La(2)	2a	0.0000	0.0000	0.00000	0.511(20)	1.00
La(1)	4e	0.0000	0.0000	0.37089(7)	0.494(20)	1.00
Ni	4d	0.0000	0.5000	0.25000	0.647(17)	1.00
B	4e	0.0000	0.0000	0.19438(9)	0.853(26)	1.00
N(1)	4e	0.0000	0.0000	0.12429(7)	0.652(20)	1.00
N(2)	2b	0.0000	0.0000	0.50000	0.697(20)	0.92

Table 3.1: Crystal structure and Lattice parameters data for nominal compositions  $\text{La}_3\text{Ni}_2\text{B}_2\text{N}_{2.65}$ ,  $\text{La}_3\text{Ni}_2\text{B}_2\text{N}_{2.85}$  and  $\text{La}_3\text{Ni}_2\text{B}_2\text{N}_{2.90}$  at room temperature.

		300 K	180 K	80 K	30 K	4 K
$B_{iso}$ ( $\text{\AA}^2$ )	$a$ (nm)	0.37188	0.3714	0.3711	0.3710	0.3710
	$c$ (nm)	2.05221	2.0510	2.0511	2.0517	2.0519
	$c/a$	5.519	5.522	5.528	5.531	5.530
	$V$ (nm <sup>3</sup> )	0.2838	0.2829	0.2824	0.2824	0.2824
	$z(\text{La}2)$	0.37037	0.37057	0.37074	0.37071	0.37066
	$z(\text{B})$	0.19432	0.19422	0.19411	0.19415	0.19414
	$\text{La}(2)$	0.4300	0.2590	0.1740	0.1590	0.144
$R$ -factors	$\text{La}(1)$	0.4130	0.2420	0.1570	0.1420	0.1270
	Ni	0.5510	0.3860	0.2720	0.2270	0.2230
	B	0.7610	0.5450	0.4400	0.4140	0.3960
	$\text{N}(1)$	0.6110	0.4770	0.3900	0.3500	0.3530
	$\text{N}(2)$	0.6550	0.4920	0.4360	0.3960	0.3980
	$R_p$	6.91	7.04	7.25	7.23	7.70
	$R_{wp}$	6.52	6.77	7.04	7.12	7.54
	$R_{exp}$	4.49	4.33	4.21	4.18	2.35
	$R_{Bragg}$	2.37	2.27	2.60	2.29	2.65
	$\chi^2$	2.10	2.44	2.80	2.91	2.96

Table 3.2: Crystal structure and lattice parameter data for  $\text{La}_3\text{Ni}_2\text{B}_2\text{N}_{2.65}$  at various temperatures as listed.

neutron powder diffraction data and the refined occupancy of N(2) propose a relatively narrow real width of formation of  $\text{La}_3\text{Ni}_2\text{B}_2\text{N}_{3-\delta}$  with  $\delta$  varying from  $\sim 0.06$  to  $0.10$ . A nominal composition  $\text{La}_3\text{Ni}_2\text{B}_2\text{N}_{2.7}$  thus corresponds to a real composition  $\text{La}_3\text{Ni}_2\text{B}_2\text{N}_{2.9}$ . It seems that in order to realize the actual width of formation it requires to accept certain amounts of secondary phases for reaching limiting compositions. Accordingly, to achieve a composition dependent change in  $T_c$  and other physical properties, one needs to vary the N stoichiometry within the much wider nominal width of formation. The  $a$  and  $c$  lattice parameters for the three samples studied at D1A are summarized in table 3.1. They are relatively close to each other and do not show a clear dependence on nitrogen vacancies, which is in line with the observed narrow real width of formation.

### 3.6.3 Thermal expansion

Neutron powder diffraction performed at temperatures ranging from 4 K to 300 K allows to investigate the thermal and vibrational properties of  $\text{La}_3\text{Ni}_2\text{B}_2\text{N}_{3-\delta}$ . The refined lattice parameters for  $\text{La}_3\text{Ni}_2\text{B}_2\text{N}_{2.65}$  at various temperatures are listed in table 3.2. The  $R$ -factors and the corresponding  $\chi^2$  values suggest the quality of the fits. The temperature dependent variation of lattice parameters  $a$  and  $c$  of  $\text{La}_3\text{Ni}_2\text{B}_2\text{N}_{2.65}$  and  $\text{La}_3\text{Ni}_2\text{B}_2\text{N}_{2.90}$  is shown in figure 3.9. The data reveal a decrease of the  $a$  lattice parameter

with decreasing the temperature while the  $c$  lattice parameter shows a non monotonic variation with a minimum. A similar temperature dependent variation of lattice parameters of  $\text{CeNi}_2\text{B}_2\text{C}$  borocarbide has been reported [52] which was explained on the basis of geometrical effects of rather rigid B-C and Ni-B bond lengths. For the borocarbides a decrease in temperature effects the lattice in a similar manner as the lanthanide contraction leading to an increase in the B-Ni-B tetrahedral angle and thus to a stretching of the tetragonal  $c$ -axis when the basal plane lattice constant  $a$  contracts [53, 52]. Since the NiB layers in  $\text{La}_3\text{Ni}_2\text{B}_2\text{N}_{3-\delta}$  are isostructural with that of the single layer borocarbides, a similar approach for explaining the structural variation may be adopted. In  $\text{La}_3\text{Ni}_2\text{B}_2\text{N}_{3-\delta}$  the reduction in temperature results in a reduction in the volume of La-N triple layer which is reflected by decrease in La(2)-N(2) distance from 0.263 nm at 300 K to 0.262 nm at 4 K. This has a direct effect on the  $a$  lattice parameter as seen in figure 3.9. The change in the  $c$  lattice parameter is attributed to rather rigid Ni-B bonds in the  $\text{Ni}_2\text{B}_2$  layers. The Ni-B bond length hardly exhibits any variation with temperature. If the Ni-B distance is not effected by temperature, then this requires an increase in the B-Ni-B tetrahedral angle from  $105.9^\circ$  to  $106.1^\circ$  and also in the  $\text{Ni}_2\text{B}_2$  layer thickness. For  $\text{La}_3\text{Ni}_2\text{B}_2\text{N}_{2.65}$  the  $\text{Ni}_2\text{B}_2$  layer thickness increases from 0.228 nm at 300 K to 0.229 nm at 4 K. A similar increase in  $\text{Ni}_2\text{B}_2$  layer thickness and corresponding increase in the B-Ni-B tetrahedral angle is observed for  $\text{La}_3\text{Ni}_2\text{B}_2\text{N}_{2.90}$ . Another important factor effecting the  $c$  lattice parameter is the variation in the thickness of the La-N triple layers. For  $\text{La}_3\text{Ni}_2\text{B}_2\text{N}_{2.65}$  the thickness of the La-N triple layer decreases from 0.532 nm at 300 K to 0.530 nm at 100 K while it remains almost constant at further lowering of the temperature to 4 K. An identical temperature dependent behavior of the La-N triple layer is observed for  $\text{La}_3\text{Ni}_2\text{B}_2\text{N}_{2.90}$ . So the non-monotonic variation of the  $c$  lattice parameter for both samples is a consequence of the superposition of positive and negative contributions to the  $c$ -axis expansion from  $\text{Ni}_2\text{B}_2$  and La-N triple layers. In the temperature range 300-100 K the effect of the reduction in the La-N triple layer thickness is dominant over the increase in the  $\text{Ni}_2\text{B}_2$  layer thickness resulting in a decrease in the  $c$  lattice parameter. At temperatures below 100 K the thickness of the La-N triple layers becomes almost constant resulting in an increase in the  $c$  lattice parameter. The variation of the unit-cell volume with temperature for  $\text{La}_3\text{Ni}_2\text{B}_2\text{N}_{2.65}$  and  $\text{La}_3\text{Ni}_2\text{B}_2\text{N}_{2.90}$  is shown in figure 3.10. The unit cell volume varies like the  $a$  lattice parameter and shows a reduction with decreasing temperature. From 300 K, to about 100 K the lattice volume reduces almost linearly while at low temperature it becomes almost temperature independent. The experimental data of the unit cell volume is modeled by the Grüneisen approximation for the zero-pressure equation of state, in which the effects of the thermal expansion are considered to be equal to the



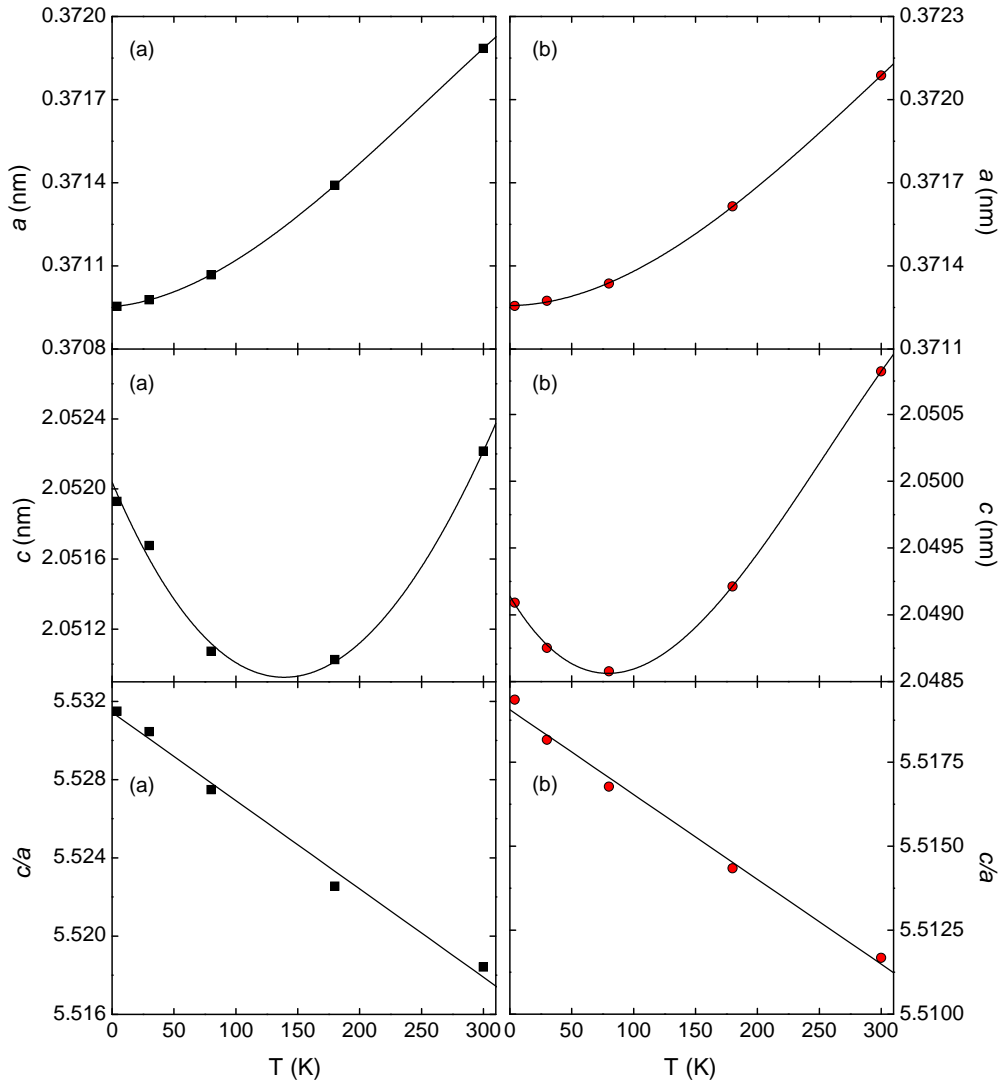


Figure 3.9: Variation of lattice parameters of  $\text{La}_3\text{Ni}_2\text{B}_2\text{N}_{2.65}$  (a) and  $\text{La}_3\text{Ni}_2\text{B}_2\text{N}_{2.90}$  (b) as a function of temperature. Lines are guides to eye.

elastic strain [54]. Thus, the temperature dependence of the volume can be described by

$$V(T) = \frac{\gamma U(T)}{K_o} + V_o + BT^2 \quad (3.1)$$

where  $\gamma$  is the Grüneisen parameter,  $K_o$  is the bulk modulus,  $V_o$  is the volume at  $T = 0$  K and  $B$  is the electronic contribution to the volume expansion. The internal energy in the Debye approximation is given by

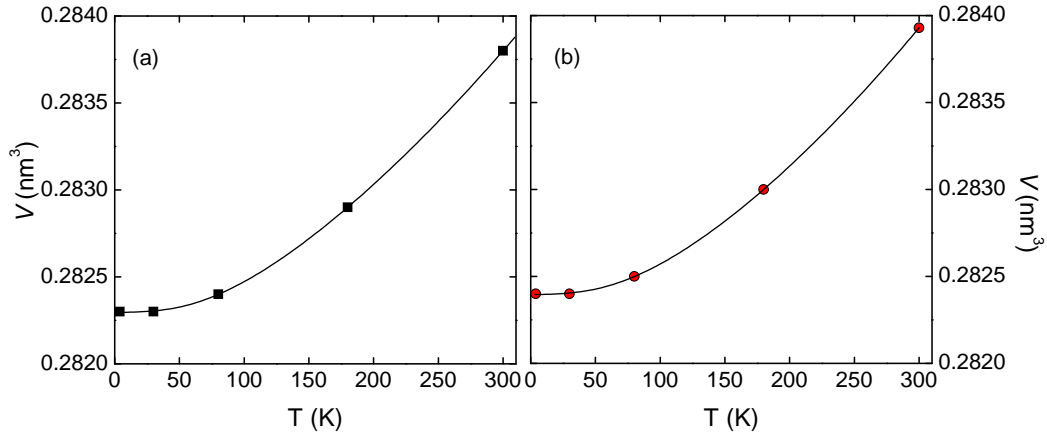


Figure 3.10: Variation of the lattice volume of  $\text{La}_3\text{Ni}_2\text{B}_2\text{N}_{2.65}$  (a) and  $\text{La}_3\text{Ni}_2\text{B}_2\text{N}_{2.90}$  (b) as a function of temperature. Lines indicate a fit of the data on the basis of the Debye model (see text).

$$U(T) = 9Nk_B T \left( \frac{T}{\theta_D} \right)^3 \int_0^{\Theta_D/T} \frac{x^3}{e^x - 1} dx \quad (3.2)$$

where  $N$  is the number of atoms in the unit cell,  $k_B$  is the Boltzmann constant and  $\theta_D$  is the Debye temperature. The variation of the lattice volume with temperature can be very well approximated by the above model as represented by the solid line in figure 3.10(a) for  $\text{La}_3\text{Ni}_2\text{B}_2\text{N}_{2.65}$ . The fit yields  $\gamma/K_o$  of  $1.85 \times 10^{-7} \text{ Pa}^{-1}$ ,  $\Theta_D$  of 345 K,  $V_o = 0.2823 \text{ nm}^3$  and a very small  $T^2$  dependent contribution with a coefficient  $B = 7.1 \times 10^{-9}$ . For  $\text{La}_3\text{Ni}_2\text{B}_2\text{N}_{2.9}$  (figure 3.10) the values of  $\theta_D$  and  $V_o$  are 356 K and  $0.2824 \text{ nm}^3$ , respectively, while other fit parameters remain similar. The value of Debye temperature determined from the neutron diffraction measurements is in reasonable agreement with that determined from specific heat measurements (see chapter 5). A similar approximation of the refined lattice volume of  $\text{La}_3\text{Ni}_2\text{B}_2\text{N}_{2.90}$  is shown in figure 3.10(b). To compare with the results of neutron diffraction measurements, the linear thermal expansions ( $\alpha_L$ ) of selected compositions were measured from 4.2 K to 300 K in a miniature capacitive dilatometer [55]. The measurement setup includes a lower ringlike capacitor plate made of silver with a hole in which the sample is placed. The lower capacitor plate is separated from the upper plate by two needle bearings for the support. The calibration of the capacitor plate sensor is performed using the tilted plate principle [56]. Since the  $\alpha_L$  data for all the measured samples are in reasonable agreement, it is obvious that the thermal expansion of all polycrystalline samples is isotropic and the volume thermal expansion can be calculated by

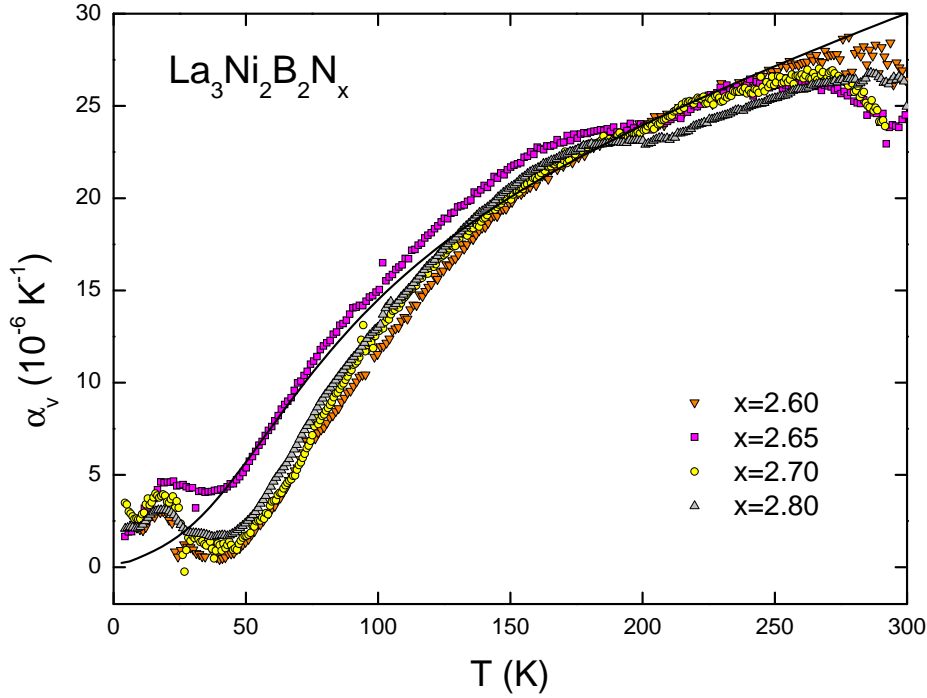


Figure 3.11: Measured volume thermal expansion of various  $\text{La}_3\text{Ni}_2\text{B}_2\text{N}_{3-x}$  samples with  $x$  as labeled. The line shows a Debye fit of the volume thermal expansion of  $\text{La}_3\text{Ni}_2\text{B}_2\text{N}_{2.65}$  from neutron diffraction measurements.

the equation  $\alpha_v = 3\alpha_L$ . The volume thermal expansion of selected samples is shown in figure 3.11 all showing a kink at 200K which is an artifact from the temperature regulation. The anomaly visible below 30 K may be associated with the non monotonic variation of  $c$  lattice parameter but it is not clear because we have no neutron diffraction data in temperature range between 4 and 30 K. Also it could be an artifact from cell calibration because absolute expansion of  $\text{La}_3\text{Ni}_2\text{B}_2\text{N}_x$  is small below 50 K. The solid line in figure 3.11 indicates  $\alpha_v$  as determined from the approximation of lattice volume on the basis of Debye theory (see figure 3.10). The data in figure 3.11 reveals good quantitative agreement with the  $\alpha_v$  determined by neutron diffraction measurements.

### 3.6.4 Atomic displacement parameters

In any kind of Bragg diffraction measurement a rise in the temperature of the crystal results in a reduction in the intensity of the Bragg reflected beam, but the angular width of reflected lines does not change [57]. The intensity

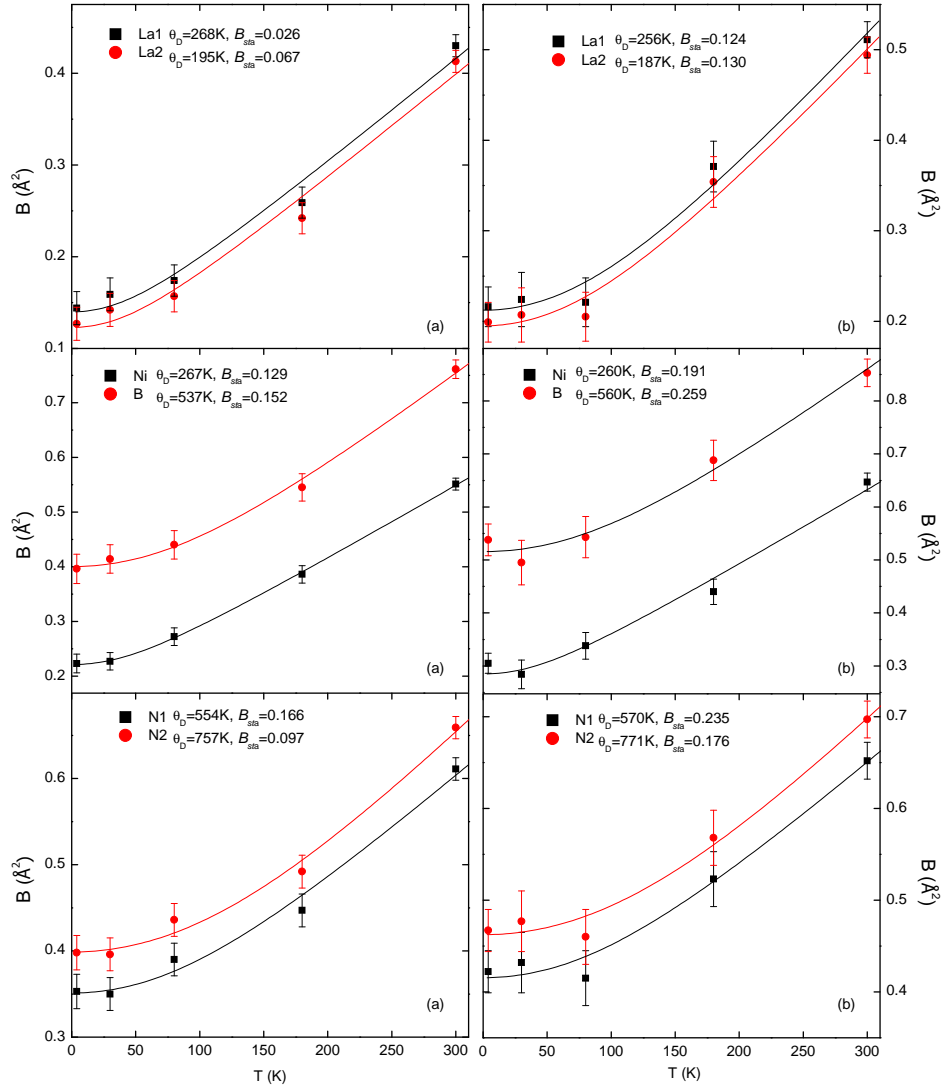


Figure 3.12: Isotropic thermal parameters for different atoms in  $\text{La}_3\text{Ni}_2\text{B}_2\text{N}_{2.65}$  (a) and  $\text{La}_3\text{Ni}_2\text{B}_2\text{N}_{2.90}$  (b). Solid lines are fit according to equation 3.7.

of a typical Bragg peak is qualitatively given as

$$I = I_o \exp\left(-\frac{1}{3}\langle U^2 \rangle G^2\right) \quad (3.3)$$

where  $I_o$  is the intensity from a rigid lattice with static atoms and  $G$  is the magnitude of scattering vector. The exponential factor in equation 3.3 is the Debye-Waller factor [57] which corresponds to the thermal parameters ( $B$  factors). The term  $\langle U^2 \rangle$  in equation 3.3 represents atomic displacement

	La <sub>3</sub> Ni <sub>2</sub> B <sub>2</sub> N <sub>2.65</sub>		La <sub>3</sub> Ni <sub>2</sub> B <sub>2</sub> N <sub>2.90</sub>	
	$\theta_D$ (K)	$\omega_D$ (THz)	$\theta_D$ (K)	$\omega_D$ (THz)
La(1)	268	5.58	256	5.33
La(2)	195	4.06	187	3.89
Ni	267	5.56	260	5.41
B	537	11.18	560	11.66
N(1)	554	11.54	570	11.87
N(2)	757	15.76	771	16.05

Table 3.3: Debye temperatures and Debye frequencies of different atoms for La<sub>3</sub>Ni<sub>2</sub>B<sub>2</sub>N<sub>2.65</sub> and La<sub>3</sub>Ni<sub>2</sub>B<sub>2</sub>N<sub>2.90</sub> as listed.

parameters (ADP) of different atomic species in the crystal. The ADP's are basic crystallographic parameters that reflect the atomic thermal motion and provide useful information on thermal properties of the materials. ADP measure the mean-square displacement amplitudes of the atoms away from their equilibrium position in a crystal lattice and can be due to vibration of the atoms or due to static disorder. Most often an isotropic ADP  $U_{iso}$  is given corresponding to mean square displacement of an atom averaged over all directions. Within the Debye model the  $U_{iso}$  is given as [58]

$$\langle U_{iso}^2 \rangle = \frac{3h^2T}{4\pi^2mk_B\theta_D^2} \left[ \Phi(\Theta_D/T) + \frac{\Theta_D}{4T} \right] \quad (3.4)$$

with  $\theta_D$  being a Debye temperature of the atom vibrating at a particular lattice site and  $k_B$  is the Boltzmann constant. The term  $\Phi(\theta_D/T)$  is given by

$$\Phi(\theta_D/T) = \frac{T}{\theta_D} \int_0^{\Theta_D/T} \frac{x}{e^x - 1} dx. \quad (3.5)$$

At high temperatures ( $T > \theta_D$ )  $U_{iso}$  varies linearly with  $T$  and is given as

$$\langle U_{iso}^2 \rangle = \frac{3h^2}{4\pi^2mk_B\theta_D^2} T \quad (3.6)$$

and at low temperature  $U_{iso}$  reaches the zero point value of  $3h^2/16\pi^2mk_B\theta_D$ . The ADP of different crystallographic sites for nominal compositions La<sub>3</sub>Ni<sub>2</sub>B<sub>2</sub>N<sub>2.65</sub> and La<sub>3</sub>Ni<sub>2</sub>B<sub>2</sub>N<sub>2.90</sub> are investigated over the measured temperature range. The isotropic thermal parameter  $B_{iso}$  is related to the mean-square displacement amplitude  $\langle U_{iso} \rangle$  as [59]

$$B_{iso} = 8\pi\langle U_{iso}^2 \rangle + B_{sta} \quad (3.7)$$

where  $B_{sta}$  is the component of the thermal parameter caused by the presence of a certain amount of static disorder in the compound. The thermal

parameters of all the atoms were analyzed on the basis of the model described above and the results are summarized in figure 3.12. The solid lines in figure 3.12 indicate a fit of  $B_{iso}$  values according to equation 3.7 revealing that the  $B_{iso}$  of all atoms being reasonably well described by the Debye model in the measured temperature range. The Debye temperatures along with the corresponding Debye frequencies for different atomic species are listed in table 3.3. The Debye frequencies of B and N(1) are comparable while N(2) which is located in central LaN layer has a slightly higher frequency.

# Chapter 4

## Normal state properties of $\text{La}_3\text{Ni}_2\text{B}_2\text{N}_{3-\delta}$

### 4.1 Introduction

After their discovery, the rare-earth nickel borocarbides  $R\text{Ni}_2\text{B}_2\text{C}$  remained center of interest for more than 10 years mainly due to the rich variety of their physical properties [34]. Many investigations of the normal state transport and magnetic properties of  $R\text{Ni}_2\text{B}_2\text{C}$  has been reported (see Ref. [34, 60] for reviews), whereas no comprehensive study of normal state transport and magnetic properties of  $\text{La}_3\text{Ni}_2\text{B}_2\text{N}_{3-\delta}$  is yet reported. Detailed studies of superconducting properties of bulk  $\text{La}_3\text{Ni}_2\text{B}_2\text{N}_{3-\delta}$  samples have been published [41, 61].

To achieve a better understanding of the interactions responsible for superconductivity, it is important to investigate the normal state properties of a superconductor. The following chapter presents an analysis of normal state specific heat, susceptibility and resistivity of  $\text{La}_3\text{Ni}_2\text{B}_2\text{N}_{3-\delta}$ . The normal state thermal conductivity and thermopower are reported for the first time and data of the high temperature magnetic susceptibility is also presented. The specific heat data are analyzed on the basis of Debye and Einstein models and measured data are compared with phonon density of states (PDOS) obtained from *ab initio* calculations. The density functional theory calculations were performed by Reith and Podloucky using the *Vienna ab initio simulation* (VASP) package [62].

## 4.2 Transport properties

### 4.2.1 Electrical resistivity

The electrical resistivity is a direct probe of electron scattering inside the material. The dependence of the electrical resistivity on temperature, pressure, magnetic field or any other parameter thus, provides information of the interactions present. The electrical resistivity of a metal in the case of simple independent scattering processes obeys Matthiessen's rule and can be considered as a sum of partial resistivities [57, 63]

$$\rho_{total}(T) = \rho_o + \rho_{ph}(T) + \rho_e(T) \quad (4.1)$$

where  $\rho_o$  is the temperature independent residual resistivity due to elastic electron scattering by any kind of static defects scattering while  $\rho_{ph}$  and  $\rho_e$  represent resistivities corresponding to the inelastic electron-phonon and electron-electron scattering respectively. The  $\rho_{ph}$  in the simplest case is described by the Bloch-Grüneisen model which assumes a phonon spectrum based on the Debye model whereas  $\rho_e$  displays a  $T^2$  dependence at lowest temperatures [57, 63].

#### Residual resistivity

The electrical resistivity versus temperature of selected  $\text{La}_3\text{Ni}_2\text{B}_2\text{N}_{3-\delta}$  samples is plotted in figure 4.1(a). The room temperature resistivity for  $\text{La}_3\text{Ni}_2\text{B}_2\text{N}_{2.6}$  is  $\sim 75 \mu\Omega\text{cm}$  which decreases with increasing nominal nitrogen stoichiometry and reaches a value of  $\sim 60 \mu\Omega\text{cm}$  for  $\text{La}_3\text{Ni}_2\text{B}_2\text{N}_{2.9}$ . The residual resistivity,  $\rho_o$ , for all the samples was taken to be the resistivity at 15 K. The resistivity data in figure 4.1(a) reveal an increase in  $\rho_o$  with increase in nitrogen off-stoichiometry. The variation of  $\rho_o$  as a function of nominal N-stoichiometry shown in figure 4.2(a) reveals an increase of  $\rho_o$  from about  $12 \mu\Omega\text{cm}$  for  $\text{La}_3\text{Ni}_2\text{B}_2\text{N}_{2.90(5)}$  to about  $24 \mu\Omega\text{cm}$  for  $\text{La}_3\text{Ni}_2\text{B}_2\text{N}_{2.60(5)}$ . The increase in  $\rho_o$  is accompanied by a concomitant reduction of the room temperature to residual resistivity ratio (RRR) from 5.0 to 3.2. These changes are obviously related to the increasing density of nitrogen vacancies, since any lattice vacancy acts as scattering potential for conduction electrons and thus contributes to the temperature independent residual resistivity.  $\rho_o$  as a function of N-vacancies  $\delta$  as determined from neutron powder diffraction (see section 3.6) is shown in figure 4.2(b). The dashed line in the figure 4.2(b) reveals that the data approximately extrapolates to  $\rho_o = 0$  for a vacancy and impurity free  $\text{La}_3\text{Ni}_2\text{B}_2\text{N}_3$ .



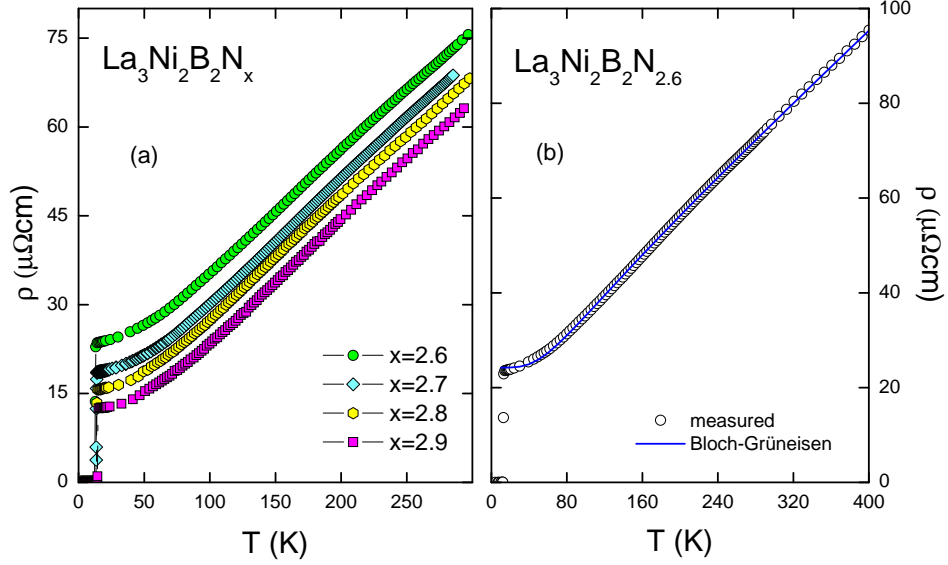


Figure 4.1: Temperature dependent electrical resistivity of selected  $\text{La}_3\text{Ni}_2\text{B}_2\text{N}_x$  samples (a) and  $\text{La}_3\text{Ni}_2\text{B}_2\text{N}_{2.6}$  (b). Solid line in (b) represents a fit according to the Bloch-Grüneisen relation.

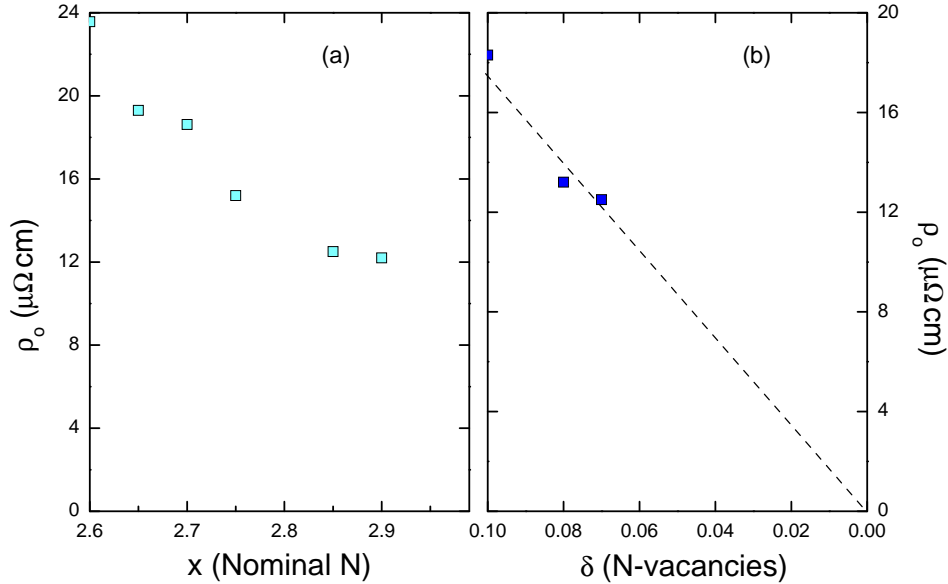


Figure 4.2: Residual resistivity  $\rho_0$  as a function of nominal nitrogen stoichiometry  $x$  (a) and nitrogen vacancies  $\delta$  (b) determined by neutron powder diffraction. Dashed line in (b) is a guide to eye.

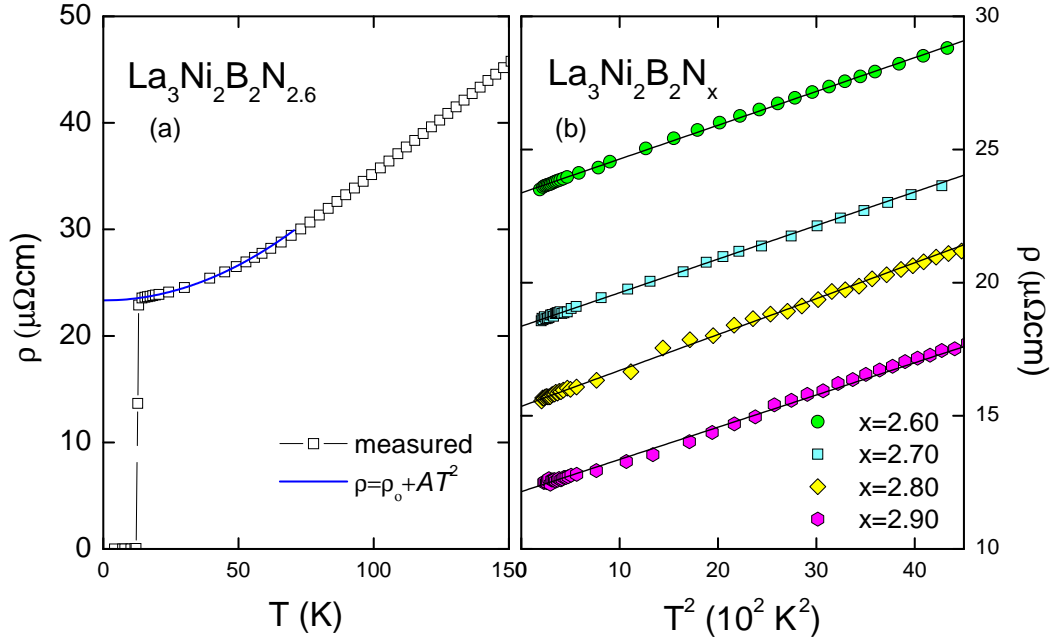


Figure 4.3: (a):  $\rho(T)$  of selected  $\text{La}_3\text{Ni}_2\text{B}_2\text{N}_{2.6}$  with solid line representing a fit of low  $T$  part according to equation 4.3. (b):  $\rho(T)$  of selected  $\text{La}_3\text{Ni}_2\text{B}_2\text{N}_x$  compositions with solid lines representing linear fits.

### $T^5$ versus $T^2$ dependence

The resistivity of  $\text{La}_3\text{Ni}_2\text{B}_2\text{N}_{3-\delta}$  reveals simple metallic behaviour at  $T > T_c$ , and may roughly be accounted for by the standard model for the temperature dependent electrical resistivity of metals given by the Bloch-Grüneisen relation

$$\rho(T) = \rho_0 + \frac{4B}{\Theta_D} \left( \frac{T}{\Theta_D} \right)^5 \int_0^{\frac{\Theta_D}{T}} \frac{z^5 dz}{(e^z - 1)(1 - e^{-z})}, \quad (4.2)$$

where  $\rho_0$  is residual resistivity,  $B$  is electron-phonon coupling constant and  $\Theta_D$  is Debye temperature. Figure 4.1(b) shows the temperature dependent resistivity of  $\text{La}_3\text{Ni}_2\text{B}_2\text{N}_{2.6}$  with a solid line representing a fit according to Bloch-Grüneisen relation yielding  $\rho_0 = 24.2 \mu\Omega\text{cm}$ ,  $B = 18.8 \text{ m}\Omega\text{cmK}$  and  $\Theta_D^{\rho} = 319(20) \text{ K}$ . From the analysis of selected compositions no significant impact of the N-stoichiometry on the Debye temperature  $\Theta_D^{\rho}$  as well as on the electron-phonon coupling constant  $B$  is observed. From figure 4.1(b) it is seen that equation 4.2 describes the data rather well in the temperature range  $80 \leq T \leq 300 \text{ K}$ . Below 80 K, the resistivity is not well accounted for by the Bloch-Grüneisen relation which predicts a  $T^5$  low temperature behaviour. In order to describe the temperature dependence of  $\rho(T)$  at low temperature

the data was fitted to the expression

$$\rho(T) = \rho_0 + AT^2. \quad (4.3)$$

The low temperature resistivity of selected compositions is shown in figure 4.3(b) as  $\rho(T)$  vs.  $T^2$  with solid lines representing fits of the data in the temperature interval  $T_c \leq T \leq 60$  K by equation 4.3 revealing a quadratic temperature dependence of resistivity at low  $T$  for all samples. The fit parameter  $A$  does not show any significant composition dependence and has a value  $\sim 1.3 \times 10^{-3} \mu\Omega\text{cm}/\text{K}^2$ . A quadratic temperature dependence of the low  $T$  resistivity has also been reported for the related borocarbide superconductors Y and  $\text{LuNi}_2\text{B}_2\text{C}$  [30, 64] and also for superconducting high- $T_c$   $A$ -15 compounds [65] which belong to the same class of superconductors as  $\text{La}_3\text{Ni}_2\text{B}_2\text{N}_{3-\delta}$ . The most plausible explanations for a  $T^2$  dependence of the resistivity are electron-electron (e-e) and electron-phonon (e-ph) scattering processes. The  $T^2$  behaviour in the low temperature resistivity of  $A$ -15 compounds was initially suggested by Webb *et al.* [66] to be due to e-ph interaction resulting from a non-Debye phonon spectrum. However this idea was discounted by Gurvitch *et al.* [65] who later proposed that strong e-ph coupling together with high disorder in  $A$ -15 compounds may lead to a  $T^2$  dependence of low temperature resistivity. However this mechanism of e-ph scattering in a disordered compound is highly unlikely in well crystalline borocarbides and  $\text{La}_3\text{Ni}_2\text{B}_2\text{N}_{3-\delta}$ .

In case of the borocarbide superconductors, Rathnayaka *et al.* [30] argued that the Gurvitch model is not applicable because of the relatively high value of  $A$  coefficient of  $T^2$ . They attributed the quadratic temperature dependence of resistivity at low  $T$  to e-e correlation effects caused by narrow Ni  $3d$  derived bands. This was explained by Rice [67] in terms of the Baber mechanism for  $d$  metal compounds where the main contribution to resistivity is from the scattering of  $s$  electrons (with highest mobility and small effective mass) from heavier  $d$  holes due to screened Coulomb interactions.

The validity of Gurvitch model of e-ph scattering was later questioned [68] on several basis, one of which was the MacDonald model [69, 70] of e-e scattering. The MacDonald model suggests that the  $T^2$  dependence of  $\rho$  is due to phonon mediated e-e interactions which are expected to weaken at about  $\Theta_D/T$  to yield the limited temperature range in which the power law is observed. The model asserts that the e-e interaction induced by e-ph coupling is almost 20 times the value expected e.g. from Baber mechanism [67] which has been calculated in terms of Kadowaki-Woods ratio [71].

### Kadowaki-Woods ratio

The  $A$  coefficient of  $T^2$  dependent  $\rho$  and the Sommerfeld coefficient  $\gamma$  are related in terms of the Kadowaki-Woods ratio (KWR)  $A/\gamma^2$  [71]. In case of

*d* metals, the Fermi liquid calculations by Rice based on Baber mechanism implies a KWR of  $0.9 \times 10^{-6} \mu\Omega\text{cm}(\text{mol K/mJ})^2$  however the mean experimental trend revealed a KWR  $0.4 \times 10^{-6} \mu\Omega\text{cm}(\text{mol K/mJ})^2$  [67]. A universal behaviour of KWR with  $A/\gamma^2 = 1.0 \times 10^{-5} \mu\Omega\text{cm}(\text{mol K/mJ})^2$  has also been observed for heavy fermion compounds and for *A*-15 superconductors [72].

For  $\text{La}_3\text{Ni}_2\text{B}_2\text{N}_{3-\delta}$  with  $A \simeq 1.3 \times 10^{-3} \mu\Omega\text{cm/K}^2$  and  $\gamma \simeq 13.0 \text{mJ/mol-NiK}^2$  a Kadowaki-Woods ratio of  $0.8 \times 10^{-5} \mu\Omega\text{cm}(\text{mol-Ni K/mJ})^2$  is obtained which is in reasonable agreement with *A*-15 superconductors. The KWR of boronitrides is exactly 20 times the mean experimental trend for *d* metals mentioned by Rice [67] and is consistent with the MacDonald model discussed before. This explains the comparatively higher values of *A* estimated for borocarbides and some *A* – 15 compounds. Since the value of  $A \sim 1.3 \times 10^{-3} \mu\Omega\text{cm/K}^2$  for boronitrides is significantly higher than the value expected from Baber mechanism, one may conclude that the quadratic dependence of  $\rho$  at low temperature is a consequence of phonon mediated e-e correlation effects in term of MacDonalds model. The same mechanism may also be responsible for higher values of *A* in borocarbides and *A*-15 compounds.

It should be noted that in the case of *A*-15 compounds, a common practice is to take the Sommerfeld coefficient in units of  $\text{mJ/g-at K}^2$  which results in a  $A/\gamma^2 \simeq 1.0 \times 10^{-5} \mu\Omega\text{cm}(\text{mol K/mJ})^2$ . However if one uses  $\gamma$  in units of  $\text{mJ/g-at K}^2$  for  $\text{La}_3\text{Ni}_2\text{B}_2\text{N}_{3-\delta}$ , the KWR gets very large and could be misleading because the *d* metal fraction is much smaller than that of the *A*-15 compounds.

## Transport electron-phonon coupling constant

The resistivity data can be used to determine the transport electron-phonon coupling constant ( $\lambda_{tr}$ ). The Bloch-Grüneisen transport theory relates the temperature dependence of resistivity  $\rho$  to electron-phonon coupling constant  $\lambda_{tr}$  as [73]

$$\frac{d\rho}{dT} = \frac{8\pi^2}{3\hbar\omega_p^2} k_B \lambda_{tr} \quad (4.4)$$

where  $\omega_p$  is the Drude plasma frequency given by

$$\omega_p^2 = \frac{4}{3}\pi^2 N(E_f) e^2 v_F^2 \quad (4.5)$$

with  $N(E_f)$  as density of states at Fermi level and  $v_F$  the Fermi velocity. Equation 4.4 is valid in temperature range  $T > 0.7\Theta_D$  and assumes that the residual resistivity  $\rho_o$  as well as other contributions to be small compared to the electron-phonon contribution described by the Boltzman theory [73]. The value of  $v_F$  is taken to be  $2.4 \times 10^5 \text{m/s}$  from electronic structure calculations [74]. For the nominal composition  $\text{La}_3\text{Ni}_2\text{B}_2\text{N}_{2.70}$  with  $\Theta_D \simeq 329 \text{K}$  and

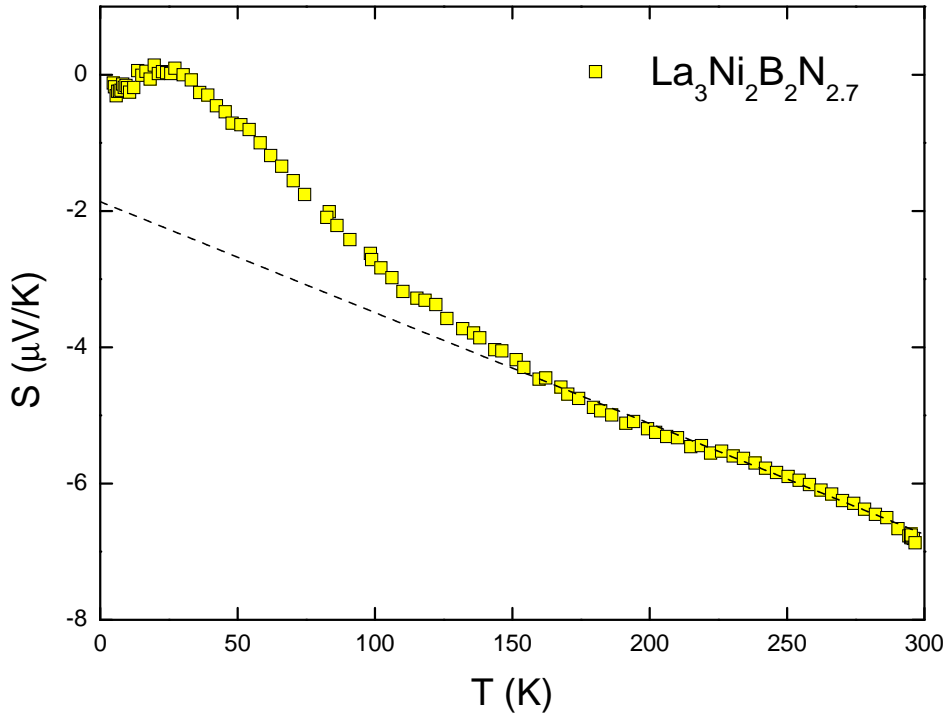


Figure 4.4: Temperature dependent thermopower of  $\text{La}_3\text{Ni}_2\text{B}_2\text{N}_{2.7}$ . Dashed line indicates a least square fit of the data in range  $200 \text{ K} < T < 300 \text{ K}$ .

$N(E_f) \simeq 6.0 \text{ states/eV. f.u}$  (see section 5.4.5) a value  $\lambda_{tr} \simeq 0.9$  which is in good agreement with  $\lambda_{ep}$  obtained from  $T_c$  in terms of Mc Millan formula (section 5.4.3). Allen [75] calculated a  $\lambda_{tr}$  of 0.29 using the data of Ref. [41] which however is in disagreement with the present results and obviously wrong by a factor of about 3 and is the obvious reason for the discrepancy in the values of  $\lambda_{tr}$  as compared to the present estimate.

### 4.2.2 Thermopower

Thermopower measurements were carried out from 4 K to 300 K by employing the so called differential seasaw heating technique. The temperature dependence of the thermopower  $S(T)$  of  $\text{La}_3\text{Ni}_2\text{B}_2\text{N}_{2.7}$  is shown in figure 4.4.  $S(T)$  is negative above the superconducting transition temperature ( $T_c \simeq 13 \text{ K}$ ) indicating a positive slope of electron density of states at Fermi level. The room temperature thermopower  $S(300 \text{ K}) = -6.77 \mu\text{V/Ks}$  is close to the values reported for single crystals of the nonmagnetic borocarbide superconductors Y and  $\text{LuNi}_2\text{B}_2\text{C}$  [30]. The thermopower decreases almost linearly with  $T$  near room temperature within the accuracy of the measurement and an extrapolation of the data in temperature range  $200 \text{ K} < T < 300 \text{ K}$  ac-

According to  $S(T) = a + bT$  gives a linear contribution to  $S(T)$  with a slope  $b = -15.2 \text{ nV/K}^2$  and an intercept  $a = -1.85 \mu\text{V/K}$ . A similar behaviour of the absolute thermopower has been reported for most borocarbides with the coefficient of the linear contribution to the thermopower  $b$ , varying between  $-10.4 \text{ nV/K}^2$  and  $-23.5 \text{ nV/K}^2$  and magnitude of the parameter  $a$ , slightly higher than that of the boronitrides [76]. For a conventional nonmagnetic metal the thermopower consists of contributions from diffusion and phonon-drag thermopowers which results from the transfer of phonon momentum to electrons. The diffusion thermopower is proportional to the temperature while the phonon-drag thermopower vanishes at high temperature as phonon-phonon scattering increases, and also at low temperatures where phonons freeze out. This temperature dependence of the phonon-drag thermopower normally results in a peak with a  $T^3$  dependence below  $0.1\Theta_D$  and a  $1/T$  dependence above  $0.3\Theta_D$ , where  $\Theta_D$  is the Debye temperature.

The thermopower data shown in figure 4.4 reveals a change in the slope at about 170 K while a peak is observed at  $\sim 30$  K indicating additional contributions to the thermopower other than diffusion. Such a non linear temperature dependence of  $S(T)$  is similar to that of Y and  $\text{LuNi}_2\text{B}_2\text{C}$  single crystals [30]. Rathnayaka *et al.* [30] found that  $S - bT$ , representing contributions to  $S(T)$  other than diffusion, is almost constant between 100 to 300 K and varies as  $1/T$  below 100 K for both,  $\text{YNi}_2\text{B}_2\text{C}$  and  $\text{LuNi}_2\text{B}_2\text{C}$ , single crystals. They attributed the observed change of slope in  $S(T)$  to phonon drag effects. Analyzing  $S(T)$  of  $\text{La}_3\text{Ni}_2\text{B}_2\text{N}_{2.7}$  in the same manner, it is found that  $S - bT$  is almost constant above 170 K and varies as  $1/T$  in temperature range  $0.3\Theta_D < T < 170 \text{ K}$  and as  $T^3$  in  $T_c < T < 0.1\Theta_D$  ( $\Theta_D = 330 \text{ K}$ ). This temperature dependence of  $S(T)$  together with a peak at 30 K suggests that a phonon drag contribution to thermopower is dominant at low temperature.

### 4.2.3 Thermal Conductivity

The thermal conductivity of metallic systems is given by  $\lambda = \lambda_e + \lambda_{ph}$  where  $\lambda_e$  and  $\lambda_{ph}$  represent the contributions from electrons and phonons, respectively. In the case of simple metals the Wiedemann-Franz law is expected to be valid approximating  $\lambda_e$  as

$$\lambda_e = L_o T / \rho \quad (4.6)$$

with the Lorentz number  $L_o = 2.44 \times 10^{-8} \text{ W}\Omega\text{K}^{-2}$  and  $\rho$  being the electrical resistivity. The temperature dependent thermal conductivity of a  $\text{La}_3\text{Ni}_2\text{B}_2\text{N}_{2.7}$  is shown in figure 4.5. The thermal conductivity shows an overall behaviour typical of an intermetallic compound. The high temperature  $\lambda(T)$  is approximately linear which may not be intrinsic and most likely due to radiation losses during the measurement. A similar trend in the high temperature thermal conductivity has been reported for single crystal boro-

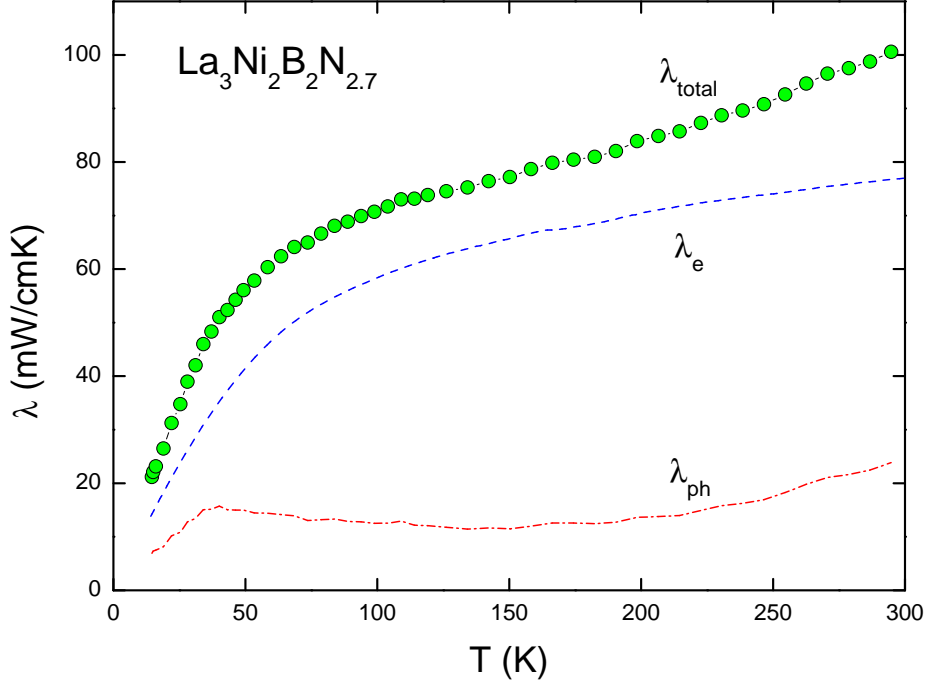


Figure 4.5: Temperature dependent thermal conductivity of  $\text{La}_3\text{Ni}_2\text{B}_2\text{N}_{2.7}$ .  $\lambda_e$  and  $\lambda_{ph}$  represent electronic and lattice contributions, respectively.

cabides but with absolute values relatively higher than reported here [77, 78]. To disentangle the electronic and lattice contributions, equation 4.6 is applied to the resistivity data (figure 4.1) to calculate  $\lambda_e(T)$  and  $\lambda_{ph} = \lambda_{exp} - \lambda_e$ . The resulting electronic and lattice thermal conductivities are displayed in figure 4.5 labeled as  $\lambda_e$  and  $\lambda_{ph}$  respectively. The dominant contribution to the total thermal conductivity comes from the  $\lambda_e$  but there is no peak in  $\lambda_e(T)$  below  $0.1\Theta_D$  which is expected for a good metallic behaviour. According to Matthiessen's rule, the electrical resistivity can be represented as a sum of partial resistivities, corresponding to different processes of electron scattering. By analogy, the inverse electronic thermal conductivity,  $1/\lambda_e$ , can be expressed as a partial sum of thermal resistivities  $W$ . So for non-magnetic materials, the temperature dependence of  $\lambda_e$  (e.g. for  $T < 0.1\Theta_D$ ) is approximated as [79]

$$1/\lambda_e(T) \equiv W_{e,0}(T) + W_{e,ph}(T) = \frac{\alpha}{T} + \beta T^2 \quad (4.7)$$

where  $W_{e,0}$  and  $W_{e,ph}$  represent the thermal resistivities due to interactions of electrons with imperfections and thermally excited phonons, respectively while  $\alpha$  and  $\beta$  are constants. The electronic thermal resistivity  $W_e(T)$  as calculated from the Wiedemann-Franz law is shown in figure 4.6. The solid

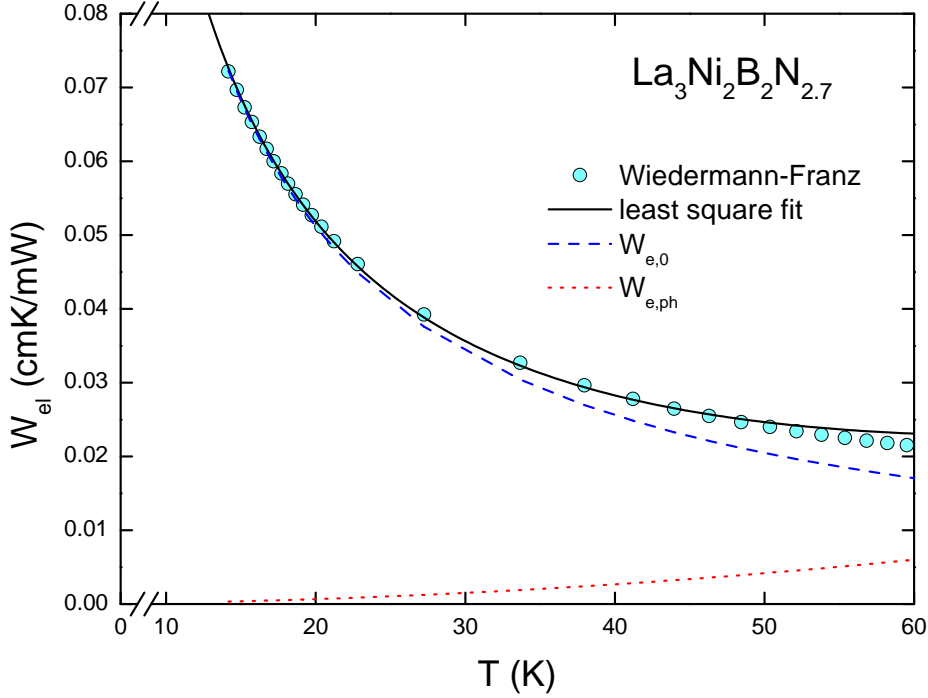


Figure 4.6: Temperature dependent electronic thermal resistance of  $\text{La}_3\text{Ni}_2\text{B}_2\text{N}_{2.7}$  in the normal state. The solid line indicates a fit according to equation 4.7 while dashed and dotted lines indicate contributions from electron-impurity and electron-phonon scattering, respectively.

line indicates a fit of  $W_e(T)$  according to equation 4.7 yielding  $\alpha = 1.02 \times 10^3 \text{ cmK}^2/\text{W}$  and  $\beta = 1.67 \times 10^{-3} \text{ cm/WK}$ . These fit parameters give the electron-impurity and electron-phonon contribution to thermal resistivity shown as dashed and dotted lines in figure 4.6 respectively. The electronic thermal conductivity,  $\lambda_e$  can be written as [80]

$$1/\lambda_e(T) = \frac{3}{C_e v_f^2} [\tau_{ei}^{-1} + \tau_{ep}^{-1}] \quad (4.8)$$

where  $\tau_{ei}^{-1}$  and  $\tau_{ep}^{-1}$  represent the relaxation rates for electron imperfection and electron phonon scattering processes respectively. At low temperature i.e.  $T \ll \Theta_D$  where  $\Theta_D$  is Debye temperature, the electron-phonon relaxation processes freeze out and electron-impurity scattering is dominant in  $\lambda_e$ . Since  $\lambda_{e,0}$  varies linearly with  $T$  as in equation 4.7, it causes an overall linear behaviour of  $\lambda(T)$  above the superconducting transition temperature ( $\sim 13 \text{ K}$ ). As the temperature increases, electron-phonon scattering increases as indicated by figure 4.6 and becomes the dominant process for the thermal resistivity. At high temperature ( $T \geq \Theta_D$ ), the electron-phonon scattering processes are elastic with  $\tau_{ep}^{-1} \propto T$  resulting in  $\lambda_e = \text{const}$ .



The phonon thermal conductivity  $\lambda_{ph}$  for a normal metal is expected to vary as  $T^3$  at low temperature and to fall as  $1/T$  at high  $T$ . The  $\lambda_{ph}$  of  $\text{La}_3\text{Ni}_2\text{B}_2\text{N}_{2.7}$  roughly reveals a normal metal like behaviour except for the increase at high temperature which could be an artifact of the measurement.

### 4.3 Magnetic Properties

The normal state magnetic susceptibility,  $\chi(T)$ , of selected  $\text{La}_3\text{Ni}_2\text{B}_2\text{N}_{3-\delta}$  samples was studied from  $T_c$  up to 300 K by means of magnetization measurements on a dc-SQUID magnetometer at 1 T while the high temperature measurements were performed on a Quantum-Design Physical Property Measurement System, vibrating sample magnetometer (VSM) at 9 T. The susceptibility plot of  $\text{La}_3\text{Ni}_2\text{B}_2\text{N}_{2.7}$  is shown in figure 4.7 at an applied field of 1T. The data in circles represents the original measurement from VSM which is adjusted by a factor to match the low temperature SQUID measurement. The susceptibility is weakly temperature dependent between 50 and 1000 K while an upturn at low temperatures is most likely due to the presence of small amounts of paramagnetic impurities. The normal state  $\chi(T)$  data for samples with various nominal compositions are almost matching and can be accounted for by a weakly temperature dependent Pauli susceptibility (from Sommerfeld expansion) plus a Curie-Weiss term for the impurity contribution as

$$\chi = \chi_o(1 - aT^2) + C/(T - \Theta_p) \quad (4.9)$$

where  $\chi_o$  is the low temperature Pauli susceptibility,  $a$  is its temperature coefficient,  $\Theta_p$  is paramagnetic Curie temperature, and  $C$  is the Curie constant. A fit of the data in the temperature range 15-1000 K is shown as a solid line in figure 4.7. The fit yields a  $\chi_o \simeq 0.22 \times 10^{-3}$  emu/mol,  $a = 3.4 \times 10^{-7} \text{ K}^{-2}$ ,  $C \simeq 7.2 \times 10^{-3}$  emu K/mol and a paramagnetic Curie temperature  $\Theta_p$  of the order of -10 K.  $\chi_o$  obtained from the fit includes contributions from core diamagnetism, the Landau diamagnetism and the enhanced Pauli paramagnetism

$$\chi_o = \chi_{core} + \chi_{Landau} + S\chi_{Pauli}. \quad (4.10)$$

The core diamagnetic contribution  $\chi_{core}$  is estimated to be  $-8.4 \times 10^{-5}$  emu/mol [61, 81] while  $\chi_{Pauli}$  and  $\chi_{Landau}$  are given as

$$\chi_{Pauli} = \mu_B^2 N(E_f) \quad (4.11)$$

and

$$\chi_{Landau} = \frac{-\mu_B^2 N(E_f)}{3(1 + \lambda)^2} \quad (4.12)$$

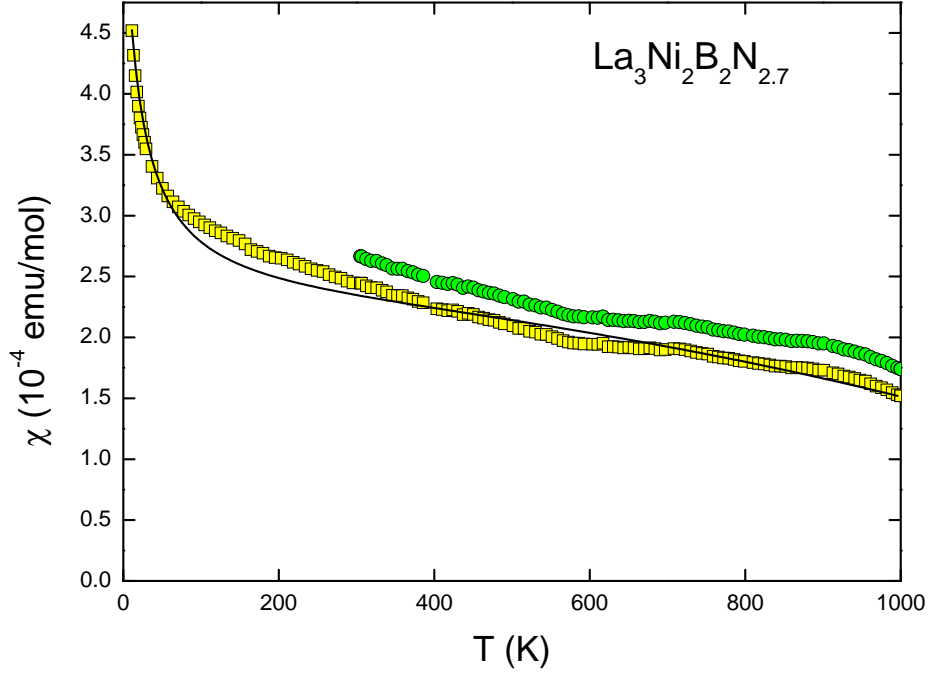


Figure 4.7: Normal state temperature dependent magnetic susceptibility of  $\text{La}_3\text{Ni}_2\text{B}_2\text{N}_{2.7}$  at an applied field of 1T (from 4-300 K) and 9T (from 300-1000 K). Circles represent high  $T$  susceptibility as measured on the VSM (see text). Solid line represents a fit according to equation 4.9.

where  $\mu_B$  is the Bohr magneton,  $N(E_f)$  is the density of states at the Fermi level and  $\lambda$  is the electron-phonon coupling constant.  $\text{La}_3\text{Ni}_2\text{B}_2\text{N}_{2.7}$  has an electron-phonon coupling constant  $\lambda \simeq 0.89$  and a Sommerfeld coefficient  $\gamma \simeq 26\text{mJ/molK}^2$  (see chapter 5). Using  $\gamma$  one can calculate the  $N(E_f)$  from the relation

$$\gamma = \frac{\pi^2}{3} k_B^2 (1 + \lambda) N(E_f) \quad (4.13)$$

yielding  $N(E_f) \simeq 6\text{states/eV-f.u.}$  Inserting the values in equation 4.11 and 4.12 results in  $\chi_{Pauli}$  and  $\chi_{Landau}$  of  $0.19 \times 10^{-3}\text{emu/mol}$  and  $1.75 \times 10^{-5}\text{emu/mol}$  respectively. The equation 4.10 allows to determine the Stoner enhancement factor as

$$S = \frac{\chi_o - \chi_{core}}{\mu_B^2 N(E_f)} + \frac{1}{3(1 + \lambda)^2} \quad (4.14)$$

yielding  $S \simeq 1.6$  which is slightly smaller than the value reported earlier [61].

For a non-interacting Fermi gas the density of states as probed by magnetic measurements enters as given in equation 4.11 while the density of states probed by the specific heat measurements enters in equation 4.13. One can

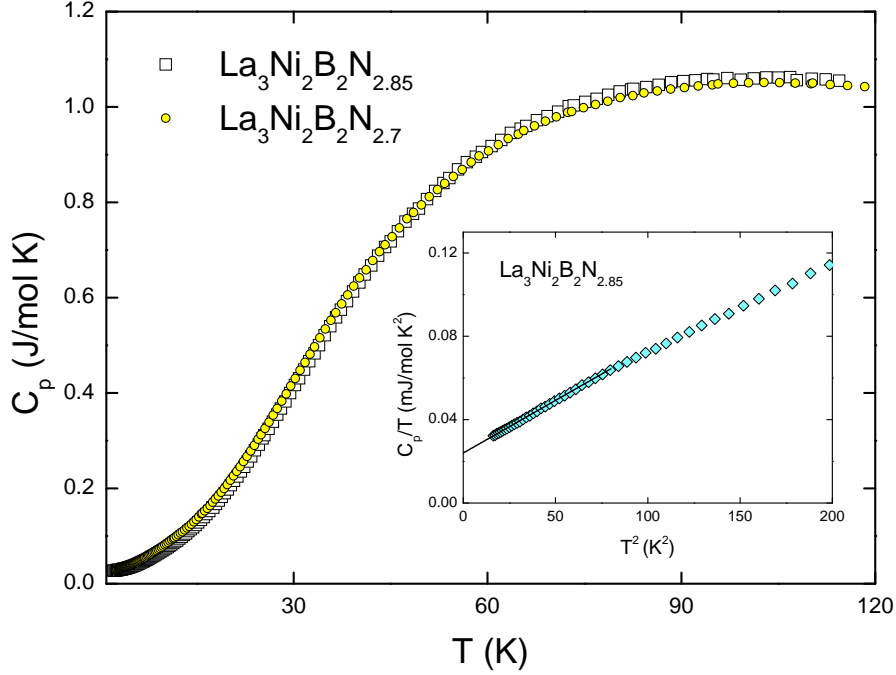


Figure 4.8: The normal state specific heat of  $\text{La}_3\text{Ni}_2\text{B}_2\text{N}_{2.7}$  and  $\text{La}_3\text{Ni}_2\text{B}_2\text{N}_{2.85}$  up to 120 K. inset:  $C/T$  vs.  $T^2$  graph of the low temperature part with a solid line indicating a  $C/T = \gamma + \beta T^2$  linear fit.

therefore define a dimensionless Wilson ratio [82]

$$R_W = \frac{\pi^2 k_B^2}{3\mu_B^2} \left( \frac{\chi_o}{\gamma} \right) \quad (4.15)$$

where  $\gamma_o$  is the Sommerfeld coefficient. Using the experimentally determined values of  $\chi_o$  and  $\gamma$ , equation 4.15 gives a Wilson ratio of 0.6 which is close to unity, as expected for a material with nearly filled  $d$ -bands.

## 4.4 Specific Heat

Specific heat measurements were performed from 2 to 180 K in order to study electronic and lattice contributions. The normal state specific heat of  $\text{La}_3\text{Ni}_2\text{B}_2\text{N}_x$  shown in figure 4.8 as obtained at high enough field (9T) to suppress superconductivity. The low temperature electronic and lattice contributions to the specific heat of the normal metal are given by  $C_p = C_e + C_{ph} \simeq \gamma T + \beta T^3$  where  $\gamma$  is Sommerfeld parameter and  $\beta$  is related to the low-temperature value of the Debye temperature,  $\Theta_D^{LT} = (1944 \times N/\beta)^{1/3}$  where  $N$  being the number of atoms per formula unit. The low temperature ( $16 \text{ K}^2 > T^2 > 40 \text{ K}^2$ ) fit of  $\text{La}_3\text{Ni}_2\text{B}_2\text{N}_{2.85}$  shown in the inset of figure 4.8,

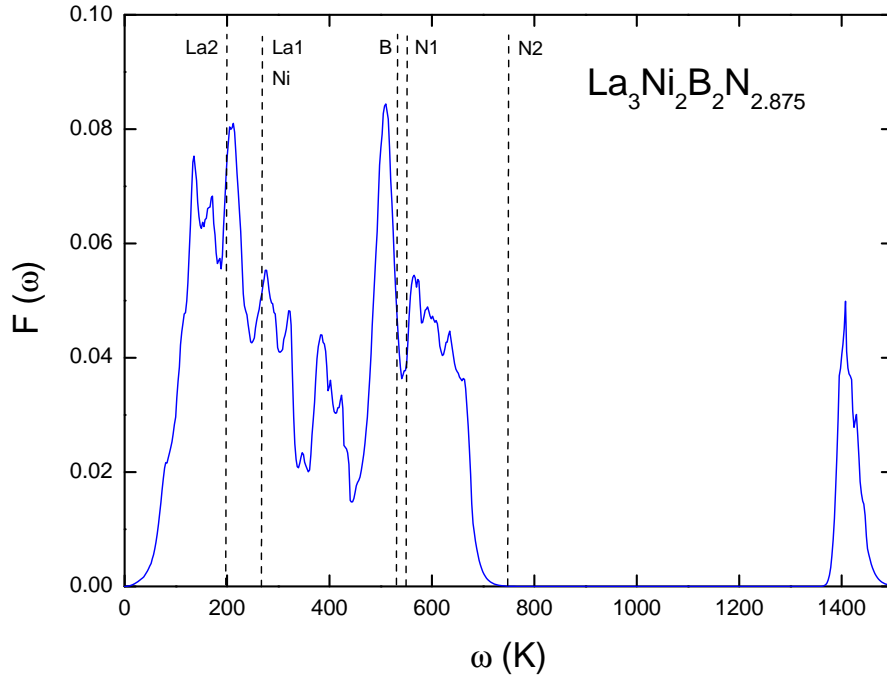


Figure 4.9: Calculated phonon spectrum of  $\text{La}_3\text{Ni}_2\text{B}_2\text{N}_{2.875}$  [83]. Dashed lines indicate frequencies of individual atoms obtained from neutron powder diffraction.

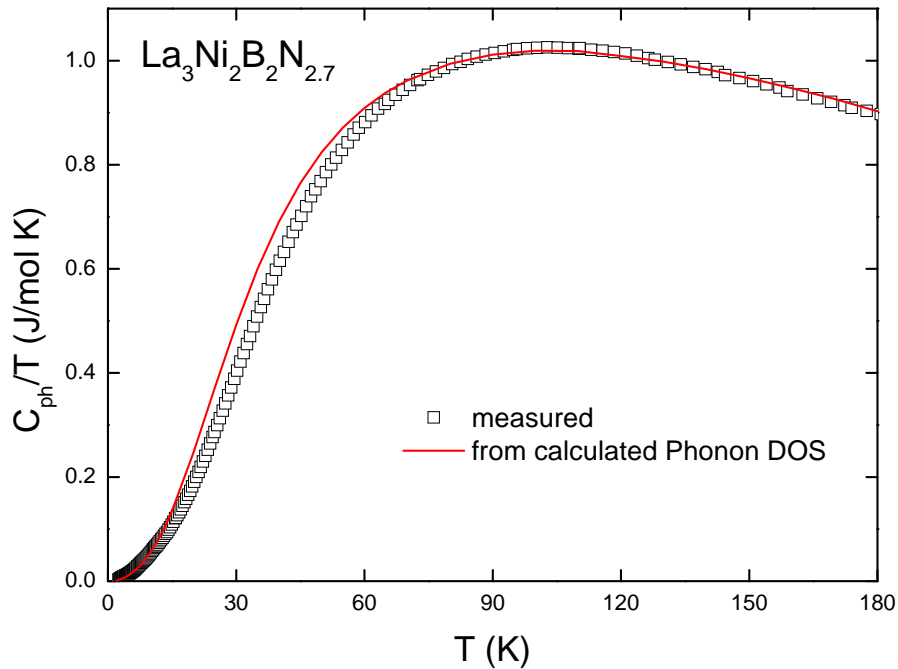


Figure 4.10: Phonon specific heat of  $\text{La}_3\text{Ni}_2\text{B}_2\text{N}_{2.7}$ . Solid line represents phonon specific heat calculated from the DFT phonon spectrum (figure 4.9) on the basis of equation 4.16

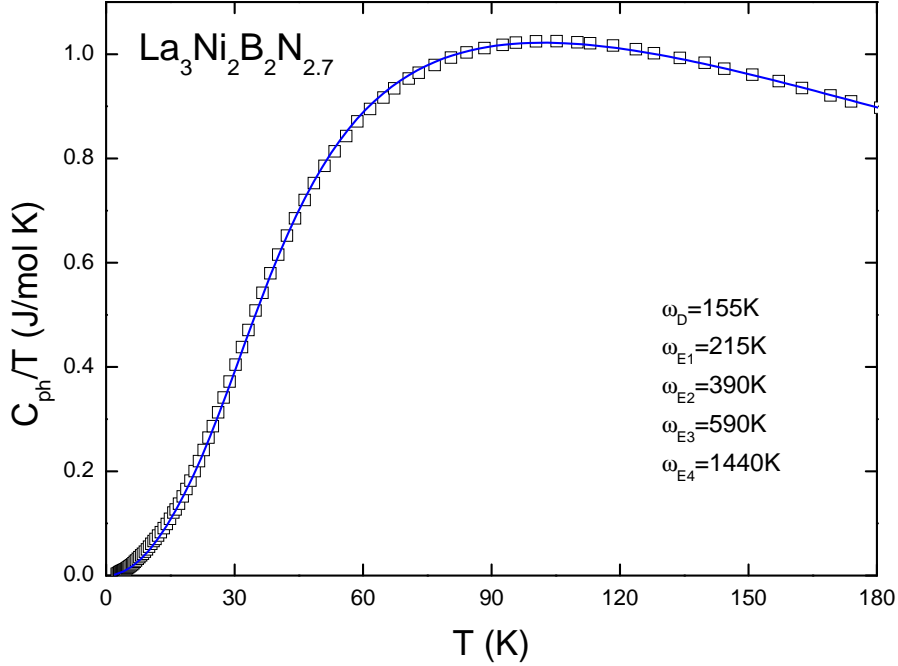


Figure 4.11: The normal state specific heat of  $\text{La}_3\text{Ni}_2\text{B}_2\text{N}_{2.7}$  up to 180 K. Solid line represents a fit according to equation 4.17 with fit parameters also listed.

yields  $\gamma \simeq 24.0 \text{ mJ/molK}^2$  and  $\beta \simeq 0.51 \text{ mJ/molK}^4$ , i.e.  $\Theta_D^{LT} \simeq 340 \text{ K}$ . In order to perform an in-depth analysis of vibrational properties of  $\text{La}_3\text{Ni}_2\text{B}_2\text{N}_{3-\delta}$ , the Density Functional Theory (DFT) calculations were performed by Reith and Podloucky VASP [62]. The experimentally determined lattice volume was used in *ab initio* calculations. The model phonon density of states (PDOS) spectrum obtained from DFT calculations is shown in figure 4.9 for a composition close to  $\text{La}_3\text{Ni}_2\text{B}_2\text{N}_{2.9}$ . To compare the contribution from local atomic modes, the frequencies of individual atoms obtained from isotropic atomic displacement parameters (see section 3.6.4) are indicated with dashed lines. From the spectrum it is evident that the low frequency vibrational spectrum up to  $\sim 250 \text{ K}$  is dominated by the heavy atoms La and Ni. Above 400 K the dominant contribution to the phonon DOS comes from vibrations of lighter elements B and N. The PDOS is related to the phonon specific heat in terms of a general relation

$$C_{ph}(T) = R \int_0^\infty F(\omega) \frac{\left(\frac{\omega}{2T}\right)^2}{\sinh^2\left(\frac{\omega}{2T}\right)} d\omega \quad (4.16)$$

where  $F(\omega)$  is a phonon spectrum, e.g. the one obtained from *ab initio* calculations. Based on equation 4.16,  $C_{ph}$  is calculated and is shown in figure 4.10 together with the measured data. The electronic contribution to the total

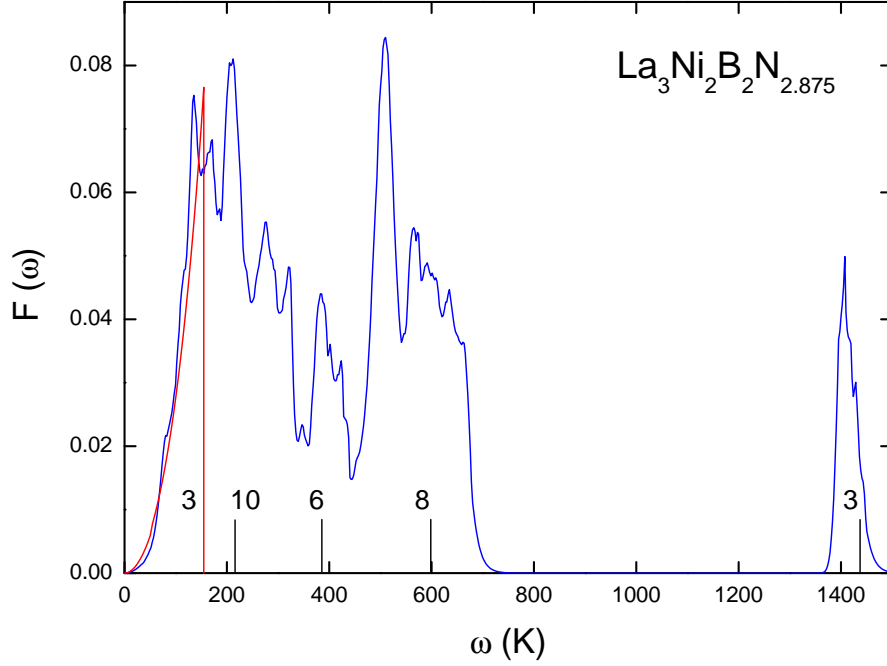


Figure 4.12: Model phonon spectrum of  $\text{La}_3\text{Ni}_2\text{B}_2\text{N}_{2.875}$ . Dashed line represents the Debye spectrum with the cutoff representing Debye frequency. The refined Einstein frequencies and indicated by short vertical lines with corresponding spectral weights.

specific heat was subtracted from the measured data to get the phonon specific heat ( $C_{ph}$ ). The calculated  $C_{ph}$  indicated by solid line in figure 4.10 is in reasonable agreement with measured one at low and high temperature while a small mismatch is observed at intermediate temperatures. This small error can be expected from *ab initio* calculations and may be due to the over estimate of nitrogen vacancies. To analyze the measured specific heat in context of PDOS, a model with combination of one Debye function and 4 Einstein functions is adopted to describe the phonon specific heat as

$$C_{ph}(T) = \frac{9R}{\omega_D^3} \int_0^{\omega_D} \frac{\omega^2 \left(\frac{\omega}{2T}\right)^2}{\sinh^2\left(\frac{\omega}{2T}\right)} d\omega + \sum_{i=1}^4 c_i R \frac{\left(\frac{\omega_i}{2T}\right)^2}{\sinh^2\left(\frac{\omega_i}{2T}\right)} \quad (4.17)$$

Thereby 3 acoustical and 27 optical branches of the phonon dispersion of  $\text{La}_3\text{Ni}_2\text{B}_2\text{N}_3$  represent a minimum set of parameters to describe the overall temperature dependence of the specific heat. The spectral weights and positions of Debye and Einstein contributions were estimated by hand from the PDOS. A fit of the measured  $C_{ph}$  according to equation 4.17 is shown as a solid line in figure 4.11. Reasonable agreement between measured and calculated  $C_{ph}$  is achieved and the obtained Debye and Einstein temperatures

---

are listed in figure 4.11. The spectral weights of the Debye and Einstein contributions are indicated in figure 4.12. The analysis reveals good agreement between measured and calculated specific heat and is a good starting point for analyzing the superconducting state properties. The PDOS spectrum is used in Eliashberg model calculations of the superconducting properties of  $\text{La}_3\text{Ni}_2\text{B}_2\text{N}_{2.7}$  (see chapter 5).

# Chapter 5

## Superconducting properties of $\text{La}_3\text{Ni}_2\text{B}_2\text{N}_{3-\delta}$

### 5.1 Introduction

$\text{La}_3\text{Ni}_2\text{B}_2\text{N}_{3-\delta}$  was reported to be superconducting with a transition temperature of  $\sim 11.7 - 13$  K [40, 41]. Detailed studies of superconducting properties of  $\text{La}_3\text{Ni}_2\text{B}_2\text{N}_{3-\delta}$  by means of resistivity, specific heat and magnetic measurements have been reported earlier [41, 36] suggesting it to be a phonon mediated medium- to strong-coupling BCS superconductor. In previous reports the specific role of the nitrogen stoichiometry has not been explored which is expected to have relevant influence on the superconducting properties.

The following chapter presents studies of superconducting state properties of  $\text{La}_3\text{Ni}_2\text{B}_2\text{N}_{3-\delta}$  by means of resistivity, specific heat and magnetic measurements. The composition dependence of physical properties is investigated for nominal compositions of  $\text{La}_3\text{Ni}_2\text{B}_2\text{N}_{3-\delta}$  with  $\delta$  varying from 0.1 to 0.4. The thermodynamic and microscopic parameters of the superconducting state are and briefly compared with model calculations based on the Eliashberg theory for anisotropic  $s$ -wave superconductor and are analyzed in context with new *ab initio* calculation performed using Vienna simulation package [62].

### 5.2 Results of resistivity measurements

#### 5.2.1 Resistivity in zero field

The temperature dependent electrical resistivity of  $\text{La}_3\text{Ni}_2\text{B}_2\text{N}_{3-\delta}$  was measured using standard four probe technique in a  $^4\text{He}$  cryostat. The resistivity  $\rho(T)$  for several compositions of  $\text{La}_3\text{Ni}_2\text{B}_2\text{N}_x$  (measured in zero magnetic field) is depicted in figure 5.1 to highlight the superconducting transition temperature. All samples exhibit a relatively sharp superconducting transition with a



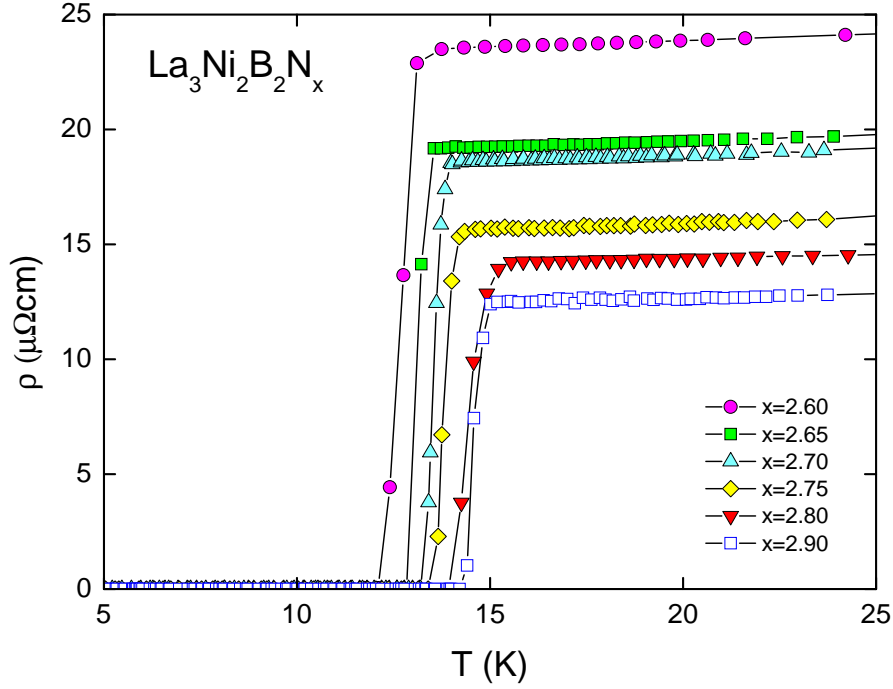


Figure 5.1: Temperature dependent electrical resistivity of  $\text{La}_3\text{Ni}_2\text{B}_2\text{N}_x$  with  $x$  as labeled.

systematic increase in the resistive transition temperature  $T_c^{\rho}$  from  $\sim 12.5$  K to  $\sim 14.5$  K as the nitrogen stoichiometry ( $x$  in fig. 5.1) increases from 2.6 to 2.9. The resistive transition temperature  $T_c^{\rho}$  is determined by the mean of the temperatures corresponding to 10% and 90% of the resistive jump which matches well with  $T_c$  onset obtained from specific heat measurements. The width of the transition is evaluated from  $\Delta T_c = T(0.9\rho_0) - T(0.1\rho_0)$  yielding about 0.5 K for most of the samples. The normal state resistivity above 80 K for all samples behaves like a simple metal and can be roughly described in terms of the Bloch-Grüneisen (BG) relation (equation 4.2) whereas below 80 K a low temperature dependence close to  $T^2$  is observed. A detailed description of normal state resistivity is given in section 4.2.1.

Besides having an effect on the superconducting transition, the nitrogen off-stoichiometry also affects the temperature independent residual resistivity. The electrical resistivity for several  $\text{La}_3\text{Ni}_2\text{B}_2\text{N}_x$  samples is shown in figure 5.2(a) revealing an increase of the residual resistivity  $\rho_0$  from about  $12 \mu\Omega\text{cm}$  for samples near  $\text{La}_3\text{Ni}_2\text{B}_2\text{N}_{2.90(5)}$  to about  $24 \mu\Omega\text{cm}$  for  $\text{La}_3\text{Ni}_2\text{B}_2\text{N}_{2.60(5)}$ . As demonstrated in detail in chapter 4, this variation of  $\rho_0$  is related to the increasing density of nitrogen vacancies which act as scattering potentials for conduction electrons and thus contribute to the temperature independent residual resistivity. Scattering originating from vacancies,

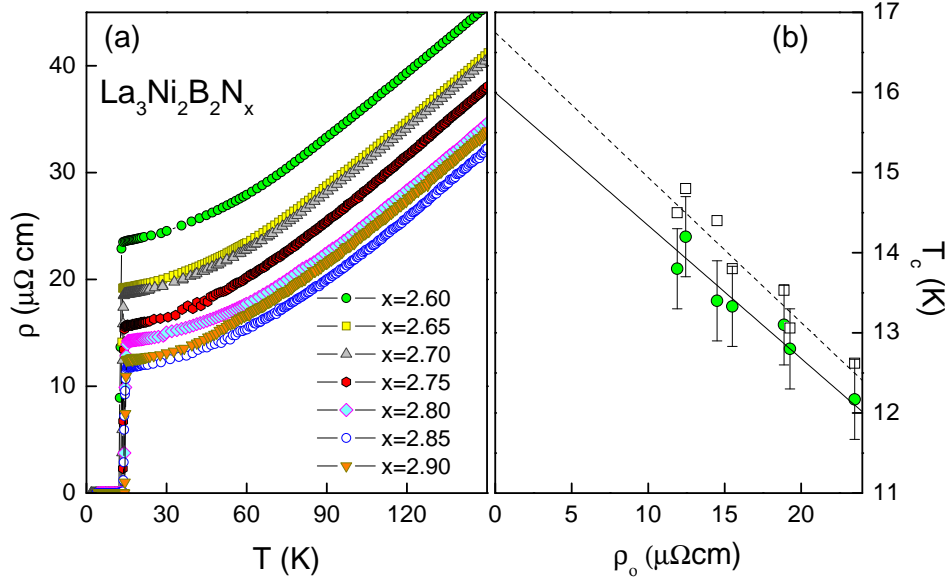


Figure 5.2: Temperature dependent electrical resistivity for various  $\text{La}_3\text{Ni}_2\text{B}_2\text{N}_{3-x}$  samples (a);  $T_c^{C_p}$  (circles) and  $T_c^p$  (squares) vs  $\rho_0$  for  $\text{La}_3\text{Ni}_2\text{B}_2\text{N}_{3-x}$  with error bars indicating width of the specific heat transition (b).

impurity atoms or other lattice defects may further act as non-magnetic pair-breaking for Cooper electrons, thereby reducing  $T_c$  to below the clean limit value of the ideally pure and crystalline material (see section 2.4). Accordingly, figure 5.2(b) shows the correlation between  $\bar{T}_c$  (obtained from specific heat) and the corresponding values of the normal state residual resistivity  $\rho_0$  of the samples in figure 3a. A linear regression of the available data points  $\bar{T}_c(\rho_0)$  extrapolates to a clean limit  $T_c^{cl} \sim 16$  K for terminal, vacancy- and impurity free  $\text{La}_3\text{Ni}_2\text{B}_2\text{N}_3$  approximately matching the  $T_c$  value of  $\text{LuNi}_2\text{B}_2\text{C}$ . It is very suggestive that impurities which increase the residual resistivity would at the same time be the reason for the decrease in  $T_c$  via a potential scattering effect (see chapter 2).

### 5.2.2 Magnetoresistance measurement

In order to determine the upper critical field,  $H_{c2}(T)$ , the temperature dependent magnetoresistance of various compositions of  $\text{La}_3\text{Ni}_2\text{B}_2\text{N}_x$  was measured in magnetic fields up to 9.5 T in a  $^3\text{He}$  cryostat. The electrical resistivity curves for  $\text{La}_3\text{Ni}_2\text{B}_2\text{N}_{2.6}$  and  $\text{La}_3\text{Ni}_2\text{B}_2\text{N}_{2.9}$  under various applied external magnetic fields are shown in figure 5.3 (a) and (b) respectively. At zero applied external magnetic field  $T_c^p$  of  $\text{La}_3\text{Ni}_2\text{B}_2\text{N}_{2.9}$  is 14.3 K with a width

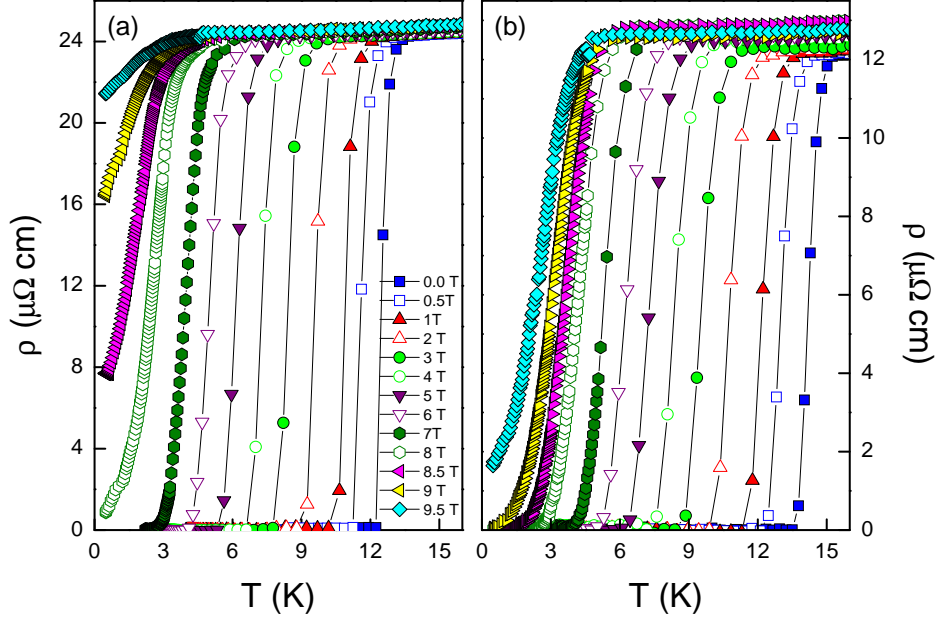


Figure 5.3: Temperature dependent electrical resistivity of  $\text{La}_3\text{Ni}_2\text{B}_2\text{N}_{2.6}$  (a) and  $\text{La}_3\text{Ni}_2\text{B}_2\text{N}_{2.9}$  (b) under various external magnetic fields as labeled.

$\Delta T_c \simeq 0.7\text{K}$ . For the resistive superconducting transition we define temperature  $T_c^{on}$  for the onset of superconducting transition and  $T_c^o$  where the resistivity becomes zero. With an increase in magnetic field the transition width  $\Delta T_c$  increases and may point towards an anisotropy of the upper critical field  $H_{c2}(T)$  in this layered superconducting material. Quantitatively, the temperatures  $T_c^{on}$  and  $T_c^o$  of  $\text{La}_3\text{Ni}_2\text{B}_2\text{N}_{2.9}$  are shifted by 9 K and 13 K respectively when the external field is increased from 0 to 9 T. At 9 T the  $T_c^o$  is reduced to  $\sim 3\text{K}$  while  $\Delta T_c$  increases to  $\sim 2.5\text{K}$ . Similarly for  $\text{La}_3\text{Ni}_2\text{B}_2\text{N}_{2.6}$  the  $T_c^o$  at zero applied external magnetic field is  $\sim 12.5\text{K}$  with  $\Delta T_c \simeq 0.5\text{K}$  while at 7 T the value of  $T_c^o$  decreases to  $\sim 4\text{K}$  with  $\Delta T_c$  increasing to  $\sim 1.5\text{K}$ . Above 7 T the superconductivity of  $\text{La}_3\text{Ni}_2\text{B}_2\text{N}_{2.6}$  is suppressed significantly and tails in superconducting transition start to appear. The temperature dependence of upper critical field for selected  $\text{La}_3\text{Ni}_2\text{B}_2\text{N}_{3-\delta}$  compositions determined by resistivity measurements under applied magnetic is shown in figure 5.4. An important feature of the  $H_{c2}(T)$  curve is its positive curvature near  $T_c$  which is evident for all the samples. The conventional single band theory as worked out by Werthamer *et al.* [32] suggests that the slope of  $H_{c2}(T)$  does not change significantly below  $T_c$  over a wide range of temperature. The experimentally observed significant curvature near  $T_c$ , thus, refers to multiband features. A similar positive curvature of the upper critical field  $H_{c2}(T)$  of Y- and  $\text{LuNi}_2\text{B}_2\text{C}$  was successfully described with high accuracy

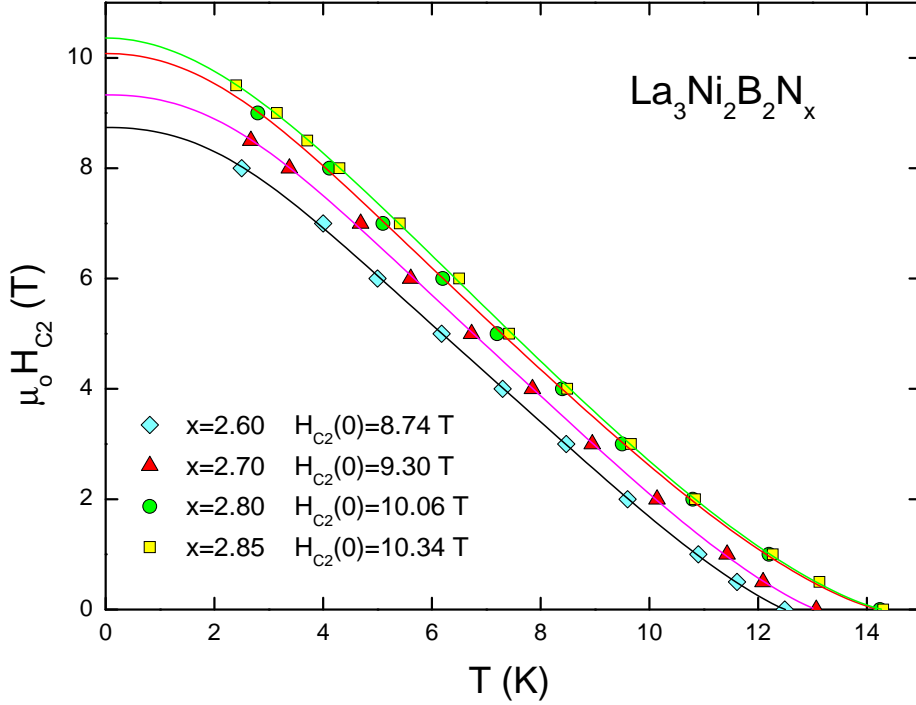


Figure 5.4:  $H_{c2}$  of selected  $\text{La}_3\text{Ni}_2\text{B}_2\text{N}_x$  samples obtained by magnetoresistivity measurements. Solid lines indicate a fit of the data according to equation 5.1.

by a simple phenomenological relation [84, 85]

$$H_{c2} = \frac{H_{c2}(0)z}{1 - (1 + \alpha)tz + L(tz)^2 + M(tz)^3} \quad (5.1)$$

where  $t = T/T_c$  and  $z = (1 - T/T_c)^{1+\alpha}$ . The positive curvature of  $H_{c2}$  near  $T_c$  is characterized by the value of the critical exponent  $\alpha$  and is very sensitive to disorder or the quality of samples while the negative curvature at low temperature is described by the ratio  $L/M$ . The lines in figure 5.4 represent a fit of the data according to equation 5.1. It has to be noted that equation 5.1 has too many parameters and may yield multiple solutions, a reference set of fit parameters for  $\text{La}_3\text{Ni}_2\text{B}_2\text{N}_{2.85}$  is  $\alpha = 0.25$ ,  $L = 1.75$  and  $M = 0.93$ . The parameter  $\alpha$  shows an increase from 0.11 for  $N \sim 2.6$  to 0.25 for  $N \sim 2.85$ . The  $H_{c2}(0)$  for  $\text{La}_3\text{Ni}_2\text{B}_2\text{N}_{2.6}$  is about 8.7 T which increases to about 10.3 T for  $\text{La}_3\text{Ni}_2\text{B}_2\text{N}_{2.9}$ . An analysis of upper critical field in terms of Eliashberg theory is presented in section 5.4.6.

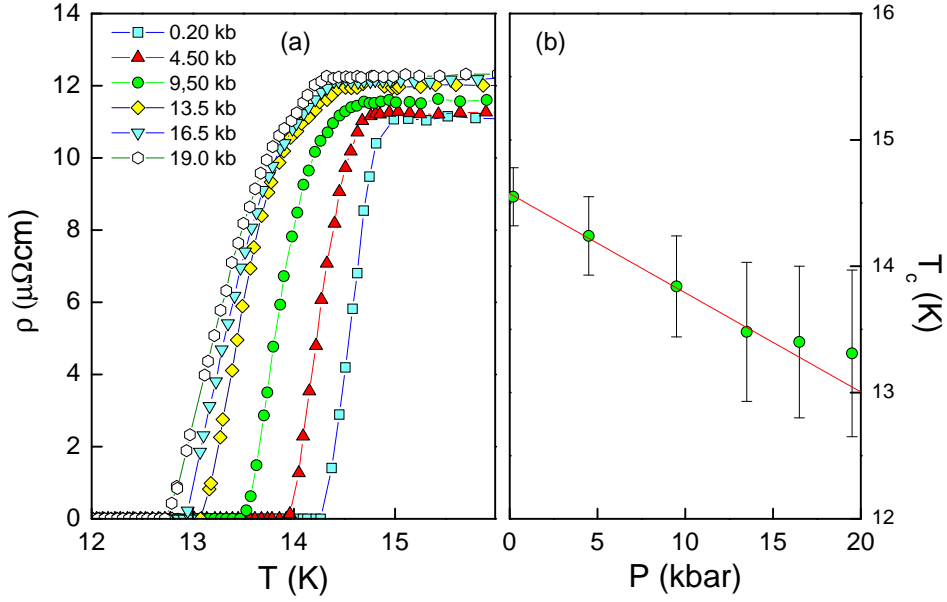


Figure 5.5: Temperature dependent electrical resistivity of  $\text{La}_3\text{Ni}_2\text{B}_2\text{N}_{2.9}$  under hydrostatic pressure as labeled (a) and corresponding values of  $T_c$  Vs  $p$  (b); the line in (b) indicate a linear regression for  $p < 14$  kbar.

### 5.2.3 Resistivity under hydrostatic pressure

The effect of hydrostatic pressure up to 19.5 kbar for selected  $\text{La}_3\text{Ni}_2\text{B}_2\text{N}_{3-x}$  samples is studied by means of resistivity measurements employing a standard piston-cylinder technique with Daphne oil as pressure transmitting medium. Earlier hydrostatic pressure measurements up to 12 kbar on  $\text{La}_3\text{Ni}_2\text{B}_2\text{N}_{3-\delta}$  with  $\bar{T}_c = 11.7$  K [41] revealed a relatively large negative  $dT_c/dp \simeq -130$  mK/kbar and a significant increase of the residual resistivity by about 10% at 12 kbar. Having a composition  $\text{La}_3\text{Ni}_2\text{B}_2\text{N}_{2.92}$  with defined nitrogen stoichiometry and significantly higher  $\bar{T}_c = 14.2$  K than the earlier studied  $\text{La}_3\text{Ni}_2\text{B}_2\text{N}_{3-\delta}$  with  $\bar{T}_c = 11.7$  K, the effect of pressure on the superconducting properties is re-investigated. The temperature dependent electrical resistivity data obtained at hydrostatic pressures up to 19.0 kbar is shown in figure 5.5(a). The pressure dependent superconducting transition temperature  $T_c$  reveals a reduction of  $T_c$  from 14.6 K to 13.3 K as pressure is increased from 0.2 kbar to 19.0 kbar. The transition to superconducting state is reasonably sharp at 0.2 kbar with a width  $\Delta T_c \simeq 0.4$  K that increases to  $\sim 1.4$  K at 19 kbar. The  $T_c(P)$  data of  $\text{La}_3\text{Ni}_2\text{B}_2\text{N}_{2.9}$  shown in figure 5.5(b) reveals an initial linear reduction before tending to saturate for  $p > 14$  kbar. The linear regression of the data for  $P < 14$  kbar (dashed line in figure 5.5(b)) yields  $dT_c/dp \simeq -80$  mK/kbar as compared to  $dT_c/dp \simeq -130$  mK/kbar re-

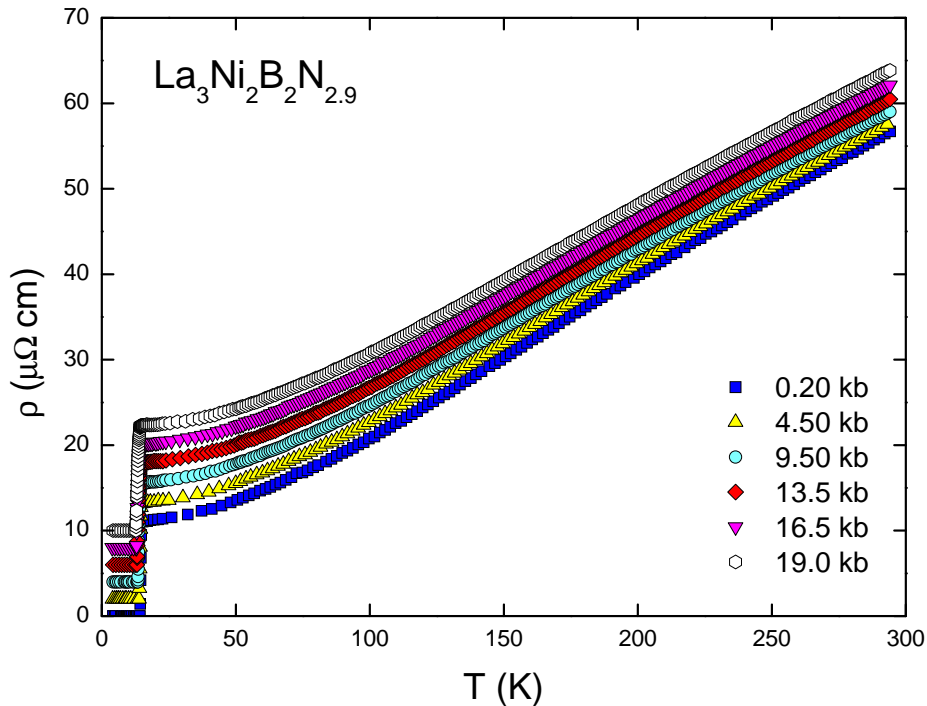


Figure 5.6: Temperature dependent electrical resistivity of  $\text{La}_3\text{Ni}_2\text{B}_2\text{N}_{2.9}$  under hydrostatic pressure up to room temperature. For clarity, curves are shifted by offsets of  $2\mu\Omega\text{cm}$  with increasing pressure.

ported earlier [41] for a sample with lower  $T_c \simeq 11.7\text{K}$ . On the other hand very small values of  $dT_c/dp$  for related borocarbides  $\text{YNi}_2\text{B}_2\text{C}$  ( $\simeq -6\text{mK/kbar}$ ) and  $\text{LuNi}_2\text{B}_2\text{C}$  ( $\simeq +18\text{mK/kbar}$ ) has been observed [86]. The effect of hydrostatic pressure upon  $T_c$  of  $\text{La}_3\text{Ni}_2\text{B}_2\text{N}_x$  provides further information about the elastic and electronic properties of the boronitrides. In general, a pressure dependence of  $T_c$  is mainly a consequence of two effects: Firstly, a volume compression gives rise to a lattice stiffening and results in an increase of the mean phonon frequency and secondly, causes a broadening of the bandwidth concomitant with a change in the density of states  $N(E_f)$  either in positive or negative direction. The  $T_c$  depression under hydrostatic pressure can be analyzed in terms of the Mc Millan model [19]. Both quantities,  $N(E_f)$  and the mean phonon frequency  $\bar{\omega}_2$ , enter the Mc Millan formula via the electron-phonon coupling constant

$$\lambda = N(E_f)\langle I^2 \rangle / (M\bar{\omega}_2^2) \quad (5.2)$$

with  $M$  the mean atomic mass and  $\langle I^2 \rangle$  the average electron-phonon matrix elements. In earlier analysis [41] the pressure dependence of  $T_c$  via the Mc Millan formula simply on the basis of the experimentally observed pressure

$P$ (kbar)	$\Theta_D$ (K)	$T_c^\rho$ (K)	$\lambda(\Theta_D)$	$T_c^*$ (K)
0.2	352	14.55	0.91	14.6
4.5	356	14.24	0.89	14.1
9.5	361	13.84	0.86	13.5
13.5	365	13.48	0.85	13.1

Table 5.1: Pressure induced increase in Debye temperature for  $\text{La}_3\text{Ni}_2\text{B}_2\text{N}_{2.9}$  estimated from a Bloch-Grüneisen fit.  $T_c^*$  represents transition temperature calculated from  $\lambda(\Theta_D)$  using the Mc Millan formula.

dependence of the characteristic phonon frequency (i.e. Debye temperature) yielded  $dT_c/dp \simeq -150$  mK/kbar in close agreement with the experimental result [41], thus, suggesting that pressure affects  $T_c$  in this material primarily via the effect of lattice stiffening. To re-investigate the previous claim, the present data is analyzed again on the basis of Mc Millan formula which describes  $T_c$  as

$$T_c = \frac{\Theta_D}{1.45} \exp \left[ -\frac{1.04(1 + \lambda)}{\lambda - \mu^*(1 + 0.62\lambda)} \right] \quad (5.3)$$

where  $\Theta_D$  is the Debye temperature,  $\mu^*$  is Coulomb pseudopotential and  $\lambda$  is the electron phonon coupling constant as given before. Ignoring any pressure dependence of  $\mu^*$  and  $\langle I^2 \rangle$ , the pressure induced stiffening of lattice generally leads to a decrease of  $T_c$ . The pressure induced electronic changes may either increase or decrease  $T_c$  depending on whether  $N(E_f)\langle I^2 \rangle$  is enhanced or diminished. Figure 5.6 shows the temperature dependent electrical resistivity of  $\text{La}_3\text{Ni}_2\text{B}_2\text{N}_{2.9}$  under hydrostatic pressure up to room temperature. The analysis of normal state data in terms of the Bloch-Grüneisen relation reveals a pressure induced increase of the Debye temperature  $\Theta_D$  by about 4% at 13.5 kbar. The pressure induced increase in Debye temperature along with the corresponding decrease in electron-phonon coupling constant ( $\lambda_{\Theta_D}$ ) is summarized in table 5.1. The increase of  $\Theta_D$  is also directly evident from the decreasing slope of  $\rho(T)$  on increasing pressure in figure 5.6 and is used as a first estimate for the stiffening of the mean phonon frequency  $\bar{\omega}_2$  (assuming  $\bar{\omega}_2 \propto \Theta_D$ ) under hydrostatic pressure. In the framework of Mc Millan formula, these purely phononic changes yield a decrease in  $\lambda$  (see table 5.2.3 and a corresponding decrease in  $T_c^*$  with  $dT_c^*/dp \simeq -110$  mK/kbar which is in reasonable agreement with the experimentally determined  $dT_c/dp \simeq -80$  mK/kbar. This rather close agreement between experimental and calculated rate of  $T_c$  depression indicates that the electronic effects plays a minor role, i.e. pressure induced changes of  $N(E_f)$  are rather small. The pressure results of a higher- $T_c$  sample are in line with earlier conclusions of Ref. [41] though the pressure induced changes in  $T_c$ , i.e.  $dT_c/dp$  mentioned in the above analysis are roughly 30% smaller than those reported earlier in Ref. [41] and may

be a consequence of a smaller number of nitrogen vacancies and, thus, lower compressibility of the material.

### 5.3 Magnetic measurements

The magnetization measurements were performed on a dc-SQUID magnetometer. The temperature dependence of the zero-field and field-cooled magnetization data of  $\text{La}_3\text{Ni}_2\text{B}_2\text{N}_{2.6}$  and  $\text{La}_3\text{Ni}_2\text{B}_2\text{N}_{2.9}$  in applied magnetic fields up to 1.0 T is shown in figure 5.7. Relatively sharp superconducting transitions are observed for both the samples with  $T_c$  values of  $\sim 12.5$  K and  $\sim 14.1$  K for  $\text{La}_3\text{Ni}_2\text{B}_2\text{N}_{2.6}$  and  $\text{La}_3\text{Ni}_2\text{B}_2\text{N}_{2.9}$  respectively which are close to the values obtained from resistivity measurements. The transition width defined as the temperature difference between 10% and 90% of the transition is  $\Delta T_c \simeq 0.5$  K for both the samples. The irreversibility upon field cooling and zero field cooling is due to hard type II superconductivity with strong pinning effects. With increasing strength of applied magnetic field  $T_c$  decreases gradually but it becomes difficult to determine the superconducting transition temperature by means of susceptibility measurement in fields above 0.5 T. The normal state DC magnetic susceptibility of  $\text{La}_3\text{Ni}_2\text{B}_2\text{N}_{3-\delta}$  is discussed in section 4.3. The lower critical field of a type-II superconductor is the limiting field at which flux quanta first enter the superconductor and cause a

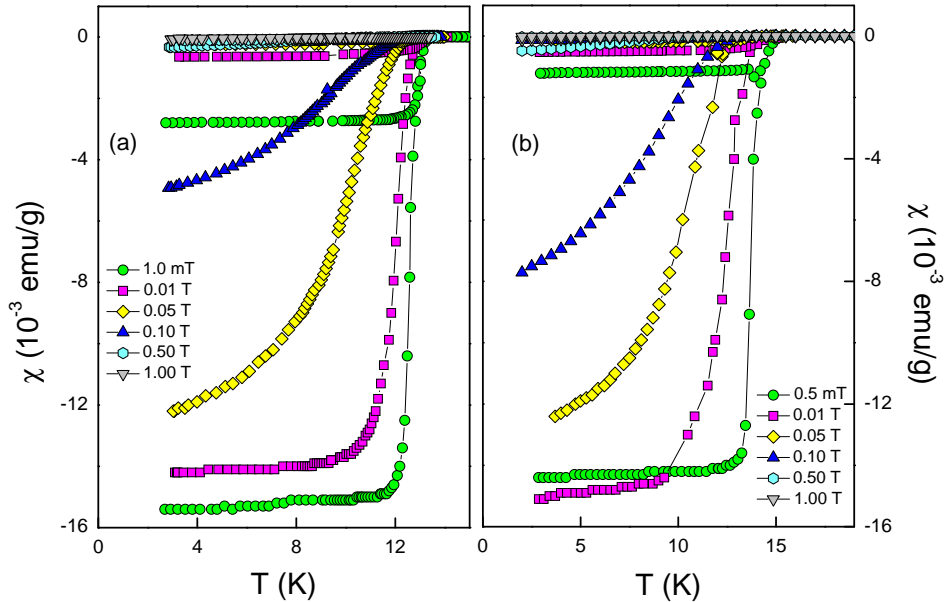


Figure 5.7: Temperature dependent magnetic susceptibility of  $\text{La}_3\text{Ni}_2\text{B}_2\text{N}_{2.6}$  (a) and  $\text{La}_3\text{Ni}_2\text{B}_2\text{N}_{2.9}$  (b) under applied magnetic fields as labeled.



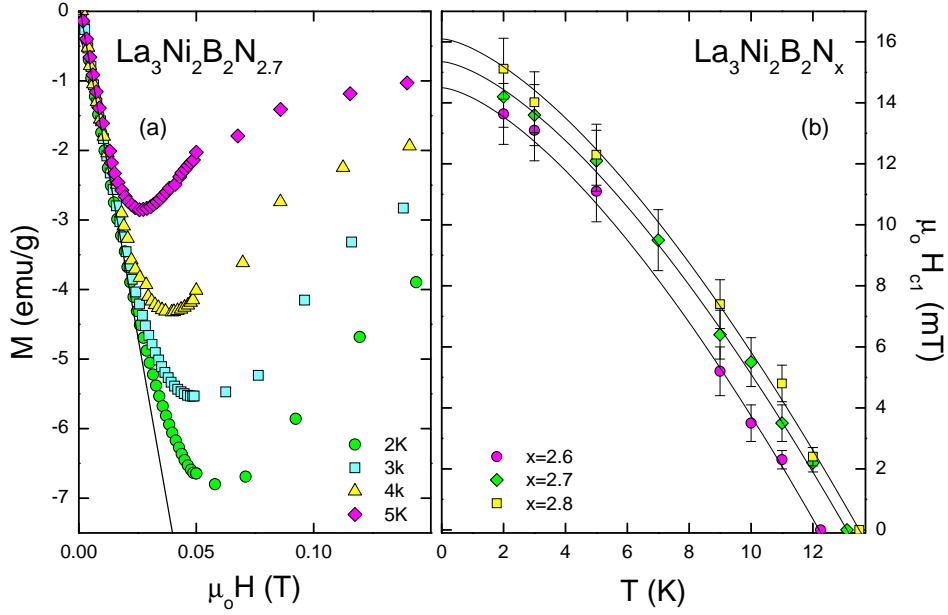


Figure 5.8: Magnetization as a function of applied magnetic field for  $\text{La}_3\text{Ni}_2\text{B}_2\text{N}_{2.7}$  at selected temperatures (a). Lower critical field of selected  $\text{La}_3\text{Ni}_2\text{B}_2\text{N}_x$  samples (b); solid lines indicate a fit of the data according to equation 5.4

deviation from perfect diamagnetism. Various techniques are used for the determination of the lower critical field such as magnetization, radio frequency, mechanical oscillation, electron spin resonance and optical visualization of magnetic flux methods [87]. In the present work  $H_{c1}(T)$  of various compositions  $\text{La}_3\text{Ni}_2\text{B}_2\text{N}_x$  is determined by isothermal magnetization measurements. The initial part of isothermal magnetization curves of  $\text{La}_3\text{Ni}_2\text{B}_2\text{N}_{2.7}$  is shown in figure 5.8(a) for selected temperatures with a solid line indicating perfect diamagnetism in the Meissner state. The lower critical field at any particular temperature is determined as the field where  $M(H)$  deviates from the linear behavior. The temperature dependence of lower critical field for selected samples is shown in figure 5.8(b) with solid lines in indicating an extrapolation of the data according to relation

$$H_c(T) = H_c(0) [1 - (T/T_c)^{3/2}] \quad (5.4)$$

which yields a lower critical field  $\mu_0 H_{c1}(0) = 14.5(2)$  mT for the nominal composition  $\text{La}_3\text{Ni}_2\text{B}_2\text{N}_{2.6}$ . As expected, the lower critical field increases with increasing  $T_c$  and reaches a value of  $16.1(2)$  mT for  $\text{La}_3\text{Ni}_2\text{B}_2\text{N}_{2.8}$  with a  $T_c \simeq 13.5$  K. The increase in the lower critical field  $H_{c1}(0)$  goes hand in hand with the increase in  $T_c$  of  $\text{La}_3\text{Ni}_2\text{B}_2\text{N}_x$ .

## 5.4 Specific heat measurements

The superconducting properties of bulk  $\text{La}_3\text{Ni}_2\text{B}_2\text{N}_{3-\delta}$  were studied by low temperature specific heat measurements in applied fields up to 9.0 T. The temperature dependent specific heat of  $\text{La}_3\text{Ni}_2\text{B}_2\text{N}_{2.7}$  for various external magnetic fields is shown in figure 5.9(a) as  $C_p/T$  vs.  $T^2$ . At zero field,  $\text{La}_3\text{Ni}_2\text{B}_2\text{N}_{2.7}$  shows a reasonably sharp superconducting transition around 13 K. With the application of an external magnetic field  $T_c$  is reduced and a field of 9 T is sufficient to suppress superconductivity and to observe the normal state specific heat. A detailed analysis of the low and high temperature normal state specific heat is given in section 4.4.

The specific heat jump  $(\Delta C)_{T_c} = C_s - C_n$  (where  $C_s$  and  $C_n$  are the specific heat in the superconducting and normal state, respectively) is one of the important quantities to characterize the superconducting state. The difference between superconducting and normal state specific heat,  $\Delta C$ , for  $\text{La}_3\text{Ni}_2\text{B}_2\text{N}_{2.7}$  is shown in figure 5.9(b). By idealizing the specific heat anomaly under the constraint of entropy balance between the superconducting and the normal state we get the thermodynamic mean value of the superconducting transition temperature  $\bar{T}_c = 13.0$  K and the height of the specific heat jump at  $T_c$  is  $(\Delta C)_{T_c} \simeq 0.42$  J/mol K. The effect of the nitrogen

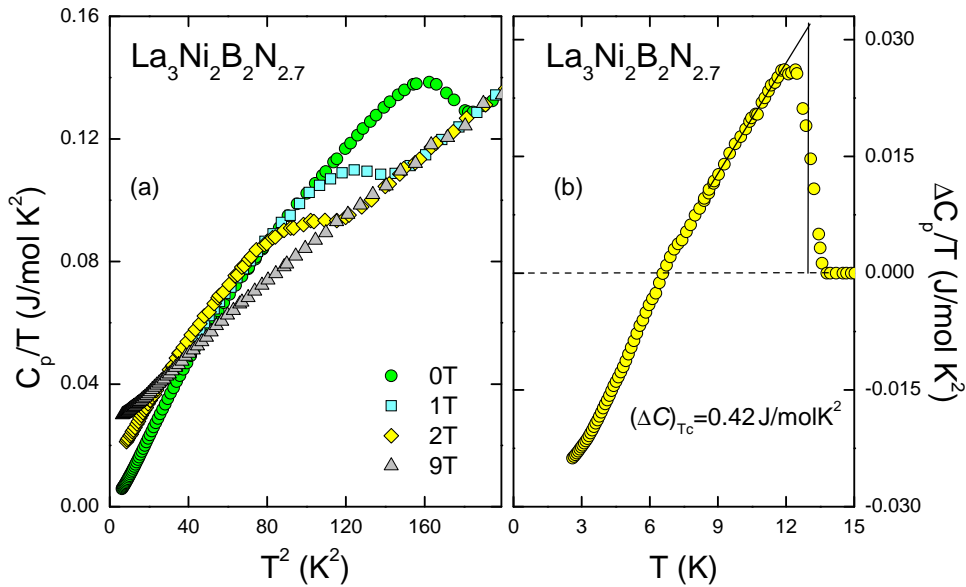


Figure 5.9: Temperature dependent  $C/T$  at various external magnetic fields as labeled (a) and difference of specific heat between superconducting and normal state  $\Delta C$  at 0 T of  $\text{La}_3\text{Ni}_2\text{B}_2\text{N}_{2.7}$  (b).

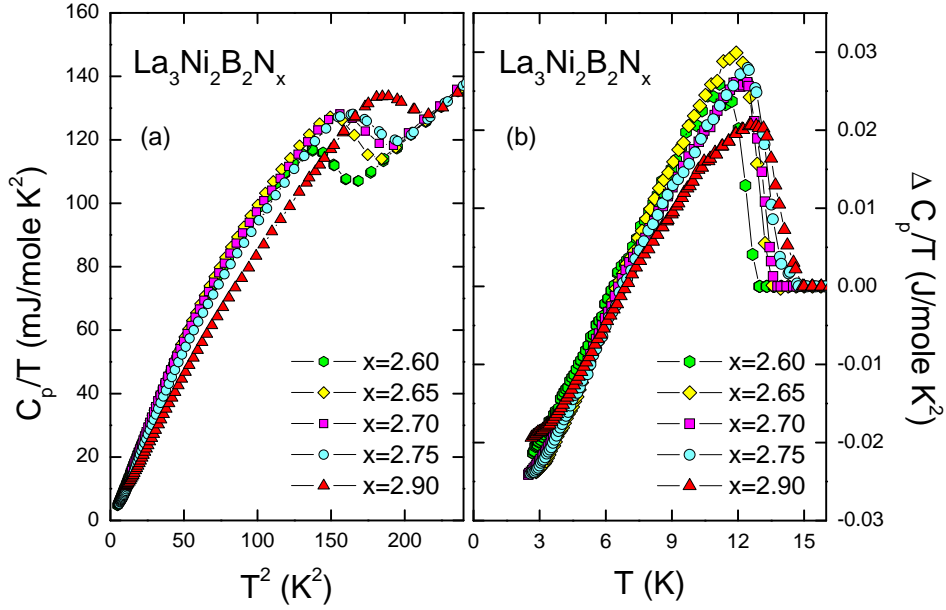


Figure 5.10: Temperature dependent  $C/T$  (a) and  $\Delta C$  (b) for selected compositions of  $\text{La}_3\text{Ni}_2\text{B}_2\text{N}_x$ .

stoichiometry on the superconducting properties of  $\text{La}_3\text{Ni}_2\text{B}_2\text{N}_x$  is shown in figure 5.10(a) revealing that the superconducting transition shifts to higher temperature with filling the nitrogen vacancies. The same can be seen in figure 5.10(b) where the difference  $\Delta C(T)$  for selected composition is plotted. The transition temperature  $\bar{T}_c$  increases from 12.2 K for  $\text{La}_3\text{Ni}_2\text{B}_2\text{N}_{2.6}$  to 14.0 K for  $\text{La}_3\text{Ni}_2\text{B}_2\text{N}_{2.9}$ . With increasing nitrogen stoichiometry of the compound, the width of superconducting transition tends to broaden while the height of the jump at  $T_c$  decreases. Samples with nominal nitrogen stoichiometry  $\sim 2.65 - 2.7$  have the sharpest specific heat anomaly and highest jump at  $T_c$ .

The low temperature electronic and lattice contributions to specific heat are analyzed in terms of  $C_p = C_e + C_{ph} \simeq \gamma T + \beta T^3$ . From low temperature ( $16 \text{ K}^2 > T^2 > 40 \text{ K}^2$ ) fit of the normal state specific heat data of  $\text{La}_3\text{Ni}_2\text{B}_2\text{N}_{2.65}$  a  $\gamma \simeq 26.0 \text{ mJ/molK}^2$  is obtained (see figure 4.8). The Sommerfeld coefficient of selected compositions along with  $T_c$ ,  $\Delta C$  and  $\rho_o$  is summarized in table 5.2. Also listed in the table is the fraction of impurity phase  $\text{LaNiBN}$  for each composition as obtained from X-ray or neutron diffraction measurements. A clear composition dependent variation in  $T_c$  and a correspondence between  $\rho_o$  and  $T_c$  (see figure 5.2) is observed which is clearly an intrinsic behaviour of  $\text{La}_3\text{Ni}_2\text{B}_2\text{N}_x$ . However  $\gamma$  as well as  $\Delta C$  do not correlate with  $T_c$  which is unexpected and obviously an effect of the impurity phase  $\text{LaNiBN}$  in those samples.

$x$	LaNiBN (%)	$\rho_o$ ( $\mu\Omega\text{cm}$ )	$T_c$ (K)	$(\Delta C)_{T_c}$ (J/molK)	$(\Delta C_{\text{intr.}})_{T_c}$ (J/molK)	$\gamma$ (mJ/mol K <sup>2</sup> )	$\gamma_{\text{intr.}}$ (mJ/mol K <sup>2</sup> )
2.60	14	23.5	12.2	0.38(5)	0.44(5)	23.4(10)	24.3(10)
2.65 $a$	7	19.3	12.8	0.44(5)	0.47(5)	26.0(10)	26.6(10)
2.65 $b$	5*	18.8	13.0	0.46(5)	0.48(5)	26.5(10)	27.0(10)
2.70 $a$	5	18.9	13.1	0.42(5)	0.44(5)	26.5(10)	27.0(10)
2.70 $b$	5	18.5	13.1	0.43(5)	0.44(5)	24.5(10)	24.9(10)
2.75	8	15.5	13.3	0.44(5)	0.47(5)	24.4(10)	25.1(10)
2.85	19*	11.9	13.7	0.34(5)	0.42(5)	24.1(10)	25.5(10)
2.90	15	12.2	14.0	0.41(5)	0.48(5)	24.6(10)	26.0(10)

Table 5.2: Characteristic superconducting and normal state properties for various  $\text{La}_3\text{Ni}_2\text{B}_2\text{N}_x$  samples. Asterisks represent the LaNiBN phase fraction determined by neutron powder diffraction.

**Specific heat of LaNiBN.** - In order to investigate the influence of impurities on intrinsic properties of  $\text{La}_3\text{Ni}_2\text{B}_2\text{N}_x$ , a LaNiBN sample was synthesized. It is very difficult to get a phase pure LaNiBN and the X-ray diffraction analysis indicated only about 80% phase purity. The specific heat of LaNiBN is shown in figure 5.11 with an inset showing the low temperature part of the specific heat curve. A very broad superconducting anomaly is observed with  $T_c$  onset of about 4K. A fit of the data in temperature range  $30\text{K}^2 < T^2 < 50\text{K}^2$  according to  $C_p = C_e + C_{ph} \simeq \gamma T + \beta T^3$  results in  $\gamma \simeq 6.1\text{mJ/molK}^2$  and  $\beta \simeq 0.1106\text{mJ/molK}^4$  yielding  $\Theta_D^{LT} = 412\text{K}$ . The normal state specific heat is estimated by extrapolating the  $C_p$  curve as shown in the inset of figure 5.11. The specific heat data of  $\text{La}_3\text{Ni}_2\text{B}_2\text{N}_x$  are corrected by the simple formula

$$C_{pm} = [C_p - F_i \times C_{pi}] / F_m \quad (5.5)$$

where  $C_{pm}$  and  $C_{pi}$  represent the specific heat (in mJ/gK) of matrix and impurity phase, respectively, and  $F$  representing the corresponding phase fractions. The measured and corrected specific heat of  $\text{La}_3\text{Ni}_2\text{B}_2\text{N}_{2.85}$  are shown in figure 5.12 which reveal a significant influence of the LaNiBN fraction on specific heat anomaly and also on the low temperature behaviour. A similar correction for selected compositions yields the intrinsic Sommerfeld coefficient,  $\gamma_{\text{intr.}}$ , and the specific heat jump  $(\Delta C_{\text{intr.}})_{T_c}$  which are summarized in table 5.2. The values of  $\gamma_{\text{intr.}}$  in table 5.2 reveal a generally increasing trend with increasing nitrogen stoichiometry with the exception of  $\text{La}_3\text{Ni}_2\text{B}_2\text{N}_{2.65\sim 2.7}$  samples. No clear correlation between  $T_c$  and  $(\Delta C_{\text{corr}})_{T_c}$  is observed, rather an approximately constant height of specific heat jumps (within error bars) in phase pure materials is revealed.

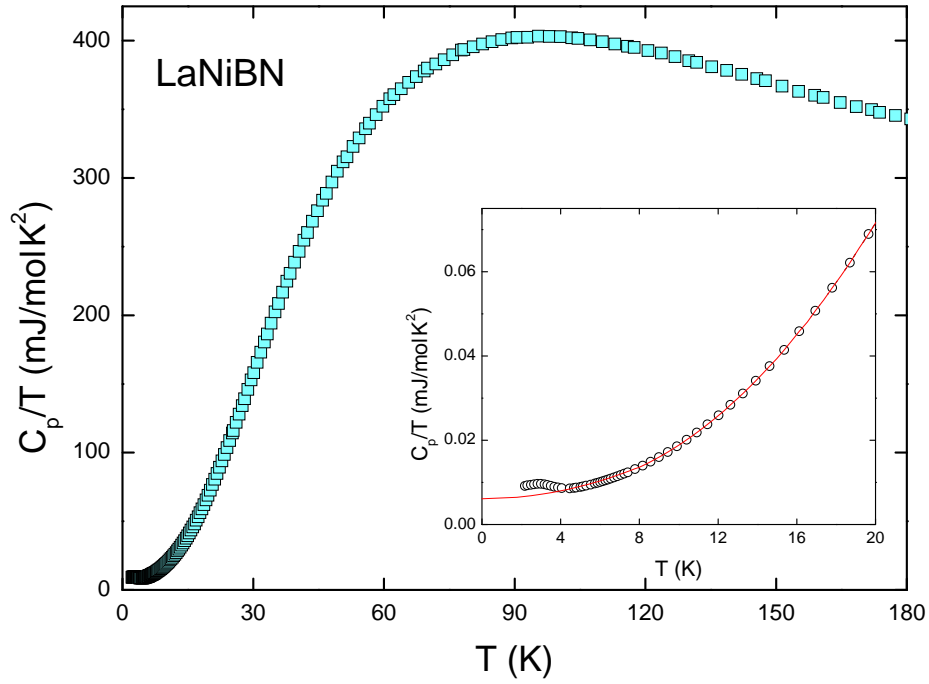


Figure 5.11: Temperature dependent  $C/T$  of LaNiBN; inset shows a zoomed view of low temperature specific heat.

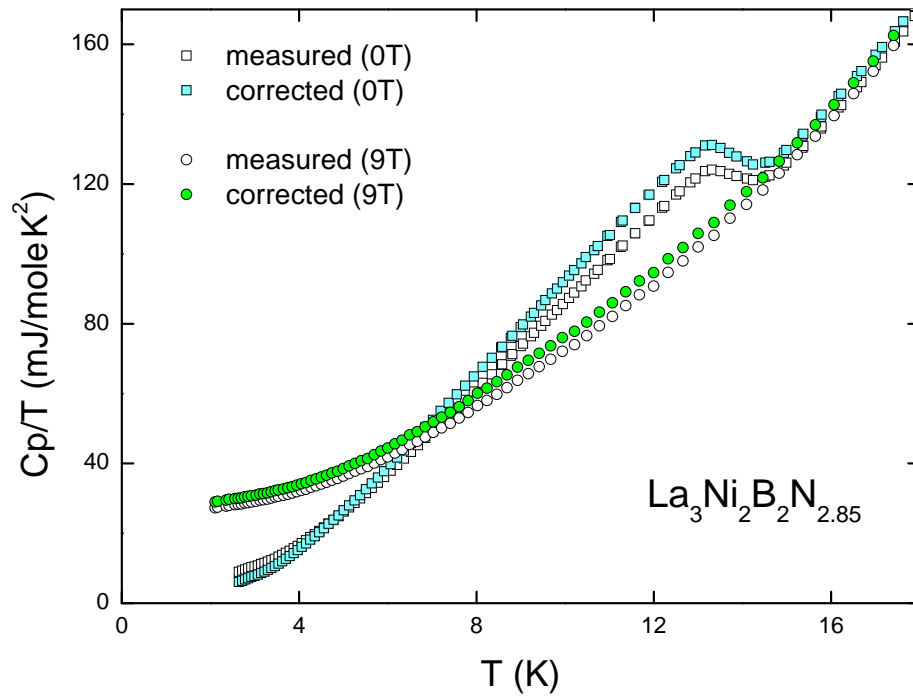


Figure 5.12: Temperature dependent  $C/T$  of  $\text{La}_3\text{Ni}_2\text{B}_2\text{N}_{2.85}$  at 0 and 9T; Open symbols represent the measured data while close symbols represent corrected data according to the LaNiBN phase fraction (see text).

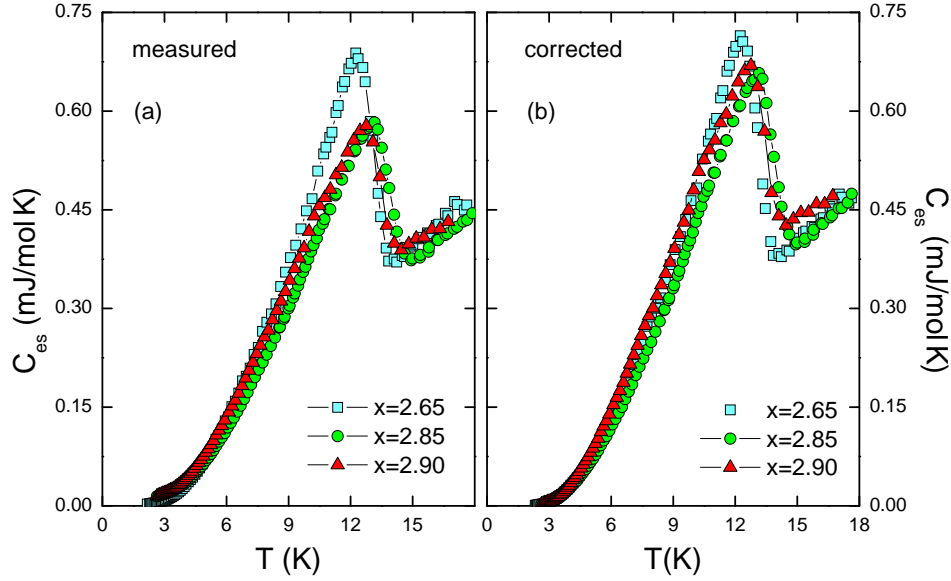


Figure 5.13: The electronic specific heat of selected  $\text{La}_3\text{Ni}_2\text{B}_2\text{N}_x$  samples with  $x$  as labeled calculated from measured data (a) and corrected according to the phase fraction of LaNiBN (b).

#### 5.4.1 Electronic specific heat and superconducting gap

The temperature dependence of the SC state electronic specific heat  $C_{es}$ , is obtained by subtracting the phonon contributions  $C_{ph}$  (derived from the normal state specific heat) from the zero-field specific heat measurement. The electronic specific heat of selected compositions of  $\text{La}_3\text{Ni}_2\text{B}_2\text{N}_x$  is shown in figure 5.13(a). In order to get an insight on the influence of the LaNiBN fraction, only those samples for the analysis of electronic specific heat are chosen for which a reliable estimates of the LaNiBN fraction by neutron powder diffraction analysis are available. Reasonably sharp specific heat anomaly is observed for  $\text{La}_3\text{Ni}_2\text{B}_2\text{N}_{2.65}$  which has a LaNiBN fraction of only 5% while for other two compositions (with LaNiBN > 15%) the height of specific heat anomaly is reduced.  $C_{es}$  calculated from the corrected specific heat data according to the phase fraction of LaNiBN is shown in figure 5.13(b) which reveals an almost constant height of specific heat jump of all three samples. The BCS expression for the electronic specific heat in the superconducting for  $2.5 < T_c/T < 6$  is given by

$$C_{es} = 8.5\gamma T_c \exp\left(-0.82 \frac{\Delta(0)}{k_B T}\right) \quad (5.6)$$

where  $\Delta(0)$  is the width of the superconducting gap at zero temperature. The normalized electronic specific heat  $C_{es}/\gamma T_c$  of  $\text{La}_3\text{Ni}_2\text{B}_2\text{N}_{2.65}$  and

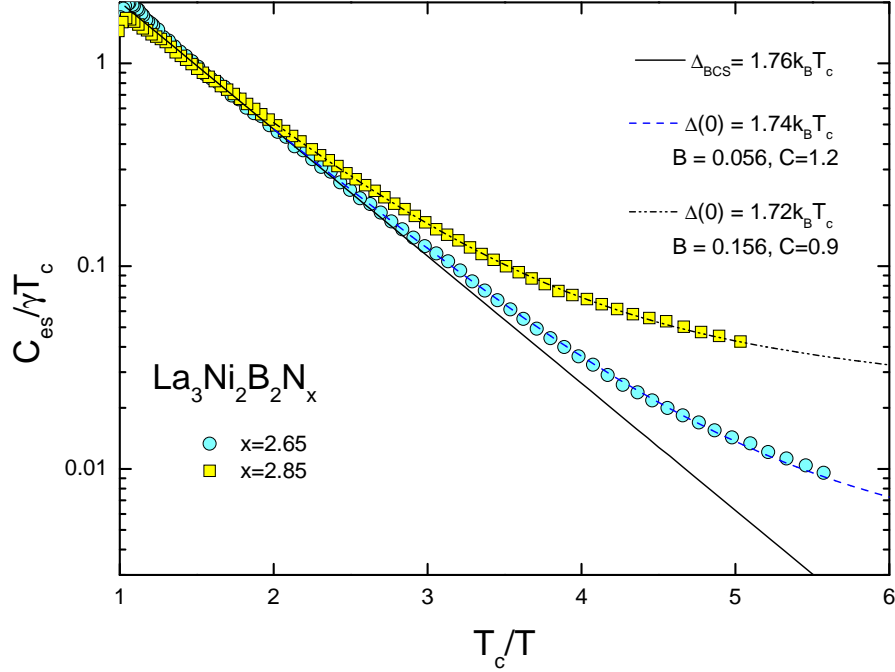


Figure 5.14:  $C_{es}/\gamma T_c$  of selected  $\text{La}_3\text{Ni}_2\text{B}_2\text{N}_x$  compositions. The solid line represent the exponential temperature dependence according to BCS theory while broken lines are fit of the data according to equation 5.7.

$\text{La}_3\text{Ni}_2\text{B}_2\text{N}_{2.85}$  as a function of  $T_c/T$  is shown in figure 5.14 in a semi logarithmic plot where the solid line indicates an exponential dependence according to the BCS theory. The  $C_{es}$  of  $\text{La}_3\text{Ni}_2\text{B}_2\text{N}_{3-\delta}$  reported previously showed an exponential dependence and a fit of the data by equation 5.6 yielded a gap to critical temperature ratio  $\Delta(0)/k_B T_c \simeq 1.85$  [41]. As measured  $C_{es}$  data shown in figure 5.6 do not reveal an exponential dependence and may follow a power law at low temperature. The electronic specific heat of the related borocarbides  $\text{YNi}_2\text{B}_2\text{C}$  and  $\text{LuNi}_2\text{B}_2\text{C}$  has been reported to show a  $T^3$  power law dependence [33] which is well described by the two fluid model  $C_{es}(T) = 3\gamma T_c (T/T_c)^3$  [88]. In order to investigate phenomenologically the behaviour of electronic specific heat equation 5.6 is modified as

$$\frac{C_{es}}{\gamma T_c} = 8.5 \exp\left(-0.82 \frac{\Delta(0)}{K_B T}\right) (1 - B) + 3B \left(\frac{T}{T_c}\right)^C \quad (5.7)$$

where the term  $3B(T/T_c)^C$  represent a power law dependence similar to the two fluid model and  $B$  is a factor for phase factors related to exponential and power law behaviours. The fit of experimental data according to equation 5.7 for  $T_c/T > 2.5$  is indicated by broken lines in figure 5.14 with fit parameters as labeled. The data are well reproduced by equation 5.7 with an

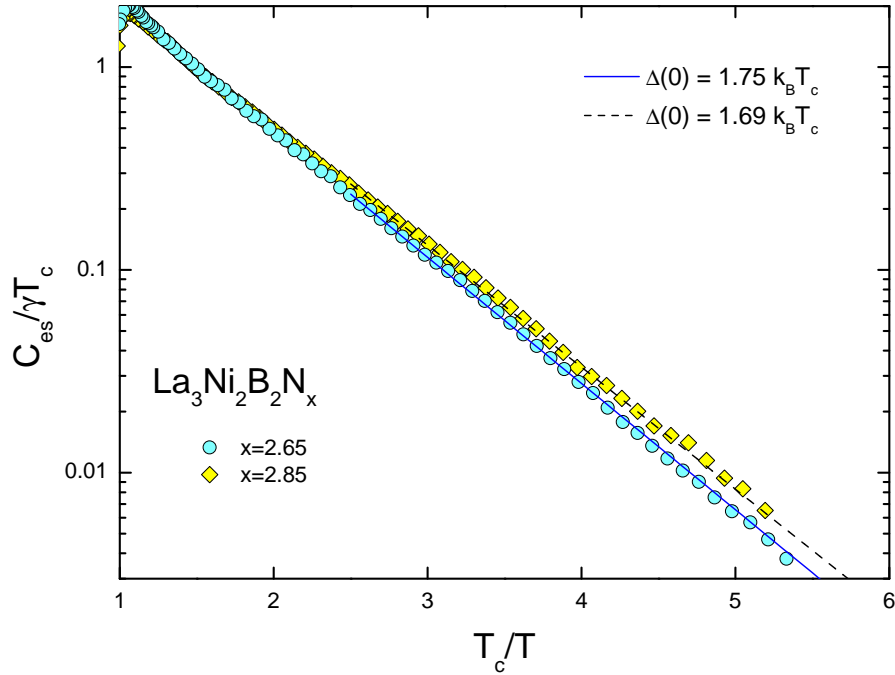


Figure 5.15: Corrected  $C_{es}/\gamma T_c$  of selected  $\text{La}_3\text{Ni}_2\text{B}_2\text{N}_x$  compositions according to equation 5.5. Lines represent a fit of the data according to equation 5.6.

almost linear contribution together with  $\Delta(0)/k_B T_C$  which is close to BCS value  $\Delta(0)/k_B T_C = 1.76$  for both samples. The linear term in  $C_{es}$  may not be an intrinsic behaviour of  $\text{La}_3\text{Ni}_2\text{B}_2\text{N}_x$  and could possibly be a consequence of the impurity phase  $\text{LaNiBN}$ . This is corroborated by the fact that the fit parameter  $B$  of 5.6% and 15.6% for  $\text{La}_3\text{Ni}_2\text{B}_2\text{N}_{2.65}$  and  $\text{La}_3\text{Ni}_2\text{B}_2\text{N}_{2.85}$  respectively is very close to the phase fraction of  $\text{LaNiBN}$  determined by neutron powder diffraction (see table 5.2). To investigate the influence of  $\text{LaNiBN}$  on low temperature specific heat the corrected (according to  $\text{LaNiBN}$  phase fraction) intrinsic  $C_{es}/\gamma T_c$  is shown in figure 5.15. The lines in figure 5.15 represent a fit of the data for  $T_c/T > 2.5$  according to equation 5.6. It is evident that after subtracting the impurity contribution to the electronic specific heat, clearly shows an exponential dependence is well described by the BCS relation. The gap to critical temperature ratio  $\Delta(0)/k_B T_C$  for  $\text{La}_3\text{Ni}_2\text{B}_2\text{N}_{2.65}$  and  $\text{La}_3\text{Ni}_2\text{B}_2\text{N}_{2.85}$  is 1.75 and 1.69 respectively, i.e. close to BCS value of 1.76. These results indicate that the  $\text{LaNiBN}$  phase has a significant impact on low temperature results of  $\text{La}_3\text{Ni}_2\text{B}_2\text{N}_x$ . In phase pure  $\text{La}_3\text{Ni}_2\text{B}_2\text{N}_x$  the electronic specific heat reveals an exponential temperature dependence while in case of dirty samples it is a mixture of an exponential term and an approximately linear contribution from impurities. The low temperature exponential temperature dependence of  $C_{es}$  is in line with BCS theory prediction and points



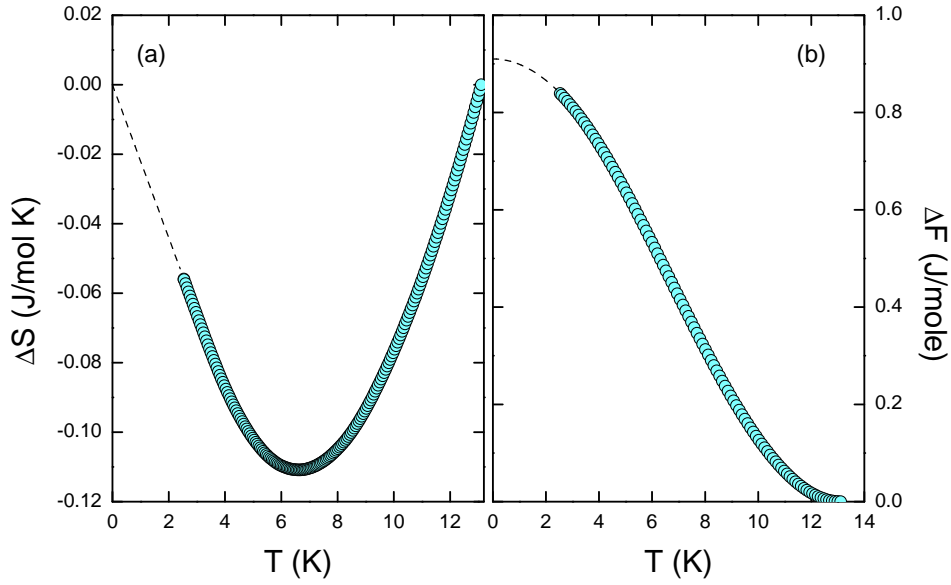


Figure 5.16: Entropy difference (a) and free energy difference (b) between the superconducting and normal state of  $\text{La}_3\text{Ni}_2\text{B}_2\text{N}_{2.7}$ . Dashed lines indicate extrapolations of data to absolute zero.

towards an  $s$ -wave symmetry of the superconducting order parameter and strongly supports that an  $s$ -wave model like the Eliashberg theory shall be applicable.

### 5.4.2 Thermodynamic critical field

The thermodynamic critical field corresponds to the free energy gain of the superconducting state and is obtained by integrating the entropy difference between the superconducting and normal state, according to equation 2.1. By starting with the specific heat difference ( $C_s - C_n$ ) for the composition  $\text{La}_3\text{Ni}_2\text{B}_2\text{N}_{2.7}$  and integrating it according to equation 2.1 gives the entropy and free energy displayed in figure 5.16. The dashed lines indicate the extrapolation of the data to absolute zero. The thermodynamic critical field of selected samples of  $\text{La}_3\text{Ni}_2\text{B}_2\text{N}_x$  as calculated from equation 2.1 is shown in figure 5.17(a). For  $\text{La}_3\text{Ni}_2\text{B}_2\text{N}_{2.6}$  with a  $T_c$  of about 12.2 K an  $H_c$  of  $\sim 147(5)$  mT is obtained. One would expect an increase in  $H_c$  with increase in  $T_c$  but figure 5.17(a) reveals a different trend of  $H_c$  for  $\text{La}_3\text{Ni}_2\text{B}_2\text{N}_{2.85}$  with a  $T_c$  of about 13.7 K. The reduction of  $H_c$  with increasing nitrogen stoichiometry is a consequence of enhanced impurity fraction which is labeled in figure 5.17(a) for each sample. The increase of impurity fraction results in a concomitant reduction of the volume fraction of the main phase which is reflected in the decrease of  $H_c$ . The corrected (according to impurity fraction) intrinsic ther-

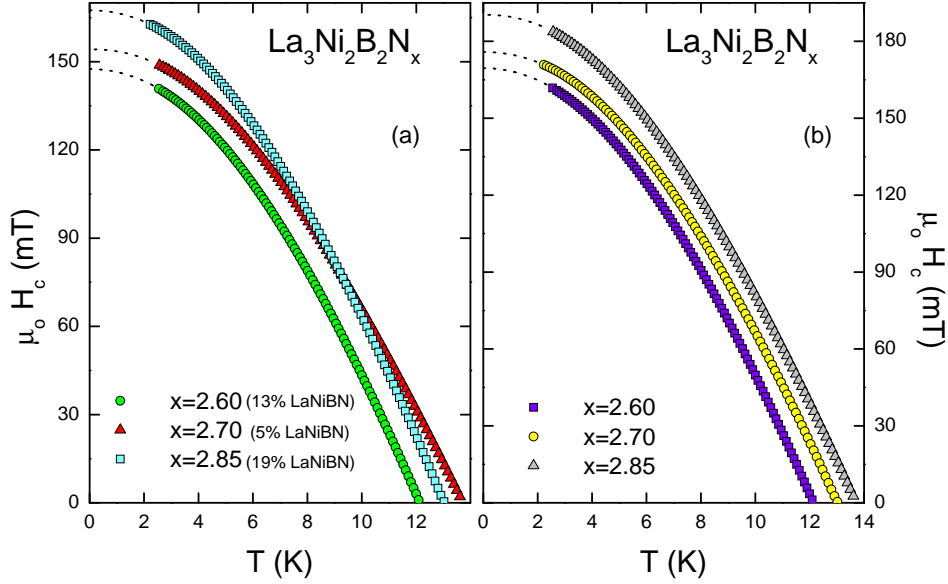


Figure 5.17: Thermodynamic critical field of  $\text{La}_3\text{Ni}_2\text{B}_2\text{N}_x$  samples with  $x$  as labeled (a). The corrected (intrinsic)  $H_c(T)$  according to the LaNiBN phase fraction is shown in (b).

thermodynamic critical fields are shown in figure 5.17(b) which reveals that the thermodynamic critical field is in line with  $T_c$  if the contribution from the LaNiBN phase is taken into account. The highest value of  $H_c \simeq 190$  mT is estimated is for  $\text{La}_3\text{Ni}_2\text{B}_2\text{N}_{2.85}$  which is almost as large as the  $H_c$  reported for related borocarbide superconductors  $(\text{Y},\text{Lu})\text{Ni}_2\text{B}_2\text{C}$ .

### 5.4.3 Electron phonon mass enhancement $\lambda_{ep}$

An evaluation of the electron-phonon mass enhancement  $\lambda_{ep}$  from the transition temperature  $T_c$  and the low  $T$  Debye temperature is based on the McMillan model [19]. Within this model  $T_c$  is given by the McMillan formula (equation 5.3) which can be inverted to obtain  $\lambda_{ep}$  in terms of  $T_c$ ,  $\Theta_D$  and  $\mu^*$  as

$$\lambda_{ep} = \frac{1.04 + \mu^* \ln \left( \frac{\Theta_D}{1.45T_c} \right)}{(1 - 0.62\mu^*) \ln \left( \frac{\Theta_D}{1.45T_c} \right) - 1.04} \quad (5.8)$$

The value of  $\lambda_{ep}$  determines the attractive part of the Cooper pair bonding while  $\mu^*$  is the repulsive screened Coulomb part. The values of  $\Theta_D$  and  $T_c$  of selected samples are listed in table 5.3. Taking  $\mu^* = 0.1 - 0.13$  we obtain for  $\text{La}_3\text{Ni}_2\text{B}_2\text{N}_{2.7}$   $\lambda_{ep} = 0.8 - 0.9$ . The  $\lambda_{ep}$  values for selected compositions are listed in table 5.3 and exhibit an increase with increasing N-stoichiometry.

Property	$x=2.6$	$x=2.7$	$x=2.85$
$T_c$ (K)	12.2	13.1	13.7
$\Theta_D^{LT}$ (K)	335(5)	329(5)	340(5)
$\lambda$	0.85	0.89	0.90
$*N(E_f)$ (states/eV-f.u)	5.6	5.8	5.7
$*\Delta C_{Tc}$ (J/molK)	0.44	0.44	*0.42
$*\Delta C/\gamma T_c$ (BCS: 1.43)	1.48(10)	1.35(10)	1.22(10)
$*\Delta(0)/k_B T_c$ (BCS: 1.76)	1.74(5)	1.75(5)	1.69(5)
$*\mu_0 H_c(0)$ (mT)	169(5)	176(5)	190(5)
$\mu_0 H_{c1}(0)$ (mT)	14.5(1)	15.3(1)	16.8
$\mu_0 H_{c2}(0)$ (T)	8.7(5)	10.0(5)	10.4(5)
$\kappa_{GL}(0)$	38(2)	40(2)	41(2)
$\xi_{GL}(0)$ (nm)	6.2(5)	5.8(5)	5.7(5)
$\lambda_{GL}(0)$ (nm)	236	232	233

Table 5.3: The critical fields and superconducting parameters for selected samples of  $\text{La}_3\text{Ni}_2\text{B}_2\text{N}_x$  with  $x$  as listed. (\*) indicates correction in the corresponding value according to phase fraction of  $\text{LaNiBN}$  obtained from X-ray or neutron powder diffraction measurements.

It should be mentioned here that  $\lambda_{ep}$  calculated from Mc Millan's formula is in good agreement with the transport electron phonon coupling constant  $\lambda_{tr}$  estimated from resistivity measurements (see section 4.2.1). Having estimated  $\lambda_{ep}$  the electronic density of states at the Fermi level  $N(E_f)$  can be estimated from the value of the Sommerfeld coefficient  $\gamma$  using the relation

$$\gamma = \frac{2}{3}\pi^2 k_B^2 N(E_f)(1 + \lambda_{ep}) \quad (5.9)$$

$N(E_f)$  for selected nominal compositions shown in table 5.3 does not show a significant composition dependent variation suggesting that the nitrogen vacancies have only a small effect on the density of states at the Fermi level  $N(E_f)$  of  $\text{La}_3\text{Ni}_2\text{B}_2\text{N}_{3-\delta}$ . From  $\gamma$  and  $\lambda_{ep}$  the bare Sommerfeld coefficient  $\gamma_{bs}$  can be estimated as

$$\gamma_{bs} = \frac{\gamma}{1 + \lambda} \quad (5.10)$$

resulting in a value of  $\gamma_{bs} = 13.7 \text{ mJ/molK}^2$  in close agreement with the value calculated by Mattheiss [89].

#### 5.4.4 Ginzburg-Landau parameter $\kappa$ and characteristic lengths $\xi$ and $\lambda_{GL}$

The Ginzburg-Landau parameter ( $\kappa_{GL}$ ) is determined by low temperature extrapolation of upper critical field  $\mu_o H_{c2}(0)$  and thermodynamic critical field  $\mu_o H_c(0)$  according to Abrikosov's relation

$$\lambda_{GL}/\xi_{GL}(0) \equiv \kappa_{GL}(0) = \frac{H_{c2}(0)}{\sqrt{2}H_c(0)} \quad (5.11)$$

yielding a Ginzburg-Landau parameter of 40(2) for  $\text{La}_3\text{Ni}_2\text{B}_2\text{N}_{2.7}$ . Using the GLAG relations (Eqs. 2.3-2.5) given in chapter 2 and with the results of  $H_{c2}(0)$ ,  $H_C(0)$  and  $\kappa_{GL}(0)$ , one can estimate the characteristic lengths  $\lambda_{GL}(0)$  and  $\xi_{GL}(0)$  as well as the lower critical field  $H_{c1}(0)$ . The superconducting parameters determined of selected  $\text{La}_3\text{Ni}_2\text{B}_2\text{N}_{3-\delta}$  samples determined from GLAG relations are summarized in table 5.3. In comparison to an earlier report [41], a larger  $\lambda_{GL}(0) \sim 230$  nm while smaller  $\xi_{GL} \sim 6$  nm is obtained resulting in an increase in  $\kappa_{GL}(0) \simeq 40$  as compared to earlier proposed  $\kappa_{GL} \simeq 33$ . Within the width of formation the characteristic lengths do not indicate any composition dependence which is unexpected. The variation in  $\rho_o$  within the width of formation is approximately  $10\mu\Omega\text{cm}$  (see figure 4.2). Thus, on the basis of Gor'kov-Goodman relation (equation 2.17), an increase in  $\kappa_{GL}$  with increase in  $\rho_o$  is expected. For  $\text{La}_3\text{Ni}_2\text{B}_2\text{N}_{2.7}$  with  $\gamma = 304.05 \text{ J/m}^3\text{K}^2$ , the Gor'kov-Goodman relation suggests a variation  $\Delta\kappa \sim 4$ . So one would expect an increase of  $\kappa$  by 4 for  $\text{La}_3\text{Ni}_2\text{B}_2\text{N}_{2.6}$  as compared to  $\text{La}_3\text{Ni}_2\text{B}_2\text{N}_{2.9}$  which, however, is within error bars of the experimental values of  $\kappa$  (the trend of the insignificant variation indicated in table 5.3 would be opposite to the expected one).

#### 5.4.5 Field dependent Sommerfeld coefficient $\gamma(H)$

The magnetic field dependence of the Sommerfeld coefficient  $\gamma(H)$  has been argued to provide information about the superconducting gap symmetry [90]. The application of an external magnetic field ( $H$ ) results in a gradual suppression of superconductivity and also the collapse of the specific heat anomaly. In a sufficiently strong applied external magnetic field, vortices enter the sample resulting in a rise of the normal state component in the vortex cores which contributes a linear specific heat,  $\gamma T$ . As the field increases, the vortex core grows and  $\gamma$  is expected to increase proportionally. The entropy balance also implies that the reduction of the specific heat anomaly must be accompanied by an increase of the Sommerfeld coefficient. For an  $s$ -wave superconductor the quasi particle excitations are expected to be confined in the vortex cores and  $\gamma(H)$  is proportional to the density of vortices resulting in  $\gamma(H) \propto H$  [91]. On the other hand for a  $d$ -wave superconductor the zero gap regions along

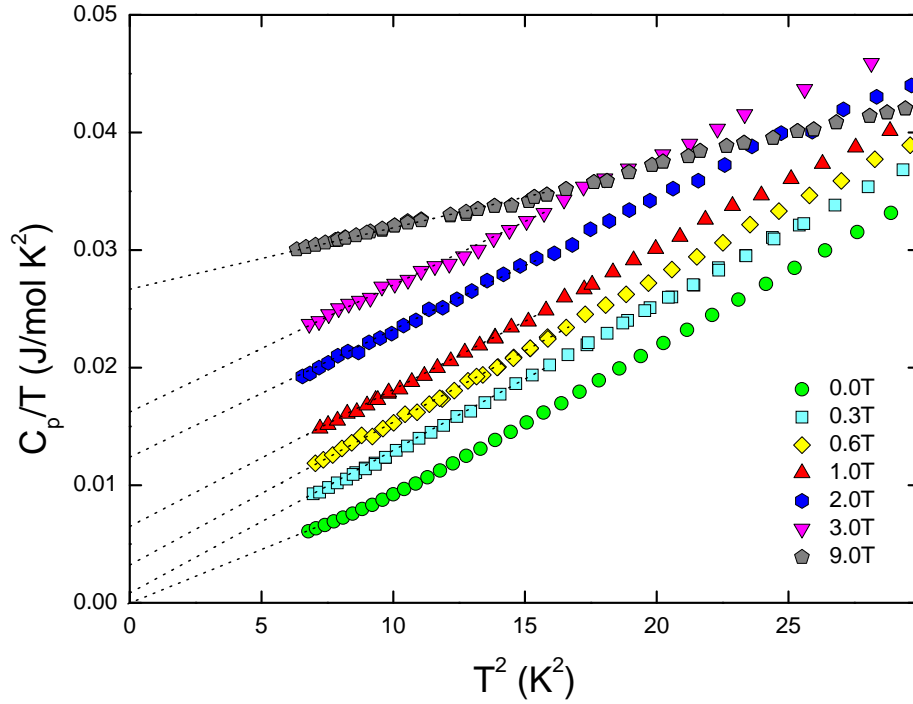


Figure 5.18: Low  $T$  specific heat of  $\text{La}_3\text{Ni}_2\text{B}_2\text{N}_{2.65}$  with dashed lines representing the extrapolation of the data to obtain  $\gamma$ .

the lines on the Fermi surface may result in a  $\sqrt{H}$  dependence of  $\gamma$  [90]. In an earlier report on  $\text{La}_3\text{Ni}_2\text{B}_2\text{N}_{3-\delta}$ , an approximately  $\sqrt{H}$  dependence of  $\gamma$  was observed but at the same time it was concluded to be a conventional  $s$ -wave superconductor [33]. A similar  $\sqrt{H}$  dependence of Sommerfeld coefficient has been observed in related borocarbide  $\text{LuNi}_2\text{B}_2\text{C}$  [92] that motivated discussions about the possibility of unconventional pairing in the superconducting state of the borocarbides. However, Ramirez [93] pointed out that for the conventional  $s$ -wave superconductor  $\text{V}_3\text{Si}$ ,  $\gamma$  shows a  $\sqrt{H}$  dependence which is interpretable from the standpoint of vortex-vortex interactions near  $H_{c1}$ .

The low temperature specific heat of  $\text{La}_3\text{Ni}_2\text{B}_2\text{N}_{2.65}$  is shown in figure 5.18. As expected,  $C_p/T$  varies linearly with  $T^2$  and a least square fit of the experimental data gives the Sommerfeld coefficient at the corresponding applied magnetic field. Figure 5.18 reveals essentially a parallel shift of the specific heat curves with increase in strength of  $H$ . The field dependence of  $\gamma$  as determined from a linear fitting of the low temperature data in figure 5.18 is shown in figure 5.19. The solid line in figure 5.19 represents a linear regression of the data in range  $0\text{T} \leq H \leq 1\text{T}$  while the dashed line represents a  $\sqrt{H}$  dependence of  $\gamma$ . Recently, a theoretical investigation by Nakai *et al.* [94] revealed that for an isotropic-gapped type II superconductor,  $\gamma(H) \propto H$  behaviour

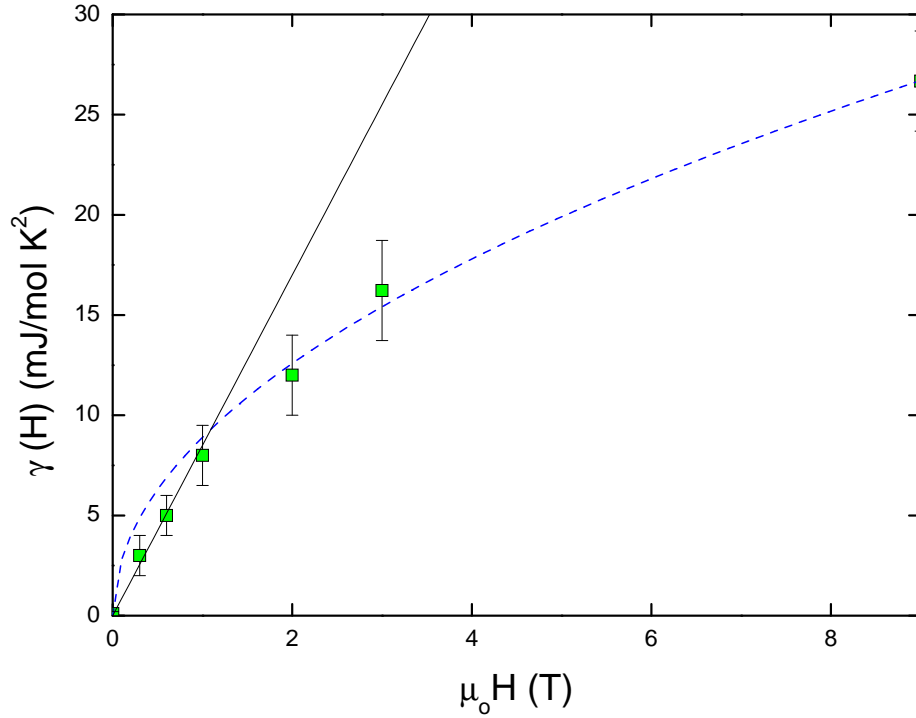


Figure 5.19: Sommerfeld coefficient  $\gamma$  as a function of applied field. Solid line represents a linear regression of the data for  $H \leq 1$ T while dashed line represents a  $\sqrt{H}$  dependence

persists only up to a certain crossover field,  $H^*$  above which an  $\sqrt{H}$  dependence is observed. For the isotropic superconducting gap,  $H^*$  is expected to be approximately  $0.32H_{c2}$  which is reduced as the degree of anisotropy of the superconducting gap increases. As shown in figure 5.19(b),  $\gamma(H)$  varies linearly only up to an  $H^* \simeq 1.1$  T above which a  $\sqrt{H}$  dependence is evident. A similar field dependence of Sommerfeld coefficient has been observed in other  $s$ -wave superconductors like pure niobium [95] and in layered nitride superconductor  $\text{Li}_x\text{ZrNCl}$  [96]. For  $\text{La}_3\text{Ni}_2\text{B}_2\text{N}_{2.65}$  with an  $H_{c2} \simeq 9$  T, the ratio  $H^*/H_{c2} \simeq 0.1$  which is lower than the value predicted by Nakai *et al.* [94] for an isotropic  $s$ -wave superconductor. This may suggest an anisotropic  $s$ -wave superconducting gap for  $\text{La}_3\text{Ni}_2\text{B}_2\text{N}_x$ .

#### 5.4.6 Discussion and analysis in terms of Eliashberg model calculations

In an earlier study Manalo *et al.* [36] performed model calculations for  $\text{La}_3\text{Ni}_2\text{B}_2\text{N}_{3-\delta}$  based on an Eliashberg theory for anisotropic  $s$ -wave superconductors (see chapter 2). Thereby, thermodynamic features, e.g. the SC

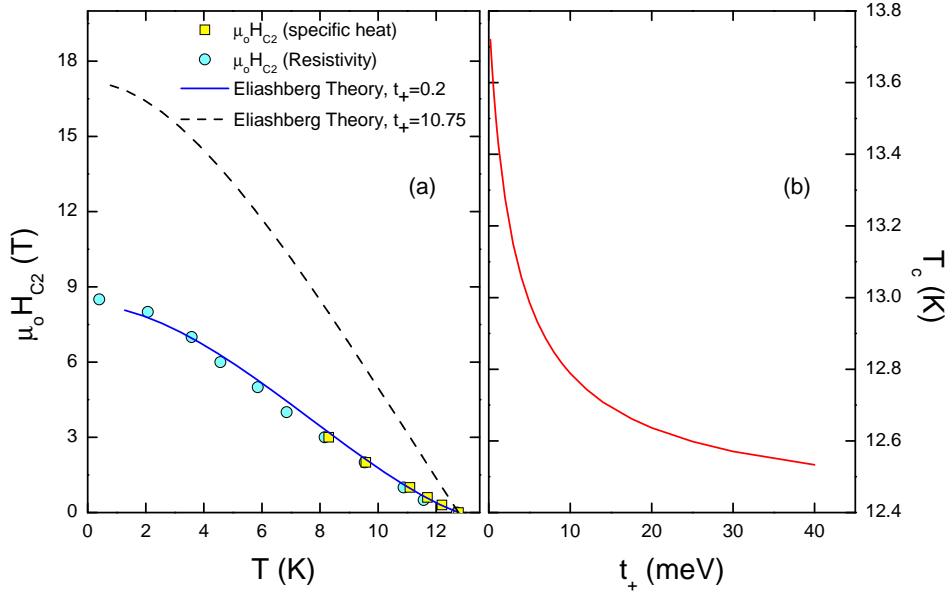


Figure 5.20:  $H_{c2}$  of  $\text{La}_3\text{Ni}_2\text{B}_2\text{N}_{2.65}$  determined by resistivity and specific heat measurements (a). Solid and dashed lines in (a) represent a fit of the data in terms of the separable Eliashberg model (see text).  $T_c$  as a function of the scattering rate  $t_+$  (b).

state electronic specific heat  $C_{eS}(T)$ , and the temperature dependent upper critical field  $H_{c2}(T)$  where reasonably well reproduced by a clean limit model using  $\langle a_{\mathbf{k}}^2 \rangle \simeq 0.08$  and  $\langle b_{\mathbf{k}}^2 \rangle \simeq 0.245$  as the set of parameters for the anisotropy of the electron-phonon coupling and the anisotropy of the Fermi velocity, respectively. For such given set of parameters the model further yields a specific relation for the effect of non-magnetic impurities (characterized by the parameter  $t_+$  upon  $T_c$  which, however, could not be analyzed in this earlier study which was based on a single sample  $\text{La}_3\text{Ni}_2\text{B}_2\text{N}_{3-\delta}$ . In the present work an extended set of good quality samples  $\text{La}_3\text{Ni}_2\text{B}_2\text{N}_x$  with  $T_c$  varying between 12.2 K and 14.0 K and a well elaborated PDOS (see figure 4.10 in chapter 4) allows a re-examination of the Eliashberg model calculations. A set of parameters which are not too far from those used in Ref. [36], namely  $\langle a_{\mathbf{k}}^2 \rangle = 0.09$ ,  $\langle b_{\mathbf{k}}^2 \rangle = 0.205$ , and  $t_+ = 0.2$  meV, allows to reproduce reasonably well  $H_{c2}(T)$  of  $\text{La}_3\text{Ni}_2\text{B}_2\text{N}_{2.65}$  as demonstrated by the solid line in figure 5.20a. The relatively large value of the parameter  $\langle a_{\mathbf{k}}^2 \rangle = 0.09$  is needed to obtain nearly BCS like thermodynamic features of the SC state (e.g. borocarbides with more pronounced strong coupling features are well described with smaller  $\langle a_{\mathbf{k}}^2 \rangle \simeq 0.02$ , see Ref. [36]) and also to enable a significant variation of  $T_c$  in this model. The latter result, i.e. the separable model result for the impurity dependence of the SC transition temperature,  $T_c(t_+)$ , is displayed in

figure 5.20b which is strongly non-linear and thus in disagreement with the experimentally established, approximately linear relation between  $T_c$  and the residual resistivity  $\rho_0$  which is expected to be directly proportional to the parameter  $t_+$ . The chosen set of model parameters further results in significant modifications of  $H_{c2}(T)$  when increasing  $t_+$  as indicated by the dashed line in figure 5.20a which displays an upper critical field calculation with  $t_+ = 10.75$  meV where  $H_{c2}(0)$  increases to above 17 T and the curvature right below  $T_c$  disappears. The present Eliashberg model calculations, thus, fail to provide a simple account for the experimentally established variation of  $T_c$  and the more modest variation of  $H_{c2}(T)$  of  $\text{La}_3\text{Ni}_2\text{B}_2\text{N}_x$ . The latter results from a rather insignificant variation of the Ginzburg-Landau parameter  $\kappa_{GL} \sim 40 \pm 2$  which, however, is quantitatively in line with the minor variation of  $\kappa$  estimated via the Gorkov-Goodman relation which yields  $\Delta\kappa \sim 4$  when the residual resistivity  $\rho_0$  increases by about  $10 \mu\Omega\text{cm}$ .

As proposed also earlier in Ref. [36], all experimental  $H_{c2}$  data of  $\text{La}_3\text{Ni}_2\text{B}_2\text{N}_x$  are compatible with a rather small impurity scattering rates. Manalo *et al.* [36] speculated that the substantial residual resistivity of their sample might be caused by scattering on the grain boundaries rather than by intrinsic scattering inside the grains, which, however, seems ruled out by the approximate proportionality between in the residual resistivity  $\rho_0$  and the density of N-vacancies revealed by NPD (see chapter 4), thus, referring to an intrinsic scattering.

The most plausible reason for the observed discrepancies between the Eliashberg model calculations in figure 5.20 and the experimental results of  $\text{La}_3\text{Ni}_2\text{B}_2\text{N}_x$  might be subtle electronic changes caused by N-vacancies. Fermi surface calculations by Reith and Podloucky [83] which were performed for a number of supercells  $(\text{La}_3\text{Ni}_2\text{B}_2\text{N}_{3-\delta})_n$  with increasing number of N-vacancies  $\delta$  possibly indicate some modification of Fermi surface nesting features while overall changes of the band structure (e.g.  $N(E_f)$ ) remain small. The significant variation of  $T_c$  of  $\text{La}_3\text{Ni}_2\text{B}_2\text{N}_x$  might, thus, be a consequence of changes in the electron-phonon coupling (i.e.  $\lambda$ ) caused by electronic effects which can not be captured by the present Eliashberg model. The relatively large value of the mean anisotropy of the electron-phonon spectral function  $\langle a^2 \rangle \simeq 0.9$ , thus, seems to be an unrealistic overestimate which is mainly motivated to obtain a large variation of  $T_c$  as shown in figure 5.20b. A more realistic modeling of the SC state properties of  $\text{La}_3\text{Ni}_2\text{B}_2\text{N}_x$  in terms of the separable model of the Eliashberg theory might be based on more moderate values of the anisotropy parameter  $\langle a^2 \rangle$  which would allow to obtain more subtle effects of  $t_+$  variations upon  $H_{c2}(T)$  (assuming that the changes of  $T_c$  are caused by electronic structure or Fermi surface effects).



# Chapter 6

## Ground state properties of $\text{Ce}_3\text{Ni}_2\text{B}_2\text{N}_{3-\delta}$

### 6.1 Introduction

Special interest in intermetallic compounds containing cerium is due to their rich low temperature physics interrelated with ground states such as e.g. the Kondo lattice with and without long range magnetic order, intermediate valence, Kondo insulator, and in some cases unconventional superconductivity (see e.g. Ref. [97] for a recent review). This variety of ground states adopted in cerium compounds is a consequence of competing interactions: RKKY-type Ce-Ce intersite exchange, crystal field effects and Kondo interaction between Ce  $4f$  and conduction electrons. A subtle balance between RKKY and Kondo interactions in some cases leads to the formation of novel ground states of correlated electrons such as magnetically mediated unconventional superconductivity. Cerium based superconductors at ambient pressure are e.g.  $\text{CeCu}_2\text{Si}_2$ ,  $\text{CeTIn}_5$ , and non-centrosymmetric  $\text{CePt}_3\text{Si}$  [98, 99, 100]. From earliest studies of magnetic pair breaking effects in rare earth elements by Matthias *et al.*[101] cerium is known to act as a strongly pair breaking impurity in a superconducting matrix.

A prominent system among intermetallics showing interplay of magnetism and superconductivity is the quaternary borocarbide,  $R\text{Ni}_2\text{B}_2\text{C}$  ( $R$  = rare earths and Y), with relatively high  $T_c$  (up to 16 K, see e.g. Refs. [34, 60]). In the corresponding solid solution with cerium,  $\text{Y}_{1-x}\text{Ce}_x\text{Ni}_2\text{B}_2\text{C}$ , a complete suppression of superconductivity was observed at  $x \geq 0.25$  [102]. Studies of structural and magnetic features of  $\text{CeNi}_2\text{B}_2\text{C}$  revealed intermediate valence of Ce and absence of superconductivity down to 2 K [53, 103]. Interestingly, El-Massalami *et al.* [104] reported conventional BCS type superconductivity for  $\text{CeNi}_2\text{B}_2\text{C}$  at temperatures below  $T_c \simeq 100$  mK. The related quaternary boronitride,  $\text{La}_3\text{Ni}_2\text{B}_2\text{N}_{3-\delta}$ , with rocksalt type triple LaN layer sheets in be-

tween the NiB layers shows superconductivity with  $T_c \sim 12\text{--}15\text{ K}$  [40, 46, 105]. A cerium based homologue,  $\text{Ce}_3\text{Ni}_2\text{B}_2\text{N}_{3-\delta}$ , was synthesized as powder material via a metathesis reaction by Glaser *et al.* [106]. Magnetic susceptibility measurements down to 5 K revealed neither superconductivity nor magnetic ordering [106].

The following chapter presents an investigation of the ground state properties of bulk metallic samples of  $(\text{La,Ce})_3\text{Ni}_2\text{B}_2\text{N}_{3-\delta}$  by means of x-ray diffraction, susceptibility, specific heat and transport measurements.

## 6.2 Sample preparation

For preparing bulk  $\text{La}_{3-x}\text{Ce}_x\text{Ni}_2\text{B}_2\text{N}_{3-\delta}$  samples the following starting materials, La ingot (Metall Rare Earth, 99.9%), Ce ingot (Metall Rare Earth, 99.9%) additionally purified by pre-melting in vacuum, Ni (Alpha Aesar, 99.99%), crystalline natural boron (HCTS, 99.5%) and nitrogen gas (Linde, 99.999%) are used. For selected  $\text{Ce}_3\text{Ni}_2\text{B}_2\text{N}_{3-\delta}$  samples Ames MPC high purity Ce was used.

For preparing  $\text{La}_{3-x}\text{Ce}_x\text{Ni}_2\text{B}_2\text{N}_{3-\delta}$  solid solution stoichiometric amounts of La and Ce was melted to get a starting rare-earth alloy. The rest of the preparation process and thermal treatment is similar as described in sections 3.2 and 3.3 for  $\text{La}_3\text{Ni}_2\text{B}_2\text{N}_{3-\delta}$ . The annealing temperature before quenching was 1130 °C for all samples.

## 6.3 Structural Characterization

The structure and phase purity of selected samples is analyzed by means of X-ray powder diffraction studies at room temperature with  $\text{Cu-K}\alpha$  radiation. Data is collected at room temperature for a range  $20^\circ < 2\theta < 120^\circ$  with steps of  $0.02^\circ$  on powders which are ground and sieved to a particle size of less than  $32\mu\text{m}$ . The XRD pattern refinement is performed on the basis of  $\text{La}_3\text{Ni}_2\text{B}_2\text{N}_3$  structure type using FULLPROF software and the parameter refined are scale factor, zero shift, shape profile, half width atomic and thermal parameters and lattice constants. The total number of reflections of  $\text{La}_3\text{Ni}_2\text{B}_2\text{N}_3$  measured in the X-ray diffraction are 85 with  $\sim 30$  having reasonable intensity relevant for refinement.

Powder XRD data of all samples of the series  $\text{La}_{3-x}\text{Ce}_x\text{Ni}_2\text{B}_2\text{N}_{3-\delta}$  display the body centered tetragonal  $\text{La}_3\text{Ni}_2\text{B}_2\text{N}_3$ -type structure with space group  $I4/mmm$ . Except for  $\text{Ce}_3\text{Ni}_2\text{B}_2\text{N}_{3-\delta}$ , some minor admixtures of the related

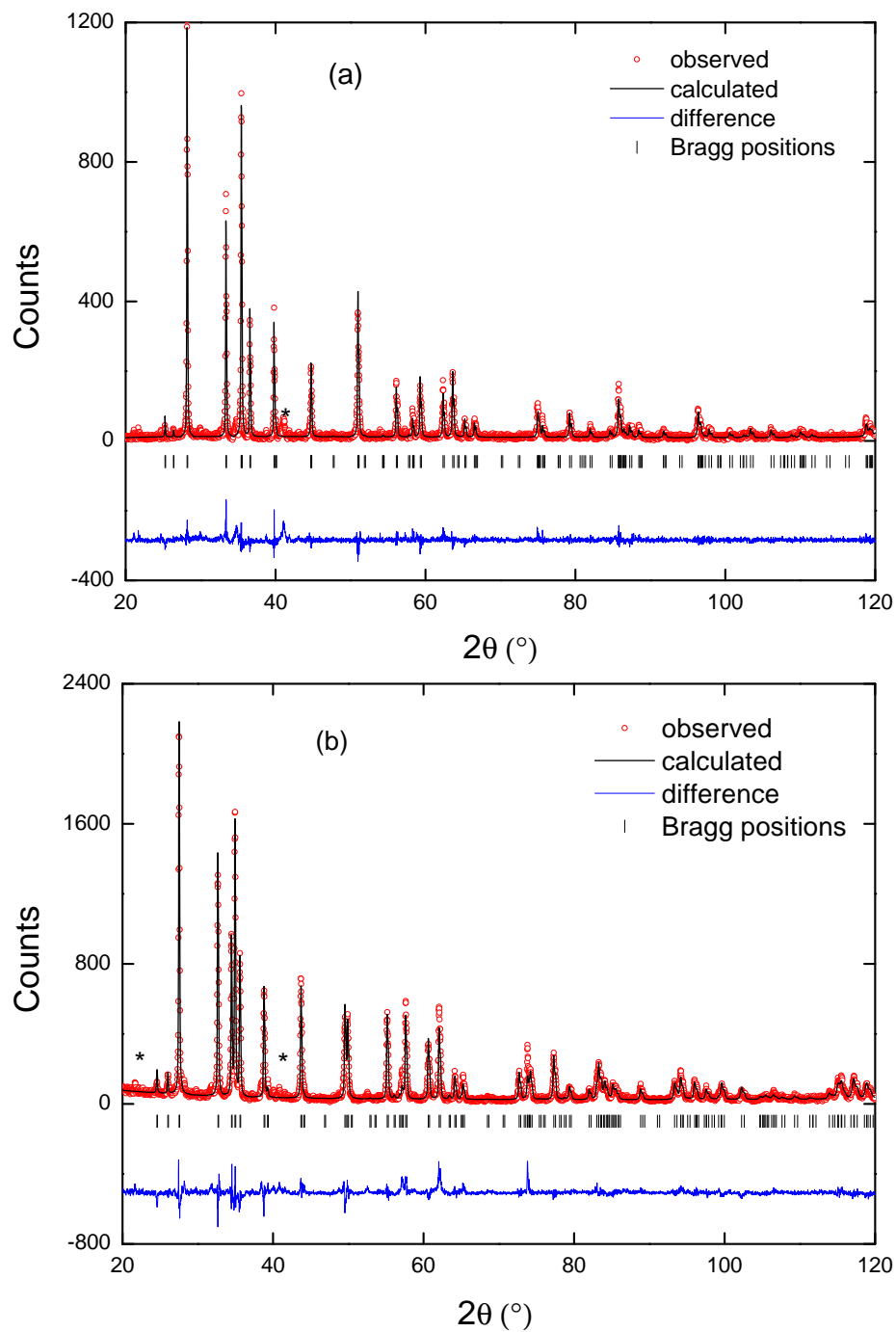


Figure 6.1: Measured room temperature XRD pattern of  $\text{LaCe}_2\text{Ni}_2\text{B}_2\text{N}_{3-\delta}$  (a) and  $\text{Ce}_3\text{Ni}_2\text{B}_2\text{N}_{3-\delta}$  (b). The solid lines are from Rietveld refinements. The strongest impurity line is marked by an asterisk.

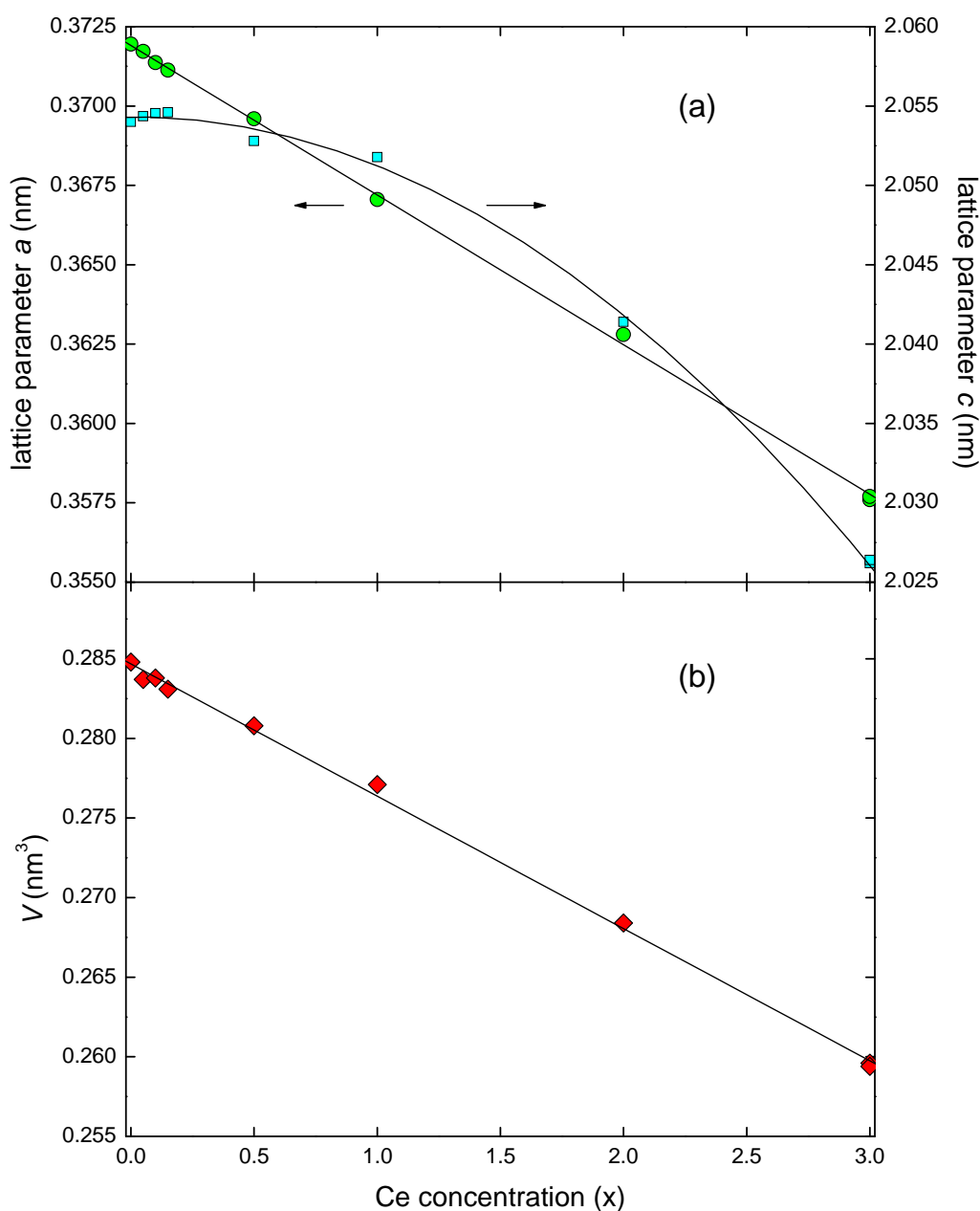


Figure 6.2: Variation of the lattice parameters  $a$  (circles) and  $c$  (squares) in (a) and unit cell volume (b) in the solid solution  $\text{La}_{3-x}\text{Ce}_x\text{Ni}_2\text{B}_2\text{N}_{2.7}$ ; lines are guides to the eye.

two-layer boronitride (La,Ce)NiBN are identified with phase fractions of up to 5%. In the case of  $\text{Ce}_3\text{Ni}_2\text{B}_2\text{N}_{3-\delta}$  traces of an unidentified impurity phase are observed for both samples, one prepared with cerium produced by Metall Rare Earth and one prepared with highest purity cerium prepared by Ames MPC, but the two-layer phase CeNiBN is not observed. Two exemplary

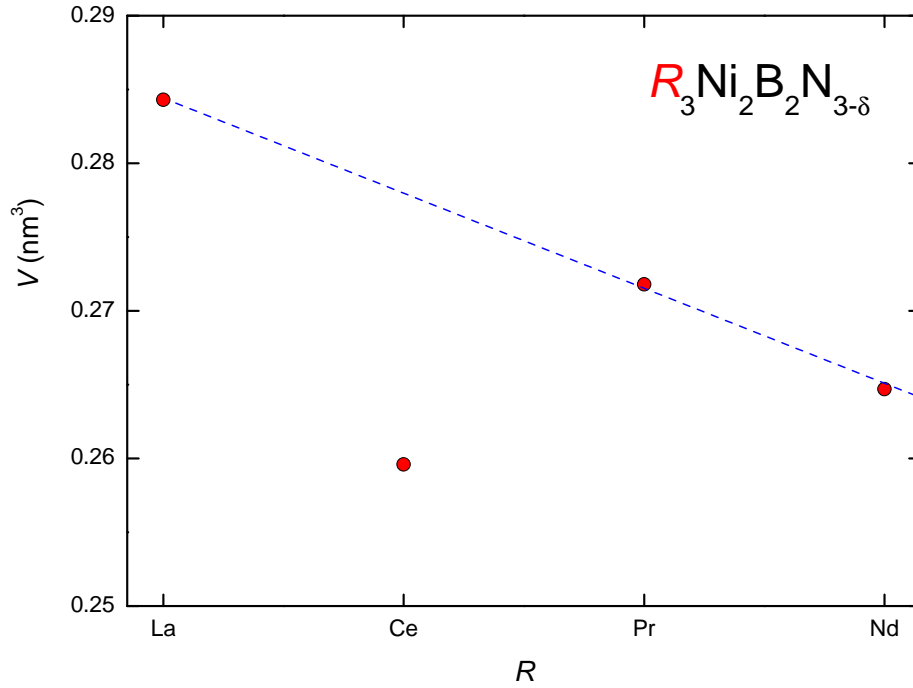


Figure 6.3: Variation of the lattice volume of  $R_3\text{Ni}_2\text{B}_2\text{N}_{3-\delta}$ ; dashed line is a guide to eye.

powder XRD patterns of  $\text{La}_{3-x}\text{Ce}_x\text{Ni}_2\text{B}_2\text{N}_{3-\delta}$  and their Rietveld refinements are shown in Fig. 6.1 while some more patterns are given in appendix A.

The variation of the lattice parameters  $a$  and  $c$  in the solid solution  $\text{La}_{3-x}\text{Ce}_x\text{Ni}_2\text{B}_2\text{N}_{3-\delta}$  is summarized in Fig. 6.2. The lattice parameters  $a$  and  $c$  obtained for  $\text{Ce}_3\text{Ni}_2\text{B}_2\text{N}_{3-\delta}$  are 0.357 nm and 2.025 nm, respectively. These values are in good agreement with the lattice parameters reported earlier [106]. The reduction of the unit cell volume of  $\text{Ce}_3\text{Ni}_2\text{B}_2\text{N}_{3-\delta}$  as compared to  $\text{La}_3\text{Ni}_2\text{B}_2\text{N}_{3-\delta}$  is about 9%. As expected from the lanthanide contraction, the  $a$  lattice parameter decreases with increasing Ce-fraction, however, the  $c$  lattice parameter shows a non-monotonic variation with a maximum at about  $x = 0.2$ . An even opposite trend for the variation of the  $a$  and  $c$  lattice parameters was reported for the related quaternary borocarbides [53] which has been attributed to rather stiff Ni-B and B-C bonds leading to an increase in B-Ni-B tetrahedral angle and thus to a stretching of the tetragonal  $c$ -axis when the basal plane lattice constant  $a$  contracts. The lanthanide contraction in  $\text{La}_{3-x}\text{Ce}_x\text{Ni}_2\text{B}_2\text{N}_{3-\delta}$  causes a similar effect on the NiB layers and their tetrahedral bonding angle which changes from  $\sim 106^\circ$  for  $\text{La}_3\text{Ni}_2\text{B}_2\text{N}_{3-\delta}$  to  $\sim 104^\circ$  for  $\text{Ce}_3\text{Ni}_2\text{B}_2\text{N}_{3-\delta}$ , however, in this case with an additional change in the width (parallel to the  $c$ -axis) of the (La,Ce)N triple layers, thus, causing the non monotonic variation of the  $c$  lattice parameter shown in Fig. 6.2. We note, that the change of the unit cell volume by about 9% in the series

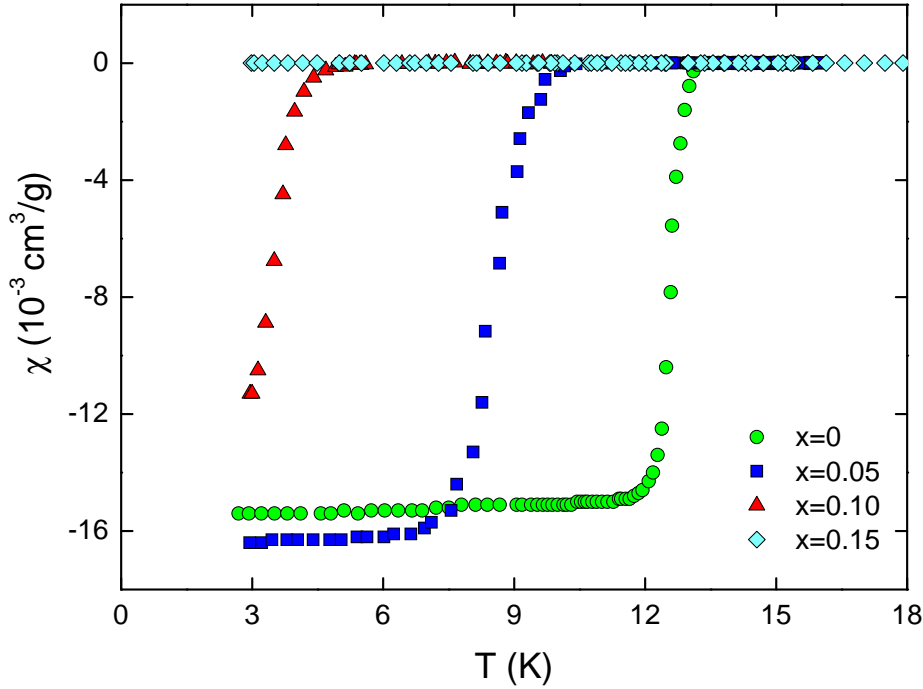


Figure 6.4: Temperature dependent susceptibility for  $\text{La}_{3-x}\text{Ce}_x\text{Ni}_2\text{B}_2\text{N}_{3-\delta}$  measured at 1 mT (ZFC) with  $x$  as labeled.

$(\text{La,Ce})_3\text{Ni}_2\text{B}_2\text{N}_{3-\delta}$  is two orders of magnitude larger than the volume changes caused by varying the nominal nitrogen stoichiometry in  $\text{La}_3\text{Ni}_2\text{B}_2\text{N}_x$  [105] and also larger than expected from the lanthanide contraction among  $R^{3+}$  ions (see figure 6.3), thus, pointing towards a intermediate valance of Ce.

## 6.4 Superconductivity in $\text{La}_{3-x}\text{Ce}_x\text{Ni}_2\text{B}_2\text{N}_{3-\delta}$

The superconducting transition temperatures of  $\text{La}_{3-x}\text{Ce}_x\text{Ni}_2\text{B}_2\text{N}_{3-\delta}$  with  $x = 0, 0.05$  and  $0.1$  were determined from dc susceptibility measurements (see Fig. 6.4) which were performed after zero field cooling (ZFC) at a field of 1 mT. Field-cooled susceptibility (not shown for the sake of clarity in Fig. 6.4) reveal Meissner fractions of about 10% due to strong pinning effects. The latter was discussed in detail in Ref. [41].

The susceptibility data reveal an almost linear reduction of  $T_c$  with increasing Ce fraction at a rate of  $dT_c/dx \simeq -8.9 \text{ K/Ce}\%$  in the formula  $\text{La}_3\text{Ni}_2\text{B}_2\text{N}_{3-\delta}$  and a corresponding critical concentration for the suppression of superconductivity of 1.3% Ce in the full formula with 10 atoms. The related light rare earth solid solutions  $\text{La}_{3-x}R_x\text{Ni}_2\text{B}_2\text{N}_{3-\delta}$  with  $R = \text{Pr}$  and  $\text{Nd}$  exhibit one order of magnitude larger critical concentrations of 19% and 10%, respectively (see chapter 7). The larger suppression rate observed for Ce which is also well

known for elemental La [101] is due to valance fluctuations and/or Kondo effects. Interestingly, although parent boronitride and borocarbide compounds,  $\text{La}_3\text{Ni}_2\text{B}_2\text{N}_{3-\delta}$  and  $\text{YNi}_2\text{B}_2\text{C}$ , exhibit similar values of  $T_c \simeq 13$  and 15 K, and similar upper critical fields  $H_{c2}(0) \sim 5-8$  T, [33] the rate of suppression of  $T_c$  by Ce-substitution in the boronitride system is significantly larger than the corresponding value of  $-2.5$  K/Ce% reported by Alleno *et al.* [102] for the related borocarbide system  $\text{Y}_{1-x}\text{Ce}_x\text{Ni}_2\text{B}_2\text{C}$ .

## 6.5 Ground state properties of $\text{Ce}_3\text{Ni}_2\text{B}_2\text{N}_{3-\delta}$

### 6.5.1 Results of thermodynamic and transport studies

The ground state properties of  $\text{Ce}_3\text{Ni}_2\text{B}_2\text{N}_{3-\delta}$  were studied by means of specific heat, magnetic susceptibility, resistivity and thermoelectric power measurements. The normal state properties of  $\text{La}_3\text{Ni}_2\text{B}_2\text{N}_{3-\delta}$  with an empty  $4f$  shell are used as a reference for non- $4f$  contributions. The specific heat of  $\text{Ce}_3\text{Ni}_2\text{B}_2\text{N}_{3-\delta}$  measured at zero external field and the normal state specific heat of  $\text{La}_3\text{Ni}_2\text{B}_2\text{N}_{3-\delta}$  measured at 9 T are shown in Fig. 6.5 as  $C_p/T$  vs.  $T$ . The low temperature electronic and lattice contributions of a plain metal are given by  $C_p = C_e + C_{ph} \simeq \gamma + \beta T^3$  where  $\gamma$  is the Sommerfeld value and  $\beta$  is related to the low-temperature Debye temperature,  $\Theta_D^{LT} = (1944 \times n/\beta)^{1/3}$  where  $n = 10$  is number of atoms per formula unit. From the low temperature fit of the  $\text{Ce}_3\text{Ni}_2\text{B}_2\text{N}_{3-\delta}$  data (see inset in Fig. 6.5) we obtain  $\gamma \simeq 54$  mJ/molK<sup>2</sup> and  $\beta \simeq 0.36$  mJ/molK<sup>4</sup> corresponding to  $\Theta_D^{LT} = 378$  K. The later, however, might be misleading because the  $C \propto \beta T^3$  lattice term is superimposed by magnetic contributions from Ce  $4f$  orbitals. In the case of  $\text{La}_3\text{Ni}_2\text{B}_2\text{N}_{3-\delta}$  the low temperature data yield  $\gamma \simeq 26$  mJ/molK<sup>2</sup> and  $\Theta_D^{LT} \simeq 329$  K (see chapter 5). The enhanced electronic contribution to the specific heat of  $\text{Ce}_3\text{Ni}_2\text{B}_2\text{N}_{3-\delta}$  as compared to  $\text{La}_3\text{Ni}_2\text{B}_2\text{N}_{3-\delta}$ , i.e.  $\Delta\gamma \simeq 28$  mJ/K<sup>2</sup>mol, is attributed to magnetic contributions of Ce- $4f$  in the intermediate valent regime. Dc magnetic susceptibilities of  $\text{Ce}_3\text{Ni}_2\text{B}_2\text{N}_{3-\delta}$  and  $\text{La}_3\text{Ni}_2\text{B}_2\text{N}_{3-\delta}$  were measured from 3 K to room temperature (RT) and from RT to 1000 K at applied fields of 1 T and 9 T, respectively (see Fig. 6.6 a). While  $\text{La}_3\text{Ni}_2\text{B}_2\text{N}_{3-\delta}$  displays (above its  $T_c$ ) a simple, weakly temperature dependent Pauli paramagnetism with a low temperature susceptibility,  $\chi_0 \simeq 0.2 \times 10^{-3}$  emu/mol,  $\text{Ce}_3\text{Ni}_2\text{B}_2\text{N}_{3-\delta}$  exhibits an about one order of magnitude larger susceptibility with a maximum at about 800 K. For both compounds, a small additional Curie-Weiss component is observed at low temperatures and a corresponding fit of the data from 10 to 200 K in terms of a temperature independent component  $\chi_0$  plus a Curie-Weiss term  $\chi = \chi_0 + C/(T - \Theta_p)$  where  $C$  is a Curie constant and  $\Theta_p$  a paramagnetic Curie temperature yields for  $\text{Ce}_3\text{Ni}_2\text{B}_2\text{N}_{3-\delta}$  a  $\chi_0 \simeq 1.6 \times 10^{-3}$  emu/mol and

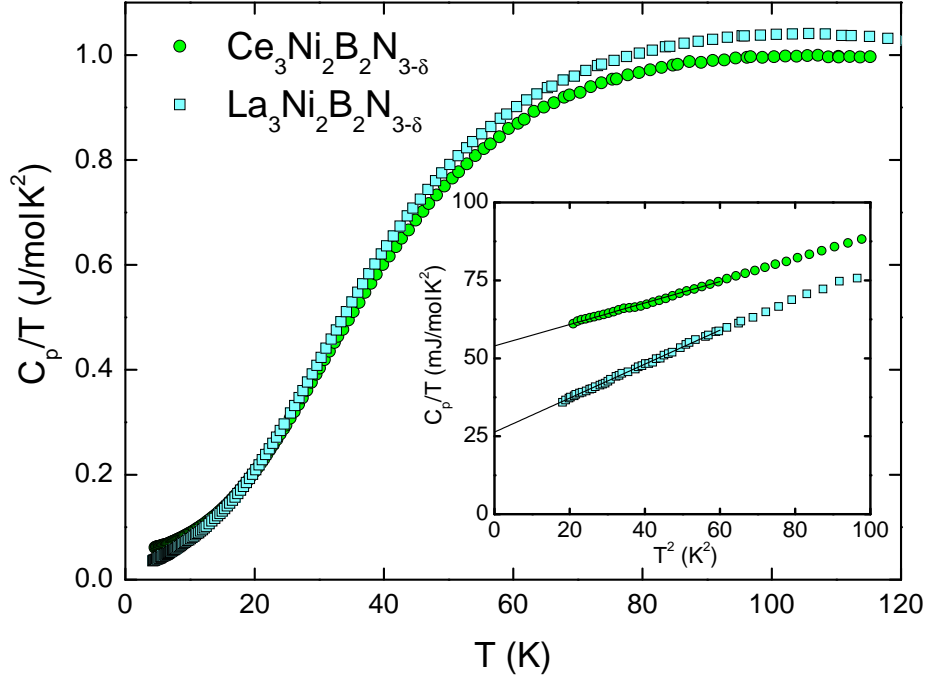


Figure 6.5: Specific heat of  $\text{Ce}_3\text{Ni}_2\text{B}_2\text{N}_{3-\delta}$  (0 T) and  $\text{La}_3\text{Ni}_2\text{B}_2\text{N}_{3-\delta}$  (9 T) at selected temperatures; inset:  $C/T$  vs.  $T^2$  graph of the low temperature part with solid lines indicating  $C/T = \gamma + \beta T^2$  linear fits.

$C \simeq 9 \times 10^{-3}$  emu K/mol. In case of  $\text{La}_3\text{Ni}_2\text{B}_2\text{N}_{3-\delta}$  the fit of the low temperature magnetic susceptibility data gives  $\chi_0 \simeq 0.2 \times 10^{-3}$  emu/mol and  $C \simeq 4 \times 10^{-3}$  emu K/mol. The paramagnetic Curie temperature for both the samples is of the order of  $-10$  K. The Curie-Weiss like contribution in  $\text{Ce}_3\text{Ni}_2\text{B}_2\text{N}_{3-\delta}$  is attributed to paramagnetic impurities (e.g. Gd traces of the order of 100 ppm in the La and Ce raw elements) and seems to be not an intrinsic property. The values of  $\chi_0$  and  $C$  obtained for  $\text{La}_3\text{Ni}_2\text{B}_2\text{N}_{3-\delta}$  are close to values reported earlier [61]. The moderately temperature dependent, but nevertheless largely enhanced susceptibility of  $\text{Ce}_3\text{Ni}_2\text{B}_2\text{N}_{3-\delta}$  is attributed to  $f$ -electron contributions from intermediate valent Ce ions with strongly Kondo screened Ce  $4f$  moments. In order to obtain a measure for the  $4f$  occupation from the susceptibility data an approach proposed by Wohleben and Röhler [107] (see also Ref. [108]). Comparing the  $\text{Ce}_3\text{Ni}_2\text{B}_2\text{N}_{3-\delta}$   $4f$  susceptibility (obtained by subtracting the  $\text{La}_3\text{Ni}_2\text{B}_2\text{N}_{3-\delta}$  data) with the theoretical susceptibility of  $\text{Ce}^{3+}$  ions ( $4f^1$  configuration with a ground state total angular momentum  $J = 5/2$  and excited state  $J = 7/2$  separated by a spin-orbit splitting  $\Delta \simeq 3150$  K, see e.g. Ref. [109]) in a  $\chi T$  versus  $T$  plot in Fig. 6.6 b suggests a  $4f$  occupation clearly larger than 0.7.  $\chi T(1000 \text{ K}) \simeq 0.63$  emu K/mol-Ce compares with  $\text{CePd}_3$  and  $\text{CeRh}_3$  with valences near 3.2+ obtained from  $L_{\text{III}}$  x-ray absorption studies [107]. Thus, a



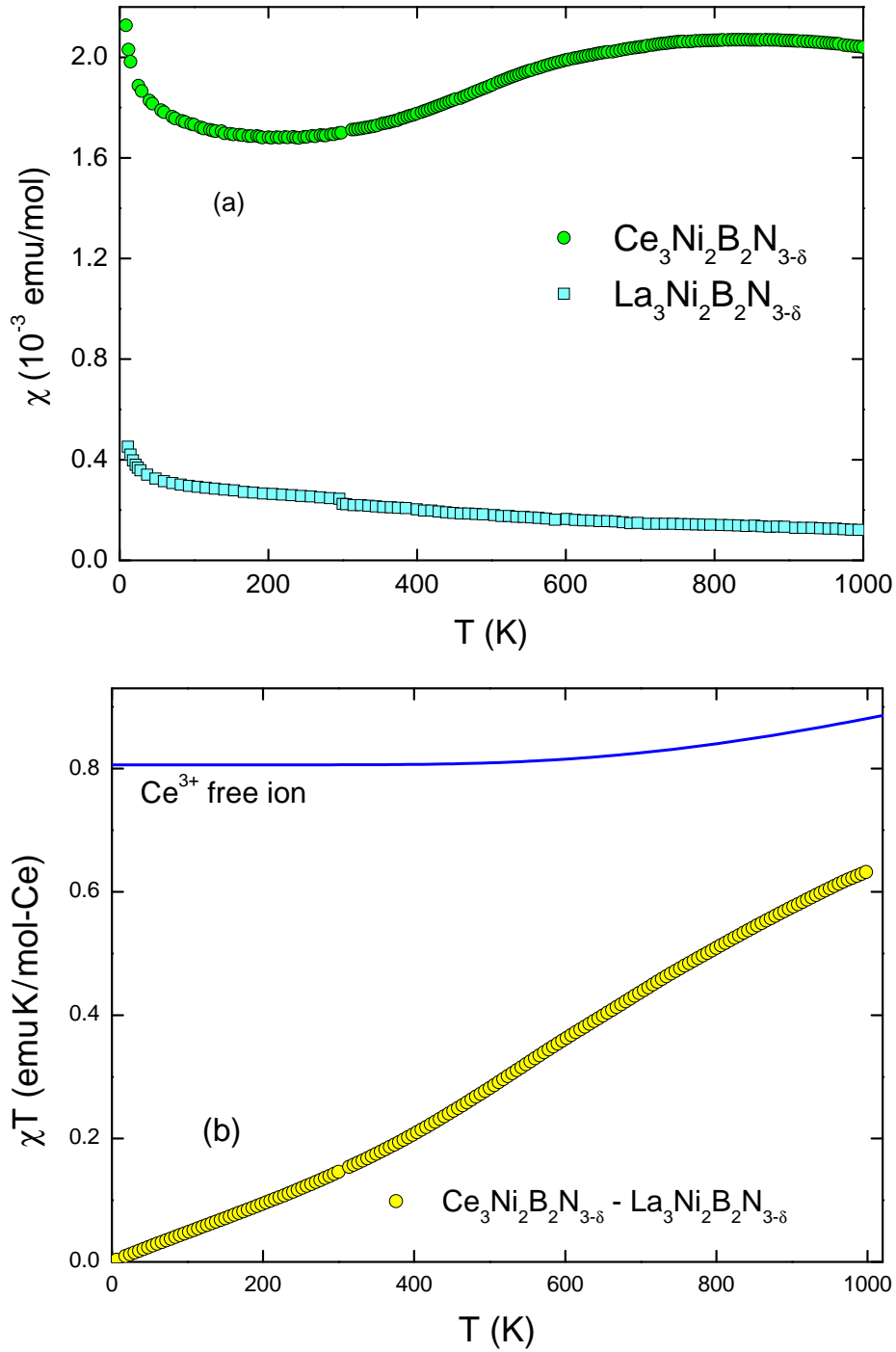


Figure 6.6: Temperature dependent susceptibility of  $\text{Ce}_3\text{Ni}_2\text{B}_2\text{N}_{3-\delta}$  and  $\text{La}_3\text{Ni}_2\text{B}_2\text{N}_{3-\delta}$  measured at applied fields of 1 T below 300 K and at 9 T above (a). Product of the Ce-4*f* magnetic susceptibility with temperature,  $\chi T$ , versus temperature (b); the solid line indicates the theoretical product  $\chi T$  of free  $\text{Ce}^{3+}$  ions.

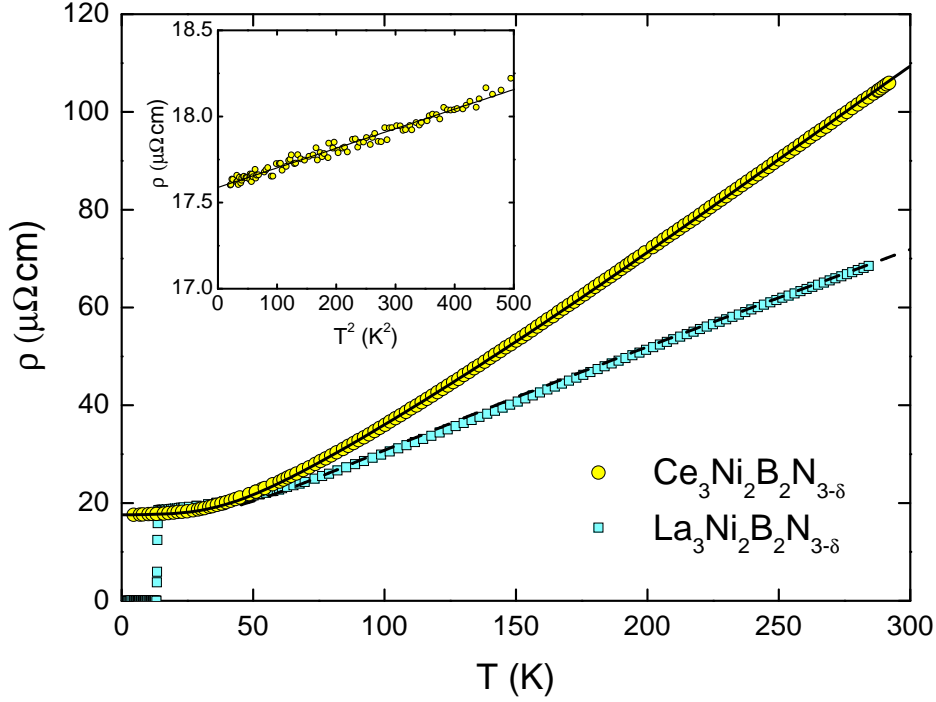


Figure 6.7: The electrical resistivity  $\rho(T)$  of  $\text{Ce}_3\text{Ni}_2\text{B}_2\text{N}_{3-\delta}$  and  $\text{La}_3\text{Ni}_2\text{B}_2\text{N}_{3-\delta}$ . The solid line indicates a fit according to the ALM and the dashed line shows the normal metal  $\rho_0 + \rho_{\text{BG}}$  contribution included in this fit; inset:  $\rho$  vs.  $T^2$  graph of the  $\text{Ce}_3\text{Ni}_2\text{B}_2\text{N}_{3-\delta}$  data.

realistic estimate for the  $4f$  occupation of  $\text{Ce}_3\text{Ni}_2\text{B}_2\text{N}_{3-\delta}$  is near 0.8.

The  $4f$  contribution to the low temperature susceptibility  $\Delta\chi(0) \simeq 1.4 \times 10^{-3} \text{emu/mol}$  and the Sommerfeld value  $\Delta\gamma \simeq 28 \text{mJ/K}^2\text{mol}$  is analyzed in terms of the Fermi-liquid relation (see e.g. Ref. [110]),

$$Rg_J^2 J(J+1)\mu_B^2 \Delta\gamma = \pi^2 k_B^2 \Delta\chi \quad (6.1)$$

yielding with  $J = 5/2$  an experimental value of the Wilson ratio,  $R \simeq 1.8$  which is slightly larger than the value expected for a degenerate  $\text{Ce}^{\sim 3.2+}$  state [111, 112],  $R = N/[N - 1 + (n_f - 1)^2] \simeq 1.19$  for a degeneracy  $N = 6$  and  $n_f \simeq 0.8$ .

The temperature dependent electrical resistivity,  $\rho(T)$ , of  $\text{La}_3\text{Ni}_2\text{B}_2\text{N}_{3-\delta}$  and  $\text{Ce}_3\text{Ni}_2\text{B}_2\text{N}_{3-\delta}$  is shown in Fig. 6.7. Except for small variations of the residual resistivities, absolute values of  $\rho(T)$  obtained in this study have been well reproduced with several samples of  $\text{La}_3\text{Ni}_2\text{B}_2\text{N}_{3-\delta}$  [105] and  $\text{Ce}_3\text{Ni}_2\text{B}_2\text{N}_{3-\delta}$ . The superconducting  $\text{La}_3\text{Ni}_2\text{B}_2\text{N}_{3-\delta}$  has a  $T_c^\rho \simeq 12.5 \text{K}$  while  $\text{Ce}_3\text{Ni}_2\text{B}_2\text{N}_{3-\delta}$  remains in the normal state at least down to the base temperature of the experiment, i.e. 0.35 K. At temperatures below 30 K, the  $\rho(T)$  vs.  $T^2$  graph of the experimental data shown as inset in Fig. 3 reveals a quadratic

temperature dependence  $\rho(T) = \rho_0 + AT^2$ , with  $A \simeq 1.2 \times 10^{-9} \Omega \text{ cm}/\text{K}^2$ . This coefficient  $A$  yields a Kadowaki-Woods ratio  $A/\gamma^2 \simeq 4 \times 10^{-6} \mu\Omega \text{ cm}(\text{Kmol-Ce}/\text{mJ})^2$  which is in between the typical Kadowaki-Woods ratio  $A/\gamma^2 \sim 10^{-5} \mu\Omega \text{ cm}(\text{Kmol-Ce}/\text{mJ})^2$  of (mostly twofold degenerate) cerium Kondo-lattice systems and the expected generalized Kadowaki-Woods ratio of Kondo lattice systems with sixfold degenerate Ce-4*f* moments [113] yielding  $A/\gamma^2 \sim 0.7 \times 10^{-6} \mu\Omega \text{ cm}(\text{molK}/\text{mJ})^2$ .

The value of the coefficient  $A$  together with the Sommerfeld coefficient of the electronic specific heat, is indicative of Kondo interaction in  $\text{Ce}_3\text{Ni}_2\text{B}_2\text{N}_{3-\delta}$  with a relatively high Kondo temperature as compared to typical crystal field splittings of the  $J = 5/2$  multiplet of the Ce 4*f*<sup>1</sup> state. Accordingly, numerical results of a sixfold degenerate Anderson lattice model (ALM) without Ce-Ce intersite coupling compiled by Cox and Grewe [114] are used to analyze the resistivity and thermoelectric power [ALM model provides  $S(T > 0.2T_K^{\text{ALM}})$ , see below] of  $\text{Ce}_3\text{Ni}_2\text{B}_2\text{N}_{3-\delta}$ . In the simple fully degenerate case, i.e. for strong Kondo coupling as compared to the crystal field splitting, the ALM yields a universal temperature dependency for the magnetic contribution to the resistivity and also the thermoelectric power, which simply scale with the Kondo temperature  $T_K^{\text{ALM}}$ .

To analyze the temperature dependent resistivity data of  $\text{Ce}_3\text{Ni}_2\text{B}_2\text{N}_{3-\delta}$  a magnetic contribution according to the numerical ALM results,  $\rho_{\text{ALM}}(T/T_K^{\text{ALM}})$  is combined with a Bloch-Grüneisen model for the normal metal phonon contribution yielding

$$\begin{aligned} \rho(T) = & \rho_0 + \alpha \cdot \rho_{\text{ALM}}(T/T_K^{\text{ALM}}) + \\ & + \frac{4B}{\Theta_D} \left( \frac{T}{\Theta_D} \right)^5 \int_0^{\Theta_D/T} \frac{z^5 dz}{(e^z - 1)(1 - e^{-z})}. \end{aligned} \quad (6.2)$$

A reasonable set of parameters (further corroborated by the analysis of the thermoelectric power discussed below) is:  $\rho_0 = 17.6 \mu\Omega \text{ cm}$  [essentially fixed by  $\rho(T \rightarrow 0)$  data],  $\alpha = 89.6 \mu\Omega \text{ cm}$  and  $T_K^{\text{ALM}} = 1100 \text{ K}$  (characteristic Kondo temperature of the ALM model), the electron-phonon coupling constant  $B = 0.013 \Omega \text{ cmK}$  and Debye-temperature  $\Theta_D = 262 \text{ K}$  of the Bloch-Grüneisen model. The resulting fit is indicated as solid line in Fig. 6.7. The resulting normal metal contribution, i.e. residual resistivity  $\rho_0$  plus phonon contribution according to the Bloch-Grüneisen fit, is in remarkably close agreement with the resistivity data of  $\text{La}_3\text{Ni}_2\text{B}_2\text{N}_{3-\delta}$  (in absolute values).

The temperature dependent thermopower,  $S(T)$ , of  $\text{La}_3\text{Ni}_2\text{B}_2\text{N}_{3-\delta}$  and  $\text{Ce}_3\text{Ni}_2\text{B}_2\text{N}_{3-\delta}$  is shown in Fig. 6.8b. For  $\text{La}_3\text{Ni}_2\text{B}_2\text{N}_{3-\delta}$ ,  $S(T)$  is negative above  $T_c$  indicating a positive slope of the electronic density of states near the Fermi level. The mismatch between  $T < 300 \text{ K}$  and  $T > 300 \text{ K}$  data

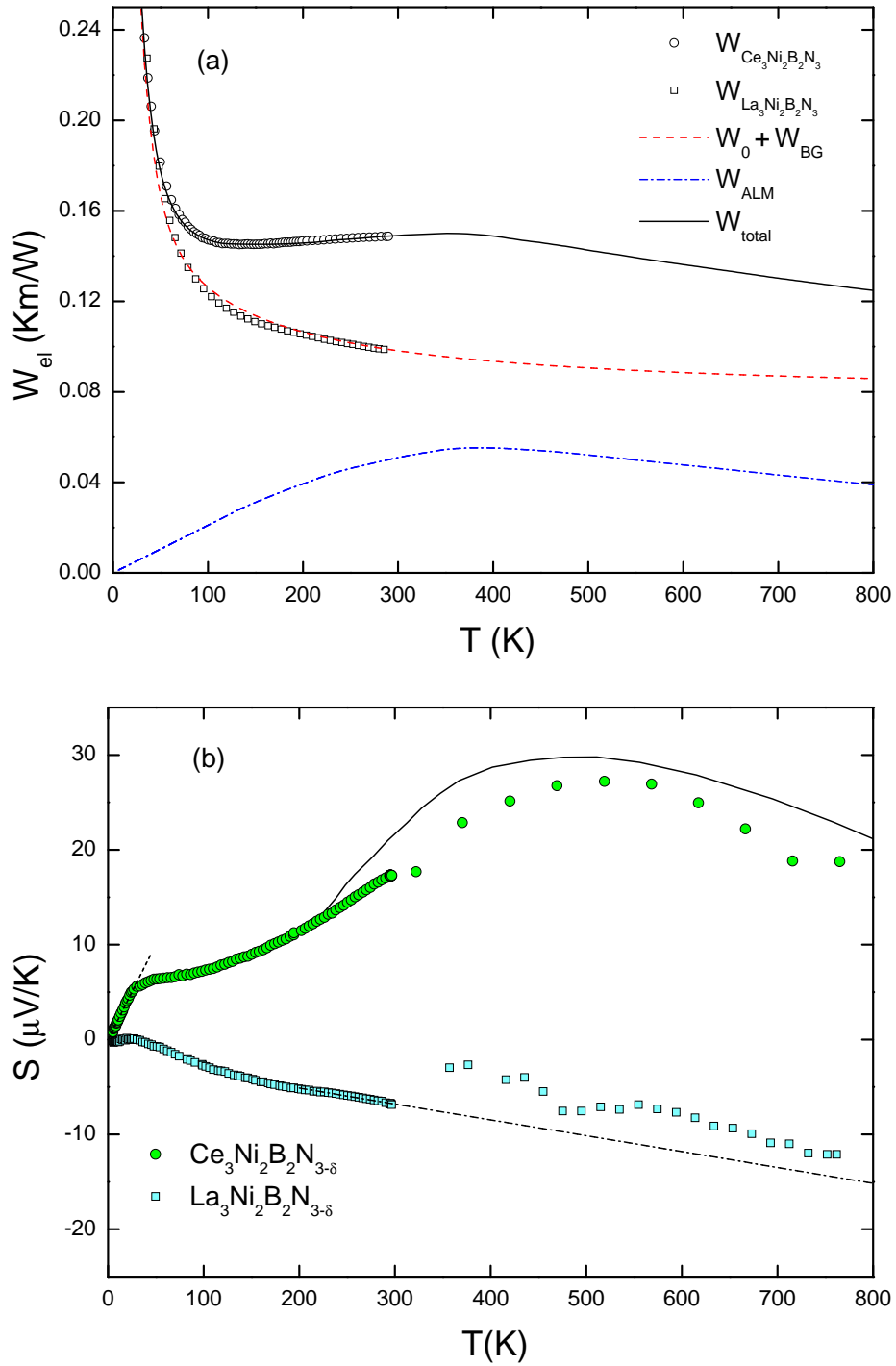


Figure 6.8: The electronic thermal resistance contributions estimated via the Wiedeman-Franz law from the electrical resistivity data and fitting by equation 2 (a). Temperature dependent thermopower of  $\text{Ce}_3\text{Ni}_2\text{B}_2\text{N}_{3-\delta}$  and  $\text{La}_3\text{Ni}_2\text{B}_2\text{N}_{3-\delta}$  (b); the solid line indicates the ALM fit (see text), dashed and dash-dotted lines are straight lines.

is an artifact of having used two different measuring techniques with imperfect overlap. The dashed-dotted line in Fig. 6.8b indicates a linear high temperature extrapolation of the  $T < 300$  K measurement corresponding to  $S(T) = a + bT$  with  $a = -16.7$  nV/K and  $b = -1.77$   $\mu\text{V}/\text{K}^2$ .

The TEP for  $\text{Ce}_3\text{Ni}_2\text{B}_2\text{N}_{3-\delta}$  exhibits a sharp linear increase at low temperature with an initial slope  $S/T \simeq 0.2\mu\text{V}/\text{K}$  and a broad Kondo maximum at high temperature with  $S_{\text{max}} \simeq 26\mu\text{V}/\text{K}$  at about 500 K. The latter is analyzed in terms of the ALM data by Cox and Grewe [114] using the characteristic Kondo temperature  $T_{\text{K}} = 1100$  K derived above. When comparing the TEP of  $\text{Ce}_3\text{Ni}_2\text{B}_2\text{N}_{3-\delta}$  with the *clean limit* ALM calculation for sixfold degenerate  $\text{Ce}^{3+}$  which yields a broad maximum  $S_{\text{max}} = 103\mu\text{V}/\text{K}$  at  $T/T_{\text{K}} \simeq 0.6$  (see Fig. 3 of Ref. [114]), it is necessary to consider in addition to Kondo scattering, at least, defect and phonon scattering. At elevated temperatures, an estimate for the total diffusion thermopower  $S_d$  due to different types of scattering mechanisms  $\alpha$ , e.g. electron-defect ( $S_{e,0}$ ), electron-electron ( $S_{e,e}$ ) or in the case of  $\text{Ce}_3\text{Ni}_2\text{B}_2\text{N}_{3-\delta}$  the Kondo contribution  $S_{\text{ALM}}$  according to the ALM) and electron-phonon ( $S_{ep}$ ) scattering, is obtained via the Kohler relation [115],

$$S_d = W^{-1} \sum_{\alpha} S_{d\alpha} W_{\alpha}, \quad (6.3)$$

with  $W$  being the electronic thermal resistance. The latter obeys the Matthiessen rule,  $W = \sum_{\alpha} W_{\alpha}$  where  $W_{\alpha}$  are the contributions due to particular scattering mechanisms  $\alpha$ . For simplicity of the analysis,  $W_{\alpha}$  is estimated via the Wiedeman-Franz law,  $W_{\alpha}(T) = \rho_{\alpha}(T)/L_{\alpha}T$ , assuming  $L_{e,0} \approx L_{ep} \approx L_{e,e} \approx L_0 = 2.44 \times 10^{-8} \text{W}\Omega/\text{K}^2$  ( $L_0$  is the Lorenz-number) where equation 3 conforms to the Norheim-Gorter rule. Accordingly, contributions  $W_{\text{ALM}}$ ,  $W_0 + W_{\text{BG}}$ , and the total electronic thermal resistance  $W_{\text{total}}$  corresponding to the above analysis of the resistivity data are displayed in Fig. 6.8a. An estimate for the contribution  $S_{e,0} + S_{ep}$  is obtained from the  $\text{La}_3\text{Ni}_2\text{B}_2\text{N}_{3-\delta}$  reference data (see the dashed-dotted line in Fig. 6.8b). The latter together with the Kondo contribution  $S_{\text{ALM}}$  are added according to the Kohler relation, thus yielding a total TEP based on the degenerate ALM with  $T_{\text{K}} = 1100$  K as indicated by the solid line in Fig.6.8b which is in reasonable agreement with the experimental data. In the low temperature limit, the Seebeck coefficient  $S$  and the Sommerfeld coefficient  $\gamma$  are related by [116]

$$\frac{S}{T} = q \frac{\gamma}{N_A e} \quad (6.4)$$

where  $N_A$  is Avogadro's number and  $q$  is a dimensionless quantity which is found to be close to unity for most of the Ce based compounds [116]. For  $\gamma \simeq 18$  mJ/K<sup>2</sup>mol-Ce, the fit of the low temperature part of thermopower data of  $\text{Ce}_3\text{Ni}_2\text{B}_2\text{N}_{3-\delta}$  (dashed line in Fig.6.8b) yields  $S/T \simeq 0.2\mu\text{V}/\text{K}^2$  revealing

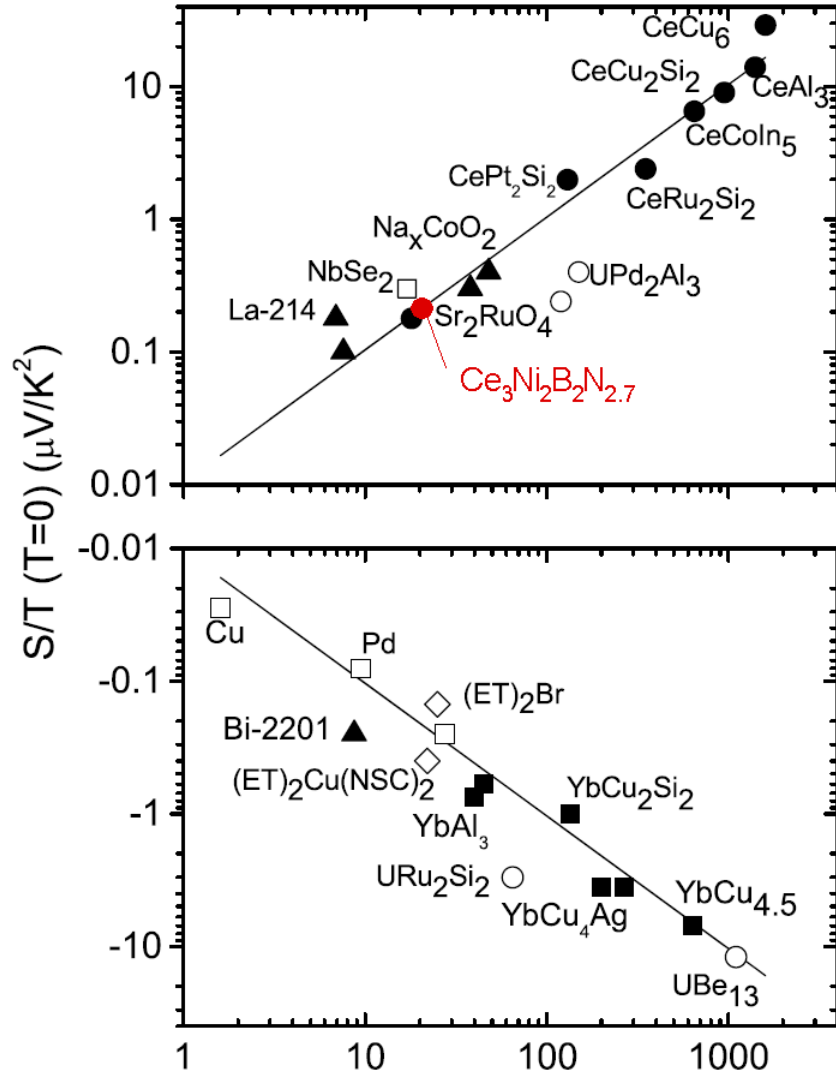


Figure 6.9:  $S/T$  versus  $\gamma$  as adopted from Ref. [116] where the two solid lines represent  $\pm\gamma/(eN_{Av})$ . Solid circles represent Ce based systems where  $\text{Ce}_3\text{Ni}_2\text{B}_2\text{N}_{2.7}$  has been added to the original graph.

$q \simeq 1$  which is well in line with the empirical trend observed for a large number of Ce based compounds compiled in Ref. [116] (see figure 6.9).

# Chapter 7

## Formation and ground state properties of $\text{La}_{3-x}\text{R}_x\text{Ni}_2\text{B}_2\text{N}_{3-\delta}$ with $R = \text{Pr}, \text{Nd}$

The following chapter presents a description of the preparation procedure of solid solutions  $\text{La}_{3-x}\text{R}_x\text{Ni}_2\text{B}_2\text{N}_{3-\delta}$  as well as the novel compounds  $\text{Pr}_3\text{Ni}_2\text{B}_2\text{N}_{3-\delta}$  and  $\text{Nd}_x\text{Ni}_2\text{B}_2\text{N}_{3-\delta}$ . The structural characterization is carried out by means of X-ray diffraction while ground state properties are investigated by magnetic susceptibility, resistivity and specific heat measurements.

### 7.1 Sample preparation

For  $\text{La}_{3-x}\text{R}_x\text{Ni}_2\text{B}_2\text{N}_{3-\delta}$  samples (with  $R = \text{Pr}, \text{Nd}$ ) the following starting materials, La ingot (Metall Rare Earth, 99.9%), Nd ingot (Strem Chemicals 99.9%), Pr ingot (Strem Chemicals 99.9%), additionally purified by pre-melting in vacuum, Ni (Alpha Aesar, 99.99%), crystalline natural boron (HCTS, 99.5%) and nitrogen gas (Linde, 99.999%) were used.

For preparing  $\text{La}_{3-x}\text{R}_x\text{Ni}_2\text{B}_2\text{N}_{3-\delta}$  solid solutions a three step melting process similar to the one described in section 3.2 was adopted. For pure  $\text{Pr}_3\text{Ni}_2\text{B}_2\text{N}_{3-\delta}$  samples an approximately 2-5% excess to the stoichiometric amount of Pr is added to compensate for the excessive losses because of the high vapour pressure of Pr. The process of preparing  $\text{Nd}_3\text{Ni}_2\text{B}_2\text{N}_{3-\delta}$  is the same as for other quaternary boronitride compounds in this work. The only difference is that under Ar/N atmosphere the melting temperature of the  $\text{Nd}_3\text{Ni}_2\text{B}_2\text{N}_x$  alloy becomes too high and it becomes impossible to melt it with the available facility. To prepare  $\text{Nd}_3\text{Ni}_2\text{B}_2\text{N}_{3-\delta}$  a technique of glowing the material in Ar/N<sub>2</sub> is adopted with multiple cycles such that the N-stoichiometry is slowly increased to reach a composition close to the stoichiometric one. Thereby,  $\text{Nd}_3\text{Ni}_2\text{B}_2$  is glowed at the full power of Hüttinger

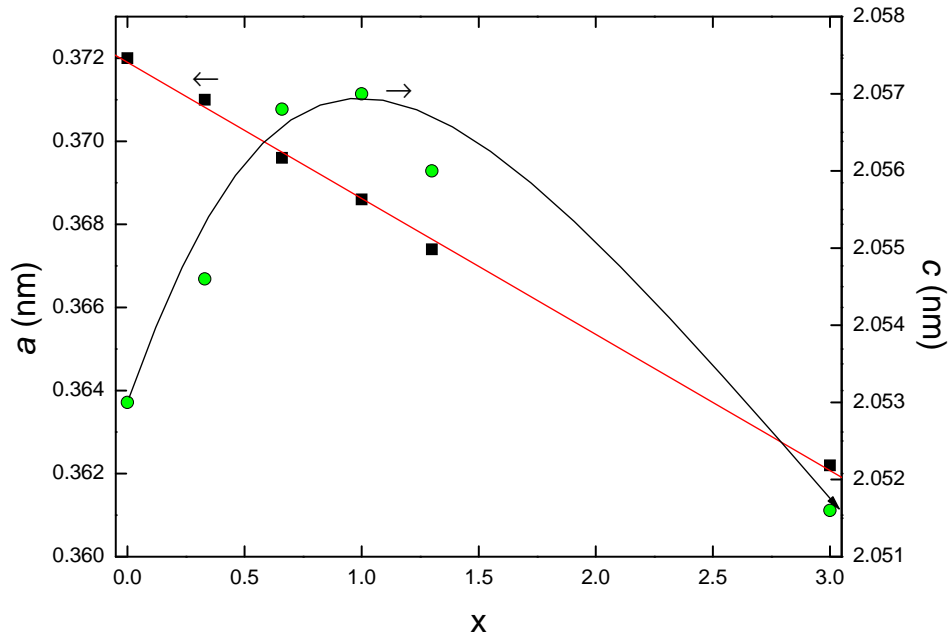


Figure 7.1: Variation of the lattice parameters  $a$  (squares) and  $c$  (circles) in the solid solution  $\text{La}_{3-x}\text{Pr}_x\text{Ni}_2\text{B}_2\text{N}_{2.7}$ ; lines are guides to eye.

IG, 30/400, 220 KHz high frequency generator with the material absorbing nitrogen by the process of diffusion. The N-stoichiometry was determined by measuring the mass gain after each glowing cycle and by measuring the pressure drop within the recipient. After preparation the  $\text{La}_{3-x}\text{Pr}_x\text{Ni}_2\text{B}_2\text{N}_{3-\delta}$  were annealed in a two step process similar to the one described in section 3.3 for  $\text{La}_3\text{Ni}_2\text{B}_2\text{N}_{3-\delta}$ . The only difference is that in the final step all  $\text{La}_{3-x}\text{Pr}_x\text{Ni}_2\text{B}_2\text{N}_{3-\delta}$  were annealed at  $1150^\circ\text{C}$  before quenching. All the samples were prepared with a nominal nitrogen stoichiometry near 2.7.

## 7.2 Structural characterization

### 7.2.1 Phase analysis of $\text{La}_{3-x}\text{Pr}_x\text{Ni}_2\text{B}_2\text{N}_{3-\delta}$

Polycrystalline  $\text{La}_{3-x}\text{Pr}_x\text{Ni}_2\text{B}_2\text{N}_{2.7}$  solid solution with  $x$  varying from 0 to 3 were prepared and phase purity of the samples was studied by means of powder XRD. The observed, calculated and difference XRD pattern of  $\text{Pr}_3\text{Ni}_2\text{B}_2\text{N}_{2.7}$  is shown in figure 7.2 while the patterns for some  $\text{La}_{3-x}\text{Pr}_x\text{Ni}_2\text{B}_2\text{N}_{2.7}$  are given in the appendix A. The solid line in figure 7.2 indicates the calculated pattern from FULLPROF refinement while the vertical bars represent the Bragg positions. The refinement revealed the related two layer boronitride  $\text{PrNiBN}$  as the main impurity phase with a refined fraction



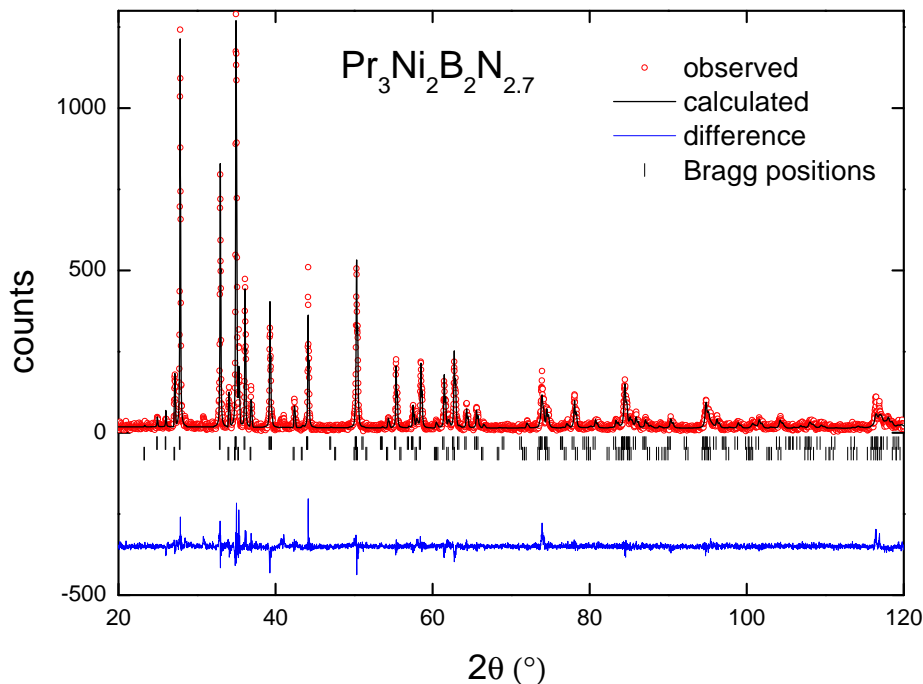


Figure 7.2: Measured, calculated and difference XRD pattern of  $\text{Pr}_3\text{Ni}_2\text{B}_2\text{N}_{2.7}$ . Short vertical lines indicate the positions of Bragg reflections.

of about 10%. The variation of  $a$  and  $c$  lattice parameters in the solid solution  $\text{La}_{3-x}\text{Pr}_x\text{Ni}_2\text{B}_2\text{N}_{2.7}$  is summarized in figure 7.1. An almost linear reduction of the  $a$  lattice parameter is observed which is a direct consequence of the lanthanide contraction. However, the  $c$  lattice parameter shows a non-monotonic variation with a maximum at about  $x = 1.0$ . A similar variation of lattice parameters has been observed for the solid solutions  $\text{La}_{3-x}\text{Ce}_x\text{Ni}_2\text{B}_2\text{N}_{3-\delta}$  while a directly opposite trend of the  $a$  and  $c$  lattice parameters has been observed for the related borocarbides [53]. In the borocarbides the increase in the  $c$  lattice constant is attributed to an increase in the NiB tetrahedral angle resulting in a stretching of the lattice along the  $c$ -axis. The NiB tetrahedral angle increases from  $\sim 105.8^\circ$  for  $\text{La}_3\text{Ni}_2\text{B}_2\text{N}_{2.7}$  to  $\sim 107.3^\circ$  for  $\text{Pr}_3\text{Ni}_2\text{B}_2\text{N}_{2.7}$  which tends to stretch the lattice but a concomitant reduction of the (La,Pr)N triple layer thickness is observed. The combined effect of these variations leads to a non-monotonic variation of the  $c$  lattice parameter within the  $\text{La}_{3-x}\text{Pr}_x\text{Ni}_2\text{B}_2\text{N}_{2.7}$  solid solution. The structural data of  $\text{Pr}_3\text{Ni}_2\text{B}_2\text{N}_{2.70}$  are summarized in table 7.1. It should be mentioned here that since N and B scattering lengths are small in X-ray diffraction, the positions of B and N(1) sites are initially refined and then fixed to an appropriate value before the final refinement. Also the occupation of all the crystallographic sites is fixed while the occu-

Pr <sub>3</sub> Ni <sub>2</sub> B <sub>2</sub> N <sub>2.7</sub>					
Structure type: La <sub>3</sub> Ni <sub>2</sub> B <sub>2</sub> N <sub>3</sub> , Space group: <i>I4/mmm</i>					
$a = 0.3622(2)$ nm, $c = 2.05161(2)$ nm, $V = 0.272(4)$ nm <sup>3</sup> , $c/a = 5.664$					
Atom	Site	x	y	z	Occ.
Pr(2)	2a	0.0000	0.0000	0.00000	1.00
Pr(1)	4e	0.0000	0.0000	0.37241(11)	1.00
Ni	4d	0.0000	0.5000	0.25000	1.00
B	4e	0.0000	0.0000	0.19249	1.00
N(1)	4e	0.0000	0.0000	0.12775	1.00
N(2)	2b	0.0000	0.0000	0.50000	0.90

Table 7.1: Crystal structure and lattice parameters data of Pr<sub>3</sub>Ni<sub>2</sub>B<sub>2</sub>N<sub>2.70</sub> at room temperature.

pation of N(2) is fixed to 0.9 on the basis of the neutron powder diffraction results of La<sub>3</sub>Ni<sub>2</sub>B<sub>2</sub>N<sub>2.65</sub>. Finally refined parameters are given with error bars in table 7.1. The lattice volume of 0.272nm<sup>3</sup> for Pr<sub>3</sub>Ni<sub>2</sub>B<sub>2</sub>N<sub>2.70</sub> represents a ~5% reduction as compared to La<sub>3</sub>Ni<sub>2</sub>B<sub>2</sub>N<sub>2.7</sub> which is due to the lanthanide contraction.

### 7.2.2 Phase analysis of La<sub>3-x</sub>Nd<sub>x</sub>Ni<sub>2</sub>B<sub>2</sub>N<sub>3-δ</sub>

The XRD pattern of Nd<sub>3</sub>Ni<sub>2</sub>B<sub>2</sub>N<sub>2.7</sub> is shown in figure 7.3. The pattern does not reveal a significant fraction of the related two layer phase NdNiBN but some reflections of an unidentified phase are observed. The variation of lattice parameters within the solid solution La<sub>3-x</sub>Nd<sub>x</sub>Ni<sub>2</sub>B<sub>2</sub>N<sub>3-δ</sub> is shown in figure 7.4 while the structural data of Nd<sub>3</sub>Ni<sub>2</sub>B<sub>2</sub>N<sub>2.7</sub> are summarized in table 7.2. In the refinement, the positions of B and N(1) were fixed and may, thus, be ambiguous. The occupation of all crystallographic sites were also fixed. An almost linear reduction of the *a* lattice parameter similar to the Pr case is observed while the *c* lattice parameter shows again a non-monotonic variation with a maximum at  $x = 0.8$  which is attributed to a competition between the NiB tetrahedral angle and the (La,Nd)N layer thickness. In La<sub>3-x</sub>Nd<sub>x</sub>Ni<sub>2</sub>B<sub>2</sub>N<sub>3-δ</sub> the lattice volume shows a reduction with increasing Nd concentration and reaches a value of 0.265nm<sup>3</sup> for pure Nd<sub>3</sub>Ni<sub>2</sub>B<sub>2</sub>N<sub>2.7</sub>.

## 7.3 Magnetic and resistivity measurements

### 7.3.1 Magnetic measurements

The magnetic susceptibility,  $\chi(T)$ , of La<sub>3-x</sub>R<sub>x</sub>Ni<sub>2</sub>B<sub>2</sub>N<sub>3-δ</sub> ( $R=Pr, Nd$ ) was studied from 3K up to 300 K by means of magnetization measurement on a dc SQUID magnetometer. The low temperature dc magnetic susceptibility

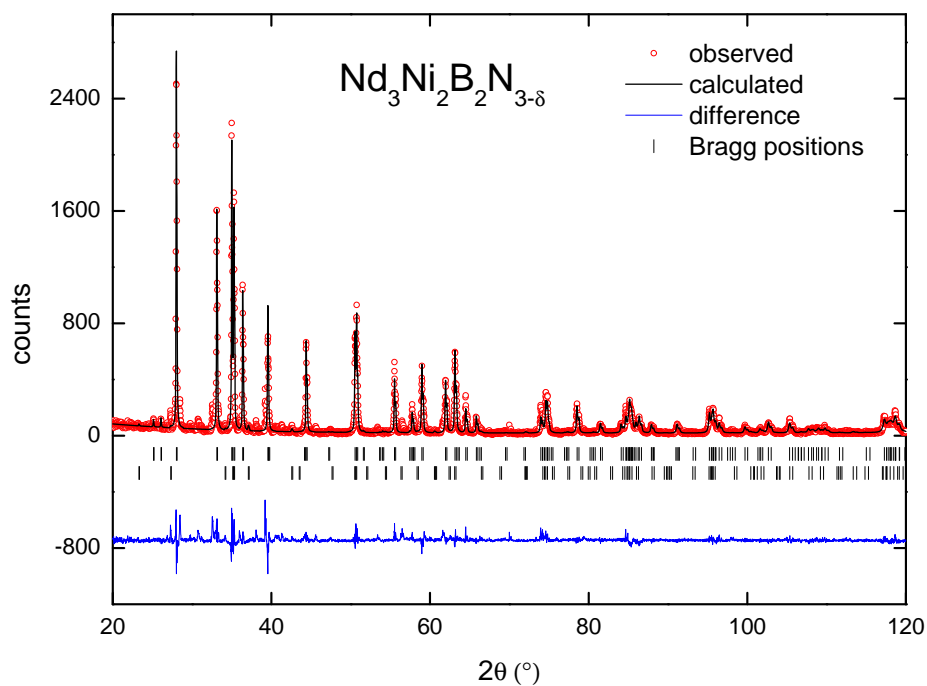


Figure 7.3: Measured, calculated and difference XRD pattern of  $\text{Nd}_3\text{Ni}_2\text{B}_2\text{N}_{2.7}$ . Short vertical lines indicate the positions of Bragg reflections.

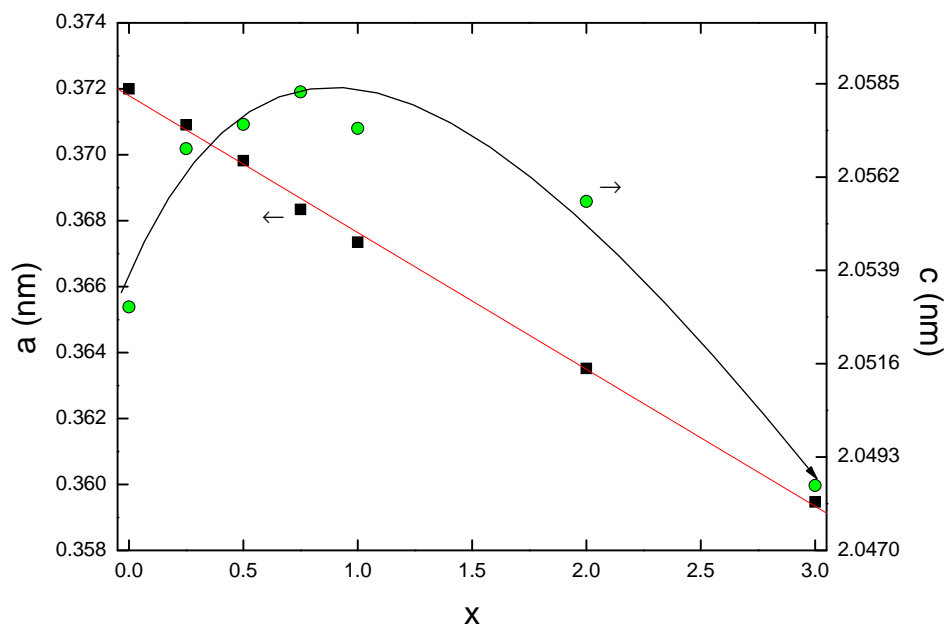


Figure 7.4: Variation of the lattice parameters  $a$  (squares) and  $c$  circles in solid solution  $\text{La}_{3-x}\text{Nd}_x\text{Ni}_2\text{B}_2\text{N}_{2.7}$ ; lines are guides to eye.

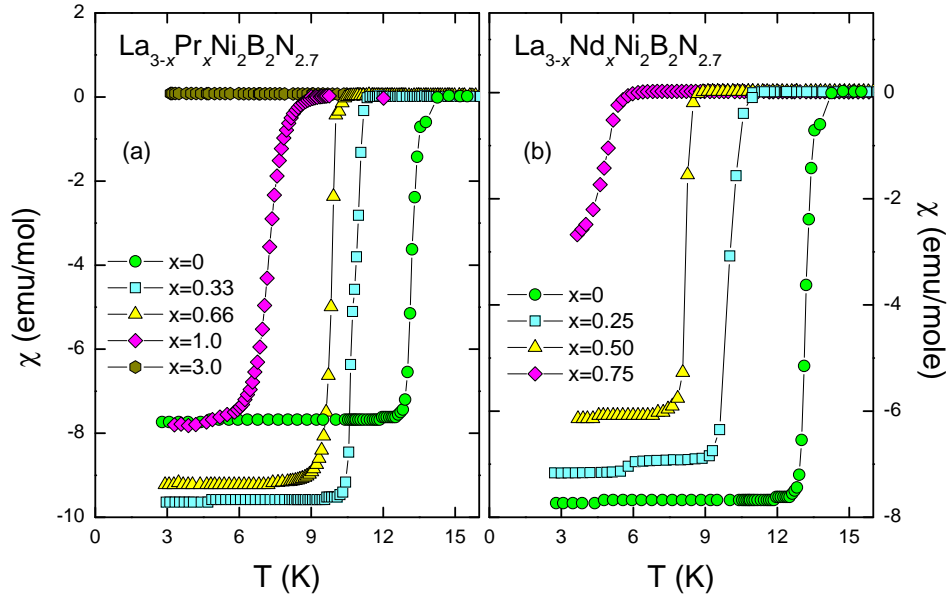


Figure 7.5: Dc magnetic susceptibility of  $\text{La}_{3-x}\text{Pr}_x\text{Ni}_2\text{B}_2\text{N}_{2.7}$  (a) and  $\text{La}_{3-x}\text{Nd}_x\text{Ni}_2\text{B}_2\text{N}_{2.7}$  (b) at 1 mT for  $x$  as labeled.

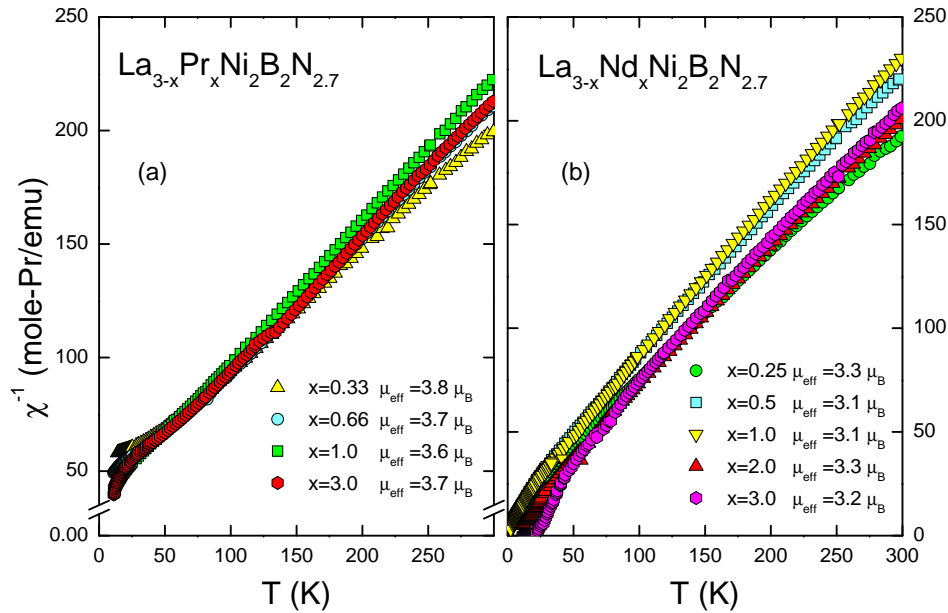


Figure 7.6: Inverse dc magnetic susceptibility ( $\text{La}_3\text{Ni}_2\text{B}_2\text{N}_{2.7}$  subtracted) of  $\text{La}_{3-x}\text{Pr}_x\text{Ni}_2\text{B}_2\text{N}_{2.7}$  (a) and  $\text{La}_{3-x}\text{Nd}_x\text{Ni}_2\text{B}_2\text{N}_{2.7}$  (b) at 1.0 T for  $x$  as labeled. The effective paramagnetic moment for each composition from Curie-Weiss fitting is also labeled.

Nd <sub>3</sub> Ni <sub>2</sub> B <sub>2</sub> N <sub>2.7</sub>					
Structure type: La <sub>3</sub> Ni <sub>2</sub> B <sub>2</sub> N <sub>3</sub> , Space group: <i>I4/mmm</i>					
<i>a</i> = 0.3595(2) nm, <i>c</i> = 2.0486(2) nm, <i>V</i> = 0.265(4) nm <sup>3</sup> , <i>c/a</i> = 5.698					
Atom	Site	x	y	z	Occ.
Nd(2)	2a	0.0000	0.0000	0.00000	1.00
Nd(1)	4e	0.0000	0.0000	0.37281(10)	1.00
Ni	4d	0.0000	0.5000	0.25000	1.00
B	4e	0.0000	0.0000	0.20910	1.00
N(1)	4e	0.0000	0.0000	0.12816	1.00
N(2)	2b	0.0000	0.0000	0.50000	0.90

Table 7.2: Crystal structure and lattice parameters data for Nd<sub>3</sub>Ni<sub>2</sub>B<sub>2</sub>N<sub>2.70</sub> at room temperature.

for La<sub>3-x</sub>Pr<sub>x</sub>Ni<sub>2</sub>B<sub>2</sub>N<sub>2.7</sub> as well as for La<sub>3-x</sub>Nd<sub>x</sub>Ni<sub>2</sub>B<sub>2</sub>N<sub>2.7</sub> measured in an applied field of 1 mT after zero field cooling is shown in figure 7.5. As shown in figure 7.5(a) La/Pr substitution shifts the superconducting transition temperature,  $T_c$ , from about 13 K for  $x = 0$  to about 7 K for  $x = 1.0$ . Superconductivity is suppressed more strongly in case of La/Nd substitution with  $T_c$  decreasing from 13 K for pure La system to about 8 K for  $x = 0.5$  while no superconductivity is observed in La<sub>3-x</sub>Nd<sub>x</sub>Ni<sub>2</sub>B<sub>2</sub>N<sub>2.7</sub> for compositions beyond  $x = 0.75$ . A detailed discussion about the suppression of superconductivity in La<sub>3-x</sub>R<sub>x</sub>Ni<sub>2</sub>B<sub>2</sub>N<sub>3-δ</sub> analyzed in terms of Abrikosov-Gor'kov type pair breaking is given in section 7.4.

In order to study the normal state magnetic properties of La<sub>3-x</sub>R<sub>x</sub>Ni<sub>2</sub>B<sub>2</sub>N<sub>3-δ</sub> solid solutions, dc magnetic susceptibilities were measured up to room temperature in an applied field of 1.0 T. To investigate the magnetism of Pr and Nd ions, the magnetic susceptibility of the reference non-magnetic system La<sub>3</sub>Ni<sub>2</sub>B<sub>2</sub>N<sub>2.7</sub> was subtracted and the results are displayed figure 7.6. The inverse susceptibility is analyzed for  $T > 60$  K in terms of the Curie-Weiss model,  $\chi = C/(T - \Theta_p)$  with  $\Theta_p$  being the paramagnetic Curie temperature and  $C$  the Curie constant,  $C = \mu_o N_A \mu_{eff}^2 / 3k_B$ . The latter allows to calculate the effective paramagnetic moments ( $\mu_{eff}$ ) which are listed in figure 7.6 for each composition. It is evident that  $\mu_{eff}$  as obtained from the Curie constant ( $\mu_{eff} = \sqrt{8C}$  with  $C$  given in units of emuK/mol) for the La/Pr and La/Nd systems are in good agreement (within experimental error) with the free ion values of  $3.58 \mu_B$  and  $3.62 \mu_B$  for Pr and Nd, respectively. The paramagnetic Curie temperatures  $\Theta_p$  for Pr and Nd are of the order of -50 K and -10 K, respectively.

The low temperature resistivities of La<sub>3-x</sub>Pr<sub>x</sub>Ni<sub>2</sub>B<sub>2</sub>N<sub>3-δ</sub> are shown in figure 7.7 revealing a suppression of superconductivity with increasing Pr concentration. An almost linear reduction of  $T_c$  is evident at a rate  $dT_c/dx \simeq -0.44$  K/Pr% with  $T_c$  being reduced from  $\sim 13$  K for pure La<sub>3</sub>Ni<sub>2</sub>B<sub>2</sub>N<sub>2.7</sub> to

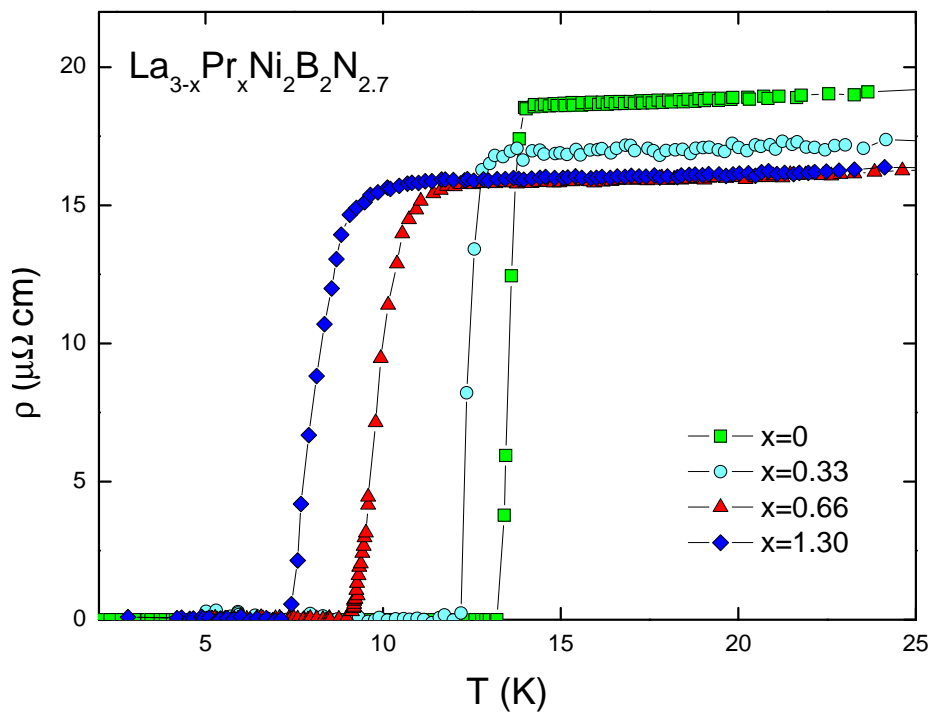


Figure 7.7: Resistivity measurements of solid solutions  $\text{La}_{3-x}\text{Pr}_x\text{Ni}_2\text{B}_2\text{N}_{2.7}$  for  $x$  as labeled.

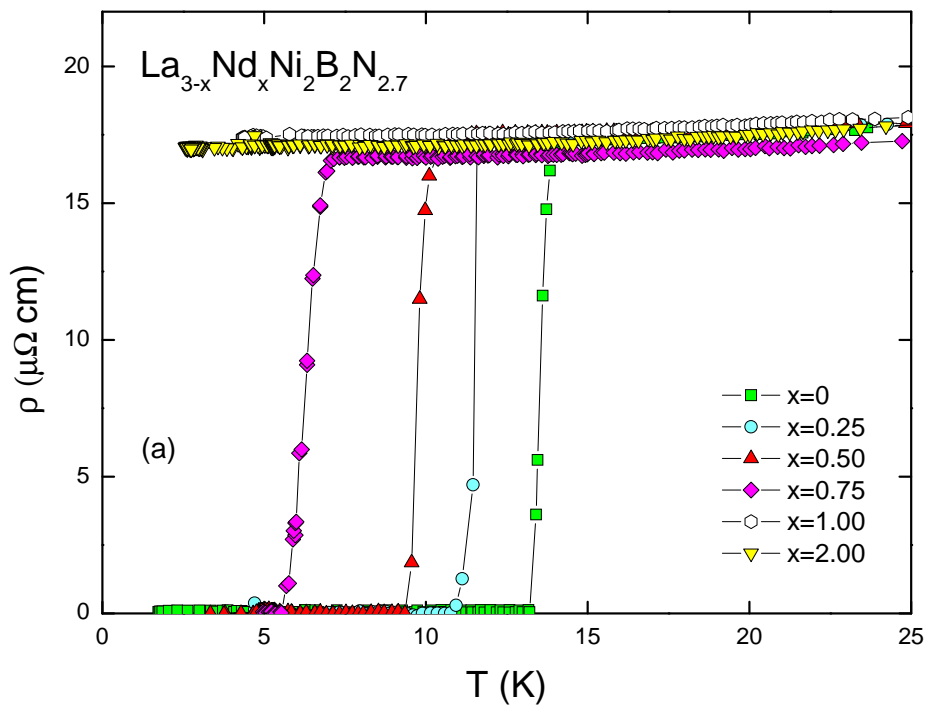


Figure 7.8: Resistivity measurements of solid solutions  $\text{La}_{3-x}\text{Nd}_x\text{Ni}_2\text{B}_2\text{N}_{2.7}$  for  $x$  as labeled.

$\sim 8.0$  K for a Pr concentration  $x = 1.3$ . These values of  $T_c$  are consistent with those determined from magnetic susceptibility measurements. The resistivity data of solid solutions  $\text{La}_{3-x}\text{Nd}_x\text{Ni}_2\text{B}_2\text{N}_{3-\delta}$  are summarized in figure 7.8. With Nd substitution, superconductivity is suppressed at a faster rate with  $dT_c/dx \simeq -0.93$  K/Nd% as compared to Pr. Nd destroys superconductivity completely for  $x \gtrsim 1.0$ .

## 7.4 Discussion of Abrikosov Gor'kov type pair breaking

From the results of magnetic susceptibility as well as resistivity it is clearly seen that the magnetic rare-earths Pr and Nd result in a suppression of superconductivity in  $\text{La}_3\text{Ni}_2\text{B}_2\text{N}_{3-\delta}$ . The antagonistic nature of superconductivity and magnetism is well known from earliest studies of paramagnetic rare-earth impurities in La metal [101] and has been explained theoretically by Abrikosov and Gor'kov (AG) [117] as a consequence of the exchange interaction between impurities carrying local magnetic moments and the conduction electrons which leads to (Cooper) pair breaking. The superconducting transition temperature of the samples within the  $\text{La}_{3-x}\text{R}_x\text{Ni}_2\text{B}_2\text{N}_{3-\delta}$  series ( $R=\text{Ce, Pr, Nd}$ ) determined from dc-susceptibility are plotted as a function of the respective rare-earth concentration in figure 7.9. The depression of the superconducting transition temperature due to spin disorder scattering by paramagnetic impurities is described in terms of the AG formula

$$\ln\left(\frac{T_c^0}{T_c}\right) = \Psi\left(\frac{T_c^0}{2T_c}\rho + \frac{1}{2}\right) - \Psi\left(\frac{1}{2}\right) \quad (7.1)$$

where  $T_c$  and  $T_c^0$  are the critical temperatures with and without magnetic impurities and  $\Psi$  is the digamma function. The pair breaking parameter  $\rho$  is given by

$$\rho = \frac{cN(E_f)J_{sf}^2(g_J - 1)^2J(J + 1)}{k_B T_c^0} \quad (7.2)$$

where  $T_c^0 \simeq 13$  K for  $\text{La}_3\text{Ni}_2\text{B}_2\text{N}_{2.7}$ ,  $c$  is the impurity concentration ( $c = x/10$ ),  $N(E_f)$  is density of states at Fermi energy ( $\simeq 6$  states/eV f.u),  $J_{sf}$  is the exchange integral and  $(g_J - 1)^2J(J + 1)$  is the de Gennes factor ( $dG_{\text{Ce}} = 0.18$ ,  $dG_{\text{Pr}} = 0.8$  and  $dG_{\text{Nd}} = 1.8$ ). The dashed lines in figure 7.9 represent fits of the data in terms of the AG theory. A significantly stronger depression of  $T_c$  is observed for  $\text{La}_{3-x}\text{Ce}_x\text{Ni}_2\text{B}_2\text{N}_{2.7}$  while for La/Pr and La/Nd substitution an initially almost linear reduction of  $T_c$  is observed before rapidly reaching zero. This trend agrees with the AG theory. The  $s$ - $f$  exchange integral  $J_{sf}$  is an important parameter that can be evaluated from the AG theory. The fits yield  $J_{sf} \sim 77.0$  meV and  $\sim 84.0$  meV for La/Nd and La/Pr substitution,

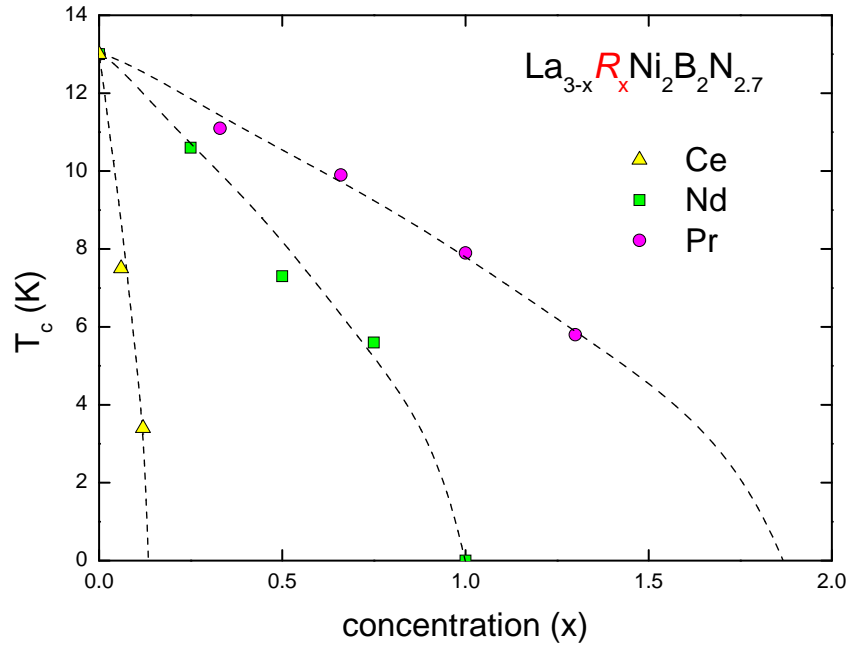


Figure 7.9:  $T_c$  reduction in  $\text{La}_{3-x}\text{R}_x\text{Ni}_2\text{B}_2\text{N}_{3-\delta}$  ( $R = \text{Ce}, \text{Pr}, \text{Nd}$ ) solid solution as a function of concentration  $x$  of the impurity atom as labeled. The dashed lines represent fits in terms of Abrikosov-Gor'kov pair breaking theory.

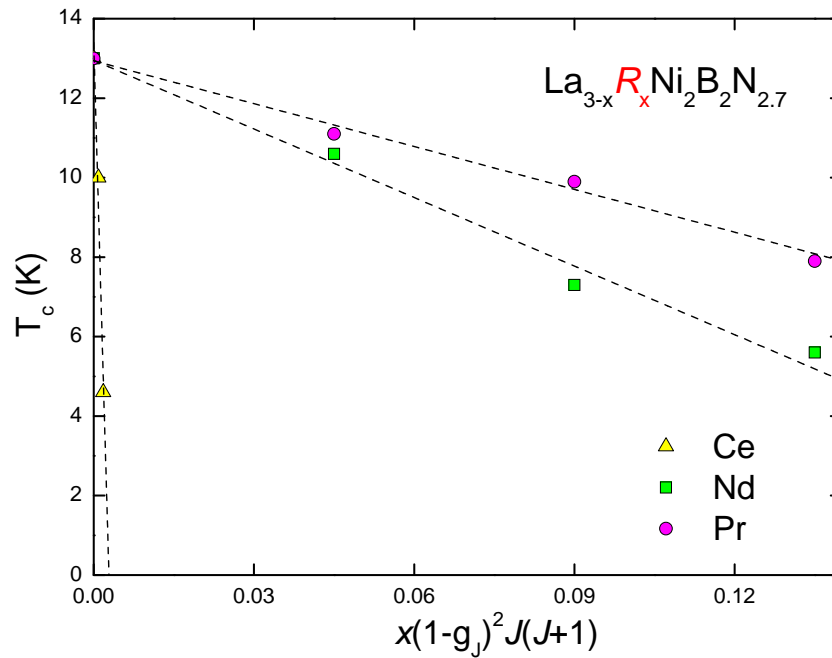


Figure 7.10:  $T_c$  reduction in  $\text{La}_{3-x}\text{R}_x\text{Ni}_2\text{B}_2\text{N}_{3-\delta}$  solid solution as a function of  $R$  concentration times the de Gennes factor. Solid lines are guides to eye.



respectively. The observed weak variation of  $J_{sf}$  is in line with the local spin density approximation which predicts a small variation of  $J_{sf}$  within the rare-earths series [118].

In the case of the related borocarbide superconductors  $\text{Y}_{1-x}\text{RNi}_2\text{B}_2\text{C}$  (with  $R = \text{La, Pr, Nd, Sm}$ ) it was shown that the AG theory may account qualitatively for the rapid breakdown of superconductivity in light rare-earth systems [119]. However, the suppression of superconductivity in borocarbides by light rare-earths (La, Pr, Nd) is more realistically attributed to the reduction of the density of states at the Fermi level [120]. For  $\text{La}_{3-x}\text{R}_x\text{Ni}_2\text{B}_2\text{N}_{3-\delta}$ , the values of  $J_{sf}$  for Pr and Nd substitution are similar, accordingly, the chemical pressure induced changes in  $N(E_f)$  may be relatively small. This implies that for Pr and Nd the only parameter governing the significant  $T_c$  depression is the effective de Gennes factor. The  $T_c$  reduction as a function of the effective dG factor is plotted in figure 7.10 which indicates that the pair breaking effect of Pr and Nd roughly scales with de Gennes factor. Thereby, one may conclude that AG pair breaking with critical  $R$  concentrations  $x_{cri}$  of about 1.9 and 1.0 for Pr and Nd may account for the suppression of superconductivity in  $\text{La}_{3-x}\text{R}_x\text{Ni}_2\text{B}_2\text{N}_{3-\delta}$ . However, for Ce which has a smaller dG factor, a strong pair breaking effect in  $\text{La}_{3-x}\text{Ce}_x\text{Ni}_2\text{B}_2\text{N}_{2.7}$  series is attributed to intermediate valance and/or Kondo effect (see chapter 6).

## 7.5 Ground state properties of $\text{Pr}_3\text{Ni}_2\text{B}_2\text{N}_{3-\delta}$

The ground state properties of  $\text{Pr}_3\text{Ni}_2\text{B}_2\text{N}_{3-\delta}$  were investigated by means of magnetic susceptibility, specific heat and resistivity measurements. The dc magnetic susceptibility of two different  $\text{Pr}_3\text{Ni}_2\text{B}_2\text{N}_{2.7}$  samples measured in an applied field of 3T is shown in figure 7.11. The susceptibilities of both samples are almost matching at high temperature while at low temperature sample (a) exhibits a slightly higher impurity contribution. The inverse susceptibility of sample (a) is also shown in figure 7.11 and is analyzed in terms of the modified Curie-Weiss law. Contrary to the previous analysis of the solid solution, the susceptibility of  $\text{La}_3\text{Ni}_2\text{B}_2\text{N}_{2.7}$  is not subtracted but a Pauli paramagnetic contribution is included in the fit. The solid line in figure 7.11 represents a fit of the data for  $T > 90\text{K}$  according to  $\chi = \chi_o + C/(T - \Theta_p)$  yielding a  $\chi_o = 4 \times 10^{-4}$  emu/mole, a paramagnetic Curie temperature  $\Theta_P \simeq -40\text{K}$  and a Curie constant  $C \simeq 1.53$  emu K/mol-Pr. The latter gives an effective magnetic moment  $\mu_{eff} \simeq 3.49\mu_B$  which is close to free ion value of  $3.58\mu_B$  for Pr.

The specific heat of  $\text{Pr}_3\text{Ni}_2\text{B}_2\text{N}_{2.7}$  samples (a) and (b) is shown in figure 7.12 and reveals a normal metallic behaviour with two different magnetic anomalies observed in the two samples. Small anomalies below 10 K in sample (a) and at about 23 K in sample (b) may be attributed to some impurity

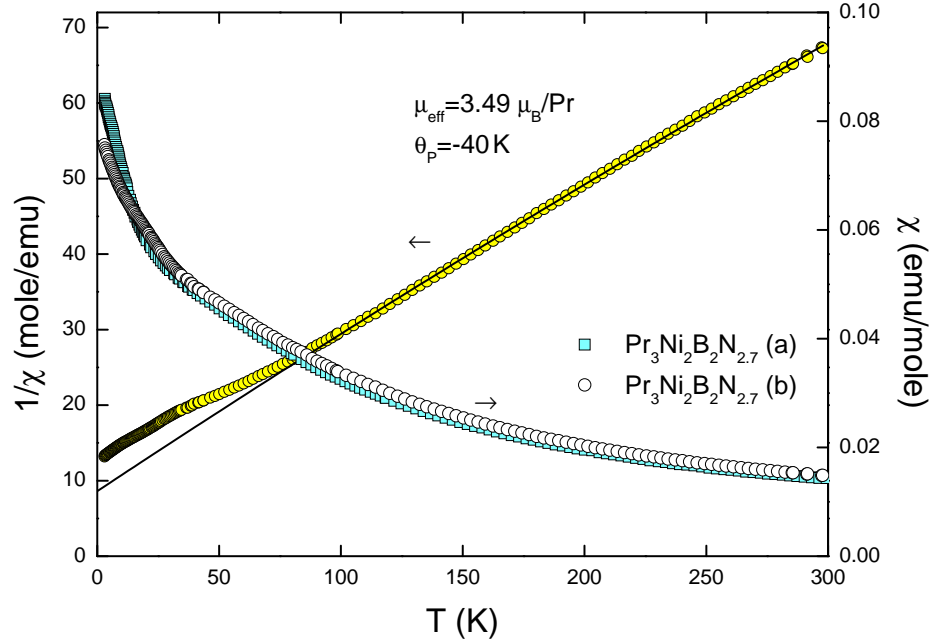


Figure 7.11: magnetic susceptibility of two different  $\text{Pr}_3\text{Ni}_2\text{B}_2\text{N}_{2.7}$  in an applied field of 3 T. Solid line indicates a fit for  $T > 90$  K in terms of a modified Curie-Weiss model.

phases. The solid line in figure 7.12 represents the phonon specific heat ( $C_{ph}$ ) of the reference compound  $\text{La}_3\text{Ni}_2\text{B}_2\text{N}_{2.7}$  while the inset shows the low temperature specific heat of sample (b) revealing a linear behaviour in a very narrow temperature range. For related borocarbide  $\text{PrNi}_2\text{B}_2\text{C}$  an antiferromagnetic order at about 4 K with a relatively high value of the Sommerfeld coefficient  $\gamma = 250 \text{ mJ/molK}^2$  was reported [121]. However, Mazmudar *et al.* [122] performed detailed neutron scattering studies on  $\text{PrNi}_2\text{B}_2\text{C}$  and demonstrated that crystalline electric field (CEF) level schemes explains the low temperature behaviour very well.

The low  $T$  specific heat of  $\text{Pr}_3\text{Ni}_2\text{B}_2\text{N}_{2.7}$  shows a very small enhancement which means that the CEF splitting is relatively large. Figure 7.13 shows the difference specific heat ( $\Delta C_p/T$ ) obtained by subtracting  $C_{ph}$  of  $\text{La}_3\text{Ni}_2\text{B}_2\text{N}_{2.7}$  from the measured specific heat of  $\text{Pr}_3\text{Ni}_2\text{B}_2\text{N}_{2.7}$ . The inset in figure 7.13 shows the magnetic entropy of  $\text{Pr}_3\text{Ni}_2\text{B}_2\text{N}_{2.7}$  as calculated from  $\Delta C_p/T$ . At about 15 K (corresponding to the minimum in  $\Delta C_p/T$ ), the entropy is about 0.6 which is far less than the entropy ( $S = 3R\ln 2$ ) for a doublet ground state of  $\text{Pr}_3\text{Ni}_2\text{B}_2\text{N}_{2.7}$  suggesting that the upturn in  $\Delta C_p/T$  at low temperature is an impurity contribution.

The electrical resistivity of  $\text{Pr}_3\text{Ni}_2\text{B}_2\text{N}_{2.7}$  along with the resistivity of  $\text{La}_3\text{Ni}_2\text{B}_2\text{N}_{2.7}$  is shown in figure 7.14 while the inset shows the difference  $\Delta\rho$ .

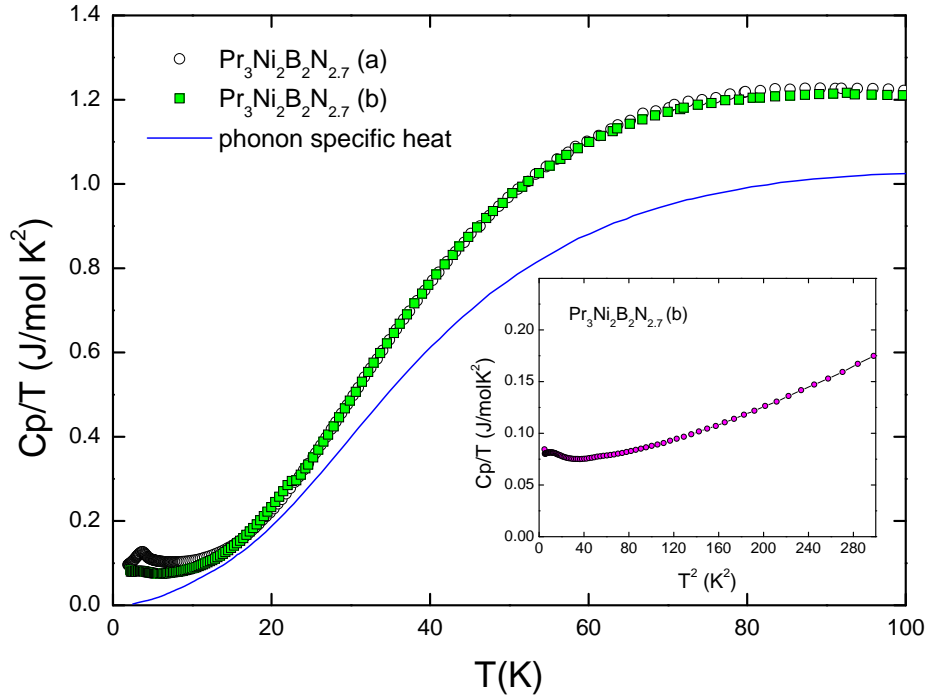


Figure 7.12: Specific heat of two different samples of  $\text{Pr}_3\text{Ni}_2\text{B}_2\text{N}_{2.7}$  with solid line indicating the phonon specific heat of the reference compound  $\text{La}_3\text{Ni}_2\text{B}_2\text{N}_{2.7}$ . The inset shows the low temperature specific heat of  $\text{Pr}_3\text{Ni}_2\text{B}_2\text{N}_{2.7}$ .

Interestingly,  $\Delta\rho$  exhibits a remarkably similar variation as the magnetic entropy gain in the inset of figure 7.13. Since the specific heat measurement indicates a singlet ground state, the increase of the resistivity with temperature may be attributed to spin disorder scattering which increases as the CEF levels are populated because more and more scattering channels for conduction electrons become available. The specific heat and resistivity data of  $\text{Pr}_3\text{Ni}_2\text{B}_2\text{N}_{2.7}$  point towards a singlet ground state, however, the magnetic susceptibility shows a strong upturn at low temperature. For a singlet ground state, one would expect a flattening of the susceptibility at low  $T$ . The magnetic properties of  $\text{Pr}_3\text{Ni}_2\text{B}_2\text{N}_{2.7}$  do not suggest any magnetic ordering but a clear evidence of a singlet ground state of Pr is possibly hindered by a significant Curie-Weiss like impurity susceptibility.

## 7.6 Ground state properties of $\text{Nd}_3\text{Ni}_2\text{B}_2\text{N}_{3-\delta}$

The ground state properties of  $\text{Nd}_3\text{Ni}_2\text{B}_2\text{N}_{3-\delta}$  were investigated by means of specific heat, resistivity and magnetic susceptibility measurements. The spe-

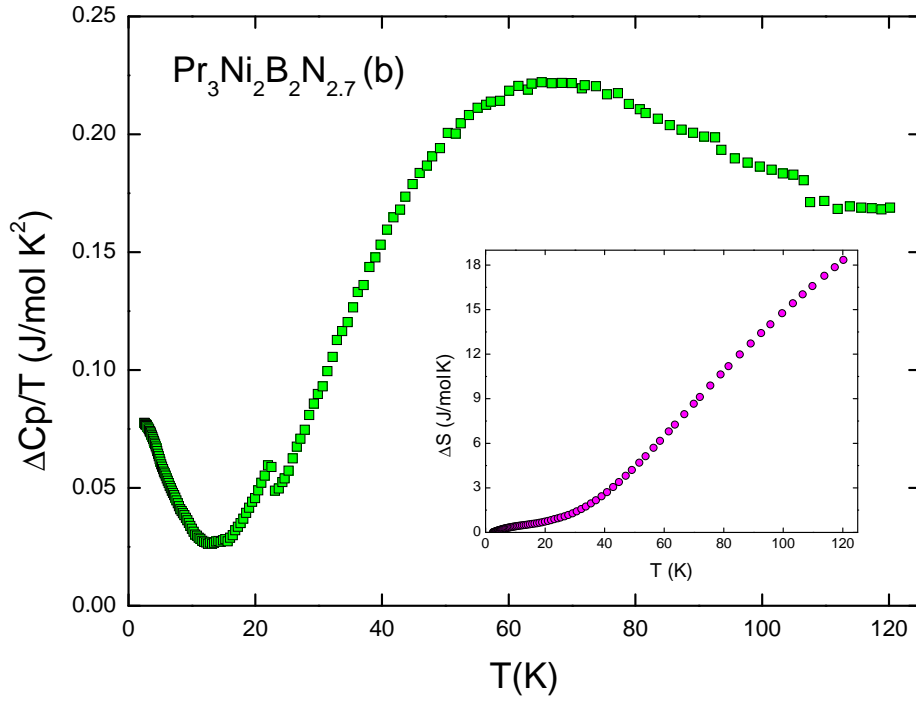


Figure 7.13:  $\Delta C_p/T$  Vs.  $T$  of  $\text{Pr}_3\text{Ni}_2\text{B}_2\text{N}_{2.7}$  (sample b, see text). The inset shows the magnetic entropy calculated from  $\Delta C_p/T$ .

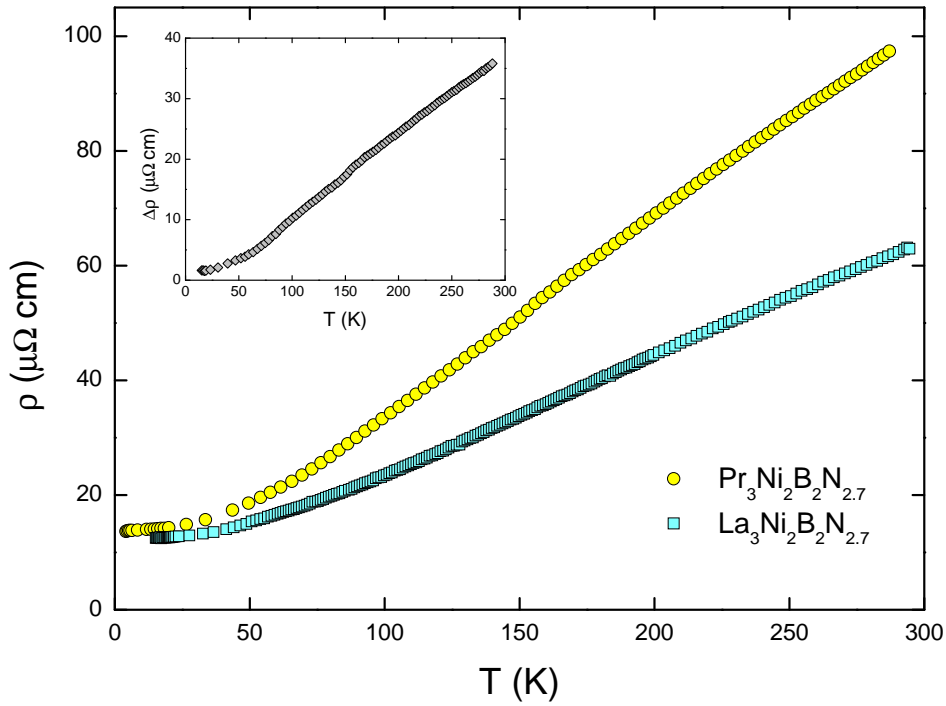


Figure 7.14: Temperature dependent electrical resistivities of  $\text{Pr}_3\text{Ni}_2\text{B}_2\text{N}_{2.7}$  and  $\text{La}_3\text{Ni}_2\text{B}_2\text{N}_{2.7}$ . The inset shows the difference between these resistivities, i.e. the magnetic contribution  $\Delta\rho$ .

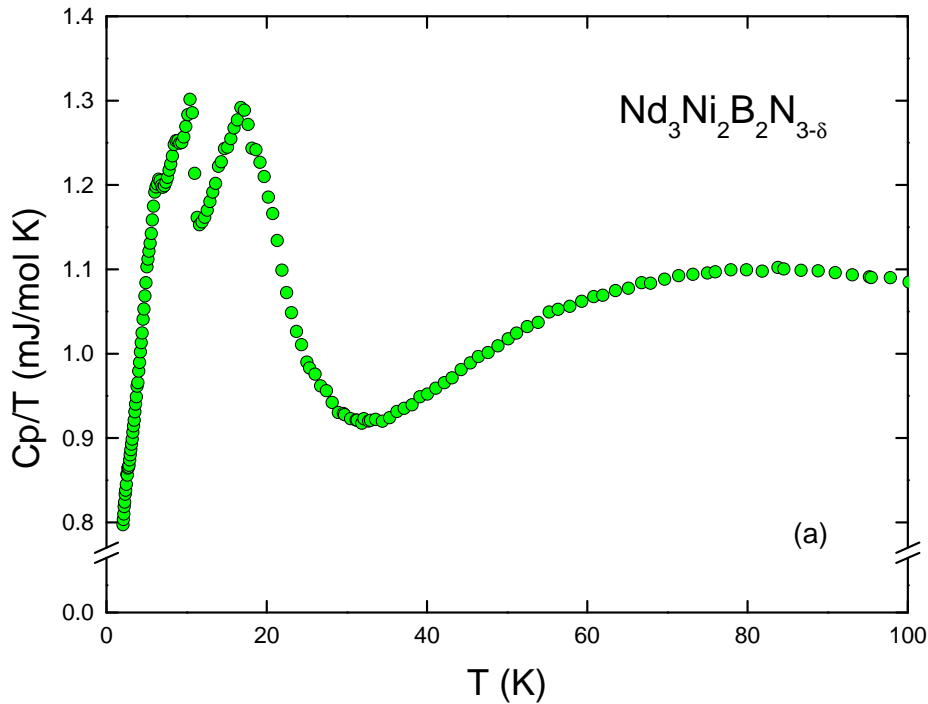


Figure 7.15: Specific heat of  $\text{Nd}_3\text{Ni}_2\text{B}_2\text{N}_{2.7}$  measured in zero field.

cific heat of  $\text{Nd}_3\text{Ni}_2\text{B}_2\text{N}_{2.7}$  measured in zero field is shown in figure 7.15. The specific heat clearly reveals two magnetic transitions at approximately 20 K and 10 K respectively. The small anomalies at low temperature may be some impurity contributions. The electrical resistivity of  $\text{Nd}_3\text{Ni}_2\text{B}_2\text{N}_{2.7}$  is shown in figure 7.16 which indicates normal metallic behaviour at high  $T$  and an onset of magnetic ordering at around 20 K. The low temperature part of the resistivity shown as inset in figure 7.16 clearly shows two magnetic transitions at temperatures matching with the specific heat measurement. To investigate the nature of the magnetic transitions, the resistivity was measured in applied magnetic field and the results are shown in figure 7.17. Under applied magnetic field, the anomaly at low temperature (10 K) is suppressed which corresponds to an antiferromagnetic behaviour. On the other hand the anomaly at 20 K is shifted to higher temperatures which is typical for a ferromagnetic ordering [123].

Magnetization measurements were performed on a dc SQUID magnetometer. The dc magnetic susceptibility of  $\text{Nd}_3\text{Ni}_2\text{B}_2\text{N}_{2.7}$  is shown in figure 7.18(a) under applied magnetic fields as labeled. The susceptibility under an applied field of 0.01 T reveals magnetic transitions in agreement with the specific heat and resistivity measurements. The inverse susceptibility in an applied field of 3 T is shown in figure 7.18(b). The solid line in figure 7.18(b) represents a fit of

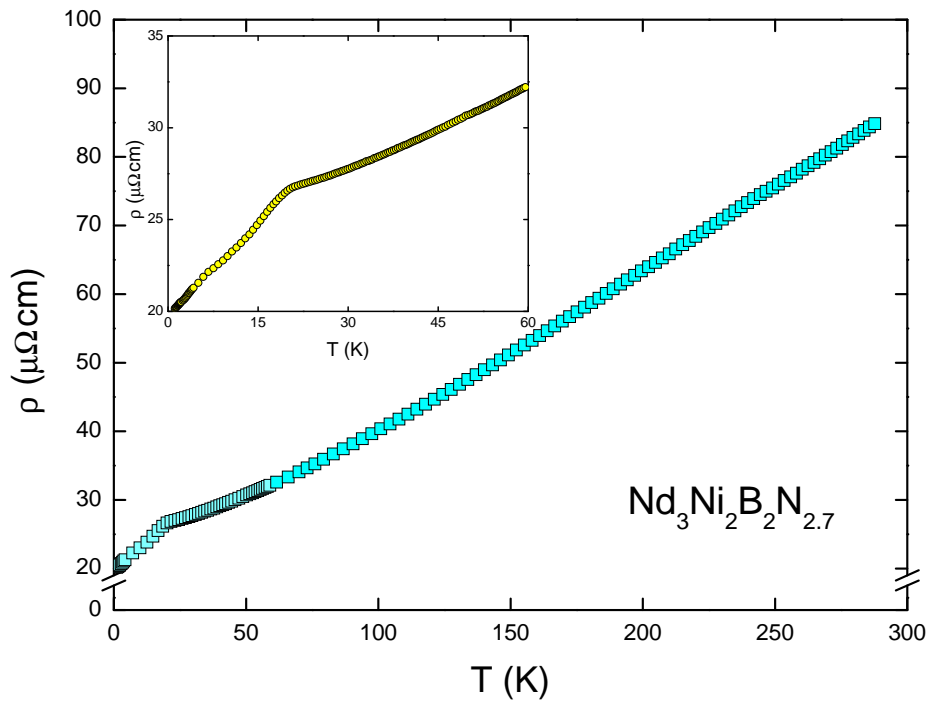


Figure 7.16: Electrical resistivity of  $\text{Nd}_3\text{Ni}_2\text{B}_2\text{N}_{2.7}$  with an inset zooming out the low temperature part.

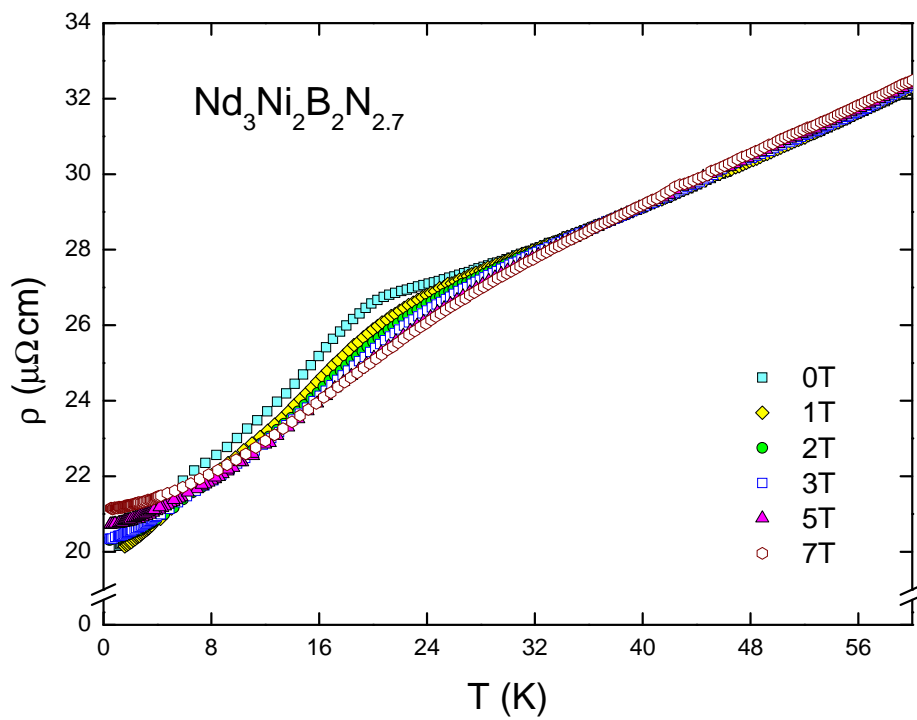


Figure 7.17: Electrical resistivity of  $\text{Nd}_3\text{Ni}_2\text{B}_2\text{N}_{2.7}$  at applied magnetic fields as labeled.

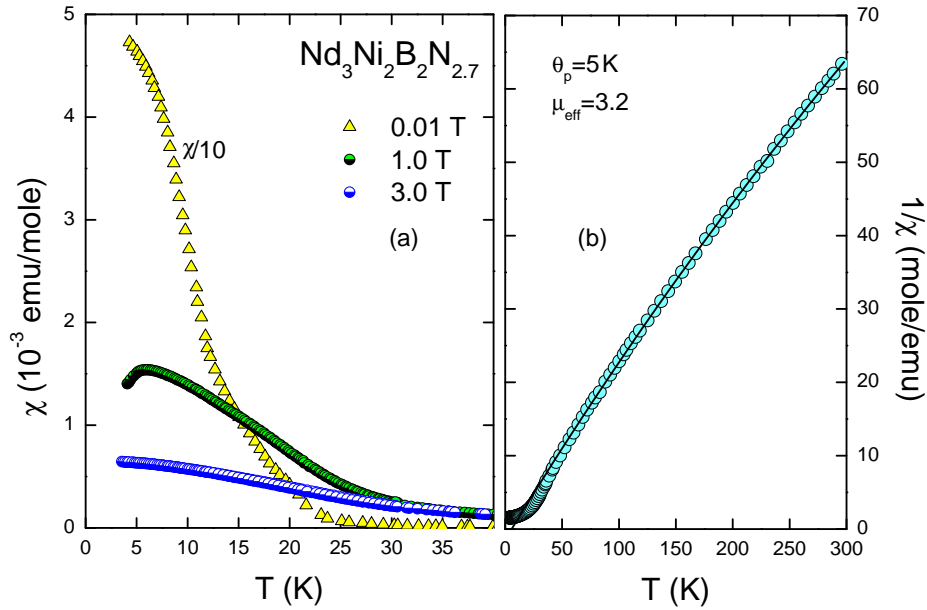


Figure 7.18: Dc magnetic susceptibility at applied magnetic fields as labeled (a) and inverse susceptibility at 3 T (b) of  $\text{Nd}_3\text{Ni}_2\text{B}_2\text{N}_{2.7}$ . Solid line in (b) indicates a fit for  $T > 60$  K in terms of a modified Curie-Weiss model.

the data above 60 K in terms of,  $\chi = \chi_o + C/(T - \Theta_p)$  yielding a paramagnetic Curie temperature  $\Theta_p = -8$  K and a Curie constant  $C = 1.31 \text{ emu K/mol Nd}$  that allows to calculate an effective magnetic moment  $\mu_{eff} = 3.24 \mu_B/\text{Nd}$  which is slightly reduced as compared to the free ion value  $3.62 \mu_B$  for Nd may be due to crystal field effects.

The isothermal magnetization up to 6 T for a wide range of temperatures is shown in figure 7.19. Normal paramagnetic behaviour is observed at higher temperatures while ferrimagnetic ordering is revealed at 20 K. The magnetization tends to increase at further lowering the temperature but no hysteresis is observed. A spin reorientation transition towards a nearly antiferromagnetic state with a small ferrimagnetic component is observed at 10 K below which a hysteresis starts to open. At 3 K the isothermal magnetization displays a metamagnetic spin flip transition at about 1 T connected with a strongly hysteretic behaviour and a saturation magnetization of about  $1.3 \mu_B/\text{Nd}$ . This reduction of the ordered moment as compared to the free ion value of fully polarized Nd moments ( $\mu_s = 3.3 \mu_B$ ) may have different origins. One possible origin can be that the CEF of Nd(1) and Nd(2) may have different easy directions resulting in a canted ferromagnetic state. Another possible explanation could be a strong  $c$ -axis anisotropy which reduces the measured  $\mu_s$  of polycrystalline material to one-third of the free ion value. However, a strong  $a$ -axis anisotropy has been observed in related borocarbide

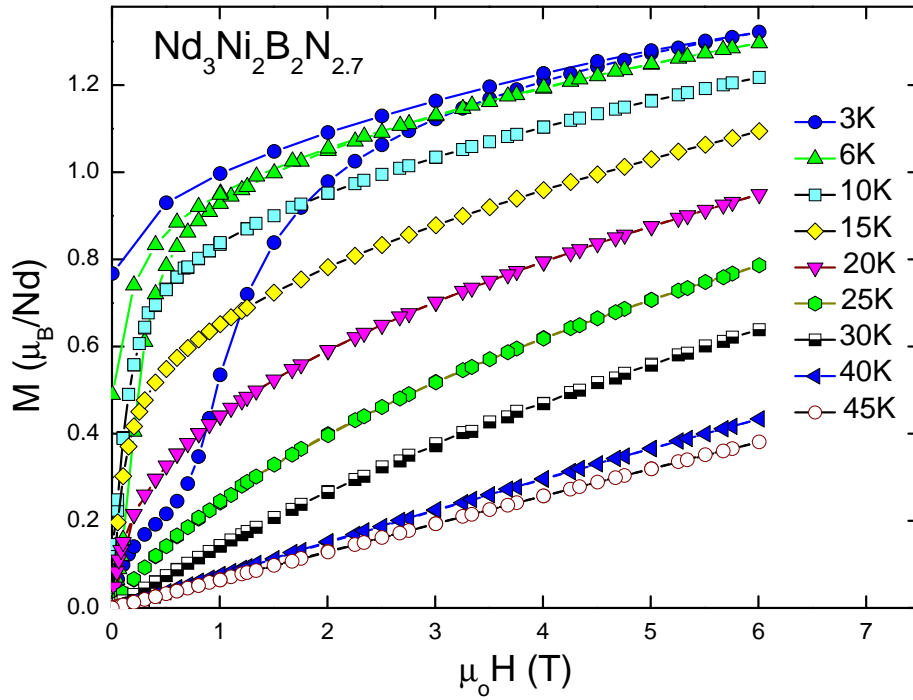


Figure 7.19: Isothermal magnetization  $M(H)$  of  $\text{Nd}_3\text{Ni}_2\text{B}_2\text{N}_{2.7}$  at temperatures as labeled.

$\text{NdNi}_2\text{B}_2\text{C}$  [52]. The most plausible interpretation for the observed reduced ordered moment of  $\text{Nd}_3\text{Ni}_2\text{B}_2\text{N}_{2.7}$  is a ferrimagnetic coupling of Nd moments. Since  $\text{Nd}_3\text{Ni}_2\text{B}_2\text{N}_{2.7}$  contains two different crystallographic sites i.e. Nd(1) and Nd(2) atom in the unit cell, it is possible that the two Nd(1) moments are aligned parallel and have ferrimagnetic coupling with Nd(2) which would, thus, result in a  $\mu_s \simeq 1.3 \mu_B$ . A final conclusion whether the magnetic structure of  $\text{Nd}_3\text{Ni}_2\text{B}_2\text{N}_{3-\delta}$  is a ferromagnetic or ferrimagnetic one would of course require neutron powder diffraction studies of the magnetic structure.



# Summary

The structural and physical properties of quaternary  $R_3\text{Ni}_2\text{B}_2\text{N}_{3-\delta}$  and their pseudo-quaternary solid solutions  $\text{La}_{3-x}\text{R}_x\text{Ni}_2\text{B}_2\text{N}_{3-\delta}$  (with  $R = \text{Ce, Pr, Nd}$ ) have been investigated.

For  $\text{La}_3\text{Ni}_2\text{B}_2\text{N}_{3-\delta}$ , the main focus was to control the nitrogen off-stoichiometry in a systematic way and to study the interrelationships between the nitrogen stoichiometry and the physical properties of this compound. Nuclear magnetic resonance studies as well as neutron powder diffraction confirmed the N-vacancies being located on a specific nitrogen lattice site. Various nominal compositions of  $\text{La}_3\text{Ni}_2\text{B}_2\text{N}_{3-\delta}$  were synthesized with a well optimized preparation technique. On the basis of powder X-ray diffraction (XRD) studies, an approximate nominal width of formation of the compound (with  $\delta \sim 0.1-0.4$ ) was anticipated. The neutron powder diffraction studies on selected compositions, however, established a relatively narrow width of formation ( $\delta \sim 0.06-0.1$ ).

The superconducting properties of  $\text{La}_3\text{Ni}_2\text{B}_2\text{N}_{3-\delta}$  revealed distinct composition dependent variations. A linear correlation of residual resistivity with the N-stoichiometry as well as with the transition temperature  $T_c$  is observed. Within the width of formation,  $T_c$  varies from 12.2 K to 14 K which is unusual for conventional  $s$ -wave superconductors and may indicate an unconventional order parameter. However,  $\text{La}_3\text{Ni}_2\text{B}_2\text{N}_{3-\delta}$  clearly exhibits an exponential temperature dependence of the electronic specific heat for  $T < T_c/2$  which is a solid evidence for an  $s$ -wave superconducting order parameter. An attempt to model SC state physical properties and their N-vacancy induced variations together with the corresponding variation of  $T_c$  in terms of an anisotropic Eliashberg model failed. The variation of  $T_c$  with the N-stoichiometry in  $\text{La}_3\text{Ni}_2\text{B}_2\text{N}_{3-\delta}$  might, thus, be a consequence of defect induced electronic changes rather than an effect of simple potential scattering.

Powder XRD confirms the existence of the solid solutions  $\text{La}_{3-x}\text{R}_x\text{Ni}_2\text{B}_2\text{N}_{3-\delta}$  with  $R = \text{Ce, Pr, Nd}$  from  $x = 0-3$  whereby the lattice parameter  $a$  follows the lanthanide contraction, i.e. decreases with increasing  $R$ -fraction, whereas the lattice parameter  $c$  shows a non-monotonic variation with a maximum at low  $R$ -fraction. Magnetic susceptibility and resistivity data of  $\text{La}_{3-x}\text{R}_x\text{Ni}_2\text{B}_2\text{N}_{3-\delta}$  reveal a rapid reduction of  $T_c$  with

increasing  $R$  content which is analyzed in terms of the Abrikosov-Gor'kov pair breaking theory. The suppression of superconductivity is stronger in the case of Ce substitution and is attributed to an intermediate valence behaviour of Ce. In case of Pr and Nd substitution,  $T_c$  scales roughly with the effective de Gennes factor of these  $R$ -ions.

The results of magnetic, thermodynamic and transport studies characterize  $\text{Ce}_3\text{Ni}_2\text{B}_2\text{N}_{3-\delta}$  as an intermediate valence system with moderately enhanced values of the Sommerfeld coefficient and the low temperature susceptibility  $\chi_0$  as compared to  $\text{La}_3\text{Ni}_2\text{B}_2\text{N}_{3-\delta}$  originating from Ce  $4f$  contributions. The high temperature susceptibility indicates a Ce valence of about 3.2. Transport properties, namely the electrical resistivity and thermoelectric power, are analyzed in terms of the degenerate Anderson lattice model revealing a Kondo temperature,  $T_K^{\text{ALM}} \sim 1100$  K.

The specific heat and resistivity data of  $\text{Pr}_3\text{Ni}_2\text{B}_2\text{N}_{3-\delta}$  point towards a non-magnetic singlet ground state though a clear evidence from magnetic susceptibility might require studies on cleaner samples. In the case of  $\text{Nd}_3\text{Ni}_2\text{B}_2\text{N}_{3-\delta}$  a ferrimagnetic ordering below 20 K and a spin reorientation transition towards a nearly antiferromagnetic state at about 10 K are observed.

# Appendix A

## Additional X-ray diffraction data

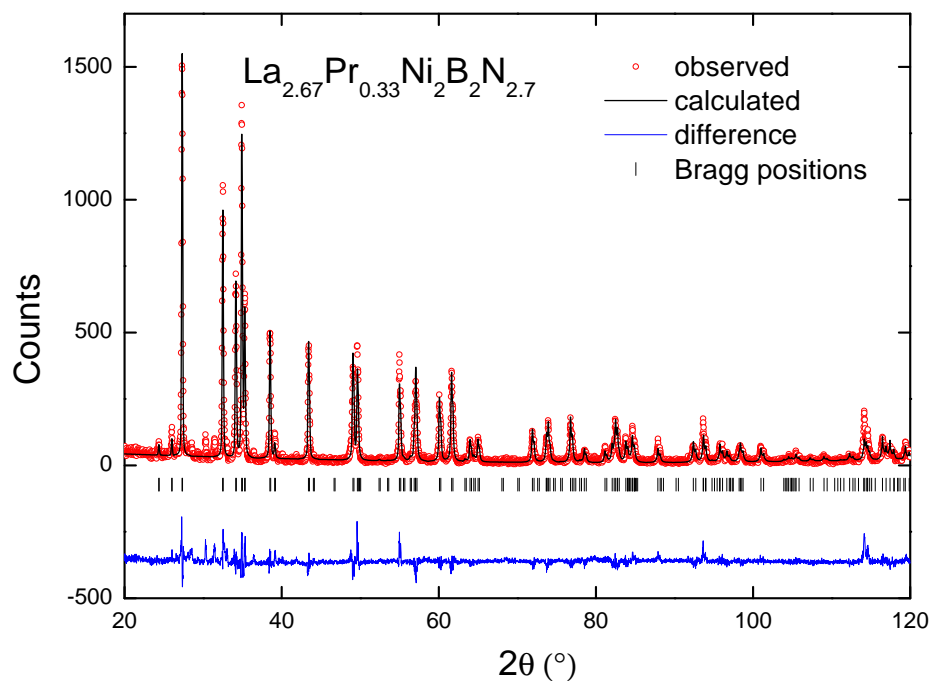


Figure A.1: Measured, calculated and difference XRD pattern of  $\text{La}_{2.67}\text{Pr}_{0.33}\text{Ni}_2\text{B}_2\text{N}_{2.7}$ . Short vertical lines indicate the position of Bragg reflections.

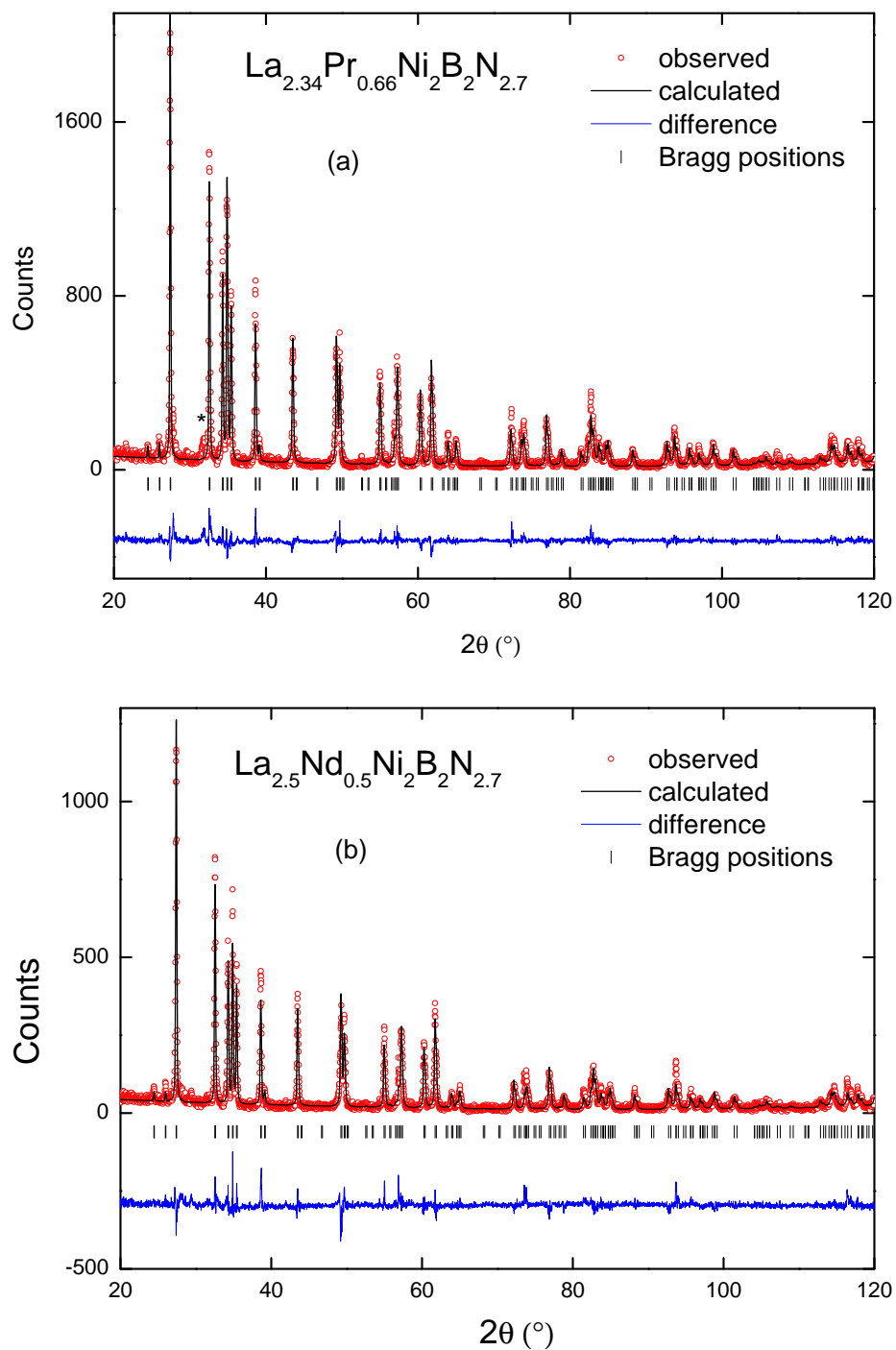


Figure A.2: Measured, calculated and difference XRD pattern of  $\text{La}_{2.34}\text{Pr}_{0.66}\text{Ni}_2\text{B}_2\text{N}_{2.7}$  (a) and  $\text{La}_{2.5}\text{Nd}_{0.5}\text{Ni}_2\text{B}_2\text{N}_{2.7}$  (b).

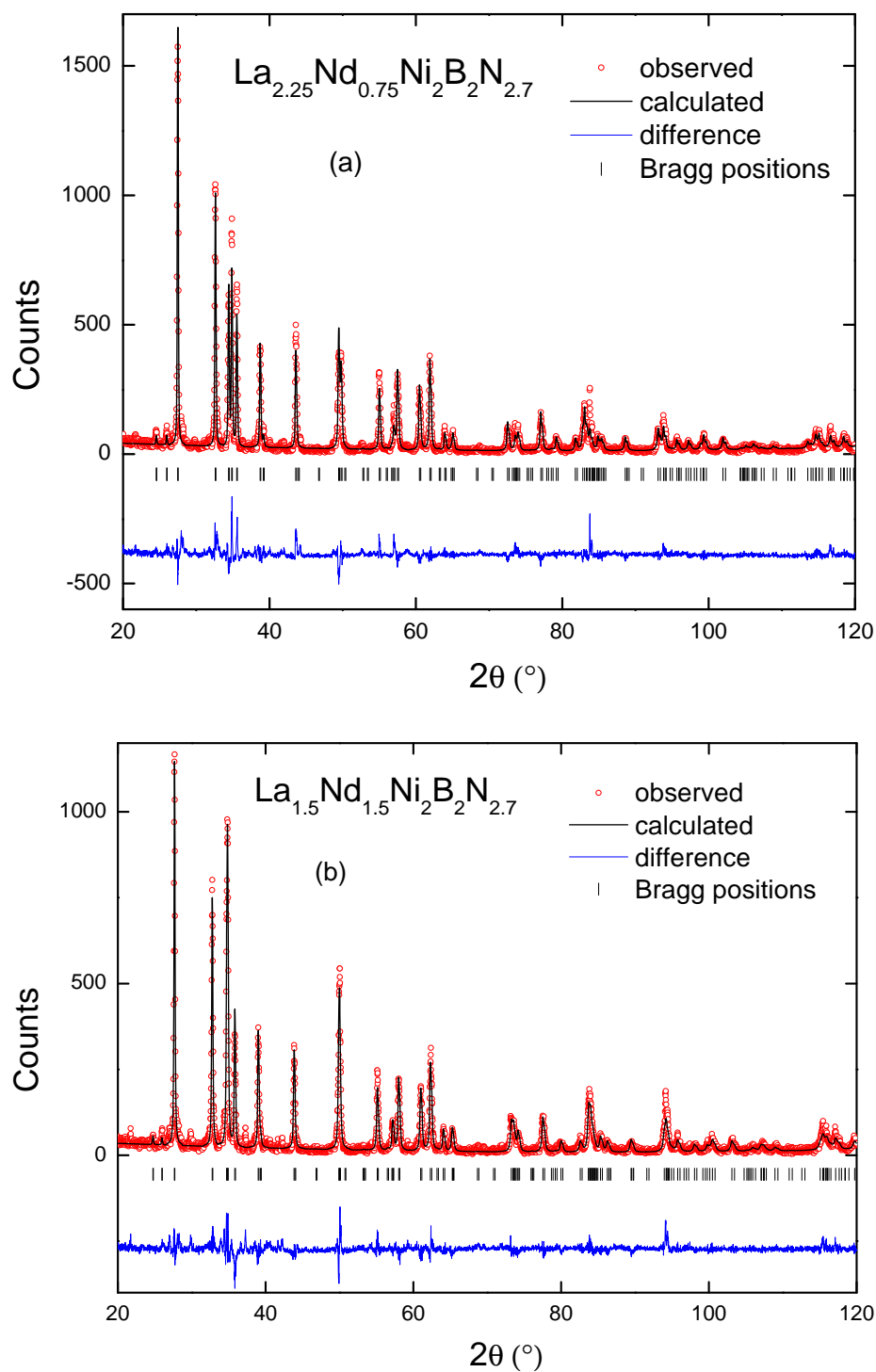


Figure A.3: Measured, calculated and difference XRD pattern of  $\text{La}_{2.25}\text{Nd}_{0.75}\text{Ni}_2\text{B}_2\text{N}_{2.7}$  (a) and  $\text{La}_{1.5}\text{Nd}_{1.5}\text{Ni}_2\text{B}_2\text{N}_{2.7}$  (b).

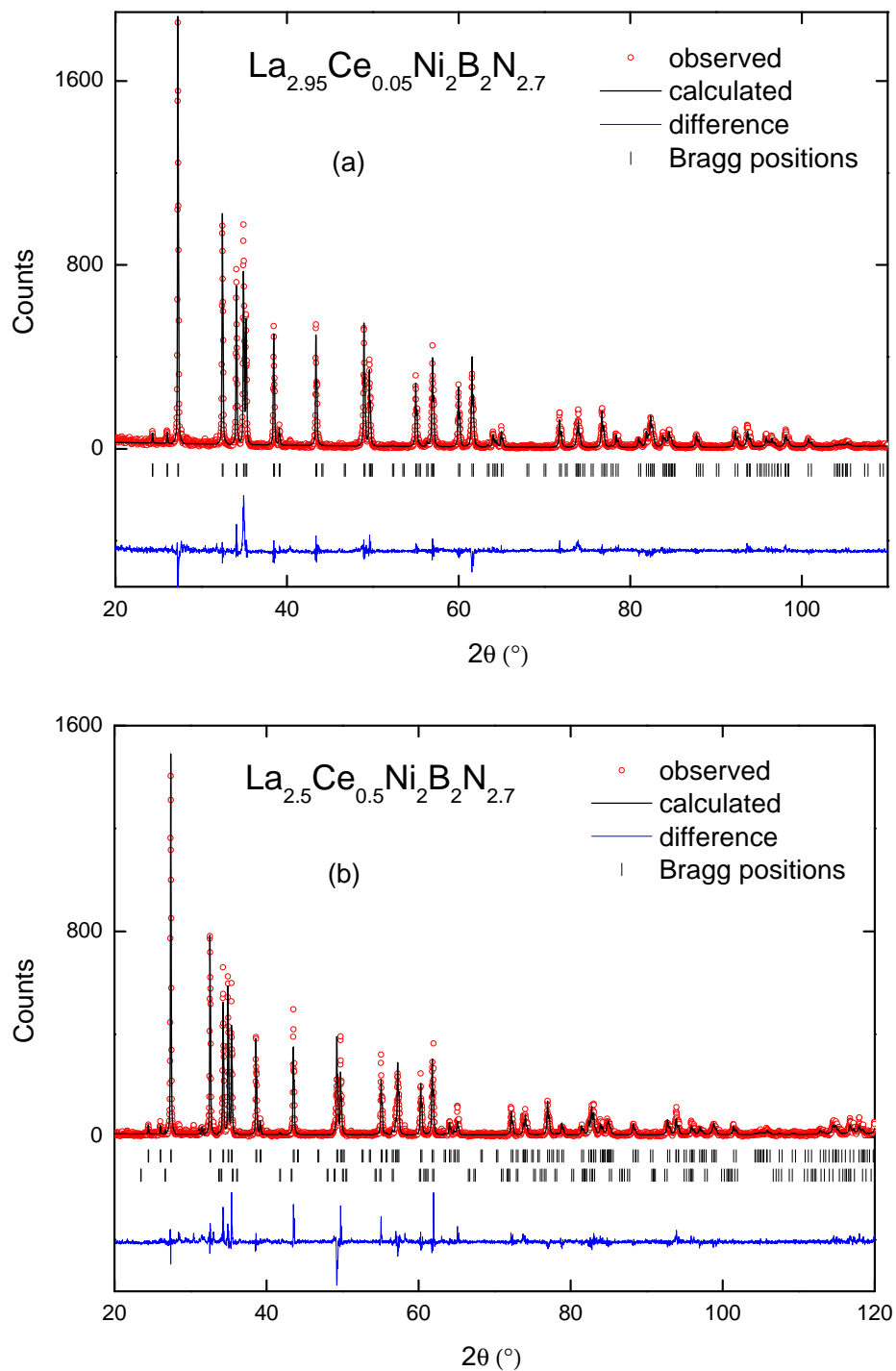


Figure A.4: Measured, calculated and difference XRD pattern of  $\text{La}_{2.95}\text{Ce}_{0.05}\text{Ni}_2\text{B}_2\text{N}_{2.7}$  (a) and  $\text{La}_{2.5}\text{Ce}_{0.5}\text{Ni}_2\text{B}_2\text{N}_{2.7}$  (b).

# Bibliography

- [1] S. Berger, Master's thesis, Institut für Festkörperphysik, TU Wien, 2000.
- [2] W. Nernst, Sitzungsbericht der K.Preuss. Akad. Wiss. **12**, 261 (1910).
- [3] G. Schaudy, PhD thesis, TU Wien, 1995.
- [4] H. Michor, PhD thesis, TU Wien, 1996.
- [5] R. Resel, E. Gratz, A. T. Burkov, T. Nakama, M. Higa, and K. Yagasaki, Rev. of Sci. Instrum. **67**, 1970 (1996).
- [6] W. Meissner and R. Ochsenfeld, Naturwissenschaften **21**, 787 (1933).
- [7] A. A. Abrikosov, Zh. Eksp. Teor. Fiz. **32**, 1442 (1957).
- [8] V. L. Ginzburg and L. D. Landau, Zh. Eksp. Teor. Fiz. **20**, 1064 (1950).
- [9] L. P. Gor'kov, Zh. Eksp. Teor. Fiz. **36**, 1918 (1959).
- [10] M. Tinkham, *Introduction to superconductivity*, McGraw-Hill, 2nd edition, 1996.
- [11] H. Fröhlich, Phys. Rev. **79**, 845 (1950).
- [12] J. Bardeen, Phys. Rev. **81**, 829 (1951).
- [13] A. B. Pippard, IEEE, MAG-23 **2**, 371 (1987).
- [14] L. N. Cooper, Phys. Rev. **104**, 1189 (1956).
- [15] J. Bardeen, L. N. Cooper, and J. R. Schrieffer, Phys. Rev. **108**, 1175 (1957).
- [16] G. Grimvall, *The electron-phonon interaction in metals*, North-Holland, 1981.
- [17] S. Vonsovskii, Y. A. Izyumov, and E. Z. Kurmaev, *Superconductivity of transition metals*, Springer-Verlag Berlin, 1982.

- [18] G. M. Eliashberg, Zh. Eksp. Teor. Fiz. **38**, 966 (1960).
- [19] W. L. McMillan, Phys. Rev. **167**, 331 (1968).
- [20] J. P. Carbotte, Rev. Mod. Phys. **62**, 1027 (1990).
- [21] D. Markowitz and L. P. Kadanoff, Phys. Rev. **131**, 563 (1963).
- [22] J. M. Daams and J. P. Carbotte, J. Low Temp. Phys. **43**, 263 (1981).
- [23] V. Ambegaokar, *Superconductivity*, volume 1, p. 259, Dekker, New York, 1969.
- [24] L. Niel, N. Giesinger, H. W. Weber, and E. Schachinger, Phys. Rev. B **32**, 2976 (1985).
- [25] M. Prohammer and E. Schachinger, Phys. Rev. B **36**, 8353 (1987).
- [26] S. Manalo, H. Michor, G. Hilscher, M. Brühwiler, and B. Batlogg, Phys. Rev. B **73**, 224520 (2006).
- [27] H. W. Weber, E. Seidl, C. Laa, E. Schachinger, M. Prohammer, A. Junod, and D. Eckert, Phys. Rev. B **44**, 7585 (1991).
- [28] B. B. Goodman, IBM J. Res. Dev. **6**, 63 (1962).
- [29] H. Takagi, R. Cava, H. Eisaki, J. Lee, K. Mizuhashi, B. Batlogg, S. Uchida, J. Krajewski, and W. P. Jr., Physica C **228**, 389 (1994).
- [30] K. D. D. Rathnayaka, A. K. Bhatnagar, A. Parasiris, D. G. Naugle, P. C. Canfield, and B. K. Cho, Phys. Rev. B **55**, 8506 (1997).
- [31] K. Ghosh, S. Ramakrishnan, A. K. Grover, G. Chandra, T. V. C. Rao, P. K. Mishra, G. Ravikumar, and V. C. Sahni, Physica B **223**, 109 (1996).
- [32] N. R. Werthamer, E. Helfand, and P. C. Hohenberg, Phys. Rev. **147**, 295 (1966).
- [33] G. Hilscher and H. Michor, *Superconductivity and Magnetism in Quaternary Borocarbides and Boronitrides, in Studies on High Temperature Superconductors*, volume 28, p. 241, Nova Science Publishers, New York, 1999.
- [34] K.-H. Mueller and V. N. Narozhnyi, Reports on Progress in Physics **64**, 943 (2001).
- [35] S. V. Shulga, S.-L. Drechsler, G. Fuchs, K.-H. Müller, K. Winzer, M. Heinecke, and K. Krug, Phys. Rev. Lett. **80**, 1730 (1998).



- [36] S. Manalo, H. Michor, M. El-Hagary, G. Hilscher, and E. Schachinger, *Phys. Rev. B* **63**, 104508 (2001).
- [37] G. Behr, W. Löser, G. Graw, and K. Nenkov, *J. Mater. Res.* **14**, 16 (1999).
- [38] H. Takeya, K. Kadowaki, K. Hirata, and T. Hirano, *J. of Alloys and Compounds* **245**, 94 (1996).
- [39] G. Behr, W. Löser, G. Graw, H. Bitterlich, J. Freudenberger, J. Fink, and L. Schultz, *Journal of Crystal Growth* **198-199**, 642 (1999).
- [40] R. J. Cava, H. W. Zandbergen, B. Batlogg, H. Eisaki, H. Takagi, J. J. Krajewski, W. F. Peck, E. M. Gyorgy, and S. Uchida, *Nature* **372**, 245 (1994).
- [41] H. Michor, R. Krendelsberger, G. Hilscher, E. Bauer, C. Dusek, R. Hauser, L. Naber, D. Werner, P. Rogl, and H. W. Zandbergen, *Phys. Rev. B* **54**, 9408 (1996).
- [42] T. Wideman, R. J. Cava, and L. G. Sneddon, *Chem. Mater.* **8**, 2215 (1996).
- [43] M. Sieberer, Master's thesis, TU Wien, 2004.
- [44] C. Rupprecht, Master's thesis, TU Wien, 2008.
- [45] Q. Huang, B. Chakoumakos, A. Santoro, R. Cava, J. Krajewski, and W. P. Jr., *Physica C: Superconductivity* **244**, 101 (1995).
- [46] H. W. Zandbergen, J. Jansen, R. J. Cava, J. J. Krajewski, and W. F. Peck Jr., *Nature* **372**, 759 (1994).
- [47] T. Roisnel and J. Rodriguez-Carvajal, **378**, 118 (2001).
- [48] V. F. Sears, *Neutron News* **3**, 29 (1992).
- [49] C. P. Slichter, *Principles of Magnetic Resonance*, Interscience, New York, 1978.
- [50] M. Pieper, to be published.
- [51] Yellow book, <http://www.ILL.fr/>, 2008.
- [52] J. W. Lynn, S. Skanthakumar, Q. Huang, S. K. Sinha, Z. Hossain, L. C. Gupta, R. Nagarajan, and C. Godart, *Phys. Rev. B* **55**, 6584 (1997).
- [53] T. Siegrist, R. Cava, J. Krajewski, and W. P. Jr., *J. Alloys Compd.* **216**, 135 (1994).

- [54] D. C. Wallace, *Thermodynamics of crystals*, Dover, New York, 1998.
- [55] M. Rotter, H. Muller, E. Gratz, M. Doerr, and M. Loewenhaupt, *Rev. Sci. Instrum.* **69**, 2742 (1998).
- [56] J. Genossar and M. Steinitz, *Rev. Sci. Instrum.* **61**, 2769 (1990).
- [57] C. Kittel, *Introduction to solid state physics*, Wiley New York, 8th edition, 2005.
- [58] B. T. M. Willis and A. W. Proyer, *Thermal vibrations in Crystallography*, Cambridge University Press, London, 1975.
- [59] C. Wang and K. Girgis, *J. of Less Comm. Met.* **158**, 319 (1990).
- [60] L. C. Gupta, *Adv. Phy.* **55**, 691 (2006).
- [61] H. Michor, G. Hilscher, R. Krendelsberger, P. Rogl, and F. Bourée, *Phys. Rev. B* **58**, 15045 (1998).
- [62] G. Kresse and D. Joubert, *Phys. Rev. B* **59**, 1758 (1999).
- [63] N. Ashcroft and N. Mermin, *Solid State Physics*, Saunders College, Philadelphia, 2005.
- [64] D. Lipp, A. Gladun, K. Bartkowski, A. Belger, P. Paufler, and G. Behr, *Physica B: Condensed Matter* **284-288**, 1103 (2000).
- [65] M. Gurvitch, A. K. Ghosh, H. Lutz, and M. Strongin, *Phys. Rev. B* **22**, 128 (1980).
- [66] G. W. Webb, Z. Fisk, J. J. Engelhardt, and S. D. Bader, *Phys. Rev. B* **15**, 2624 (1977).
- [67] M. J. Rice, *Phys. Rev. Lett.* **20**, 1439 (1968).
- [68] S. Ramakrishnan and G. Chandra, *Phys. Rev. Lett.* **57**, 1961 (1986).
- [69] M. Kaveh and N. Wiser, *Adv. Phy.* **33**, 257 (1984).
- [70] A. H. MacDonald, *Phys. Rev. Lett.* **44**, 489 (1980).
- [71] K. Kadowaki and S. B. Woods, *Solid State Communications* **58**, 507 (1986).
- [72] K. Miyake, T. Matsuura, and C. Varma, *Solid State Communications* **71**, 1149 (1989).
- [73] P. B. Allen, *Phys. Rev. B* **36**, 2920 (1987).

- [74] D. J. Singh and W. E. Pickett, *Phys. Rev. B* **51**, 8668 (1995).
- [75] P. B. Allen, Academic Press, New York, 1999, p. 478.
- [76] D. G. Naugle, D. Rathnayaka, and A. K. Bhatnagar, *Transport in Rare-earth-Nickel-Borocarbides, in Studies on High Temperature Superconductors*, volume 28, p. 189, Nova Science Publishers, New York, 1999.
- [77] M. Sera, S. Kobayash, M. Hiroi, N. Kobayashi, H. Takeya, and K. Kadwaki, *Phys. Rev. B* **54**, 3062 (1996).
- [78] B. D. Hennings, D. G. Naugle, and P. C. Canfield, *Phys. Rev. B* **66**, 214512 (2002).
- [79] P. G. Klemens, *Thermal Conductivity*, New York Academic, 1969.
- [80] B. I. Belevtsev, B. D. Hennings, K. D. D. Rathnayaka, and D. G. Naugle, Nova Science Publishers, New York, 2003, volume 46.
- [81] P. W. Selwood, *Magnetochemistry*, Interscience, New York, 1956.
- [82] K. G. Wilson, *Rev. Mod. Phys.* **47**, 773 (1975).
- [83] R. Podlucky and D. Reith, Private communication, 2010.
- [84] S.-L. Drechsler, *High-Tc Superconductors and Related materials*, volume 86, p. 167, Kluwer Academic, 2001.
- [85] I. N. Askerzade and A. Gencer, *Supercond. Sci. Tech.* **15**, L13 (2002).
- [86] H. Schmidt and H. Braun, *Physica C* **229**, 315 (1994).
- [87] E. Z. Melikhov and V. G. Shapiro, *Fiz. Khim. Tekh.* **4**, 1437 (1991).
- [88] C. J. Gorter and H. Casimir, *Physik. Zeitschr.* **35**, 963 (1934).
- [89] L. F. Mattheiss, *Phys. Rev. B* **49**, 13279 (1994).
- [90] G. E. Volovik, *JETP Lett.* **58**, 469 (1993).
- [91] A. L. Fetter and P. C. Hohenberg, *Superconductivity*, volume 2, p. 817, Dekker, New York, 1969.
- [92] M. Nohara, M. Isshiki, H. Takagi, and R. J. Cava, *J Phys. Soc. Jpn.* **66**, 1888 (1997).
- [93] A. P. Ramirez, *Phys. Lett. A* **211**, 59 (1996).

- 
- [94] N. Nakai, P. Miranović, M. Ichioka, and K. Machida, *Phys. Rev. B* **70**, 100503 (2004).
- [95] J. E. Sonier, M. F. Hundley, and J. D. Thompson, *Phys. Rev. B* **73**, 132504 (2006).
- [96] Y. Taguchi, M. Hisakabe, and Y. Iwasa, *Phys. Rev. Lett.* **94**, 217002 (2005).
- [97] J. Sereni, *Handbook on the Physics and Chemistry of Rare Earths*, volume 15, p. 1, 1991.
- [98] F. Steglich, J. Aarts, C. D. Bredl, W. Lieke, D. Meschede, W. Franz, and H. Schäfer, *Phys. Rev. Lett.* **43**, 1892 (1979).
- [99] H. Hegger, C. Petrovic, E. G. Moshopoulou, M. F. Hundley, J. L. Sarrao, Z. Fisk, and J. D. Thompson, *Phys. Rev. Lett.* **84**, 4986 (2000).
- [100] E. Bauer, G. Hilscher, H. Michor, C. Paul, E. W. Scheidt, A. Griбанov, Y. Seropegin, H. Noël, M. Sigrist, and P. Rogl, *Phys. Rev. Lett.* **92**, 027003 (2004).
- [101] B. T. Matthias, H. Suhl, and E. Corenzwit, *Phys. Rev. Lett.* **1**, 92 (1958).
- [102] E. Alleno, Z. Hossain, C. Godart, R. Nagarajan, and L. C. Gupta, *Phys. Rev. B* **52**, 7428 (1995).
- [103] S. A. Carter, B. Batlogg, R. J. Cava, J. J. Krajewski, and W. F. Peck, *Phys. Rev. B* **51**, 12829 (1995).
- [104] M. El Massalami, R. E. Rapp, and G. J. Nieuwenhuys, *Physica C: Superconductivity* **304**, 184 (1998).
- [105] T. Ali, C. Rupprecht, R. T. Khan, E. Bauer, G. Hilscher, and H. Michor, *J. Phys. Conf. Series* **200**, 012004 (2010).
- [106] J. Glaser, T. Mori, and H. Meyer, *Z. Anorg. Allg. Chem* **634**, 1067 (2008).
- [107] D. Wohlleben and J. Röhler, *J. Appl. Phys.* **55**, 1904 (1984).
- [108] P. Weidner, B. Wittershagen, B. Roden, and D. Wohlleben, *Solid State Commun.* **48**, 915 (1983).
- [109] J. Jensen and A. K. Mackintosh, *Rare Earth Magnetism*, Clarendon, Oxford, 1991.

- [110] P. Schlottmann, *Theory of Heavy Fermions and Valence Fluctuations*, p. 68, Springer, Berlin, 1985.
- [111] N. Read and D. M. News, J. Phys. C **16**, L1055 (1983).
- [112] A. C. Hewson and J. W. Rasul, J. Magn. Magn. Mater. **47-48**, 339 (1985).
- [113] N. Tsujii, H. Kontani, and K. Yoshimura, Phys. Rev. Lett. **94**, 057201 (2005).
- [114] D. L. Cox and N. Grewe, Z. Phys. C **71**, 321 (1988).
- [115] M. Kohler, Z. Phys. C **51**, 223 (1983).
- [116] K. Behnia, D. Jaccard, and J. Flouquet, J. Phys.: Condens. Matter **16**, 5187 (2004).
- [117] A. A. Abrikosov and L. P. Gor'kov, Sov. Phys.-JETP **12**, 1243 (1961).
- [118] M. S. S. Brooks and B. Johansson, *Handbook of magnetic materials*, volume 7, p. 139, North Holland, 1993.
- [119] M. El-Hagary, PhD thesis, TU Wien, 1999.
- [120] M. Diviš, K. Schwarz, P. Blaha, G. Hilscher, H. Michor, and S. Khmelevskiy, Phys. Rev. B **62**, 6774 (2000).
- [121] V. Narozhnyi, J. Freudenberger, G. Fuchs, K. Nenkov, D. Eckert, A. Czopnik, and K.-H. Müller, J. Low Temp. Phys. **117**, 1599.
- [122] C. Mazumdar, M. Rotter, M. Frontzek, H. Michor, M. Doerr, A. Kreyssig, M. Koza, A. Hiess, J. Voigt, G. Behr, L. C. Gupta, M. Prager, and M. Loewenhaupt, Phys. Rev. B **78**, 144422 (2008).
- [123] E. Gratz, in *Encyclopedia of Materials: Science and Technology*, edited by K. H. J. Buschow, R. W. Cahn, and M. C., Elsevier, Oxford, 2001, p. 5085.

# List of publications

1. T. Ali, C. Rupperecht, R.T. Khan, E. Bauer, G. Hilscher, H. Michor  
"The effect of nitrogen vacancies in  $La_3Ni_2B_2N_{3-\delta}$ ,"  
J. Physics: Conf. Series **200**, 012004 (2010).
2. T. Ali, E. Bauer, G. Hilscher, H. Michor  
"Structural, Superconducting and Magnetic Properties of  
 $La_{3-x}R_xNi_2B_2N_3$  ( $R= Ce, Pr, Nd$ )"  
Solid State Phenomena (2011), in print.
3. T. Ali, E. Bauer, G. Hilscher, H. Michor  
"Anderson lattice in the intermediate valence compound  $Ce_3Ni_2B_2N_{3-\delta}$ "  
Physical Review B (2010), Submitted.

# List of conference contributions

1. T. Ali, E. Bauer, G. Hilscher, H. Michor  
*"Structural, Superconducting and Magnetic Properties of Rare Earth Nickel Boronitride Compounds"*, 11. International Conference on Crystal Chemistry of Intermetallic Compounds, May 30 to Jun. 5, 2010, Lviv, Ukraine.
2. H. Michor, T. Ali, E. Bauer, G. Hilscher  
*"Structural, Superconducting and Magnetic Properties of  $La_{3-x}R_xNi_2B_2N_3$  ( $R= Ce, Pr, Nd$ )"*, 17. International Conference on Solid Compounds of Transition Elements, Sept. 5-10, 2010, Annecy, France.
3. H. Michor, T. Ali, E. Bauer, G. Hilscher  
*"Superconducting and Magnetic Properties of  $La_{3-x}R_xNi_2B_2N_3$  ( $R= Ce, Pr, Nd$ )"*, ECOM, COST P-16 Workshop, Emergent Behaviour in Correlated Systems, Sept. 28-29, 2009, Krakow, Poland.
4. T. Ali, C. Rupprecht, R. T. Khan, E. Bauer, G. Hilscher, H. Michor  
*"The effect of nitrogen vacancies in  $La_3Ni_2B_2N_{3-\delta}$ "*, International Conference on Magnetism, Jul. 26-31, 2009, Karlsruhe, Germany.

# Curriculum Vitae

---

## Tahir Ali

Date of Birth 7 July 1977  
Place of Birth Peshawar, Pakistan  
Nationality Pakistani

### Education:

1982-1986 Primary school in Peshawar, Pakistan  
1986-1992 Secondary school in Peshawar, Pakistan  
1992-1994 Higher secondary school, Peshawar Pakistan  
1994-1996 Graduation, Government College Peshawar, Pakistan  
(Physics, Mathematics, Statistics)  
1997-1999 Masters Degree, M.Sc. in Physics,  
University of Peshawar, Pakistan  
1999-2001 Masters Degree, M.Sc. in Nuclear Engineering,  
Pakistan Institute of Engineering and Applied Sciences,  
Islamabad, Pakistan

### Job Experience:

2001-2007 Senior Scientist at Informatics Complex,  
Islamabad, Pakistan

### PhD Studies:

2007-2010 Ph. D student at Institute of Solid State Physics,  
Vienna University of Technology, Austria.  
Thesis Title: "*Superconductivity and Magnetism  
in Rare-earth Nickel Boronitrides*" under supervision  
of Prof. Herwig Michor.